Dipl.-Ing. Stefan Christian Polster

Enhancing Secure Grid Operation with Power Flow Controlling Devices and WAMS

DOCTORAL THESIS

to achieve the university degree of

Doktor der technischen Wissenschaften

submitted to

Graz University of Technology

Supervisor

Ao. Univ.-Prof. Dipl.-Ing. Dr. techn. Herwig Renner

Institute of electrical Power Systems

Graz University of Technology

External Reviewer

Prof. Olof Samuelsson, PhD

Industrial Electrical Engineering and Automation

Lund University

Graz, April 2021

AFFIDAVIT

I declare that I have authored this thesis independently, that I have not used other than the declared sources/resources, and that I have explicitly indicated all material which has been quoted either literally or by content from the sources used. The text document uploaded to TUGRAZonline is identical to the present doctoral thesis.

Date, Signature

Acknowledgements

The creation of a PhD-Thesis from a crude research idea to the final document is a long and sometimes frustrating process. I would not have successfully finished it without the aid and support from colleagues, friends and family over the last five years.

I want to thank my supervisor Herwig Renner first, since he not only recruited and guided me through my PhD after already supervising my master's thesis but also gave me the necessary support acquiring projects and funding for my position. Thank you also for contributing the majority of my education in electrical power systems and being a reliable supervisor.

Further, I would like to thank Olof Samuelsson for accepting to review my thesis as well as hosting me during a research exchange at his department at Lund University.

Thanks also to Kjetil Uhlen to enable a research exchange at the NTNU Trondheim.

The academic discussions with Robert Schürhuber on topics of my thesis and other aspects of electrical power engineering have improved my thesis and publications. Thanks for your time and input.

I also thank my former and current colleagues at the Institute of Electrical Power Engineering in general for the good working atmosphere. Special thanks to Mike Lagler for helping me to find my motivation during frustrating episodes of my PhD and becoming a good friend. Further, I want to highlight him, Alexander Rainer, Philipp Schachinger and Manuel Galler for being – sometimes against their will – sparring partners discussing parts of my thesis and occurring obstacles. I also want to thank Dennis Albert, Markus Resch and Thomas Halbedl for being great office mates.

Kudos to my best men Hannes and Stephan for not getting tired of telling me, that I am still a student and should find a real work.

I thank my family for supporting me over the complete duration of my education.

Finally, special thanks to my beloved wife Karin and my son Jonathan for making my world a happier place and always reminding me, what is most important in life.

Abstract

The increasing energy consumption and the rise of renewable energy sources in combination with the unbundling of formerly vertically integrated energy suppliers into independent energy production and transmission companies create additional challenges in power system operation and stability. Despite the effort spent and the results gained in research of smart distribution grids and micro grids, transmission systems will inevitably be a part of the electrical power system in the future. On transmission system level, grid expansion in the sense of new construction or reinforcement of AC transmission lines cannot keep pace with the amount of installed generation capacity of renewables leading to a branch loading near the capacity limit. To maintain a stable network operation under these conditions, optimal use of the flexibilities given by power flow controlling devices, e. g. embedded HVDC links and phase shifting transformers, and real time measurements provided by wide area measurement systems is imperative.

In this thesis, three different aspects of the network operation with power flow controlling devices and available wide area measurement systems are addressed.

The first is the evaluation of the influence of different degrees of coordination of power flow controlling devices on the redispatch costs and volume in a flow-based market setting. It is shown thereby, that the redispatch costs only decrease, if power flow controlling devices are coordinated. However, if the power flow controlling devices are used to reduce the loading of the branches controllable by them without coordination, the redispatch costs might even increase depending on the load situation.

The second aspect is the need for accurate state awareness under strained network conditions. Therefore, an algorithm to detect multi branch outages based on a linear model and optimization techniques is developed. The algorithm is able to correctly detect multi branch outages solely using pre-fault topology information and node voltage angle measurements from synchronous wide area measurement systems as input. The algorithm’s performance is evaluated with simulations of the Nordic-32-Bus test system.

The last part of this thesis is dedicated to emergency control strategies of embedded HVDC links. In the first step, existing control strategies for HVDC links are evaluated in a small radial network and compared to a novel control strategy. The simulation results show that the novel control strategy is superior in relieving overloaded branches and equal in terms of maximum load ability and voltage stability. In the second step, an emergency control strategy combining efficient branch relief and voltage support in a meshed network is proposed. This strategy is based on linearized sensitivities to active and reactive power setpoint changes of the HVDC link converters and synchronous node voltage measurements obtained from wide are measurement systems.

Kurzfassung

Der steigende Energieverbrauch und der Ausbau von Erneuerbaren in Kombination mit der Entflechtung ehemals vertikal integrierter Energieversorger zu unabhängigen Energieerzeugungsunternehmen und Netzbetreiber stellen den Betrieb und die Stabilität des Stromnetzes vor zusätzliche Herausforderungen. Trotz der Fortschritte bei der Erforschung intelligenter Verteil- und Mikronetze werden Übertragungsnetze auch in Zukunft ein unvermeidlicher und systemkritischer Bestandteil des Stromnetzes sein. Auf der Übertragungsnetzebene kann der Netzausbau im Sinne eines Neubaus oder einer Verstärkung von Hochspannungsleitungen nicht mit der installierten Erzeugungskapazität von Erneuerbaren Schritt halten, was Leitungsbelastungen nahe den thermischen Grenzen zur Folge hat. Um unter diesen Bedingungen dennoch einen stabilen Netzbetrieb aufrechtzuerhalten, muss die durch lastflusssteuernde Elemente, z. B. netzparallele HGÜ-Leitungen und Phasenschiebertransformatoren, zusätzlich verfügbare Flexibilität unter Einsatz von Echtzeitmessungen mit Wide Area Measurement Systems optimal ausgenutzt werden.

In dieser Arbeit werden drei Fragestellungen des Netzbetriebs mit lastflusssteuernden Elementen und Wide Area Measurement Systems näher untersucht.

Die erste behandelt die Evaluierung des Einflusses der Koordination und Koordinationsstrategie von lastflusssteuernden Elementen auf die Redispatchkosten und -volumen in einem auf Flow Based Market Coupling basierenden Strommarkt. Es wird dabei gezeigt, dass die Redispatchkosten nur dann sinken, wenn lastflusssteuernde Elemente ausreichend koordiniert werden. Wird jedoch mit den lastflusssteuernden Elementen unkoordiniert die Belastung von elektrisch nahen Leitungen verringert, erhöhen sich abhängig von der Lastsituation die Redispatchkosten.

Die zweite angesprochene Fragestellung harkt bei der Notwendigkeit einer genauen Abbildung des Netzwerkzustandes in Leitsystemen bei angespannten Lastflusssituationen ein. Diese Arbeit fokussiert sich dabei auf die Entwicklung eines Algorithmus zur Erkennung von Mehrfachausfällen von Übertragungselementen basierend auf einem linearisierten Netzmodell und Optimierungstechniken. Der entwickelte Algorithmus ist in der Lage, Mehrfachausfälle ausschließlich anhand von Informationen zur Vorfehlertopologie und den mit Wide Area Measurement Systems gemessenen Winkeländerungen der Knotenspannungen korrekt zu erkennen. Die Anwendbarkeit des Algorithmus wird anhand von Simulationen des Nordic-32-Bus-Testsystems bewertet.

Der letzte Teil dieser Arbeit befasst sich mit Notfallregelkonzepten für netzparallele HGÜ-Leitungen. Es werden dafür bekannte Regelstrategien für netzparallele HGÜ-Leitungen in einem radialen Netzwerk evaluiert und mit einer in dieser Arbeit entwickelten Regelstrategie verglichen. Die Simulationsergebnisse zeigen, dass bei Anwendung der neu entwickelten Regelstrategie überlastete Zweige besser entlastet werden können und hinsichtlich der maximal möglichen Leistungsübertragung und Spannungsstabilität annähernd gleiche Grenzwerte erreicht werden. Weiters wird ein auf den linearisierten Sensivitäten von Leitungsbelastungen und Knotenspannungen gegenüber den Wirk- und Blindleistungssollwerten der HGÜ-Leitung basierendes Notfallregelkonzept erarbeitet, das eine effiziente Leitungsentlastung und Spannungsunterstützung in einem vermaschten Netzwerk ermöglicht.

List of Symbols

$\boldsymbol{\alpha}$	Vector of phase shifter angles
$\boldsymbol{\alpha}_{max}$	Vector of maximal PST angle
$\boldsymbol{\alpha}_{min}$	Vector of minimal PST angle
$\boldsymbol{\alpha}_{op}$	Vector of PST angle setpoints
$\boldsymbol{\alpha}_{PST,max}$	Vector of maximal PST angle
$\boldsymbol{\alpha}_{UPFC,max}$	Vector of maximal angle changes utilizable by UPFCs
$\Delta\boldsymbol{\vartheta}$	Vector of node voltage angle changes
$\Delta\mathbf{p}_{iO}$	Vector of branch flow change of branch i caused by all single branch outages O
$\boldsymbol{\Delta P}_{L}$	Branch flow change matrix
$\boldsymbol{\Delta p}_{L}$	Vector of branch flow change
$\Delta\mathbf{p}_{NL}$	Vector of power injections according to branch outages
$\boldsymbol{\delta}$	Newton direction
$\boldsymbol{\vartheta}$	Vector of node voltage angles
$\boldsymbol{\Phi}$	Node-to-remaining-branch incidence matrix
$\boldsymbol{\Psi}$	Node-to-outage-branch incidence matrix
$\mathbf{A}_{BOI}$	Branch of interest incidence matrix
$\mathbf{A}_{eq}$	Matrix of equality constraints
$\mathbf{A}_{eq}$	Matrix of inequality constraints
$\mathbf{A}_{PMU}$	PMU incidence matrix
$\mathbf{B}$	System susceptance matrix
$\mathbf{B}_{d}$	Branch susceptance diagonal matrix
$\mathbf{b}_{eq}$	Vector of equality constraints
$\mathbf{b}_{ineq}$	Vector of inequality constraints
$\mathbf{BPI}$	Branch-to-PST incidence matrix
$\mathbf{BOAC}$	Branch outage angle change matrix
$\mathbf{c}_{DC}$	Cost vector of HVDC active power setpoint change
$\mathbf{c}_{neg}$	Cost vector of negative redispatch activation
$\mathbf{c}_{pos}$	Cost vector of positive redispatch activation
$\mathbf{c}_{PST}$	Cost vector of PST angle change
$\mathbf{c}_{O}$	Cost vector of remaining overload
$\mathbf{DCDF}$	HVDC transfer distribution factor matrix
$\mathbf{f}$	Objective function vector
$\mathbf{H}$	Hessian matrix
$\mathbf{I}$	Identity matrix
$\underline{\mathbf{i}}$	Node current vector
$\mathbf{J}$	Jacobian matrix
$\mathbf{J}_{P\vartheta}$	Sub matrix of the Jacobian matrix linking the node voltage angle to the active power

$\mathbf{J}_{PV}$	Sub matrix of the Jacobian matrix linking the node voltage magnitude to the active power
$\mathbf{J}_{R}$	Reduced Jacobian matrix
$\mathbf{J}_{Q\vartheta}$	Sub matrix of the Jacobian matrix linking the node voltage angle to the reactive power
$\mathbf{J}_{QV}$	Sub matrix of the Jacobian matrix linking the node voltage magnitude to the reactive power
$\mathbf{K}_{D}$	Matrix describing the correlation between fictional node power injection and node voltage angle change
$\mathbf{k}_{iO}$	Vector of (n-1)-sensitivities of branch i in regard to all single branch outages O
$\mathbf{k}_{max,OL}$	Vector of allowed remaining overload
lb	Lower bounds of the trial variables
LODF	Line outage distribution factor matrix
MAC	Measured node voltage angle change vector
NBI	Node-to-branch incidence matrix
NDI	Node-to-DC incidence matrix
$\mathbf{p}_{DC}$	Vector of power flow of the embedded HVDC links
$\mathbf{p}_{DC,max}$	Vector of maximal power flow of the embedded HVDC links
$\mathbf{p}_{DC,min}$	Vector of minimal power flow of the embedded HVDC links
$\mathbf{p}_{DC,op}$	Vector of active power setpoints of the embedded HVDC links
$\mathbf{p}_{gen}$	Vector of generation
$\mathbf{p}_{HVDC,nom}$	Vector of nominal power of HVDC links
$\mathbf{p}_{L}$	Vector of active branch powers
$\mathbf{P}_{load}$	Vector of load
$\mathbf{p}_{N}$	Vector of active node powers
$\mathbf{p}_{RD,max}$	Vector of maximal active power of redispatch power plants
$\mathbf{p}_{RD,min}$	Vector of minimal active power of redispatch power plants
$\mathbf{p}_{RD,op}$	Vector of active power setpoints of redispatch power plants
$\mathbf{p}_{rn}$	Vector of receiving nodes' active power injections
$\mathbf{p}_{sn}$	Vector of sending nodes' active power injections
PSDF	Phase shifter distribution factor matrix
PTDF	Power transfer distribution factor matrix
pv	Adjustment vector for voltage-controlled nodes
S	Zonal exchange sensitivity matrix
$\mathbf{s}_{thermal}$	Vector of maximal branch power flow
SCM	Scalar combination matrix of the branch outage angle changes
U	Upper triangular matrix of ones
ub	Upper bounds of the trial variables
$\underline{\mathbf{v}}$	Node voltage vector
$\mathbf{v}_{se}$	Vector of UPFCs' serial voltages
x	Vector of trial variables

$\mathbf{x}^*$	Optimum point
$\mathbf{x}_{DC}$	Trial variable vector of HVDC active power setpoint change
$\mathbf{x}_{iO,pos}$	Vectors of scaling factors for positive flows on branch i in regard to all single branch outages O
$\mathbf{x}_{iO,neg}$	Vectors of scaling factors for negative flows on branch i in regard to all single branch outages O
$\mathbf{x}_{neg}$	Trial variable vector of negative redispatch activation
$\mathbf{x}_{pos}$	Trial variable vector of positive redispatch activation
$\mathbf{x}_{PST}$	Trial variable vector of PST angle change
$\mathbf{x}_{O}$	Trial variable vector of remaining overload
$\mathbf{x}_{U}$	Trial variable vector of solved overload
$\underline{\mathbf{Y}}$	Bus admittance matrix
$\underline{\mathbf{Y}}$'	Modified bus admittance matrix
$\underline{\mathbf{Z}}$	Bus impedance matrix
$\underline{\mathbf{Z}}$'	Modified bus impedance matrix

α_{ij}	Phase shifter angle between nodes i and j
Γ	Set of controllable branches
Δp_{min}	Minimum active power sensitivity for definition of controllable branches
E	Set of significant outage branches
ε_{GSK}	Lower limit of zonal sensitivity for the estimation of critical contingencies
ε	Value of the stopping condition for optimizers
ζ	Measure of result stability of the critical contingency estimation
ϑ_i, ϑ_j	Node voltage angle of nodes i and j
ϑ_{Local}	Node voltage angle of local HVDC terminal
ϑ_{Remote}	Node voltage angle of remote HVDC terminal
ϑ_{se}	Angle of UPFC's serial voltage
ϑ_{sh}	Angle of UPFC's shunt voltage
ξ	Threshold for branch outage detection
ψ_{ij}	Impedance angle of the branch connecting nodes i and j
b	Superscript indicating the base case
b_{i0}	Shunt susceptance at node i
b_{ij}	Serial susceptance of the branch connecting nodes i and j
b_L	Shunt susceptance of a branch
c	Superscript indicating the contingency case
CC	Set of critical contingency elements
cc	Notation of a specific contingency element
C_{RD}	Costs of redispatch activation
cs_P	Active power control signal
cs_Q	Reactive power control signal
C_{sum}	Overall redispatch costs

$\underline{c}_{\mathrm{u}}$	Complex voltage ratio of transformer
D	Number of HVDC links
d_C	sum of maximal scalar products
DR	Correct detection ratio
F	Branch loading based on DC-Load flow
FAV	Final adjustment value for RAM calculation
FRM	Flow reliability margin for RAM calculation
$i_{\mathrm{conv,max}}$	Maximum converter current
i_{d}	Converter direct axis current
$\underline{i}_{ij}$	Branch current on the branch connecting nodes i and j
$\underline{i}_i$, $\underline{i}_j$, $\underline{i}_m$	Node currents of nodes i, j and m
i_{q}	Converter quadrature axis current
L	Number of branches
ℓ	Notation of a specific branch
LD	Branch loading
LF	Linking factor
L_{OI}	Number of branches of interest
k	Controller gain
k_{OL}	Utilization factor for virtual redispatch
k_{trans}	Voltage dependent gain
k_{vj}	utilization factor of voltage bandwidth
M	Set of bidding zones with defined GSK
MT	Mean detection run time
N	Number of nodes
n	Notation of a specific node
Nl	Index indicating (n-1)-values
n_{min}	Minimum number of node pairs considered for the critical contingency estimation
NOL	Set of branches not overloaded in the base case
N_{PMU}	Number of PMU monitored nodes
O	Set of outage branches
o	Notation of specific outage branch
OL	Set of branches overloaded in the base case
P	Number of PSTs
p	Notation of a specific PST
p_{DC}	HVDC converter's active power setpoint
p_{ij}	Active power flow on the branch connecting nodes i and j
$p_{i,ij}^{\mathrm{se}}$	UPFC's serial active power seen from node i
p_{ij}^{sh}	UPFC's shunt active power seen from node i
p_{ij}^{se}	UPFC's serial active power after simplification
p_{in}	Measured active power of the converter control

p_{ref}	Active power setpoint of the converter control
$psens_{k,h}$	Sensitivity of branch k to active power change of HVDC link h
q_{DC}	HVDC converter's reactive power setpoint
q_{ij}	Reactive power flow on the branch connecting nodes i and j
q_{in}	Measured reactive power of the converter control
q_{ref}	Reactive power setpoint of the converter control
R	Set of remaining branches
RAM	Remaining available margin for FBMC
r_{L}	Branch serial resistance
RT	Detection run time of a single contingency event
S_{B}	Apparent power per unit base
$\underline{s}_{ij}$	Apparent power flow on the branch connecting nodes i and j
s_{thermal}	Maximal allowed branch power flow
U	Number of UPFCs
$v_{\text{AC,ref}}$	Measured AC voltage at the point of coupling of the converter control
$v_{\text{AC,ref}}$	AC voltage setpoint of the converter control
V_{B}	Voltage per unit base
v_{bw}	Voltage threshold bandwidth
$v_{\text{conv,AC}}$	AC side converter voltage
v_{DC}	DC voltage of HVDC link
$\underline{v}_i$, $\underline{v}_j$, $\underline{v}_m$	Node voltage of nodes i, j and m
v_{max}	Maximal normal operation voltage
v_{min}	Minimal normal operation voltage
v_{POC}	Voltage at point of coupling
$V_{\text{RD,vir}}$	Virtual redispatch volume
$\underline{v}_{\text{se}}$	Serial voltage of UPFC
$\underline{v}_{\text{sh}}$	Shunt voltage of UPFC
vsr_{ij}	Voltage sensitivity ratio between node j and i
vsr_{min}	Minimal voltage sensitivity ratio
V_{sum}	Overall redispatch volume
$v_{\text{trans,low}}$	Lower voltage level for ECS
$v_{\text{trans,up}}$	Upper voltage level for ECS
x_{L}	Branch serial reactance
x_{se}	UPFC serial reactance
x_{sh}	UPFC shunt reactance
x_{eq}	Equivalent reactance of an AC network
$\underline{z}_{ij}$	Serial impedance of the branch connecting nodes i and j
Z	Index indicating zonal values

List of Abbreviations

AC	**A**lternating **C**urrent
DC	**D**irect **C**urrent
CC	**C**ritical **C**ontingency
CNE	**C**ritical **N**etwork **E**lements
CWE	**C**entral **W**est **E**uropean Region
ECS	**E**mergency **C**ontrol **S**cheme
FACTS	**F**lexible **A**lternating **C**urrent **T**ransmission **S**ystem
FBMC	**F**low **B**ased **M**arket **C**oupling
GSK	**G**eneration **S**hift **K**ey
HPN	**H**ybrid **P**article Swarm – **N**ewton Optimizer
HVDC	**H**igh **V**oltage **D**irect **C**urrent
OHL	**O**ver **H**ead **L**ine
PFC	**P**ower **F**low **C**ontrolling Devices
PMU	**P**hasor **M**easurement **U**nit
POC	**P**oint **O**f **C**oupling
PSO	**P**article **S**warm **O**ptimisation
PSDF	**P**hase **S**hift **D**istribution **F**actor
PST	**P**hase **S**hifting **T**ransformer
PTDF	**P**ower **T**ransfer **D**istribution **F**actor
RAM	**R**emaining **A**vailable **M**argin
RMS	**R**oot **M**ean **S**quare
SCADA	**S**upervisory **C**ontrol **A**nd **D**ata **A**cquisition
UPFC	**U**niversal **P**ower **F**low **C**ontroller
VSC	**V**oltage **S**ource **C**onverter
WAMS	**W**ide **A**rea **M**easurement **S**ystem
WAMPACS	**W**ide **A**rea **M**easurement, **P**rotection and **C**ontrol **S**ystem

Table of Contents

1 Introduction

1.1 Motivation

Increasing energy consumption and the rise of renewable energy sources in combination with the unbundling of formerly vertically integrated energy suppliers into independent energy production and transmission companies create additional challenges in power system operation and stability. Despite the effort spent and the results gained in research of smart distribution grids and micro grids, transmission systems will be an inevitable part of the electrical power system in the future. However, to cope with the upcoming challenges, innovative approaches will also be necessary in the transmission sector.

Structural changes in electricity generation and transmission are going to have a significant impact on power system short-term and mid-term dynamics. Besides the classical synchronous generator, future generation systems will be based on converter technology, especially in the case of photovoltaic and full converter wind turbines. The characteristics of converter-based generation differ significantly from synchronous generation. The latter contribute by their inherent electromechanical properties to the voltage support. Additionally, the directly connected rotating mass stabilizes the frequency leading to lower frequency gradients. These positive operation characteristics are either missing from converter-based generation completely or have to be considered in terms of an adequate control strategy.

On transmission system level, grid expansion in the sense of new construction or reinforcement of AC transmission lines cannot keep pace with the amount of installed generation capacity of renewables. Transmission lines loaded near to the capacity limit, make it important to assess the actual system status in real time to obtain secure power system operation.

Power flow controlling devices (PFCs) such as embedded high voltage direct current (HVDC-) systems, universal power flow controllers (UPFCs) or phase shifting transformers (PSTs) allow new ways of enhancing transmission capacity. The number of corresponding projects in the European network development plans is continuously growing. However, the control flexibility increased by PFCs will lead to new challenges in grid stability analysis and secure system operation.

An important contribution is the usage of available data from phasor measurement units (PMUs) forming a wide area measurement systems (WAMSs) to identify the system limits and to evolve it into a wide area measurement, protection and control systems (WAMPACSs), allowing specific control actions.

The focus of the upcoming research in this field can be split into transient problems, such as inertia issues and short-term voltage stability, and the derivation of control signals and setpoints for the increasing number of power flow controlling devices, e. g. phase shifting transformers and embedded high voltage direct current links operating in parallels to the AC system. This will have a significant impact on the loading of the transmission system, congestion management and operational security.

The introduction of the flow-based market coupling (FBMC) in the Central Western European region (CWE) and its expected expansion on the CORE region lead to additional challenges in the network operation. In particular, the legal requirement to provide $70\,\%$ of the available transmission capacity under (n-1)-operation to market participants leads to the necessity to coordinate PFCs to avoid extensive redispatch measures and loop flows caused by zone internal power transactions.

1.2 Objective of the thesis

The main goal of this thesis is to evaluate the benefits of a coordinated integration of PFCs in grid operation planning and to improve the system's long-term stability under strained operation with suitable PFC control strategies. Therefore, the following objectives are defined for this thesis:

- To investigate the potential of a PFC coordination on reducing necessary redispatch cost and volume. Therefore, the optimal utilization of redispatch on a base case load flow resulting from a flow-based market simulation is evaluated for different degrees of PFC coordination in large interconnected networks.
- To develop an algorithm able to detect branch outages suitable to be applicated in decentralized controllers without the availability of the central control centres' state estimations and SCADA (Supervisory Control and Data Acquisition) systems.
- To create applicable decentral emergency-control strategies for embedded HVDC links considering branch loading and voltage stability issues. The control strategy shall also allow a coordination between electrical close HVDC link without direct information exchange between their controllers.

The therefore conducted evaluations and simulations are separated into large scale models based on linearized load flow equations for the first objective and dynamic RMS simulations of smaller models for the other two objectives.

1.3 Scope of Research

In this work the optimal utilization of the PFC's power flow controlling capabilities are of major concern. The different time frames, network sizes and degrees of detail of the conducted simulations are chosen according to the objectives. The dynamic RMS simulations are executed in the simulation software DigSilent. The linearized models and the implementation of the methods are implemented in Matlab.

The linear evaluations and the internal topology representation used for the detection algorithm and emergency control strategies are based on the linearized DC-load flow equations. The branch reactances are derived from the used standard test systems and from public available sources for the large interconnected network.

The dynamic simulations are based on symmetric RMS representation of the considered networks. The parametrization of the synchronous generators, converters, controllers under observation, automatic voltage regulators, transformers and power lines are derived from standard values or are directly adopted from standard test topologies.

The coordination of the active power setpoints of embedded HVDC links and the setpoints for the PST's and UPFC's angles are investigated on fictive day ahead market solutions in large interconnected networks. The analyses base on linear load flow calculations, whereby the redispatch activation and the setpoints of the included PFCs are optimised using linear programming algorithms. A time efficient inclusion of (n-1)-security in the optimization requires a stable estimation of the critical contingency element of the considered branch. Suitable methods robust to changing load flows are investigated. Further, existing methods such as linear contingency analysis based on line outage distribution factors are evaluated for their usability on phase shifting PFCs and applicability in networks with phase shifting PFCs.

Regarding the decentralized outage detection, the essential standalone applicability of the algorithm requires a reduction of necessary near real time data and necessary topology updates to a minimum. Therefore, the algorithm's design focuses on a method allowing already detected outages to be integrated in the unchanged and thereby outdated topology information. This shall avoid the need of an immediate topology update after a contingency event. The fast-updated data is obtained from a Wide Area Measurement System.

The investigations and developments in the topic of decentralized emergency control strategies of embedded HVDC links focus on an adequate grid supporting effect, e. g. relieving of overloaded branches or avoiding long-term voltage instabilities. The coordination between several devices shall be achieved without communication between them.

Beyond the scope of this work are fast interactions between PFCs, damping of oscillations using PFCs and evaluations of the controller stability for converter based PFCs. Also, basic event detection starting the detection algorithm or triggering control actions are not addressed in this work.

1.4 Outline of the Thesis

In **chapter 2** the general equations of the DC load flow, the integration of power flow controlling devices and contingency analyses based on line outage distribution factors are recapitulate and the novel contributions on the contingency analyses using line outage distribution factors are stated.

Chapter 3 is dedicated to the definition of different grid areas of influence. Areas of control are defined by analysing the sensitivity of PFCs on the branch loading. These areas are then expanded to areas of detection including branches, whose tripping have a major influence on the branch loading of branches in the area of control. The areas of control are used for the optimization of the PFCs' setpoints and to limit the grid area subject to corrective emergency control actions. The areas of detection define the considered branches for the setup of the developed emergency outage detection. Further, the optimal location of PMU monitored nodes for the emergency outage detection is based on the areas of detection. The selection methods for the monitored nodes are also discussed in this chapter.

The effects of an optimal coordination of PFC setpoints on the redispatch costs and volumes are evaluated in **chapter 4**. The chapter contains the formulation of the optimization problem, a method to estimate the critical (n-1)-contingency and a case study conducted in the ENTSO-E network for the fictive year 2025.

In **chapter 5** an emergency multi branch outage detection algorithm using changes in the node voltage angles is proposed. The detection is based on an optimizer estimating fictive power injections modelling the outage and thereby allowing the detection of the tripped branches. Three different optimizers are evaluated for this task – Newton's method, Particle Swarm Optimization and a hybrid optimizer combining them. The algorithm based on these three optimizers is tested on the results of a linearized static and an RMS simulation of the Nordic-32-Bus test system. The algorithm's detection performance is further evaluated considering the optimizer parameters and reduced node voltage angle information.

Chapter 6 focuses on the development of suitable emergency control strategies of embedded HVDC links considering the relief of overloaded branches as well as the long-term voltage stability and the maximum loadability. A control strategy suitable in radial network topologies is discussed and validated with dynamic simulations. Additionally, a more sophisticated control strategy for meshed networks with integrated coordination of several parallel embedded HVDC links is proposed.

The conclusions and main findings of the research chapters are summarized in **chapter 7**.

1.5 Scientific Contribution

The main contributions to science in the field of normal grid operation are

- Development of a method to estimate the critical contingency leading to a (n-1)-security violation for flow-based market simulations and redispatch optimization for changing load flow conditions
- Definition of a methodical determination of branches controllable with PFCs
- Development of a rule-based selection of PMU locations for monitoring node voltage angles in arbitrary networks for obtaining WAMS data used for branch outage detection algorithms
- Evaluation of the benefits of different degrees of control coordination of PFCs on the redispatch costs in a price driven redispatch market with optimal redispatch activation

The main contributions to science in the field of emergency and handling in the grid are:

- Development of an optimization-based multibranch outage detection useable for distributed emergency control measures using solely synchronized node voltage angle information from WAMS
- Investigations and improvements on network supporting control schemes of embedded HVDC links

1.6 State of the Art

1.6.1 PFC coordination

The ever-increasing number and importance of PFCs in nowadays transmission networks lead to the necessity of a coordination between single devices to optimally utilize their network supporting capacity. Since in this thesis the effects of the degree of PFC coordination on the redispatch cost and volume in a full year techno-economic simulation are evaluated, the following review does not include work on the coordination focusing on optimal damping, voltage control or dynamic interactions.

The obvious approach of using optimal power flow calculations to coordinate the PFCs, e. g. as discussed in [1], might become computational complex for large networks leading to impracticable simulation runtimes. To cope with this, either the model's level of detail can be reduced, e. g. by linearizing or decoupling the load flow equations, or the network is separated into different areas affected by the evaluated PFCs as used for example in [2]–[4].

In Verboomen's PhD-thesis [5] the effects of a coordination of PSTs on the total transfer capacity between two areas and on reducing necessary network extensions are discussed from a technical point of view. The results clearly show the need of a coordination to avoid additional congestions due to loop flows.

In [6] control strategies for PSTs and embedded HVDC links for long-term network development planning are evaluated. The focus of this work is set on the reduction of loop flows and thus avoiding overloading of tie lines and reducing necessary network extensions. The thereby examined PST control strategies are based on keeping the (n-1)-security of interconnectors, minimizing the branch loading, fulfilling Net Transfer Capacities and on reproduction of market flows in the physical flows. The results indicate, that the coordinated control helps to ease tensions introduced on neighbouring networks. Further, the possible relief of internal tie lines due to optimal exploitation of the net transfer capacity.

The work published in [7] compares the performance of different optimizers, e.g. Particle Swarm Optimization and differential evolution, in finding optimal PST setpoints in the IEEE 57-Bus system under the constraints of maximal line loading, node voltage deviation and generator limits.

In [8] a coordinated PST control schema with the goal to equally load cross border interconnectors is discussed. The optimal phase shifter angles are derived using the linear least squares method based on the linearized load flow sensitivity described by the Phase Shifter Distribution Factors (PSDFs). The resulting control principles and restrictions given by the relation between the number of PSTs and number of interconnectors are demonstrated for the Dutch-German and Dutch-German border. Similar to this work, the impact of parallel PSTs on the four main interconnectors between Poland and Germany and interactions between the PSTs are evaluated in [9].

The coordination between different types of PFCs, namely PSTs and HVDC links, is discussed in [10]. The conducted evaluations focus on static and dynamic security analyses and highlight the increase of the transmission capacity between different network zones. However, in this paper no coordination between PSTs and HVDC links are discussed and embedded HVDC links are not considered.

The effects of coordinated PST and embedded VSC-HVDC link control on decisions considering grid management such as investment, planning, scheduling and operations are discussed in [11]. The results show, that the possibilities of managing loop flows and congestions as well as the additional flexibility allow an operation closer to the system limits.

In [12] a method to select close to ideal power setpoints of embedded HVDC links based on functions of the voltage angle difference between the HVDC-terminals is discussed. The resulting setpoints are compared to fixed values derived with optimal power flow calculations. The method is applied for up to three parallel and electrical close HVDC-transmission corridors in a meshed network, which approximates the German grid scenario in 2023. The results indicate, that the accordance between the optimal setpoints and the setpoints derived with this method depends on the actual load flow scenario.

The coordination of HVDC links to maximise the utilization of renewable energy is discussed in [13], [14]. The thereby proposed operational strategies of the parallel HVDC links connecting multiple network areas are applied in the North-western Chinese transmission network. The results show, that due to the coordination more renewable energy can be utilized.

1.6.2 Emergency Outage Detection Methods

Accurate state awareness of a system presents an important factor for secure grid operation. The system state is usually provided by state estimators. Traditionally, the input data of state estimators consists of the topology and asynchronous measurements – voltage, current, power, etc. – based on SCADA systems with update rates down to several seconds. The increasing usage of PMUs foster the development of algorithms for dynamic state estimators using the synchronized and quickly updated measurements [15]–[17]. However, the correct system topology remains a crucial factor in the quality of the state estimation. Therefore, an accurate detection of branch outages is of great importance. A special problem situation arises in grid areas on the responsibility border of different grid operators, where only sparse real time information is shared. Recent work on outage detection focuses on a joint detection and estimation problem [18] to accurately update state estimator's topology model using all kind of available measurements from unsynchronised power, voltage and current magnitudes as well as synchronised voltage phasor measurements.

Several publications of the last years focused on the problem of outage detection using synchro phasor data and evaluated a wide range of possible algorithms. The following review is far from complete but shall give an overview on already evaluated approaches.

In [19] a method is described using pre simulated linearized node voltage angle sensitivities on branch outages to detect a tripped branch. Later this method is developed further to be used for double branch outages [20] and applied on specific parts of large networks to reduce the necessary synchro phasor data [21]. Similar to these works, a detection algorithm based on the least square error between measured and simulated node voltage angles is discussed and evaluated on its vulnerability to bad WAMS data [22] and another detection estimation algorithm is proposed using bus power mismatches calculated from node voltage angles decision criterion [23]. However, all of these approaches need the number of tripped branches as input and require the pre-calculation of the sensitivities for any possible change in the network topology. The necessary effort for these pre-calculations increase with the number of considered branches and has to be repeated after any change in the network.

The use of a decision tree identifying critical attributes in WAMS data and further applying them as detection criterion is discussed in [24]. The contingencies detectable with this approach are not limited to branch outages, but it comes at the cost of extensive pre-simulations since any considered contingencies has to be simulated and the decision tree trained on the set of contingencies.

Another method as described in [25] is based on vector estimation which is solved with adopted greedy orthogonal matching pursuit as well as the convex least-absolute shrinkage and selection operator. This method can overcome the need of a beforehand known number of tripped branches by incorporating an additional sample variance deviation criterion based on pre-calculations but requires information on line outage probabilities and expected noise level.

The exploitation of statistical properties of the generation and demand of the considered network in combination with an application of quickest change detection algorithm on node voltage angle measurements to detect transmission line outages is discussed in [26] and further evaluated in [27],

[28]. Based on this approach the ideal location of measurements and possible improvements by system partitioning are examined in [29]. This method is applicable on single and multi-branch outages, but due its need to parallelly applying the Cumulative Sum algorithm for each possible outage combination the computational burden is rather high. A comparison on statistical based outage detection is given in [30].

Several papers use optimization-based approaches. For examples the work described in [31] utilizes mixed-integer programming to identify line outages in an external system influencing load flow of the internal system. This approach is only applied on single branch outages. An evolutionary optimization-based approach using an adaptive version of the estimation of distribution algorithm in [32]. This algorithm seems to be able to detect a variable number of tripped branches and is further developed in [33]. However, from the results it is unclear, if it is suitable for a fast detection in real operation.

1.6.3 Emergency Control of Embedded HVDC links

The increasing number of embedded HVDC links already in operation, under construction or in planning, e. g. the Swedish SouthWest Link, the French-Spanish interconnection between Perpignan and Figueres or the Trans Bay Cable between San Francisco and Pittsburg, and their high potential in effectively controlling the surrounding AC network's branch loadings and node voltages make them a valuable asset for flexible network operation. Their high nominal power ratings up to several hundred MW and the fast reaction times of the converters in the millisecond range allow efficient control applications for fast dynamic problems such as interarea oscillations and short-term voltage instabilities as well as for problems with slower dynamics such as branch overloading and long-term voltage instabilities.

The combination of increasing energy consumption, changes in local distribution of generation centres and a rather slow grid expansion has led to an increased loading of the AC transmission system with higher risk of major disturbances and blackouts. When they occur, the main causes are cascading tripping of lines [34], [35] and voltage collapses [36], [37]. Due to this, the work on emergency control strategies done in this thesis focuses on avoiding cascaded line tripping due to overload and long-term voltage instabilities. The therefore resulting time frame for an emergency control action has to span a range from seconds – cascaded line tripping involving distance relays and fast overcurrent relays – up to several minutes – for long term voltage stability and overload protection relays [38], [39]. Due to this, in the following only research is reviewed which corresponds to the scope of this thesis' work.

In [40] the effects of the standard dq-control modes of an VSC-HVDC link –DC-voltage control or P-control and AC voltage control or Q-control,– and the selected priority between direct and quadrature current in case of an active current limitation are evaluated in a RMS simulation of a small radial test network and in a modified IEEE 39-Bus test system. The setpoints are thereby empirically adjusted based on sensitivities to increase the system stability considering angular and voltage instabilities as well as violations of voltage and thermal limits. The results indicate, that the AC voltage control mode is more robust than the Q-control mode and that the DC-voltage control mode should be used for the converter providing less reactive power support.

The general effect of different power setpoints of embedded VSC-HVDC links on the maximal obtainable combined AC-DC power transfer is discussed in [41]. The comparison of the discussed strategies – maximum active power transfer via the HVDC link, only voltage control on both HVDC terminals and a node voltage angle dependent active and reactive power setpoint – is based on stationary evaluations of a simple point to point network. The results show, that the node voltage angle dependent control strategy is best suited to improve the maximum load ability of the combined system. This strategy was later implemented in a dynamic simulation of the Nordic-32-Bus system leading to good results in terms of increased system stability [42].

In [43] an automated operation for embedded HVDC links during (n-1)-conditions in the parallel AC system is discussed and implemented in the modified New England Test System. The approach of this work derives the base case power setpoints of HVDC links as a function of node angle differences between the terminal nodes and allows sensitivity-based adjustments of the power setpoints to relieve overloaded branches. The changes in the setpoints are limited by pre-calculated maximal and minimal values of the HVDC's power transfer. However, the necessary (n-1)-sensitivities must be known before hand and it is not addressed in this publication, if all possible contingency are considered or a pre-selection is necessary.

In [44] and [45] a multiagent system is used for an integrated coordination of PFCs. The discussed adaptive control approach is based on the data collected by software agents installed at substation level conducting measurements of each serial network element in the considered network area. The collected data is evaluated for branch overloads and control signals for the PFCs calculated from their sensitivities on detected overloads and a weight factor are created. This approach is successfully applied in the New England and Western Europe test systems and is further expanded on integrating redispatch activation in [46].

The so far discussed concepts focus, with the exceptions of [41] and [42], only on relieving overloaded branches. In contrast to them, other control concepts are solely developed to avoid voltage instabilities exemplarily using critical voltage sensitivities derived via the Jacobian matrix [47], hierarchical voltage control [48] or weighted voltage deviations of limited areas [49].

The combination of avoiding overloaded branches and voltage instabilities at the same time within a single control strategy is so far mostly accomplished by solving an optimal power flow problem, e. g. [1], [50], [51] and [52]. However, with increasing network size, the solving of the optimal power flow problem, especially considering non-linearities of the load flow, becomes time consuming and unpracticable for emergency control actions.

2 DC Load Flow and its Application

The DC Load flow is a well-known tool mainly applied in techno-economic studies. Due to its linear nature, it allows a noniterative calculation of branch active power flows from the active power injections of the network nodes. The following description of the DC load flow and the linear modelling of load flow controlling units is based on [5], [53]–[55] and shall give an overview on the different factors defining the branch loading.

The authors own original contributions on this topic are stated at sections 2.2.3, 2.3.2 and 2.3.3.

2.1 General DC Load Flow Equations

The DC load flow is the linearization of the general AC load flow reducing the calculation complexity taking only the active power flow into account. It is mainly used for analyses of large power systems. The apparent power flow between two connected nodes i and j for a discrete PI-equivalent, in the following referred to as branch power, is calculated as

$$\underline{s}_{ij} = \underline{v}_i \cdot \underline{i}_{ij}^* = \frac{v_i^2}{\underline{z}_{ij}^*} - \frac{\underline{v}_i \cdot \underline{v}_j^*}{\underline{z}_{ij}^*} \tag{2-1}$$

with $\underline{z}_{ij}=r_\mathrm{L}+\mathrm{j}\omega x_\mathrm{L}$. The apparent power of the shunt capacitance and shunt conductance accounted to the node power[1]. The separation into active and reactive power gives the basic set of AC load flow equations

$$\begin{aligned} p_{ij} &= \frac{v_i^2}{z_{ij}} \cdot \cos(\psi_{ij}) - \frac{v_i \cdot v_j}{z_{ij}} \cdot \cos(\vartheta_i - \vartheta_j + \psi_{ij}) \\ q_{ij} &= \frac{v_i^2}{z_{ij}} \cdot \sin(\psi_{ij}) - \frac{v_i \cdot v_j}{z_{ij}} \cdot \sin(\vartheta_i - \vartheta_j + \psi_{ij}) \end{aligned} \tag{2-2}$$

The power injected or withdrawn on one node, in the following referred to as node power, is calculated as the sum of all branch powers of the branches connected to the node plus the power of the shunt elements of these branches. The resulting equations system for a N node network has $2{\cdot}N$ non-linear equations and $2{\cdot}N$ unknown, whereby a solution can be found by iteration.

[1] This is only possible for discrete branch models. The shunt capacitance and conductance behave as an additional impedance load at the corresponding node, whereby the shunt conductance is generally neglected.

The linearization of the DC load flow reduces the set of equations and unknown to N. The linearization bases on the following three assumptions:

1. *Branch impedances are dominated by the branch reactance*
   The branch impedances of the transmission networks' elements have in general a small r/x ratio. Typical values for overhead lines and cables above 220 kV are in a range around 0.05 and 0.2, whereby the actual values depend on the geometrical configuration and number of conductors as well as the conductor diameter [56, pp. 281–283], [57, p. 94]. The resistive part of the transformer impedance is insignificant for transformers installed in the transmission network [57, p. 85].
   Neglecting the resistive part and therefore the transmission losses, simplifies the branch power equations to

$$p_{ij} = \frac{v_i \cdot v_j}{x_{ij}} \cdot \sin\left(\vartheta_i - \vartheta_j\right)$$
$$q_{ij} = \frac{v_i^2}{x_{ij}} - \frac{v_i \cdot v_j}{x_{ij}} \cdot \cos\left(\vartheta_i - \vartheta_j\right) \qquad (2\text{-}3)$$

2. *The voltage angle difference between neighbouring nodes is small*
   The trigonometric functions are linearized to $\sin(\vartheta_i - \vartheta_j) \approx \vartheta_i - \vartheta_j$ and $\cos(\vartheta_i - \vartheta_j) \approx 1$.

$$p_{ij} = \frac{v_i \cdot v_j}{x_{ij}} \cdot \left(\vartheta_i - \vartheta_j\right)$$
$$q_{ij} = \frac{v_i^2}{x_{ij}} - \frac{v_\mathrm{i} \cdot v_j}{x_{ij}} \qquad (2\text{-}4)$$

3. *Optimal reactive power balance in each node*
   The voltage profile is flat due the balanced reactive power. The node voltages are assumed as $1\ \mathrm{pu}$ for all nodes. This assumption further implicates the neglect of the shunt capacitance.

$$p_{ij} = \frac{1}{x_{ij}} \cdot \left(\vartheta_i - \vartheta_j\right)$$
$$q_{ij} = 0 \qquad (2\text{-}5)$$

The conducted analyses in [58] on the DC load flow showed, that the average deviation of the calculated active power branch flows between DC load flow results and AC load flow results caused by these assumptions can be assumed around $5\ \%$ in transmission grids. The highest sensitivity is to the voltage profile, whereby the voltage deviation of singular nodes are more severe than a change in the average voltage level [54].

The node power is calculated as already mentioned from the sum of the branch powers of the connected lines. Brought into matrix form, the active branch powers $\mathbf{p}_\mathrm{L}$ can be calculated directly from the active node powers $\mathbf{p}_\mathrm{N}$ using the **PTDF** matrix, for detailed derivation see [53]. In the following all matrixes and node powers are reduced by the slack bus and no specific index is used to highlight that due to better readability.

$$\mathbf{p}_\mathrm{L} = \mathbf{PTDF} \cdot \mathbf{p}_\mathrm{N} \tag{2-6}$$

$$\mathbf{PTDF} = \mathbf{B}_\mathrm{d} \cdot \mathbf{NBI}^\mathrm{T} \cdot (\mathbf{NBI} \cdot \mathbf{B}_\mathrm{d} \cdot \mathbf{NBI}^\mathrm{T})^{-1} = \mathbf{B}_\mathrm{d} \cdot \mathbf{NBI}^\mathrm{T} \cdot \mathbf{B}^{-1} \tag{2-7}$$

NBI is the reduced node-to-branch incidence matrix with the dimension $((N\text{-}1)\times L)$, whereby N is the number of all nodes and L the number of all branches of the system. The element $nbi_{\ell n} = 1$ if branch ℓ starts at node n, $nbi_{\ell n} = -1$ if line ℓ ends at node n and $nbi_{\ell n} = 0$ if line ℓ is not incident to node n.

$\mathbf{B}_\mathrm{d}$ is a diagonal matrix containing the branch susceptances with the dimension $(L\times L)$. **B** is the reduced system susceptance matrix with the dimension $((N\text{-}1)\times(N\text{-}1))$.

$\mathbf{p}_\mathrm{L}$ and $\mathbf{p}_\mathrm{N}$ are column vectors with a length of L and $(N\text{-}1)$. The dimension of the **PTDF** matrix is given with $(L\times(N\text{-}1))$. The element $ptdf_{\ell n}$ of the **PTDF** matrix depends on the choice of the slack node, since it represents the power flow via branch ℓ for a power injection in node n and power withdrawal at the slack node of 1 pu.

2.2 Representation of Power Flow Controlling Devices in DC LF

The secure and economical operation of electric networks depends on a controllable power flow. The active power flow on lines can be influenced by a change in the generation or topology and by the use of power flow controlling (PFCs) devices. The representation of the following basic PFCs in DC load flow are based on [5], [54]. Detailed derivation of the used matrixes is given in [53].

2.2.1 Phase Shifting Transformers

Phase shifting transformers (PSTs) are included by extending the equation for branch power flow (2-5) with the phase shifter angle α. The sign convention is chosen in a way, that a positive angle increases the load flow of the PST branch.

$$p_{ij} = \frac{1}{x_{ij}} \cdot \left(\vartheta_i - \vartheta_j + \alpha_{ij}\right) \tag{2-8}$$

The phase shifter angles of all PST branches are included in the matrix notation of the branch power flows with the **PSDF** matrix. The change of the branch flow $\Delta\mathbf{p}_\mathrm{L}$ caused by the phase shifter angle calculates as follows

$$\Delta\mathbf{p}_\mathrm{L} = \mathbf{PSDF} \cdot \boldsymbol{\alpha} \tag{2-9}$$

$$\mathbf{PSDF} = (\mathbf{B}_\mathrm{d} - \mathbf{B}_\mathrm{d} \cdot \mathbf{NBI}^\mathrm{T} \cdot \mathbf{B}^{-1} \cdot (\mathbf{B}_\mathrm{d} \cdot \mathbf{NBI}^\mathrm{T})^\mathrm{T}) \cdot \mathbf{BPI} \tag{2-10}$$

The length of $\boldsymbol{\alpha}$ is P and the **PSDF** matrix has the dimension $(L\times P)$, whereby P is the number of PST. The PSDF matrix is independent of the location of the slack node and is diagonal symmetric, if all branches are assumed as equipped with a PST. The multiplication with the Branch-to-PST incidence matrix **BPI** eliminates entries not linked to PST branches. The element $bpi_{\ell p} = 1$, if branch ℓ corresponds to PST p and $bpi_{\ell p} = 0$ otherwise.

2.2.2 HVDC Links

HVDC links are only considered as PFCs, if they connect nodes of one synchronized network in parallel to the AC lines (embedded HVDC links). Their implementation in the DC load flow is rather simple, due to the fully controllable power flow of the HVDC link. The HVDC power transfer is withdrawn or injected on the nodes connected by the HVDC link. Consequently, the change in power flow in the AC system can be calculated by the negative **PDTF** matrix multiplied with the change in the node power, or with the **DCDF** matrix multiplied with the power flow via the HVDC link.

$$\Delta \mathbf{p}_{\mathrm{L}} = -\mathbf{PTDF} \cdot \mathbf{NDI} \cdot \mathbf{p}_{\mathrm{DC}} = \mathbf{DCDF} \cdot \mathbf{p}_{\mathrm{DC}} \tag{2-11}$$

$$\mathbf{DCDF} = -\mathbf{B}_{\mathrm{d}} \cdot \mathbf{NBI}^{\mathrm{T}} \cdot \mathbf{B}^{-1} \cdot \mathbf{NDI} = -\mathbf{PTDF} \cdot \mathbf{NDI} \tag{2-12}$$

NDI is the reduced node-to-HVDC incidence matrix with the dimension $((N\text{-}1)\times D)$, whereby D is the number of HVDC links.

$\mathbf{p}_{\mathrm{DC}}$ is a column vector with the length D and contains the power flow of the embedded HVDC links. The sign convention gives a positive value, if the HVDC link's power flows from the starting node to the ending node of the HVDC link.

2.2.3 Simplified Universal Power Flow Controller DC-Load Flow model

The Universal Power Flow Controller (UPFC) combines continuously controlled serial and parallel compensation with the additional possibility to transfer active power via its DC intermediate circuit. The power transfer via the DC intermediate circuit allows the additional voltage of the serial transformer to have any wished angle independent of the current trough the serial transformer. Therefore, the UPFC enables an operational plane in the phasor diagram, Fig. 2-1.

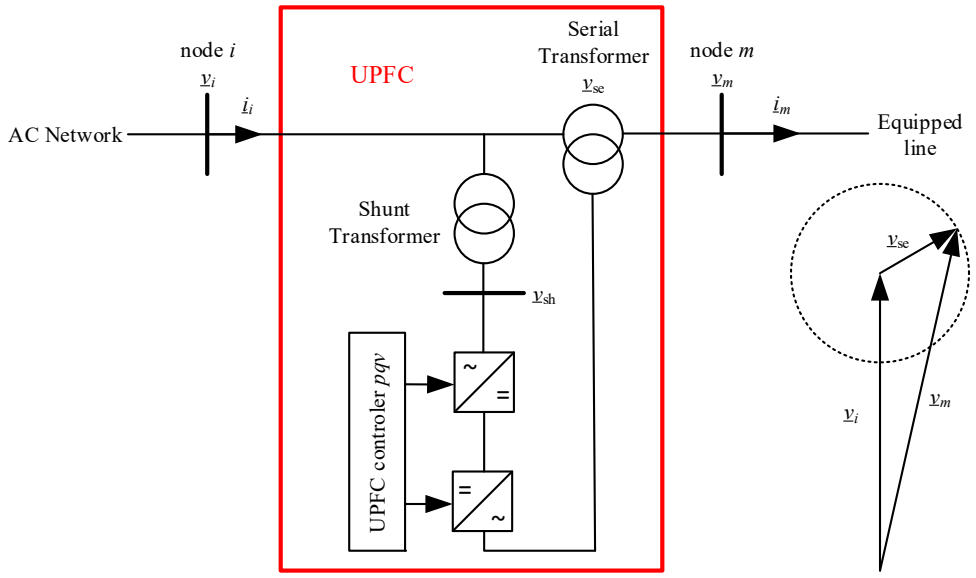

Fig. 2-1 UPFC schematic and phasor diagram

A lossless line equipped with an ideal UPFC is represented with its general equivalent circuit Fig. 2-2 [59], [60] or with an ideal transformer UPFC model Fig. 2-3 [59], [61]. These equivalent circuits are used for a derivation of a DC-Load flow model of the UPFC. The capacitive shunt elements of the line are neglected, since the target is to derive a DC-Load flow model of the UPFC. It is shown in the following, that applying the DC load flow assumptions on both equivalent circuits yields to the same result.

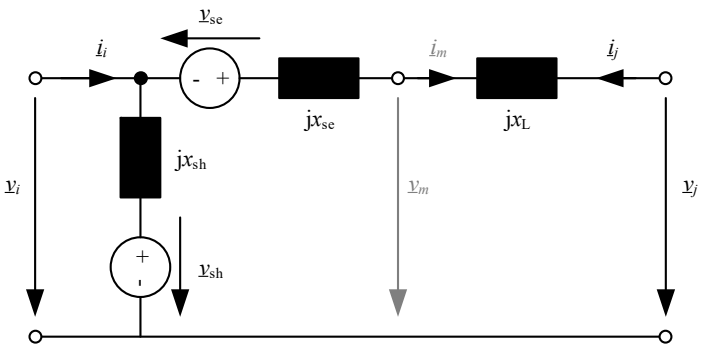

Fig. 2-2 Equivalent circuit of idealized line embedded with loss less UPFC

The following derivation of a DC-Load flow model is based on the work published in [60]. However, instead of only simplifying the AC model by setting the voltage magnitude to $1\ \mathrm{pu}$ and the sine function to the difference of voltage node angles in the active power equations as done in [60] it is shown, that the active power controlling behaviour of the UPFC can be expressed by PSDF factors. Therefore, the branch currents $\underline{i}_i$ and $\underline{i}_j$ are expressed as functions of the node voltages $\underline{v}_i$ and $\underline{v}_j$ and the voltages on the shunt transformer $\underline{v}_{sh}$ and serial transformer $\underline{v}_{se}$ of the UPFC.

$$\begin{pmatrix}\underline{i}_i\\ \underline{i}_j\end{pmatrix}=\begin{bmatrix}-\frac{\mathrm{j}}{x_L+x_{se}}-\frac{\mathrm{j}}{x_{sh}} & \frac{\mathrm{j}}{x_L+x_{se}}\\ \frac{\mathrm{j}}{x_L+x_{se}} & -\frac{\mathrm{j}}{x_L+x_{se}}\end{bmatrix}\begin{pmatrix}\underline{v}_i\\ \underline{v}_j\end{pmatrix}+\begin{bmatrix}-\frac{\mathrm{j}}{x_L+x_{se}} & \frac{\mathrm{j}}{x_{sh}}\\ \frac{\mathrm{j}}{x_L+x_{se}} & 0\end{bmatrix}\begin{pmatrix}\underline{v}_{se}\\ \underline{v}_{sh}\end{pmatrix} \tag{2-13}$$

$$\begin{pmatrix}\underline{i}_i\\ \underline{i}_j\end{pmatrix}=\begin{bmatrix}\underline{b}_{ij}+\underline{b}_{i0} & -\underline{b}_{ij}\\ -\underline{b}_{ij} & \underline{b}_{ij}\end{bmatrix}\begin{pmatrix}\underline{v}_i\\ \underline{v}_j\end{pmatrix}+\begin{bmatrix}\underline{b}_{ij} & -\underline{b}_{i0}\\ -\underline{b}_{ij} & 0\end{bmatrix}\begin{pmatrix}\underline{v}_{se}\\ \underline{v}_{sh}\end{pmatrix} \tag{2-14}$$

The model is transferred to the DC-Load flow by applying the assumption stated in 2.1 leading to the following simplifications:

1. Node voltage magnitudes v_i and v_j are equal to $1\ \mathrm{pu}$
2. Only active power transfer between the nodes
    - phase difference between branch current and node voltage is insignificant
    - shunt element $\underline{b}_{i0}$ is neglected
    - shunt and serial voltages v_{sh} and v_{se} are assumed to be in quadrature with the node voltages or are separated into a direct and quadrature part and considering only the quadrature part

The active power injections caused by the UPFC are simplified from (2-15) to (2-16). The thereby used index i,ij indicates the active power flow from node i to node j seen from node i. The index j,ij indicates the active power flow from node i to node j seen from node j. The active power balance of the UPFC

device must be 0. The sum of the active power injections modelling the serial converter is 0, consequently the active power of the shunt converter is 0 too.

$$
\begin{aligned}
p_{i,ij}^{\mathrm{se}} &= -\frac{1}{x_{\mathrm{L}} + x_{\mathrm{se}}} \cdot v_i v_{\mathrm{se}} \cdot \sin(\vartheta_i - \vartheta_{\mathrm{se}}) \\
p_i^{\mathrm{sh}} &= \frac{1}{x_{\mathrm{sh}}} \cdot v_i v_{\mathrm{sh}} \cdot \sin(\vartheta_i - \vartheta_{\mathrm{sh}}) \\
p_{j,ij}^{\mathrm{se}} &= \frac{1}{x_{\mathrm{L}} + x_{\mathrm{se}}} \cdot v_j v_{\mathrm{se}} \cdot \sin\left(\vartheta_j - \vartheta_{\mathrm{se}}\right)
\end{aligned}
\qquad \textit{(2-15)}
$$

$$
\begin{aligned}
p_{i,ij}^{\mathrm{se}} &= \frac{1}{x_{\mathrm{L}} + x_{\mathrm{se}}} \cdot v_{\mathrm{se}} = p_{ij}^{\mathrm{se}} \\
p_i^{\mathrm{sh}} &= -\frac{1}{x_{\mathrm{sh}}} \cdot v_{\mathrm{sh}} = 0 \\
p_{j,ij}^{\mathrm{se}} &= -\frac{1}{x_{\mathrm{L}} + x_{\mathrm{se}}} \cdot v_{\mathrm{se}} = -p_{ij}^{\mathrm{se}}
\end{aligned}
\qquad \textit{(2-16)}
$$

The resulting branch power of the equipped line is therefore given as (2-17). The equation is expanded for an arbitrary system with each line assumed with an UPFC as (2-18). The node powers are calculated as the sum of the branch powers

$$p_{ij} = \frac{1}{x_{\mathrm{L}} + x_{\mathrm{se}}} \cdot (\vartheta_i - \vartheta_j + v_{\mathrm{se}}) \qquad \textit{(2-17)}$$

$$\mathbf{p}_{\mathrm{L}} = \mathbf{B}_{\mathrm{d}} \cdot \mathbf{NBI}^{\mathrm{T}} \cdot \boldsymbol{\vartheta} + \mathbf{B}_{\mathrm{d}} \cdot \mathbf{v}_{\mathrm{se}} \qquad \textit{(2-18)}$$

$$\mathbf{p}_{\mathrm{N}} = \mathbf{NBI} \cdot \mathbf{B}_{\mathrm{d}} \cdot \mathbf{NBI}^{\mathrm{T}} \cdot \boldsymbol{\vartheta} + \mathbf{NBI} \cdot \mathbf{B}_{\mathrm{d}} \cdot \mathbf{v}_{\mathrm{se}} \qquad \textit{(2-19)}$$

Rewriting these equations to achieve a direct calculation of the branch powers from the node powers and removing the node power terms leads to the branch flow change caused by the UPFC serial converter voltages (2-20). Comparing it to the DC-Load flow equations stated in 2.1 it is easy to see, that the UPFC serial converter voltages influence the branch powers of the network in the same way as a phase shifter angle described by the $\mathbf{PSDF}$ matrix. The matrix $\mathbf{BPI}$ corresponds in this case to the UPFC branches.

$$\Delta\mathbf{p}_{\mathrm{L}} = (\mathbf{B}_{\mathrm{d}} - \mathbf{B}_{\mathrm{d}} \cdot \mathbf{NBI}^{\mathrm{T}}(\mathbf{NBI} \cdot \mathbf{B}_{\mathrm{d}} \cdot \mathbf{NBI}^{\mathrm{T}})^{-1} \cdot \mathbf{NBI} \cdot \mathbf{B}_{\mathrm{d}}) \cdot \mathbf{BPI} \cdot \mathbf{v}_{\mathrm{se}} \qquad \textit{(2-20)}$$

$$\Delta\mathbf{p}_{\mathrm{L}} = \mathbf{PSDF} \cdot \mathbf{v}_{\mathrm{se}} \qquad \textit{(2-21)}$$

The same result is achieved by transferring the ideal transformer based UPFC model [59], [61] to a DC load flow model. The UPFC is thereby modelled as an ideal transformer with a complex ration $\underline{c}_{\mathrm{u}}$ and a shunt element x_{sh}.

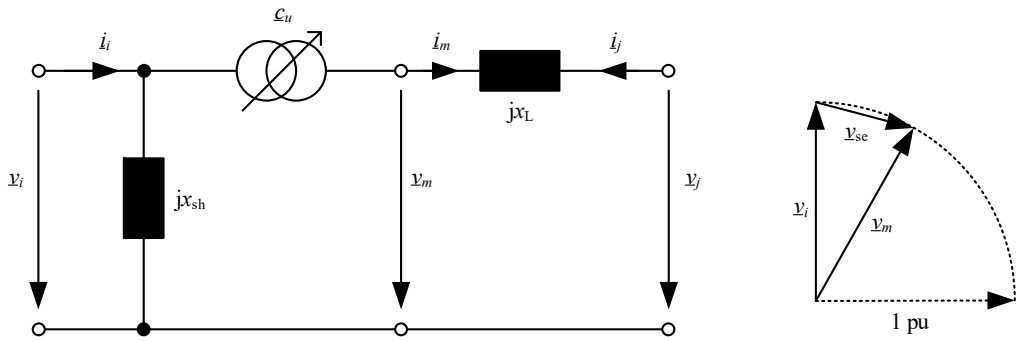

Fig. 2-3 UPFC modelled as ideal transformer with complex ratio, own illustration based on [59, p. 424]

The shunt element can be dismissed for the DC-Load flow model, since it only represents the ability of the UPFC to generate and absorb reactive power and therefore controlling the magnitude of the node voltage at the UPFC bus.

The complex voltage ratio of the transformer representing the serial part of the UPFC is depending on the serial voltage $\underline{v}_{se}$ of the UPFC.

$$\underline{c}_u = \frac{\underline{v}_m}{\underline{v}_j} = \frac{\underline{v}_j + \underline{v}_{se}}{\underline{v}_j} = c_u \cdot e^{j\alpha} \qquad (2\text{-}22)$$

Applying the DC-Load flow assumption of an ideally flat voltage profile the complex voltage ratio becomes $\underline{c}_u = 1e^{j\alpha}$. The relation between shift angle α and serial voltage is given as

$$v_{se} = 2 \cdot \sin\left(\frac{\alpha}{2}\right) \qquad (2\text{-}23)$$

Linearizing the sin-function of equation (2-23) lead to an equality of v_{se} and α in the pu-system. The linearization error is less than $1.5\,\%$ for an α of $30°$ and still below $3.5\,\%$ for an α of 30° and therefore neglectable. The branch power of the UPFC equipped line is calculated as given already in (2-17), whereby the serial conductance of the UPFC is added to the line conductance.

The linearization according to the DC-Load flow assumptions of both AC modelling approaches yield in the same result, as long as the active power transfer via the DC link of the UPFC can be neglected. In consequence the influence of the shunt part of the UPFC on the active power is not represented in the DC-Load flow model. The UPFCs are equally implemented as PSTs with the PSDF matrix in the DC-Load flow model, thusly the matrix **BPI** and vector **α** correspond to PSTs and UPFCs in the following.

2.3 Application of DC Load Flow in Contingency Calculation

The DC load flow offers a simple tool for contingency calculations. However, the results should be interpreted with care, since the error caused by the linearization tend to increase with the branch loading. The following notation will be used in all contingency related topics:

R	…	set of remaining branches
O	…	set of outage branches
$\mathbf{\Phi}$	…	node-to-remaining-branch incidence matrix, equivalent to the columns R in **NBI**
$\mathbf{\Psi}$	…	node-to-outage-branch incidence matrix, equivalent to the columns O in **NBI**
b	…	base case
c	…	contingency case

Further, a phase shifter angle $\boldsymbol{\alpha}$ at each branch is assumed. In this case **BPI** is equivalent to the identity matrix **I**, which gives a better readability due the multiplication with **BPI** for the calculation of the **PSDF** matrixes can be omitted in that configuration without any loss of generalisation.

The indexing concerning the sets O and R corresponds the following rules:

- A single index denotes a subset of a matrix or values only linked to the corresponding set of branches, e. g. $\mathbf{PTDF}_R$ are the rows of the PTDF matrix corresponding to the set R.
- Two comma separated indices denote either a subset of a matrix, e. g. $\mathbf{PSDF}_{R,R}$ are the rows and columns of the PSDF matrix corresponding to the set R, or indicate related values, e. g. $\mathbf{LODF}_{R,O}$ consists of all LODF vectors of single branch outages of the set O to the set R.

2.3.1 Concept of Line Outage Distribution Factors

The conventional way to calculate the post contingency loading of the remaining branches is to use the post contingency susceptance matrix $\mathbf{B}^{\mathrm{c}}$ and $\mathbf{\Phi}$ to determine $\mathbf{PTDF}_R^c$, $\mathbf{PSDF}_{R,R}^c$ and $\mathbf{DCDF}_R^c$.

$$\mathbf{PTDF}_R^c = \mathbf{B}_{\mathrm{d}R} \cdot \boldsymbol{\phi}^{\mathrm{T}} \cdot (\boldsymbol{\phi} \cdot \mathbf{B}_{\mathrm{d}R} \cdot \boldsymbol{\phi}^{\mathrm{T}})^{-1} = \mathbf{B}_{\mathrm{d}R} \cdot \boldsymbol{\phi}^{\mathrm{T}} \cdot \mathbf{B}^{\mathrm{c}-1} \tag{2-24}$$

$$\mathbf{PSDF}_{R,R}^c = \mathbf{B}_{\mathrm{d}R} - \mathbf{B}_{\mathrm{d}R} \cdot \boldsymbol{\phi}^{\mathrm{T}} \cdot \mathbf{B}^{\mathrm{c}-1} \cdot (\mathbf{B}_{\mathrm{d}R} \cdot \boldsymbol{\phi}^{\mathrm{T}})^{\mathrm{T}} \tag{2-25}$$

$$\mathbf{DCDF}_R^c = \mathbf{PTDF}_R^c \cdot \mathbf{NDI}^{\mathrm{c}} \tag{2-26}$$

However, the calculation of $\mathbf{PTDF}_R^c$ as well as $\mathbf{PSDF}_{R,R}^c$ involves the inversion of the susceptance matrix $\mathbf{B}^{\mathrm{c}}$, which is a time-consuming process for large systems. A more sophisticated method is the use of line outage distribution factors (LODF), which are discussed below.

The branch power for the contingency case is calculated as given in (2-27). Outages of PSTs and HVDC links are directly included by a change in the **NDI** matrix and the vectors $\boldsymbol{\alpha}$ for the phase shifter angle and power flow via the HVDC link $\mathbf{p}_{R,\mathrm{DC}}$.

$$\mathbf{p}_{\mathrm{L},R}^{\mathrm{c}} = \mathbf{PTDF}_R^c \cdot \mathbf{p}_{\mathrm{N}} + \mathbf{PSDF}_{R,R}^c \cdot \boldsymbol{\alpha}_R + \mathbf{DCDF}_R^c \cdot \mathbf{p}_{R,\mathrm{DC}} \tag{2-27}$$

A more efficient approach is the use of the **LODF** matrix [62]. The concept is already well established and applied for (n-1)-calculations [63], multiple-branch outages [64] and economic considerations [65], [66] in traditional grids. The idea behind this concept is to superpose the base case load flow with an additional load flow created by the injection of the base case branch loading of the outage branch at the starting node of the branch and its negative value at the ending node.

$$\mathbf{p}_{\mathrm{L},R}^{\mathrm{c}} = \mathbf{p}_{\mathrm{L},R}^{\mathrm{b}} + \mathbf{LODF}_{R,O} \cdot \mathbf{p}_{\mathrm{L},O}^{\mathrm{b}} \tag{2-28}$$

The **LODF** for one outage branch gives the distribution of the additional load flow in the post contingency network normalized to $1\ \mathrm{pu}$ and is generalized calculated in matrix form for O outage branches as

$$\mathbf{LODF}_{R,O} = \mathbf{PTDF}_{R}^{\mathrm{c}} \cdot \boldsymbol{\psi} = \mathbf{B}_{\mathrm{d}R} \cdot \boldsymbol{\phi}^{\mathrm{T}} \cdot \mathbf{B}^{\mathrm{c}^{-1}} \cdot \boldsymbol{\psi} \tag{2-29}$$

The **LODF** can be calculated more efficient directly from the **PTDF** of the undisturbed system [62] without the need for inversion of the contingency susceptance matrix $\mathbf{B}^{\mathrm{c}}$ as

$$\mathbf{LODF}_{R,O} = \mathbf{PTDF}_{R} \cdot \boldsymbol{\psi} \cdot (\mathbf{I} - \mathbf{PTDF}_{O} \cdot \boldsymbol{\psi})^{-1} = \mathbf{PTDF}_{R,O} \cdot \left(\mathbf{I} - \mathbf{PTDF}_{O,O}\right)^{-1} \tag{2-30}$$

The corresponding parts of the **PTDF** and **PSDF** used in (2-30) and in the following considerations are calculated as

$$\mathbf{PTDF}_{R} = \mathbf{B}_{\mathrm{d}R} \cdot \boldsymbol{\phi}^{\mathrm{T}} \cdot \mathbf{B}^{-1} \tag{2-31}$$

$$\mathbf{PSDF}_{R,R} = \mathbf{B}_{\mathrm{d}R} - \mathbf{B}_{\mathrm{d}R} \cdot \boldsymbol{\phi}^{\mathrm{T}} \cdot \mathbf{B}^{-1} \cdot (\mathbf{B}_{\mathrm{d}R} \cdot \boldsymbol{\phi}^{\mathrm{T}})^{\mathrm{T}} \tag{2-32}$$

$$\mathbf{PSDF}_{O,R} = \mathbf{PSDF}_{R,O}^{\mathrm{T}} = -\mathbf{B}_{\mathrm{d}O} \cdot \boldsymbol{\psi}^{\mathrm{T}} \cdot \mathbf{B}^{-1} \cdot (\mathbf{B}_{\mathrm{d}R} \cdot \boldsymbol{\phi}^{\mathrm{T}})^{\mathrm{T}} \tag{2-33}$$

The **PTDF** and **PSDF** matrixes for the set of branches O are calculated by changing the susceptances and incidence matrix in equations (2-31) and (2-32) to $\mathbf{B}_O$ and $\boldsymbol{\Psi}$.

$\mathbf{B}_{\mathrm{d}R}$ and $\mathbf{B}_{\mathrm{d}O}$ are diagonal matrixes of the branch susceptances containing the remaining and outage branches. The equality of $\mathbf{PSDF}_{O,R}$ and $\mathbf{PSDF}_{R,O}{}^{\mathrm{T}}$ results from the diagonal symmetry of the whole **PSDF** matrix and can be proven applying $(\mathbf{AB})^{\mathrm{T}}=\mathbf{B}^{\mathrm{T}}\mathbf{A}^{\mathrm{T}}$ on (2-33).

The principle of **LODF** as described in [62] is based on the superposition of an active and a passive network without any power flow controlling units (PFC) and without any control interaction after the contingency event.

2.3.2 Fast Multi Branch LODF Calculation

Double and multi branch outages can occur with a not negligible possibility and have to be considered in the network operation planning. A straight forward approach calculating all combinations of branch outages is computational heavy. The computational effort is decreased, if the multi branch **LODF** is derived from the corresponding single branch outage **LODF**s. The **LODF** of a multi branch outage is in general not the sum of the corresponding single branch outage **LODF**s due to the mutual effects between the tripped branches. In the following derivation the following indices and naming is used:

$o1$	…	first branch on outage
$o2$	…	second branch on outage
$\mathbf{LODF}_{R,o1}^{(1)}$	…	single branch **LODF** $o1$ to R, $((L\text{-}2)\times 1)$
$\mathrm{LODF}_{o2,o1}^{(1)}$	…	single branch LODF $o1$ to $o2$, (1×1)
$\mathbf{LODF}_{R,o2}^{(1)}$	…	single branch **LODF** $o2$ to R, $((L\text{-}2)\times 1)$
$\mathrm{LODF}_{o1,o2}^{(1)}$	…	single branch LODF $o2$ to $o1$, (1×1)
$\mathbf{LODF}_{R,o1}^{(2)}$	…	double branch **LODF** $o1$ to R, $((L\text{-}2)\times 1)$
$\mathbf{LODF}_{R,o2}^{(2)}$	…	double branch **LODF** $o2$ to R, $((L\text{-}2)\times 1)$

The term $\mathrm{LODF}_{o2,o1}$ corresponds to the share of pre contingency power flow on branch $o1$, which would be transferred to branch $o2$ in case of a single branch outage of $o1$. The term $\mathrm{LODF}_{o1,o2}$ vice versa is the transferred power flow from $o2$ to $o1$. The multiplication of these terms results in the linking factor LF_{o1o2}, which can be interpreted as the share of power flow shifted back and forth between the branches $o1$ and $o2$ in case of a simultaneous outage.

$$LF_{o1,o2} = LODF_{o2,o1}^{(1)} \cdot LODF_{o1,o2}^{(1)} \tag{2-34}$$

The double branch **LODF** for branch $o1$ is composited of the sum of the single branch $\mathbf{LODF}_{R,o1}^{(1)}$ and the single branch $\mathbf{LODF}_{R,o2}^{(1)}$ multiplied with single branch $\mathrm{LODF}_{o2,o1}^{(1)}$. The sum of these factors is further multiplied with an infinite series of the linking factor, which gives the interaction of the two branches on outage, see equation (2-35).

$$\begin{aligned}\mathbf{LODF}_{R,o1}^{(2)} &= \left(\mathbf{LODF}_{R,o1}^{(1)} + \mathbf{LODF}_{R,o2}^{(1)} \cdot \mathrm{LODF}_{o2,o1}^{(1)}\right) \cdot \left(1 + LF_{o1,o2} + LF_{o1,o2}^2 + \cdots\right) \\ &= \left(\mathbf{LODF}_{R,o1}^{(1)} + \mathbf{LODF}_{R,o2}^{(1)} \cdot \mathrm{LODF}_{o2,o1}^{(1)}\right) \cdot \sum_{n=0}^{\infty} LF_{o1,o2}^{n}\end{aligned} \tag{2-35}$$

The infinite series in (2-35) is convergent, if the linking factor LF_{o1o2} is below 1. Due to the properties of LODFs the linking factor can have only values between 0 and 1, whereby values close to 0 indicate a low interaction and a value of 1 signals a network split caused by the double branch outage. However, since LODFs are no valid tool for post contingency analyses in the case of a network split, this case can be dismissed for the further calculation. Equation (2-35) is rewritten as

$$\mathbf{LODF}_{o1}^{(2)} = \left(\mathbf{LODF}_{o1}^{(1)} + \mathbf{LODF}_{o2}^{(1)} \cdot \mathrm{LODF}_{o2,o1}^{(1)}\right) \cdot \frac{1}{1 - LF_{o1,o2}} \tag{2-36}$$

$$0 \leq LF_{o1,o2} < 1 \tag{2-37}$$

The double branch **LODF** for branch $o2$ is calculated similar to (2-36) as

$$\mathbf{LODF}_{o2}^{(2)} = \left(\mathbf{LODF}_{o2}^{(1)} + \mathbf{LODF}_{o1}^{(1)} \cdot \mathrm{LODF}_{o1,o2}^{(1)}\right) \cdot \frac{1}{1 - LF_{o1,o2}} \tag{2-38}$$

The full **LODF** for the double outage is composited of these two column vectors.

$$\mathbf{LODF}^{2}_{R,o1o2} = \left[\mathbf{LODF}^{(2)}_{o1}\ \mathbf{LODF}^{(2)}_{o2}\right] \tag{2-39}$$

The number of necessary calculation steps for the calculation of the double branch **LODF** in a network with N nodes and L branches is $6(L\text{-}1)$, if the necessary single branch **LODF** is already available. This is a significant reduction compared to the $4L(1+N)$ calculation steps needed using the standard form of calculation (2-30). The described calculation can be further reduced by dismissing branch outage combinations with negligible interdependence by introducing a minimum linking factor.

Based on the consideration for double branch outages a stepwise calculation for multi branch outage is derived. The calculation for a tripped branch set of tripped branches O with m members is based on the **LODF**s of all possible outage combinations with $(m\text{-}1)$ tripped branches of the set O. Similar to (2-35) the resulting formula for the LODF of branch oi on the remaining branches R of the network is calculated by multiplying the direct effects on the remaining branches with an infinite series of a linking factor $LF^{(m),O}_{oi}$.

$$LF^{(m),O}_{oi} = \sum_{k=O\setminus oi} \mathrm{LODF}^{(m-1),O\setminus oi}_{oi,k} \cdot \mathrm{LODF}^{(1)}_{k,oi} \tag{2-40}$$

$$\mathbf{LODF}^{(m)}_{R,oi} = \left(\mathbf{LODF}^{(1)}_{R,oi} + \sum_{k=O\setminus oi} \mathbf{LODF}^{(m-1),O\setminus oi}_{R,k} \cdot \mathrm{LODF}^{(1)}_{k,oi}\right) \cdot \frac{1}{1 - LF_{m,oi}} \tag{2-41}$$

$$\mathbf{LODF}^{(m)}_{R,O} = \left[\mathbf{LODF}^{(m)}_{R,o1}\quad \mathbf{LODF}^{(m)}_{R,o2}\quad \cdots\quad \mathbf{LODF}^{(m)}_{R,om}\right] \tag{2-42}$$

oi	…	i[th] branch of set O
O	…	set of tripped branches O
$O\setminus oi$	…	set of tripped branches O without branch oi
m	…	number of branches in O
$LF^{(m),O}_{oi}$	…	linking factor for branch oi and m tripped branches
$\mathrm{LODF}^{(m-1),O\setminus oi}_{oi,k}$	…	$(m\text{-}1)$ branch LODF k to oi, tripped branches $O\setminus oi$, (1×1)
$\mathrm{LODF}^{(1)}_{k,oi}$	…	single branch LODF oi *to* k, (1×1)
$\mathbf{LODF}^{(m)}_{R,oi}$	…	m branch LODF oi to R, $((L\text{-}m)\times1)$
$\mathbf{LODF}^{(1)}_{R,oi}$	…	single branch LODF oi to R, $((L\text{-}m)\times1)$
$\mathbf{LODF}^{(m-1),O\setminus oi}_{R,k}$	…	$(m\text{-}1)$ branch LODF k to R, $((L\text{-}m)\times1)$
$\mathbf{LODF}^{(m)}_{R,O}$	…	m branch LODF O to R, $((L\text{-}m)\times1)$

The necessary $(m\text{-}1)$ **LODF**s are consequently calculated with the $(m\text{-}2)$ **LODF**s and so on, whereby the set of tripped branches are adapted for each calculation step. This procedure is repeated until single branch **LODF**s are included in the formula. Even though the stepwise calculation becomes computational heavy for higher values of m, it is still a better option than the classic calculation of the **LODF**s classically. Further, as discussed in [67], the accuracy of the DC load flow assumptions decreases with increasing numbers of tripped branches limiting a sensible use of LODFs.

To clarify the calculation, in the following a simple example is given. Assume an arbitrary AC network in which the single branch outage LODFs between the tripped branches 2, 3 and 4 as well as the single branch LODFs from the tripped branches to branch 1 are known, Fig. 2-4. Using the notation from above, the number of outages is $m = 3$ and the sets of tripped and remaining branches are given as $O = \{2,3,4\}$ and $R = \{1\}$. In the following example, the calculations are shown for the LODFs of a double branch outage – equations (2-49) and (2-50) – and triple branch outage- equation (2-51) and (2-52). The given LODFs and the calculation results are summarized in Table 2-1.

$$LF_2^{(2),\{2,3\}} = \mathrm{LODF}_{2,3}^{(1)} \cdot \mathrm{LODF}_{3,2}^{(1)} \tag{2-43}$$

$$\mathrm{LODF}_{1,2}^{(2),\{2,3\}} = \left(\mathrm{LODF}_{1,2}^{(1)} + \mathrm{LODF}_{1,3}^{(1)} \cdot \mathrm{LODF}_{3,2}^{(1)}\right) \cdot \frac{1}{1 - LF_2^{(2),\{2,3\}}} \tag{2-44}$$

$$LF_2^{(3),\{2,3,4\}} = \mathrm{LODF}_{2,3}^{(2)} \cdot \mathrm{LODF}_{3,2}^{(2)} + \mathrm{LODF}_{2,4}^{(2)} \cdot \mathrm{LODF}_{4,2}^{(2)} \tag{2-45}$$

$$\mathrm{LODF}_{1,2}^{(3),O} = \left(\mathrm{LODF}_{1,2}^{(1)} + \mathrm{LODF}_{1,3}^{(2),\{3,4\}} \cdot \mathrm{LODF}_{3,2}^{(1)} + \mathrm{LODF}_{1,4}^{(2),\{3,4\}} \cdot \mathrm{LODF}_{4,2}^{(1)}\right) \cdot \frac{1}{1 - LF_2^{(3),\{2,3,4\}}} \tag{2-46}$$

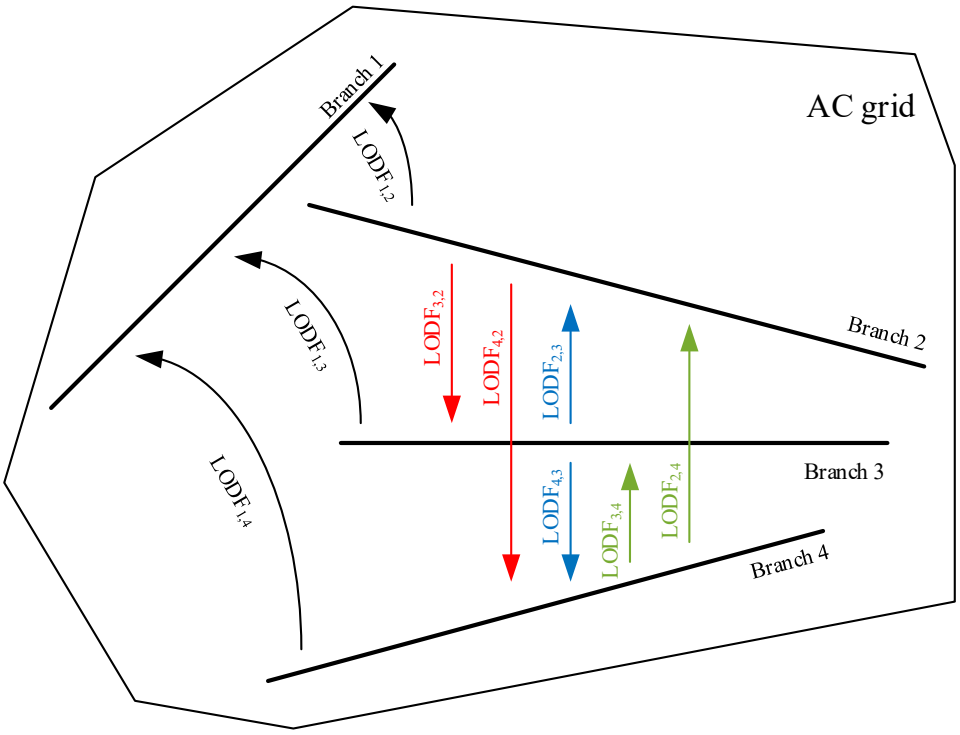

Fig. 2-4 Schematic of AC network for calculation example

Table 2-1 Given and calculated LODF values rounded to their 2nd decimal

Single Branch LODF		Double Branch LODF		Triple Branch LODF	
$LODF_{1,2}^{(1)}$	-0.63	Branch 2 and 3 out		Branch 2, 3 and 4 out	
$LODF_{1,3}^{(1)}$	0.46	$LODF_{1,2}^{(2),\{2,3\}}$	-0.76	$LODF_{1,2}^{(3),O}$	-0.79
$LODF_{1,4}^{(1)}$	0.32	$LODF_{1,3}^{(2),\{2,3\}}$	0.60	$LODF_{1,3}^{(3),O}$	0.54
$LODF_{2,3}^{(1)}$	-0.18	$LODF_{4,2}^{(2),\{2,3\}}$	-0.10	$LODF_{1,4}^{(3),O}$	0.29
$LODF_{2,4}^{(1)}$	-0.12	$LODF_{4,3}^{(2),\{2,3\}}$	-0.20		
$LODF_{3,2}^{(1)}$	-0.22				
$LODF_{3,4}^{(1)}$	-0.22	Branch 2 and 4 out			
$LODF_{4,2}^{(1)}$	-0.15	$LODF_{1,2}^{(2),\{2,4\}}$	-0.69		
$LODF_{4,3}^{(1)}$	-0.22	$LODF_{1,4}^{(2),\{2,4\}}$	0.40		
		$LODF_{3,4}^{(2),\{2,4\}}$	-0.19		
		$LODF_{3,4}^{(2),\{2,4\}}$	-0.20		
		Branch 3 and 4 out			
		$LODF_{1,3}^{(2),\{3,4\}}$	0.42		
		$LODF_{1,4}^{(2),\{3,4\}}$	0.22		
		$LODF_{2,3}^{(2),\{3,4\}}$	-0.16		
		$LODF_{24}^{(2),\{3,4\}}$	-0.09		

2.3.3 Consideration of Power flow controlling devices based on PSDF in DC Load Flow contingency analyses using LODF

The following proof shows, that the outage of power flow controlling devices manipulating node voltage angles between their connection nodes, e. g. PSTs, and branch outages in networks with these devices can be handled with LODFs. The most general configuration is assumed with the possibility to add a phase shifter angle $\boldsymbol{\alpha}$ at each branch is assumed for the proof. In this case $\mathbf{BPI}$ is equivalent to the identity matrix $\mathbf{I}$. The proof is also valid for FACT devices whose DC-Load flow model can be described with PSDF matrices, e. g. UPFCs.

The post contingency branch loading as calculated conventionally (2-47) is obviously independent of the omitted phase shifter angles $\boldsymbol{\alpha}_O$. The first step is to proof that the same is valid for (2-48). Therefore, the base case branch power of the branches R is rewritten by splitting $\boldsymbol{\alpha}$ into $\boldsymbol{\alpha}_R$ and $\boldsymbol{\alpha}_O$ (2-49). The matrix $\mathbf{PSDF}_R$ refers to the rows R of the complete $\mathbf{PTDF}$ matrix.

$$\mathbf{p}_{L,R}^{c} = \mathbf{PTDF}_R^{c} \cdot \mathbf{p}_N + \mathbf{PSDF}_{R,R}^{c} \cdot \boldsymbol{\alpha}_R \qquad (2\text{-}47)$$

$$\mathbf{p}_{L,R}^{c} = \mathbf{p}_{L,R}^{b} + \mathbf{LODF}_{R,O} \cdot \mathbf{p}_{L,O}^{b} \qquad (2\text{-}48)$$

$$\mathbf{p}_{L,R}^{b} = \mathbf{PTDF}_R^{b} \cdot \mathbf{p}_N + \mathbf{PSDF}_R^{b} \cdot \begin{pmatrix} \boldsymbol{\alpha}_R \\ \boldsymbol{\alpha}_O \end{pmatrix} \qquad (2\text{-}49)$$

The change on branch powers caused by $\boldsymbol{\alpha}_O$ can be rewritten as a power injection in the corresponding nodes distributed through the network by the $\mathbf{LODF}$ matrix for the branches O. Therefore, an active network containing all branches R and O with $\boldsymbol{\alpha}_O = 0$ is super positioned with a passive network without

branches O, but power injections according to the branch power change caused by $\boldsymbol{\alpha}_O$ in the branches O in their connection nodes. Fig. 2-5 shows the exemplary implementation for a single branch O.

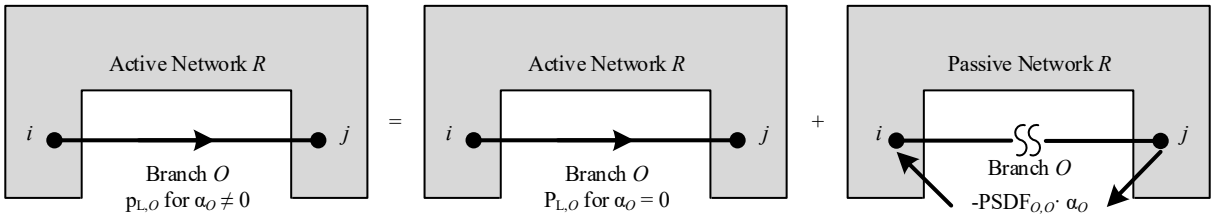

Fig. 2-5 Distribution of branch power change due to $\boldsymbol{\alpha}_O$ *with the use of* **LODF** *for a single line* O

The resulting base case load flows for branches R and O are rewritten as follows, whereby the negative sign in (2-50) is caused by the definition of the **PSDF**.

$$\mathbf{p}^{\mathrm{b}}_{\mathrm{L},R} = \mathbf{PTDF}^{\mathrm{b}}_{R} \cdot \mathbf{p}_{\mathrm{N}} + \mathbf{PSDF}^{\mathrm{b}}_{R,R} \cdot \boldsymbol{\alpha}_R - \mathbf{LODF}_{R,O} \cdot \mathbf{PSDF}^{\mathrm{b}}_{O,O} \cdot \boldsymbol{\alpha}_O \qquad (2\text{-}50)$$

$$\mathbf{p}^{\mathrm{b}}_{\mathrm{L},O} = \mathbf{PTDF}^{\mathrm{b}}_{O} \cdot \mathbf{p}_{\mathrm{N}} + \mathbf{PSDF}^{\mathrm{b}}_{O,R} \cdot \boldsymbol{\alpha}_R + \mathbf{PSDF}^{\mathrm{b}}_{O,O} \cdot \boldsymbol{\alpha}_O \qquad (2\text{-}51)$$

By substitution of (2-50) and (2-51) into (2-28) the proof is given, that by using **LODF** the contingency branch powers are independent of $\boldsymbol{\alpha}_O$.

$$\mathbf{p}^{\mathrm{c}}_{\mathrm{L},R} = \left(\mathbf{PTDF}^{\mathrm{b}}_{R} + \mathbf{LODF}_{R,O} \cdot \mathbf{PTDF}^{\mathrm{b}}_{O}\right) \cdot \mathbf{p}_{\mathrm{N}} + \left(\mathbf{PSDF}^{\mathrm{b}}_{R,R} + \mathbf{LODF}_{R,O} \cdot \mathbf{PSDF}^{\mathrm{b}}_{O,R}\right) \cdot \boldsymbol{\alpha}_R \qquad (2\text{-}52)$$

The structure of (2-52) is the same as for the conventional calculation (2-47). A simple coefficient comparison of these two equations yields the requirements to finish the proof for any arbitrary network.

$$\mathbf{PTDF}^{\mathrm{c}}_{R} \overset{!}{=} \mathbf{PTDF}^{\mathrm{b}}_{R} + \mathbf{LODF}_{R,O} \cdot \mathbf{PTDF}^{\mathrm{b}}_{O} \qquad (2\text{-}53)$$

$$\mathbf{PSDF}^{\mathrm{c}}_{R,R} \overset{!}{=} \mathbf{PSDF}^{\mathrm{b}}_{R,R} + \mathbf{LODF}_{R,O} \cdot \mathbf{PSDF}^{\mathrm{b}}_{O,R} \qquad (2\text{-}54)$$

The general fulfilment of the requirements can be shown by rewriting the matrixes by their basic elements' node-to-branch incidence matrixes, branch susceptances and system susceptance matrixes for the post contingency and base case and applying the matrix inversion lemma[2] several times on the resulting equations as shown in the authors publication [68].

The detailed derivation of this proof and application example for a small network and the ENTSO-E network is given in the authors publication [68].

[2] The matrix inversion lemma MIL is the equation $(A-BD^{-1}C)^{-1}=A^{-1}+A^{-1}B(D-CA^{-1}B)^{-1}CA^{-1}$

2.4 Application of DC Load Flow for Flow-Based Market Coupling

The flow-based market coupling (FBMC) is assumed to be implemented as the market environment for evaluations and methods discussed in chapter 4. The FBMC applies the DC load flow in for the allocation of the offered power transactions. The following paragraphs shall give a brief back ground information on the FBMC for better understanding of chapter 4. The paragraphs are mainly based on the ACER decision “Day-ahead capacity calculation methodology of the Core capacity calculation region” [69], the EU regulation 2019/943 [70] and [71], [72].

The multi-bidding zone markets of Europe has been based for most of the time on an available transfer capacity system. In this system power exchanges between zones are only limited by the given available transfer capacity. Loop flows caused by power exchanges between other zones and zone intern power transactions are not considered directly. To avoid insecure system operation, either the available transfer capacity has to be reduced beforehand or redispatch has to activated to solve the market introduced congestions. Both solutions lead to a loss in efficiency and social welfare of the market. The implementation of the flow-based market coupling methodology in the CWE, initiated in 2008 and set in force in 2015, shall take the physical network constraints into account and thereby increase the social welfare of the participating regions. The offline parallel run conducted in 2013-2014 show an increase in social welfare, price convergence and reliability for the FBMC compared to the available transfer capacity system [72], [73].

The main parameters for the FBMC are the zonal PTDF and the remaining available margin. The zonal PTDFs are calculated using the nodal PTDFs obtained by the linearized DC load flow model and generation shift keys (GSK). The nodal PTDFs are calculated as discussed in chapter 2.1 and the zonal PTDF of zone k is calculated as

$$\mathbf{PTDF}_{\mathrm{Z}k} = \mathbf{PTDF} \cdot \mathbf{GSK}_k \tag{2-55}$$

The GSK shall approximate the effects on the nodal distribution of the generation inside a given zone for the market driven change in the overall zonal generation. The GSKs of the individual zones are defined by the responsible transmission system operators based on different methods. With the resulting zonal PTDFs the critical network elements (CNE) are defined, whereby any branch with a corresponding zonal PTDF value higher than $5\ \%$ is considered as CNE.

The remaining available margin (RAM) of the CNEs defines the free capacity for market transactions. It calculates as the difference of the maximum allowable (n-1)-power flow on the CNE $F_{\mathrm{max,n1}}$ and a reference power flow F_{ref}, an adjustment value FAV and a reliability margin FRM. The RAM for a branch i is calculated as follows

$$RAM_i = F_{i,\mathrm{max,n1}} - F_{i,\mathrm{ref}} - FAV_i - FRM_i \tag{2-56}$$

The reference case is a forecast of the situation at the moment of delivery. The critical (n-1)-situation is defined by the outage of the critical contingency element (CC). The CCs or maximum allowable (n-1)-power flows are usually defined by the corresponding TSO based on load flow evaluations or historic

data or can be determined as discussed in chapter 4.2. More detailed information on the FBMC parameters and their calculation can be found in [71], [72].

The market clearing algorithm of the FBMC allocates the offered power transactions using the zonal PTDF and the RAMs of the CNE branches to reach an optimal social welfare without causing critical load flow situations.

3 Grid Areas of Interest

In general, interconnected transmission networks span large areas and are operated by several independent companies. Under these circumstances a delimitation of grid areas of interest, defining important branches and nodes, is necessary to allow an efficient execution of certain operational tasks.

The first part of this chapter focuses on the definition of grid areas controllable by PFCs. The power flow sensitivities of branches to the installed PFCs are thereby used as selection criterion. The resulting areas of control are later used for the optimization of PFCs' operation points (chapter 4) and can be used to define the operational area of emergency control strategies (chapter 6).

The areas of control are further used for the selection of branches, whose tripping have to be recognized due to its influence on the loading of the control able branches. The selection of these branches is based on the evaluation of the corresponding line outage distribution factors. The resulting areas of detection contain the selected branches and are later used in the emergency detection algorithm (chapter 5).

The last part of this chapters deals with selection of PMU monitored nodes necessary for the node voltage angle measurements needed as input for the emergency detection described in chapter 5. The goal thereby is to optimally distribute the PMU monitored nodes in the network enabling a good functionality of the emergency detection algorithm. The selection process of the PMU monitored nodes is based on the evaluation of the shared information of the node voltage angle changes caused by every single branch outage in the area of detection.

3.1 Area of Control

A power flow controlling device is only able to effectively control the load flow of certain branches. The controllable branches depend on the topology of the network and the location of the PFC. In general, the number of controllable branches is rather small compared to the overall number of branches in a large meshed grid topology. The set of controllable branches form the areas of control. The identification of the controllable branches is important to estimate the influence of single PFCs on the operation of the network by e.g. reducing necessary redispatch for (n-1)-security and on their ability to effectively react on disturbances such as line tripping to limit the impact of the disturbances e. g. avoiding cases of cascaded line tripping [34], [35].

The change in loading of all branches caused by each single PFC is analysed for the selection of the set of controllable branches Γ. The separate consideration of the single PFCs is necessary to avoid misinterpretation caused by opposite effects of PFCs. The sensitivities on the load flow are multiplied by the maximum control range of the single PFCs to allow a comparability of the effects between PFCs and is normalized to the thermal rating of the branch. Due to this, the elements of the resulting load change matrix $\Delta\mathbf{P}_{\mathrm{L}}$ are measures of the effective achievable loading change of the corresponding branch

caused by a specific PFC. The matrix $\Delta\mathbf{P}_{\mathrm{L}}$ is split into parts corresponding to embedded HVDC links, PSTs and UPFC and is calculated as follows

$$\Delta\mathbf{P}_{\mathrm{L}} = \mathrm{diag}(\mathbf{s}_{\mathrm{thermal}}^{-1}) \cdot [\mathbf{DCDF} \quad \mathbf{PSDF}] \cdot \mathrm{diag}\left(\begin{bmatrix}\mathbf{p}_{\mathrm{HVDC,nom}} \\ \boldsymbol{\alpha}_{\mathrm{PST,max}} \\ \boldsymbol{\alpha}_{\mathrm{UPFC,max}}\end{bmatrix}\right) \tag{3-1}$$

$\Delta\mathbf{P}_{\mathrm{L}}$	…	load change matrix $(L\times(D+P+U))$
$\mathbf{DCDF}$	…	HVDC transfer Distribution Factor Matrix $(L\times D)$
$\mathbf{PSDF}$	…	Phase Shift Distribution Factor Matrix $(L\times(P+U))$
$\mathbf{p}_{\mathrm{HVDC,nom}}$	…	vector of nominal power of HVDC link $(D\times 1)$
$\boldsymbol{\alpha}_{\mathrm{PST,max}}$	…	vector of maximal angle of PSTs $(P\times 1)$
$\boldsymbol{\alpha}_{\mathrm{UPFC,max}}$	…	vector of maximal angle changes utilizable by UPFCs $(U\times 1)$

The set Γ is derived by comparing the absolute values of the elements of $\Delta\mathbf{P}_{\mathrm{L}}$ with a defined limit $\Delta\mathrm{p}_{\mathrm{min}}$. The branches corresponding to rows of $\Delta\mathbf{P}_{\mathrm{L}}$ in which at least one element has a higher absolute value than $\Delta\mathrm{p}_{\mathrm{min}}$ are added to Γ. Considering only a single column of $\Delta\mathbf{P}_{\mathrm{L}}$, a subset of is found Γ, which includes only branches controllable by the PFC corresponding to the column. If one of the subsets has no common members with any other subset, the corresponding PFC has no significant interaction with other PFCs installed in the network. A branch selection based on the row wise sum of the absolute values of the elements in $\Delta\mathbf{P}_{\mathrm{L}}$ reflects the maximal change in the loading of the corresponding branch, if all PFCs are coordinated on one single branch.

The choice of $\Delta\mathrm{p}_{\mathrm{min}}$ has major influence on the selected branches and should be chosen reasonable for the purpose of the branch selection. The algorithm is run for a model the ENTSO-E network with different values of $\Delta\mathrm{p}_{\mathrm{min}}$ to illustrate the influence of $\Delta\mathrm{p}_{\mathrm{min}}$ on the number of selected branches. The model represents the presumable network status of the year 2025 including 34 PST and 10 embedded parallel HVDC links, whereby parallel PSTs in one substation and embedded HVDC links with the same connection points are counted only once. The algorithm takes overall a number of 7674 branches as candidates, which corresponds to the lines in operation in 2025. Further information on the model is given in Appendix A.

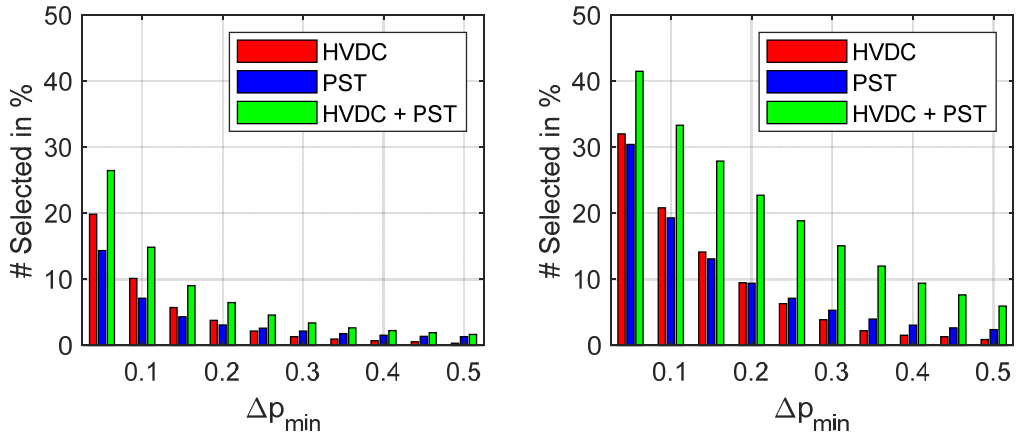

Fig. 3-1 influence of Δp_{min} on the number of selected branches. The left graph refers to a selection based on individual consideration of embedded HVDCs and PSTs. The right graph refers to a selection based on the combined effects of embedded HVDCs and PSTs on the branches. Red bars refer to embedded HVDCs, blue ones to PSTs and green ones to their combination.

Fig. 3-1 shows the number of controllable branches as a percentage of the network's lines in dependency of the value of Δp_{min}. Focusing on the left graph depicting the proportion for an individual consideration of each embedded HVDC and PST, it can be seen, that the percentage for embedded HVDCs is higher than for PSTs at smaller values of Δp_{min}. With increasing Δp_{min} values the number of selected branches decreases for both types of PFCs. For values of Δp_{min} above $0.25\ \text{pu}$ more branches are selected for PST than for embedded HVDCs. This behaviour is explained by the connection of the HVDC terminals to strong nodes in the meshed 380-kV grid. An embedded HVDC's influence on a branch therefore disperses on the grid between its terminals leading to more controllable branches with smaller influence. The PSTs on the other hand are situated on a specific branch mainly controlling the loading of it by shifting the power flow to parallel branches. Further, the higher number of installed PSTs compared to HVDC results in the slower decrease in the number of selected branches. The green bars refer to the combination of branches selected by either an individual embedded HVDC or an individual PST. The resulting proportion of the combined sets of controllable branches does not equal the sum of the proportions for embedded HVDCs and PSTs, since some branches are assigned to both sets corresponding to HVDCs and PSTs. The difference between the resulting proportion and the sum of the single proportions decrease with higher Δp_{min}, due to the smaller number of mutual affected branches.

The right graph in Fig. 3-1 shows the percentage of selected branches, if the combined effect of all considered PFCs is used for the selection. The combined effect is thereby determined by the row wise sum of the absolute values of the matrix $\Delta \mathbf{P}_L$. As expected, the proportion of selected branches is higher than the proportion of the individual selection. The higher proportion for the PSTs over all Δp_{min} values is caused by the higher number of installed PSTs compared to embedded HVDCs in the network. However, these values reflect the maximal load change achievable, if all considered PFCs in the grid use their full capacity to only control a specific branch without any restrictions due to overloading of other branches in the network. The green bars refer to the combination of embedded HVDCs and PSTs. The percentage of this combination is smaller than the sum of the proportions of HVDCs and PSTs on their own for small values of Δp_{min}, because of the assignment of selected branches to both subsets of HVDCs and PSTs.

To highlight the effect of different Δp_{min} values on the grid area with controllable branches and multiple selected branches, the network model is plotted in Fig. 3-2 and Fig. 3-3 for $\Delta p_{min} = 0.05\ \text{pu}$ and $\Delta p_{min} = 0.15\ \text{pu}$. The colouring of the selected branches corresponds to the number of subsets they are assigned to. Further evaluations on the influence of Δp_{min} on the number of multiple assigned branches is given in the Appendix B.

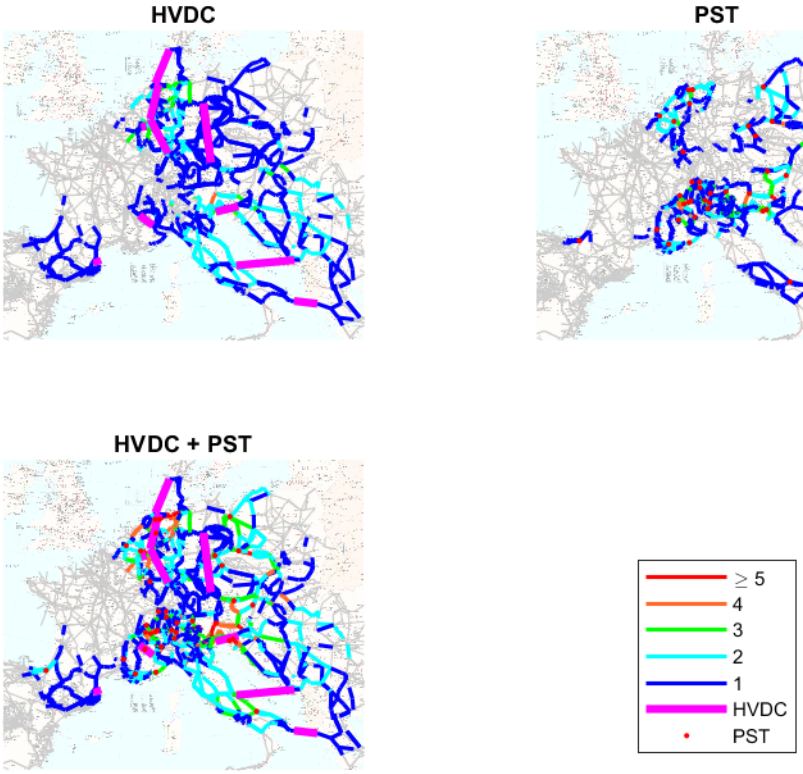

Fig. 3-2 selected branches for $\Delta p_{min} = 0.05\ pu$ upper left graph for embedded HVDC links only, upper right graph for PSTs only and lower graph for their combination. Colours of branches reflect the number of subsets they are assigned to.

The upper left graph of the figures corresponds to the individual evaluation of the embedded HVDC links. The considered embedded HVDC links are plotted in magenta. The selected branches are concentrated parallel to the HVDC connections and disperse with increasing electrical distance to the HVDC terminals. Having a closer look on the multiple selected branches for $\Delta p_{min} = 0.05$ pu depicted in Fig. 3-2 four different areas are identified. The most obvious one is on the border region between Spain and France. The other three areas do not distinguish as clearly. One of them is located on the border between France and Italy and second one around the Mediterranean Sea. The later mainly reflects the influenced of the HVDC links connecting Italy with Slovenia and Montenegro. The fourth area is created by the five HVDC links situated in Germany and between Denmark and the Netherlands, whereby multiple assigned branches are located in the northwest area of Germany.

The upper right graph shows the branches assigned to PSTs based on an individual evaluation. As can be seen, three main areas in the Benelux countries including parts of north-west Germany, on Germanies east border and the Alps stand out. The PSTs in south Italy and on the French-Spanish border are standing on their own without any interactions to other PSTs.

The lower graph combines the selected branches of embedded HVDC links and PSTs. For $\Delta p_{min} = 0.05$ pu the selected branches create one huge area with a high number of multiple assigned branches. This shows, that too small values of Δp_{min} are not suitable to select branches for control setpoint optimization of PFCs, since the optimization problem becomes computational heavy to solve. Further, the optimization would try to solve contingencies on branches, who are only ineffectively affected.

Focusing on Fig. 3-3, depicting the selected branches for $\Delta p_{min} = 0.05$ pu, the areas identified above are in principle still existing with the exception, that the HVDC area in Germany is now separated into an east part and a north-west part. The branches selected for PSTs only are now locally confined and mostly contain only the branches connected to the PSTs.

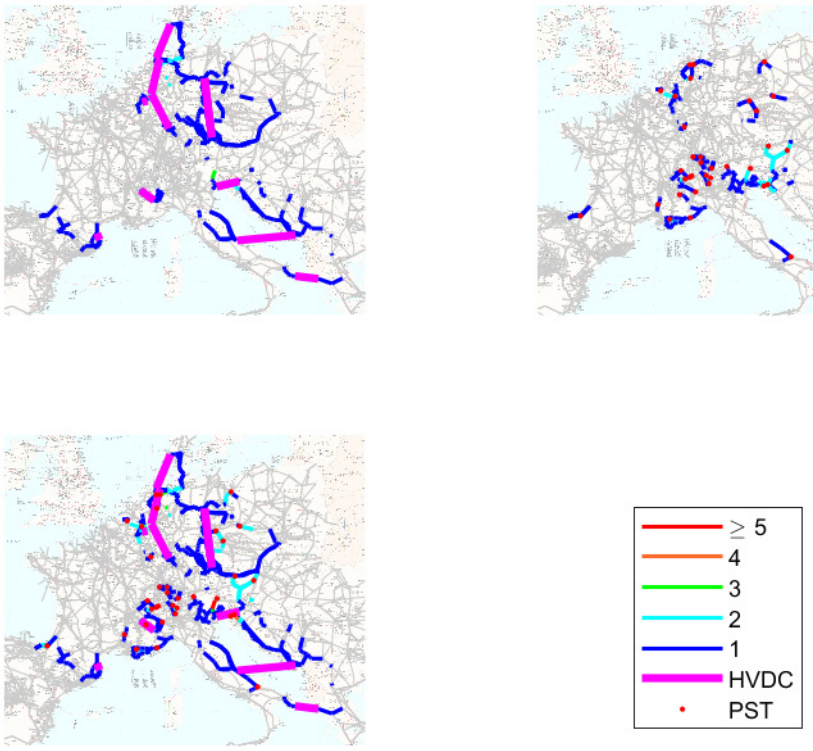

Fig. 3-3 selected branches for $\Delta p_{min} = 0.15$ pu upper left graph for embedded HVDC links only, upper right graph for PSTs only and lower graph for their combination. Colours of branches reflect the number of subsets they are assigned to.

From the discussed results, it can be concluded, that the value of Δp_{min} should be chosen only after an evaluation of its sensitivity on the number of selected branches and number of multiple assigned branches. Considering the typical operation of PSTs focusing on the line connected to the PSTs, it is sensible to choose a higher value of Δp_{min} for the selection of PSTs affected branches than for HVDC affected branches. However, the actual values are depending on the purpose of the selection of branches.

3.2 Area of Detection

The set Γ defines an area in which the PFC is an adequate instrument for emergency control measures considering branch overloading – the area of control of the considered PFC. For an efficient and correctly working emergency control it is important to recognize the tripping of branches with significant influence on the branches of Γ. Therefore, an area of detection is defined for each PFC containing a set of significant outage branches E. Any outage or outage combination of these significant outage branches have to be detected by the emergency detection algorithm, described in section 5.

The identification of these significant outage branches is based on the evaluation of the single branch LODFs of all branches in the network on the branches in Γ. Optionally, the factors can be normalized to the thermal rating of the tripped branch o and the corresponding branch in Γ to account for different thermal ratings and transferring the LODFs values to a change in branch loading.

$$\begin{aligned}\mathbf{lodf}_{\Gamma,o} &= \operatorname{diag}\left(\mathbf{s}_{\text{thermal},\Gamma}^{-1}\right) \cdot \mathbf{PTDF}_{\Gamma} \cdot \boldsymbol{\psi}_o \cdot (\mathbf{I} - \mathbf{PTDF}_o \cdot \boldsymbol{\psi}_o)^{-1} \cdot s_{\text{thermal},o} \\ &= \operatorname{diag}\left(\mathbf{s}_{\text{thermal},\Gamma}^{-1}\right) \cdot \mathbf{LODF}_{\Gamma,o} \cdot s_{\text{thermal},o}\end{aligned} \tag{3-2}$$

If one element of the column vector $\mathbf{lodf}_{\Gamma,o}$ is higher than a defined border, the branch o is added to the set E. After the evaluation of all branches, the set E contains the branches, whose single outages will lead to a significant change in the loading of the branches in Γ.

This procedure can be extended to double and multi branch outages using the corresponding LODFs and adapting equation (3-2). The multi branch LODFs can be calculated from the already known single branch LODFs as described in chapter 2.3.2.

The application of this selection procedure is demonstrated on the Nordic-32-Bus system in chapter 5.2.

3.3 PMU Bus Selection for Emergency Detection

The emergency detection discussed later in chapter 5 is based on the voltage angle changes caused by branch outages. These node voltage angle changes are monitored with PMUs. Any reduction of the number of PMU monitored nodes lead to a loss of information. However, if not all nodes can be equipped with PMUs due to economic or other reasons, the selection of the monitored nodes has a crucial influence on the applicability of detection algorithms. The following algorithm evaluates an ideal positioning of a given number of PMUs to apply the emergency monitoring on a given set E defining the areas of detection.

The selection of PMU monitored nodes is based on a matrix of node voltage angle changes for single branch outages $\mathbf{BOAC}$. The rows of this matrix refer to the nodes of the system and the columns to the tripped branch. The element $BOAC_{i,o}$ is the change of the node voltage angle of node i due to the tripping of branch o with $1\ \text{pu}$ pre contingency loading. The following derivation of the matrix is based on all *L*

branches of the network. If only the significant branches are of interest, the other branches can simply be removed without the need to change anything in the calculation of the individual parts of the matrix.

The single columns corresponding to the branch outages are calculated separately and then combined to receive the full matrix.

$$\mathbf{BOAC} = [\mathbf{BOAC}_1 \quad \mathbf{BOAC}_2 \quad \dots \quad \mathbf{BOAC}_L] \tag{3-3}$$

A formula for the column vector for a single branch outage of an arbitrary branch o is derived starting with the DC load flow relation between the branch power flows and node voltage angles for pre and post contingency for the remaining branches R – equations (3-4) and (3-5). The superscripts b and c relate to pre and post contingency

$$\mathbf{p}_{\mathrm{L},R}^{\mathrm{b}} = \mathbf{b}_{\mathrm{d},R} \cdot \mathbf{\Phi}_R^{\mathrm{T}} \cdot \boldsymbol{\vartheta}^{\mathrm{b}} \tag{3-4}$$

$$\mathbf{p}_{\mathrm{L},R}^{\mathrm{c}} = \mathbf{p}_{\mathrm{L},R}^{\mathrm{b}} + \mathbf{LODF}_{R,o} \cdot \mathbf{p}_{\mathrm{L},o}^{\mathrm{b}} = \mathbf{b}_{\mathrm{d},R} \cdot \mathbf{\Phi}_R^{\mathrm{T}} \cdot \boldsymbol{\vartheta}^{\mathrm{c}} \tag{3-5}$$

Inserting (3-4) in (3-5) and solving for the angle difference gives (3-7).

$$\mathbf{b}_{\mathrm{d},R} \cdot \mathbf{\Phi}_R^{\mathrm{T}} \cdot \boldsymbol{\vartheta}^{\mathrm{b}} + \mathbf{LODF}_{R,o} \cdot \mathrm{p}_{\mathrm{L},o}^{\mathrm{b}} = \mathbf{b}_{\mathrm{d},R} \cdot \mathbf{\Phi}_R^{\mathrm{T}} \cdot \boldsymbol{\vartheta}^{\mathrm{c}} \tag{3-6}$$

$$\left(\boldsymbol{\vartheta}^{\mathrm{c}} - \boldsymbol{\vartheta}^{\mathrm{b}}\right) = \left(\mathbf{b}_{\mathrm{d},R} \cdot \mathbf{\Phi}_R^{\mathrm{T}}\right)^{+} \cdot \mathbf{LODF}_{R,o} \cdot \mathbf{p}_{\mathrm{L},o}^{\mathrm{b}} = \mathbf{BOAC}_o \cdot \mathbf{p}_{\mathrm{L},o}^{\mathrm{b}} \tag{3-7}$$

Replacing the line outage distribution factors $\mathbf{LODF}_{R,o}$ by its elements as given in [62] leads to (3-8).

$$\mathbf{BOAC}_o = \left(\mathbf{b}_{d,R} \cdot \mathbf{\Phi}_R^{\mathrm{T}}\right)^{+} \cdot \mathbf{LODF}_{R,o} = \left(\mathbf{b}_{d,R} \cdot \mathbf{\Phi}_R^{\mathrm{T}}\right)^{+} \cdot \mathbf{PTDF}_R \cdot \boldsymbol{\psi}_o \cdot (\mathbf{I} - \mathbf{PTDF}_o \cdot \boldsymbol{\psi}_o)^{-1} \tag{3-8}$$

$\boldsymbol{\phi}_R$	…	node-to-remaining branch incidence matrix ($(N\text{-}1)\times$# of R)
$\boldsymbol{\psi}_o$	…	node-to-outage incidence matrix ($(N\text{-}1)\times 1$)
$\mathbf{b}_{d,R}$	…	diagonal matrix of susceptances of branches R (# of $R\times$# of R)
$\mathbf{PTDF}_R$	…	PTDF of remaining branches R (# of $R\times(N\text{-}1)$)
$\mathbf{PTDF}_o$	…	PTDF of tripped branch o ($1\times(N\text{-}1)$)
$\mathbf{BOAC}_o$	…	vector of node voltage angle changes from outage o ($(N\text{-}1)\times 1$)
$\mathbf{LODF}_{Ro}$	…	LODFs from branch o to branches R (# *in* $R\times 1$)
$\boldsymbol{\vartheta}$	…	node voltage angle vector ($(N\text{-}1)\times 1$)
$\mathbf{p}_{\mathrm{L},o}$	…	power flow on branch o (1×1)

The matrix product $\mathbf{b}_{\mathrm{d},R}\cdot\boldsymbol{\phi}_R$ is in general not a square matrix with the dimension $((N\text{-}1)\times L)$. If the selection of the branch o is restricted to branches not causing islanding if removed, the minimal value of $(L\text{-}1)$ equals $(N\text{-}1)$. Therefore, the pseudo inverse $(\mathbf{b}_{\mathrm{d},R}\cdot\boldsymbol{\phi}_R)^{+}$ corresponds to the solution of an in general overdetermined set of equations. A meaningful solution for $\mathbf{BOAC}_o$ requires the definition of a reference node with a defined node voltage angle change of 0 to avoid floating values. The reference node can be chosen freely but must not change for all considered branch outages. The selection should be based on network analysis focusing on the risk of islanding of the reference node and the oscillation tendency after a contingency event. A suggestion for a selection decision is to evaluate tripping heuristics of lines connected to candidate nodes [74] to estimate the risk of islanding. The oscillation tendency can be estimated by evaluating the participation on oscillation modes based on the system right eigenvectors

for the system state before and after the contingency event. However, the optimal selection of the reference node is not addressed in this work and for simplification the slack and reference node are identical and arbitrarily chosen.

The scalar product of two information vectors gives a measure of shared information. The smaller the value of the scalar product the less information is redundant. The values of the scalar products are limited to an interval of $[-1,1]$, if the corresponding unit vectors of the information vectors are used. Expanding this measure to a set of information vectors, the redundant information of one vector to the other vectors in the set is measured by determining the maximum absolute scalar product of the vector and the other vectors in the set. Consequently, the sum of the maximum absolute scalar products of all combinations in the set are a comparative value of the overall redundant information of the set. The smaller the sum is the less redundant information exists in the set of vectors. This correlation between redundant information and the scalar products is used to determine the optimal placement of PMUs in a network. The rows of the $\mathbf{BOAC}$ can be interpreted as information vectors linked to the node voltage angle change for any single branch outage. The set PMU monitored nodes is achieved by minimizing the sum of maximal absolute scalar products of the unit vector combinations of the rows corresponding to the nodes in the set.

A scalar combination matrix $\mathbf{SCM}$ is introduced to simplify the notation and the value handling for the selection algorithm. The element $scm_{i,j}$ is the absolute value of the scalar product of the row unit vectors i and j of $BOAC$.

$$scm_{i,j} = \left| \frac{\mathbf{BOAC}_{i,\mathrm{all}} \cdot \mathbf{BOAC}_{j,\mathrm{all}}^{\mathrm{T}}}{\sqrt{\mathbf{BOAC}_{i,\mathrm{all}} \cdot \mathbf{BOAC}_{i,\mathrm{all}}^{\mathrm{T}}} \cdot \sqrt{\mathbf{BOAC}_{j,\mathrm{all}} \cdot \mathbf{BOAC}_{j,\mathrm{all}}^{\mathrm{T}}}} \right| \tag{3-9}$$

Due to its definition, the matrix $\mathbf{SCM}$ is symmetric and all main diagonal elements are 1. The sum d_C of maximal scalar products for the nodes of an arbitrary set of PMU monitored nodes is calculated as follows. The index i refers to the row and j to the columns of $\mathbf{SCM}$. The identity matrix $\mathbf{I}$ is subtracted of $\mathbf{SCM}$ to exclude the scalar product of any vector to itself.

$$d_C = \sum_{\mathrm{j}\in\mathrm{C}} \max_{i \in C} \left((\mathbf{SCM} - \mathbf{I})_{i,j} \right) \tag{3-10}$$

A straight forward – in the following called global – algorithm for finding the minimizing set has to evaluate all possible combinations. The number of combinations for k monitored nodes in an N node network is given as

$$\#_{\mathrm{combinations}} = \frac{N!}{k!\,(N-k)!} \tag{3-11}$$

This approach is only feasible for rather small networks or network parts due to the sheer number of possible node combinations. This problem can be bypassed using a stepwise algorithm. The starting nodes are either selected by the smallest value of the **SCM** matrix or by the network topology itself, e.g. HVDC terminals. The algorithm starts with these two nodes in the set of monitored nodes and adds the node with the smallest sum of corresponding values of **SCM** to the set at each step. Using the indices,

a for nodes already in the set and u for all the other possible candidate nodes for PMU monitoring, the underlying objective function is given as

$$f(u) = \min\left(\sum_{i=a} \max((\mathbf{SCM} - \mathbf{I})_{i,u})\right) \tag{3-12}$$

The evaluated combinations at each step are $(N\text{-}a)$. The procedure of adding nodes is repeated till the set has k elements. The necessary number of evaluations using this algorithm in a network of N nodes and k PMU monitored nodes is

$$\#_{\text{combinations}} = (k-1) \cdot \left(N - \frac{k}{2}\right) \tag{3-13}$$

This is a significant reduction in the number of evaluations necessary for finding the optimal placement of PMU monitored nodes in the network compared to the straight forward algorithm. In chapter 5.2 the selection algorithm is applied on the Nordic-32-Bus system and compared to the results of the evaluation of all possible node combinations.

4 Control Setpoint Coordination and Optimization

The increasing number of power flow controlling devices (PFC), e. g. phase shifting transformers, converter-based FACTs and embedded HVDC links, in the transmission network allow a more flexible use of the transmission capacity. With the increasing number of PFCs, interfering effects between the devices have to be considered for an optimal utilization of the network capacity. The coordination of the PFC operation becomes thereby a factor not to be dismissed in operational planning as well as in network optimization.

A coordinated operation strategy of parallel embedded HVDC links has been already evaluated on the capability of reducing the line loadings and applied to an reduced model of the German transmission network in [12], [43]. The coordination of PST setpoints is so far mainly evaluated by studies with respect to border flows in an multi bidding zone network, e. g. [8], [9]. Implementing a multi-agent based control strategy for PFCs [45] and combining it with redispatch activation [46] has been discussed for online-control focusing on unforeseen network conditions.

In contrast to these evaluations, the coordination of embedded HVDC links and PSTs with respect to an efficient reduction of the redispatch volume for a reference year is discussed in the following. The focus on these two types of PFCs is justified by their load flow control capacity, their number, their installed capacity and the availability of data[3]. In Fig. 4-1 the installed power of embedded HVDC links and PST as well as the number of operational facilities in the ENTSO-E grid are depicted. The data is collected from public available sources such as the ten-year development plans.

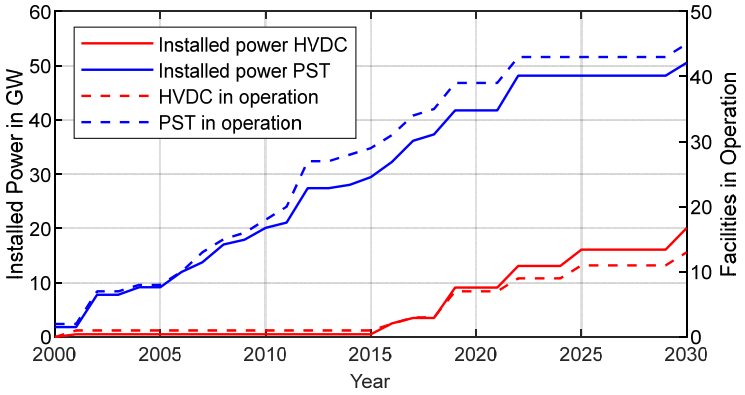

Fig. 4-1 installed power of embedded HVDC links / PST and facilities in operation for the ENTSO-E grid

The goal of reducing the necessary redispatch implies, that either (n-1)-secure flows have to be estimated and implemented as constraints or alternatively the (n-1)-PTDFs according to the critical contingencies have to be used in the problem formulation. The determination of the (n-1)-secure flow

[3] Quadrature booster transformers are included similar to PSTs, if data is available.

and the critical contingency is discussed in the chapter 4.2. In the following formulation of the cost function, equality and inequality constraints the (n-1)-security is considered by using the (n-1)-sensitivities based on the critical contingencies. This allows to set the flow limit for the branches to $1\ \mathrm{pu}$ normalized on the branches' maximum rating. The reasoning behind this decision is, that critical contingencies are more stable for variations in the load flow than a power flow limit.

4.1 Formulation of Optimization Problem

The optimization of the control setpoints is based on the linearized DC load flow equations. The optimization problem is therefore formulated linear and can be solved efficiently applying simplex algorithms [75]. The optima $\mathbf{x}^*$ minimising the costs is found solving the problem specified by

$$\mathbf{f}^{\mathrm{T}} \cdot \mathbf{x}^* = \min_{\mathbf{x}} \mathbf{f}^{\mathrm{T}} \cdot \mathbf{x} \; such\ that \begin{cases} \mathbf{A}_{\mathrm{ineq}} \cdot \mathbf{x} \leq \mathbf{b}_{\mathrm{ineq}} \\ \mathbf{A}_{\mathrm{eq}} \cdot \mathbf{x} = \mathbf{b}_{\mathrm{eq}} \\ \mathbf{lb} \leq \mathbf{x} \leq \mathbf{ub} \end{cases} \tag{4-1}$$

$\mathbf{x}$	…	vector of trial variables
$\mathbf{x}^*$	…	optimum point
$\mathbf{f}$	…	objective function vector
$\mathbf{A}_{\mathrm{ineq}}$	…	matrix for inequality constraints
$\mathbf{b}_{\mathrm{ineq}}$	…	vector for inequality constraints
$\mathbf{A}_{\mathrm{eq}}$	…	matrix for equality constraints
$\mathbf{b}_{\mathrm{eq}}$	…	vector for equality constraints
$\mathbf{lb}$	…	lower bounds of the trial variables
$\mathbf{ub}$	…	upper bounds of the trial variables

In the following, the optimization problem is formulated generally for a combined optimization of redispatch and the control setpoints of embedded HVDCs and PSTs for linear programming. The vector of trial variables consists of the active power change of the power plants participating in the redispatch pool, the active power setpoint change of the considered HVDC links and the angle change of the considered PSTs. Due to different costs and operational bounds the trial variables linked to the active power changes are split in positive and negative redispatch power. The definition of positive redispatch is hereby an increase of the active power of the corresponding power plant, negative redispatch consequently a decrease.

$$\mathbf{x}^{\mathrm{T}} = \left[\underbrace{x_1 \quad \cdots \quad x_{pp}}_{\mathbf{x}_{\mathrm{pos}}^{\mathrm{T}}} \quad \underbrace{x_{pp+1} \quad \cdots \quad x_{2 \cdot pp}}_{\mathbf{x}_{\mathrm{neg}}^{\mathrm{T}}} \quad \underbrace{x_{2 \cdot pp+1} \quad \cdots \quad x_{2 \cdot pp+dc}}_{\mathbf{x}_{\mathrm{DC}}^{\mathrm{T}}} \quad \underbrace{x_{2 \cdot pp+dc+1} \quad \cdots \quad x_{2 \cdot pp+dc+pst}}_{\mathbf{x}_{\mathrm{PST}}^{\mathrm{T}}} \right] \tag{4-2}$$

pp	…	number of power plants participating in the redispatch pool
dc	…	number of considered HVDC links
pst	…	number of considered PST
$\mathbf{x}_{\mathrm{pos}}$	…	vector of positive redispatch action

$\mathbf{x}_{\text{neg}}$	…	vector of negative redispatch action
$\mathbf{x}_{\text{DC}}$	…	vector of HVDC active power setpoints
$\mathbf{x}_{\text{PST}}$	…	vector of PST angle changes

The objective function vector $\mathbf{f}$ consists of the costs for positive and negative redispatch activation, active power transfer via HVDC links and the angle changes of PSTs.

$$\mathbf{f}^{\text{T}} = \left[\mathbf{c}_{\text{pos}}^{\text{T}} \quad \mathbf{c}_{\text{neg}}^{\text{T}} \quad \mathbf{c}_{\text{DC}}^{\text{T}} \quad \mathbf{c}_{\text{PST}}^{\text{T}}\right] \tag{4-3}$$

The equality constraints defined by the matrix $\mathbf{A}_{\text{eq}}$ and the vector $\mathbf{b}_{\text{eq}}$ depict that the activated positive and negative redispatch power must be balanced. Consequently, the matrix $\mathbf{A}_{\text{eq}}$ is a row vector whose first $2{\times}pp$ elements are 1 and all other elements are 0. The vector $\mathbf{b}_{\text{eq}}$ becomes a scalar with the value 0.

$$\mathbf{A}_{\text{eq}} = \left[\underbrace{1 \quad \cdots \quad 1}_{(1\times pp)} \middle| \underbrace{1 \quad \cdots \quad 1}_{(1\times pp)} \middle| \underbrace{0 \quad \cdots \quad 0}_{(1\times(dc+pst))}\right], b_{\text{eq}} = 0 \tag{4-4}$$

The inequality constraints defined by the matrix $\mathbf{A}_{\text{ineq}}$ and the vector $\mathbf{b}_{\text{ineq}}$ implement the actual load flow in the optimizing problem. Independent of the actual optimization goal the inequality constraints must be formulated in a way to ensure, that (n-1)-secure branches are not overloaded and (n-1)-secure branches are relieved enough to fulfil (n-1)-security. The optimization starts thereby from the base case load flow based on the solution of a market simulation. The matrix elements give the sensitivities of the corresponding branch power flow to the trial variables in $\mathbf{x}$. The dimension of each partial matrix of $\mathbf{A}_{\text{ineq}}$ corresponding to the different types of trial variables is noted in equation (4-5). The sign of the (n-1)-base case load flow on each branch is defined as positive to simplify the formulation of the equality and inequality costraints in the following. This sign convention requires a sign correction of the rows in $\mathbf{A}_{\text{ineq}}$ corresponding to initially negative values of the (n-1)-base case load flow. The sign correction is achieved by a multiplication with a diagonal matrix composed of the element's signs of vector $\mathbf{p}_{\text{L,N1}}^{\text{b}}$.

$$\mathbf{A}_{\text{ineq}} = \text{diag}\left(\text{sign}\left(\mathbf{p}_{\text{L,N1}}^{\text{b}}\right)\right) \cdot \left[\underbrace{\mathbf{PTDF}_{\text{N1},RD}}_{(B\times pp)} \middle| \underbrace{\mathbf{PTDF}_{\text{N1},RD}}_{(B\times pp)} \middle| \underbrace{-\mathbf{PTDF}_{\text{N1}} \cdot \mathbf{NDI}}_{(B\times dc)} \middle| \underbrace{\mathbf{PSDF}_{\text{N1}}}_{(B\times pst)}\right] \tag{4-5}$$

$$\mathbf{p}_{\text{L,N1}}^{\text{b}} = \mathbf{PTDF}_{\text{N1}} \cdot \mathbf{p}_{\text{N}} \tag{4-6}$$

B	…	number of branches in the network
RD	…	connection nodes of the redispatch power plants
$\mathbf{PTDF}_{\text{N1,RD}}$	…	critical (n-1)-PTDF reduced to nodes RD
$\mathbf{PSDF}_{\text{N1,RD}}$	…	critical (n-1)-PTDF reduced to nodes RD
$\mathbf{PTDF}_{\text{N1}}$	…	critical (n-1)-PTDF ($B{\times}(N\text{-}1)$)
$\mathbf{NDI}$	…	node-to-DC incidence matrix ($(N\text{-}1){\times}dc$)
$\mathbf{p}_{\text{N}}$	…	power injection vector of market solution ($(N\text{-}1){\times}1$)

The critical (n-1)-PTDFs are calculated using the LODF of the critical contingency element on the corresponding branch. The critical contingency elements are determined as discussed in chapter 4.2. The following equations show the calculation of the critical (n-1)-PTDFs and (n-1)-PSDFs of branch b and its critical contingency element cc.

$$\mathbf{PTDF}_{\mathrm{N1},b} = \mathbf{PTDF}_b + LODF_{cc,b} \cdot \mathbf{PTDF}_{cc} \quad (4\text{-}7)$$

$$\mathbf{PSDF}_{\mathrm{N1},b} = \mathbf{PSDF}_b + LODF_{cc,b} \cdot \mathbf{PTDF}_{cc} \quad (4\text{-}8)$$

The implementation of the (n-1)-security with the critical (n-1)-PTDFs allows the definition of the inequality vector $\mathbf{b}_{\mathrm{ineq}}$ as the difference between the absolute value of the critical (n-1) base case load flow $\mathbf{p}^{\mathrm{b}}_{\mathrm{L,N1}}$ and the branch's maximum rating. The vector contains therefore an allowed region for the change in the power flow of each branch.

$$\mathbf{b}_{\mathrm{ineq}} = \mathbf{s}_{\mathrm{thermal}} - \left|\mathbf{p}^{\mathrm{b}}_{\mathrm{L,N1}}\right| \quad (4\text{-}9)$$

The elements of vector $\mathbf{b}_{\mathrm{ineq}}$ are negative for branches overloaded under (n-1)-operation in the base case load flow. The optimizer's solution is therefore obliged to relieve the overloaded branch with a minimum amount of the absolute value of the corresponding negative element. Positive elements of $\mathbf{b}_{\mathrm{ineq}}$ are linked to not overloaded branches. The optimizer is allowed to increase the power flow of these branches with a maximum amount of the element's value.

At this point it must be noted, that this implementation of inequality constraints does not exclude results with power flows in opposite direction than the base case power flow and higher values than the thermal rating. If these solutions should be avoided too, the inequality constraints must be expanded to matrix $\mathbf{A}_{\mathrm{ineq,ex}}$ and $\mathbf{b}_{\mathrm{ineq,ex}}$.

$$\mathbf{A}_{\mathrm{ineq,ex}} = \begin{bmatrix} \mathbf{A}_{\mathrm{ineq}} \\ -\mathbf{A}_{\mathrm{ineq}} \end{bmatrix} \quad (4\text{-}10)$$

$$\mathbf{b}_{\mathrm{ineq,ex}} = \begin{bmatrix} \mathbf{s}_{\mathrm{thermal}} - \left|\mathbf{p}^{\mathrm{b}}_{\mathrm{L,N1}}\right| \\ \mathbf{s}_{\mathrm{thermal}} + \left|\mathbf{p}^{\mathrm{b}}_{\mathrm{L,N1}}\right| \end{bmatrix} \quad (4\text{-}11)$$

The upper and lower boundaries for the trial variables are given as follows. The lower boundaries are 0 and the upper boundaries are the difference between the maximum active power and the active power already utilized in the base case for the trial variables corresponding to positive redispatch $\mathbf{x}_{\mathrm{pos}}$. The lower boundaries of 0 avoid negative redispatch. This is necessary for power plants available for positive and negative redispatch, since the costs differ. The upper boundaries ensure, that the available active power for redispatch measures does correspond to the actual operation of the redispatch power plants. Vice versa are the upper boundaries of the negative redispatch trial variable $\mathbf{x}_{\mathrm{neg}}$ set to 0 and the corresponding lower boundaries set to the difference between the active power utilized in the base case and the minimum power of the power plant. The upper and lower boundaries of the HVDC links and PSTs are the differences between operation point of the base case and their operational limits.

$$\mathbf{lb}^{\mathrm{T}} = \left[\underbrace{\mathbf{0}_{1,RD}}_{(1\times pp)} \quad \underbrace{\left(\mathbf{p}_{RD,\min} - \mathbf{p}_{RD,\mathrm{op}}\right)^{\mathrm{T}}}_{(1\times pp)} \quad \underbrace{\left(\mathbf{p}_{\mathrm{DC,min}} - \mathbf{p}_{\mathrm{DC,op}}\right)^{\mathrm{T}}}_{(1\times dc)} \quad \underbrace{\left(\boldsymbol{\alpha}_{\min} - \boldsymbol{\alpha}_{\mathrm{op}}\right)^{\mathrm{T}}}_{(1\times pst)}\right] \quad (4\text{-}12)$$

$$\mathbf{ub}^{\mathrm{T}} = \left[\underbrace{\left(\mathbf{p}_{RD,\max} - \mathbf{p}_{RD,\mathrm{op}}\right)^{\mathrm{T}}}_{(1\times pp)} \quad \underbrace{\mathbf{0}_{1,RD}}_{(1\times pp)} \quad \underbrace{\left(\mathbf{p}_{\mathrm{DC,max}} - \mathbf{p}_{\mathrm{DC,op}}\right)^{\mathrm{T}}}_{(1\times dc)} \quad \underbrace{\left(\boldsymbol{\alpha}_{\max} - \boldsymbol{\alpha}_{\mathrm{op}}\right)^{\mathrm{T}}}_{(1\times pst)}\right] \quad (4\text{-}13)$$

$\mathbf{0}_{1,\mathrm{RD}}$	…	row vector of zeros
$\mathbf{p}_{RD,\mathrm{op}}$	…	vector of active power setpoint of redispatch power plants

$\mathbf{p}_{RD,\min}$	…	vector of minimal active power of redispatch power plants
$\mathbf{p}_{RD,\max}$	…	vector of maximal active power of redispatch power plants
$\mathbf{p}_{DC,\mathrm{op}}$	…	vector of active power setpoint of HVDC links
$\mathbf{p}_{DC,\min}$	…	vector of minimal active power of HVDC links
$\mathbf{p}_{DC,\max}$	…	vector of maximal active power of HVDC links
$\boldsymbol{\alpha}_{\mathrm{op}}$	…	vector of angle setpoint of PSTs
$\boldsymbol{\alpha}_{\min}$	…	vector of minimal angle of PSTs
$\boldsymbol{\alpha}_{\max}$	…	vector of maximal angle of PSTs

The described optimization problem is strict in avoiding overloaded lines due to their implementation in the inequality constraints, which might cause that no feasible solution can be found because of representation inaccuracies of the underlying models. This can be avoided by relaxing the constraints on overloading with penalty costs to power flows higher than the thermal rating. Since these penalty costs are only partial linear – zero if the branch is not overloaded and linear to the overload otherwise – two new trial variable vectors $\mathbf{x}_{\mathrm{U}}$ and $\mathbf{x}_{\mathrm{O}}$ are introduced to transfer the penalty costs into a linear representation. These trial variables only consider branches, who are overloaded in the base case OL. The trial variables in $\mathbf{x}_{\mathrm{U}}$ correspond to amount of power transfer the formerly overloaded branch is relived under its thermal rating. The trial variables in $\mathbf{x}_{\mathrm{O}}$ correspond to the remaining overload on these branches. Consequently, all boundaries, costs, equality and inequality constraints must be expanded in accordance with the new trial variables. The new trial variable vector is given as

$$\tilde{\mathbf{x}}^{\mathrm{T}} = [\mathbf{x}^{\mathrm{T}} \quad \mathbf{x}_{\mathrm{U}}^{\mathrm{T}} \quad \mathbf{x}_{\mathrm{O}}^{\mathrm{T}}] \tag{4-14}$$

Due to the definition of $\mathbf{x}_{\mathrm{U}}$ its values are calculated as the minimum of the sum of the power flow change and the former overload of the corresponding branches and 0. Therefore, the elements in $\mathbf{x}_{\mathrm{U}}$ are negative or 0. The upper boundary is consequently 0. A lower boundary of two times the negative thermal rating is added to avoid an overloading with changed sign. However, as discussed before, it is highly unlikely that this boundary is reached. The definition of $\mathbf{x}_{\mathrm{O}}$ implies, that it is the maximum of the sum of the power flow change on the branches and the base case overload of the corresponding branches and 0. This causes all elements in $\mathbf{x}_{\mathrm{O}}$ to be positive or zero. The lower boundary is therefore 0. The upper boundary is set to the thermal rating of the corresponding branches multiplied with a selectable factor $\mathbf{k}_{\max,OL}$. This factor controls the allowed overloading – e.g. a factor of 1 allows an optimizer solution with $100\,\%$ overload on the corresponding branch.

$$\widetilde{\mathbf{lb}}^{\mathrm{T}} = \left[\mathbf{lb}^{\mathrm{T}} \quad -2 \cdot \mathbf{s}_{\mathrm{thermal},OL}^{\mathrm{T}} \quad \mathbf{0}_{1,OL}\right] \tag{4-15}$$

$$\widetilde{\mathbf{ub}}^{\mathrm{T}} = \left[\mathbf{ub}^{\mathrm{T}} \quad \mathbf{0}_{1,OL} \quad \mathbf{s}_{\mathrm{thermal},OL}^{\mathrm{T}} \cdot \mathrm{diag}\left(\mathbf{k}_{\max,OL}\right)\right] \tag{4-16}$$

The boundaries of $\mathbf{x}_{\mathrm{U}}$ and $\mathbf{x}_{\mathrm{O}}$ ensure that for each branch only one trial variable is not equal to 0. Expanding the objective function with zero costs for $\mathbf{x}_{\mathrm{U}}$ and a nonzero cost for $\mathbf{x}_{\mathrm{O}}$ implements the pricing for remaining overload.

$$\tilde{\mathbf{f}}^{\mathrm{T}} = \left[\mathbf{c}^{\mathrm{T}} \quad \mathbf{0}_{1,OL} \quad \mathbf{c}_{\mathrm{O}}^{\mathrm{T}}\right] \tag{4-17}$$

The relaxed limits are only applied to branches already overloaded in the base case. Therefore, the branches are separated into overloaded OL and not overloaded NOL. The inequality constraints given by equations (4-5) to (4-11) are still valid for the not overloaded branches. The rows of the inequality matrix $\widetilde{\mathbf{A}}_{\text{ineq}}$ and $\tilde{\mathbf{b}}_{\text{ineq}}$ are simply reduced to the not overloaded branches and expanded with a matrix of zeros corresponding to $\mathbf{x}_{\text{U}}$ and $\mathbf{x}_{\text{O}}$. This ensures, that branches not overloaded in the base case are not overloaded in the optimizer's solution.

$$\begin{aligned}&\widetilde{\mathbf{A}}_{\text{ineq}}\\&= \operatorname{diag}\left(\operatorname{sign}\left(\mathbf{p}^{\text{b}}_{\text{L,N1},NOL}\right)\right)\\&\cdot\left[\underbrace{\mathbf{PTDF}_{\text{N1},NOL,RD}}_{(nol\times pp)}\ \underbrace{\mathbf{PTDF}_{\text{N1},NOL,RD}}_{(nol\times pp)}\ \underbrace{-\mathbf{PTDF}_{\text{N1},NOL}\cdot\mathbf{NDI}}_{(nol\times dc)}\ \underbrace{\mathbf{PSDF}_{\text{N1},NOL}}_{(nol\times pst)}\ \underbrace{\mathbf{0}_{NOL,OL}}_{(nol\times 2\cdot ol)}\right]\end{aligned} \tag{4-18}$$

$$\tilde{\mathbf{b}}_{\text{ineq}} = \mathbf{s}_{\text{thermal},NOL} - \left|\mathbf{p}^{\text{b}}_{\text{L,N1},NOL}\right| \tag{4-19}$$

$$\widetilde{\mathbf{A}}_{\text{ineq}}\cdot\tilde{\mathbf{x}} \le \tilde{\mathbf{b}}_{\text{ineq}} \tag{4-20}$$

The new equality constraints are derived to represent the following conditions. The sign correct sum of positive and negative redispatch has to be 0 and is represented in the first row of $\widetilde{\mathbf{A}}_{\text{eq}}$ and $\tilde{\mathbf{b}}_{\text{eq}}$ – compare to equation (4-4). The additional zeros are added due to the new trial variables $\mathbf{x}_{\text{U}}$ and $\mathbf{x}_{\text{O}}$. The other equality constraints are implemented to represent above described definition of $\mathbf{x}_{\text{U}}$ and $\mathbf{x}_{\text{O}}$. The change of the branches' power flow caused by redispatch, HVDC links and PSTs are marked blue in $\widetilde{\mathbf{A}}_{\text{eq}}$ – equation (4-21). The ^ on the matrices indicates the correction of the sign as already discussed above. The matrix is completed with two negative identity matrices corresponding to the size of $\mathbf{x}_{\text{U}}$ and $\mathbf{x}_{\text{O}}$. The vector $\tilde{\mathbf{b}}_{\text{eq}}$ is expanded with the difference of the thermal rating and the base case load of the branches OL. This is in accordance to transferring the inequality constraints stated in equations (4-5) to (4-9) for the branches OL to the equality constraints.

$$\widetilde{\mathbf{A}}_{\text{eq}} = \left[\begin{array}{cccccc}\overbrace{\mathbf{1}_{1,RD}}^{(1\times pp)} & \overbrace{\mathbf{1}_{1,RD}}^{(1\times pp)} & \overbrace{\mathbf{0}_{1,DC}}^{(1\times dc)} & \overbrace{\mathbf{0}_{1,PST}}^{(1\times pst)} & \overbrace{\mathbf{0}_{1,OL}}^{(1\times ol)} & \overbrace{\mathbf{0}_{1,OL}}^{(1\times ol)}\\ \underbrace{\widehat{\mathbf{PTDF}}_{\text{N1},OL,RD}}_{(ol\times pp)} & \underbrace{\widehat{\mathbf{PTDF}}_{\text{N1},OL,RD}}_{(ol\times pp)} & \underbrace{-\widehat{\mathbf{PTDF}}_{\text{N1},OL}\cdot\mathbf{NDI}}_{(ol\times dc)} & \underbrace{\widehat{\mathbf{PSDF}}_{\text{N1},OL}}_{(ol\times pst)} & \underbrace{-\mathbf{I}_{OL}}_{(ol\times ol)} & \underbrace{-\mathbf{I}_{OL}}_{(ol\times ol)}\end{array}\right] \tag{4-21}$$

$$\tilde{\mathbf{b}}_{\text{eq}} = \begin{bmatrix}\mathbf{0}\\ \mathbf{s}_{\text{thermal},OL} - \left|\mathbf{p}^{\text{b}}_{\text{L,N1},OL}\right|\end{bmatrix} \tag{4-22}$$

The following simple example shall illustrate the behaviour of $\mathbf{x}_{\text{U}}$ and $\mathbf{x}_{\text{O}}$ and the corresponding constraints and costs. Assume two branches i and j, who are overloaded with 0.5 pu and 1.5 pu in the base case. Consequently, they are added to the branches OL and corresponding elements. The corresponding elements in the vector $\tilde{\mathbf{b}}_{\text{eq}}$ are -0.5 pu and -1.5 pu. The power changes caused by the optimal solution for redispatch, HVDC links and PSTs are -0.8 pu for branch i and -1 pu for branch j. To comply with the equality constraints the elements corresponding to i and j in $\mathbf{x}_{\text{U}}$ and $\mathbf{x}_{\text{O}}$ are nonzero. Focusing first on branch i, the sum of the power change and initial overload is -0.3 pu. Since this value is smaller than 0, the value of the corresponding elements in $\mathbf{x}_{\text{U}}$ becomes -0.3 pu and in $\mathbf{x}_{\text{O}}$ 0 due to its lower limit. The sum of power change and initial overload for branch j is 0.5 pu. Since this value is higher than 0, the value of the corresponding elements in $\mathbf{x}_{\text{U}}$ becomes 0 due to its upper limit and the value in

$\mathbf{x}_{\mathrm{O}}$ 0.5 pu. The costs corresponding to $\mathbf{x}_{\mathrm{U}}$ are all 0, therefore only the remaining overload equalling the values in $\mathbf{x}_{\mathrm{O}}$ increases the overall costs.

4.2 Determination of Critical (n-1) Contingency

The optimization of the working point of PFCs meets the optimization target, e.g. minimising losses or necessary redispatch, under the constraint of a (n-1)-secure operation. Since the (n-1)-secure power flow and the critical contingency depend on the load flow distribution, the actual (n-1)-secure branch load and the critical contingency differ in general for each scenario and changes with the operation points of PFCs and redispatch actions. Hence, it is rather simple to evaluate the (n-1)-security of a given load situation, but the (n-1)-secure branch load and the critical contingency need further investigations.

In the following, the critical (n-1) contingency is either defined as the last remaining contingency event causing a (n-1)-violation for a down scaled base case load flow or as the first occurring contingency event causing a (n-1)-violation for a up scaled base case load flow. If the load flow is up or down scaled depends on the (n-1)-security of the considered branch in the base case load flow.

4.2.1 Determination Methods

The intuitive approach of increasing the actual node power injections until the (n-1)-security is violated works well for load situations already close to the (n-1)-security border. The (n-1)-secure loading of a branch i $\mathrm{F}_{i,\mathrm{n1}}$ is determined by the minimal absolute value of the quotients of the branch flow without contingency $\mathrm{p}_{\mathrm{L},i}$ and the contingency branch flows corresponding to all considered tripped branches in the set O – equation (4-23). The changes of the branch flow of branch i are calculated based on the single branch LODFs and the branch flows of all branches O – equation (4-24).

$$F_{i,\mathrm{n1}} = \min\left(\left|p_{\mathrm{L},i} \cdot \mathrm{diag}\left(p_{\mathrm{L},i} + \Delta\mathbf{p}_{iO}\right)^{-1}\right|\right) \qquad \textit{(4-23)}^{4}$$

$$\Delta\mathbf{p}_{iO} = \mathrm{diag}(\mathbf{LODF}_{iO}) \cdot \mathbf{p}_{\mathrm{L},O} \qquad \textit{(4-24)}$$

$F_{i,\mathrm{n1}}$	…	maximal (n-1)-secure loading of branch i
$\mathrm{p}_{\mathrm{L},i}$	…	power flow on branch i without contingency
$\mathbf{p}_{\mathrm{L},O}$	…	power flow on branches in O without contingency ($\#\,in\ O \times 1$)
$\Delta\mathbf{p}_{iO}$	…	vector of power flow change of branch i ($\#\,in\ O \times 1$)
$\mathbf{LODF}_{iO}$	…	LODFs from branches in O to branch i ($\#\,in\ O \times 1$)

[4] The addition of a vector and a scalar in this and the following equations has to be interpreted as an elementwise addition. The notation is chosen in that way to allow a better readability.

The critical contingency cc_i is consequently given by the branch in O corresponding to the minimum found in equation (4-23).

A more sophisticated approach is based on the evaluation of the sensitivity of the branch flows on the power transfers between given sets of sending and receiving nodes. The sending nodes are denoted with the index sn, the receiving nodes with the index rn. Possible selection algorithms and weighting of the selected nodes are discussed in chapter 4.2.2. However, independent of the actual selection, the sum of the power injections in the sending nodes and the sum of the power injections in the receiving nodes must be equal to avoid any influence of the slack node. The sensitivity on the branch flows of the investigated branch i and the considered branches of set O are calculated as follows.

$$PTDF_{i,\mathrm{sn-rn}} = \mathbf{PTDF}_{\mathrm{i}} \cdot (\mathbf{p}_{\mathrm{sn}} - \mathbf{p}_{\mathrm{rn}}) \tag{4-25}$$

$$\mathbf{PTDF}_{O,\mathrm{sn-rn}} = \mathbf{PTDF}_{O} \cdot (\mathbf{p}_{\mathrm{sn}} - \mathbf{p}_{\mathrm{rn}}) \tag{4-26}$$

$\mathbf{p}_{\mathrm{sn}}$	…	vector of sending nodes power injections $((N\text{-}1)\times 1)$
$\mathbf{p}_{\mathrm{rn}}$	…	vector of receiving nodes power injections $((N\text{-}1)\times 1)$
$\mathbf{PTDF}_{O,\mathrm{sn-rn}}$	…	power transfer sensitivity of branches O $(\#\ in\ O \times 1)$
$PTDF_{i,\mathrm{sn-rn}}$	…	power transfer sensitivity of branch i

Only the elements corresponding to the selected sending or receiving nodes are nonzero in the vectors of power injections $\mathbf{p}_{\mathrm{sn}}$ and $\mathbf{p}_{\mathrm{rn}}$. With the use of the single branch LODFs of the branches in O on the investigated branch i, a vector of (n-1)-sensitivities $\mathbf{k}_{iO}$ to the power transfer is defined as

$$\mathbf{k}_{iO} = \mathrm{PTDF}_{i,\mathrm{sn-rn}} + \mathrm{diag}(\mathbf{LODF}_{iO}) \cdot \mathbf{PTDF}_{O,\mathrm{sn-rn}} \tag{4-27}$$

The (n-1)-sensitivities are further used to calculate a vectors of scaling factors for positive and negative values of the thermal rating $\mathbf{x}_{iO,\mathrm{pos}}$ and $\mathbf{x}_{iO,\mathrm{neg}}$. The consideration of positive and negative values of the thermal rating is necessary to avoid the exclusion of branches with opposite sing of the branch flow. The vector $(\mathrm{p}_{\mathrm{L},i} + \Delta\mathbf{p}_{iO})$ corresponds to the (n-1)-branch flow on branch i for any single branch outage of the branches in the set O. The elements in the vectors $\mathbf{x}_{iO,\mathrm{pos}}$ and $\mathbf{x}_{iO,\mathrm{neg}}$ give the scaling factors of the power transfer necessary to reach a (n-1)-branch flow that equals the positive or negative thermal rating of the branch i for each considered single branch outage.

$$\mathbf{x}_{iO,\mathrm{pos}} = \left(s_{\mathrm{thermal},i} - \left(p_{\mathrm{L},i} + \Delta\mathbf{p}_{iO}\right)\right) \cdot \mathrm{diag}(\mathbf{k}_{iO})^{-1} \tag{4-28}$$

$$\mathbf{x}_{iO,\mathrm{neg}} = \left(-s_{\mathrm{thermal},i} - \left(p_{\mathrm{L},i} + \Delta\mathbf{p}_{iO}\right)\right) \cdot \mathrm{diag}(\mathbf{k}_{iO})^{-1} \tag{4-29}$$

The fictive (n-1)-secure loadings of branch i and the corresponding loading of the branches in O are calculated for positive and negative scaling factors with the already calculated sensitivities of the power transfer.

$$\mathbf{F}_{i,\mathrm{pos}} = \left|p_{\mathrm{L},i} + PTDF_{i,\mathrm{sn-rn}} \cdot \mathbf{x}_{iO,\mathrm{pos}}\right| \cdot s^{-1}_{\mathrm{thermal},i} \tag{4-30}$$

$$\mathbf{F}_{O,\mathrm{pos}} = \mathrm{diag}\left(\mathbf{s}_{\mathrm{thermal},O}\right)^{-1} \cdot \left|\mathbf{p}_{\mathrm{L},O} + \mathbf{PTDF}_{O,\mathrm{sn-rn}} \cdot \mathbf{x}_{iO,\mathrm{pos}}\right| \tag{4-31}$$

$$\mathbf{F}_{i,\mathrm{neg}} = \left|p_{\mathrm{L},i} + PTDF_{i,\mathrm{sn-rn}} \cdot \mathbf{x}_{iO,\mathrm{neg}}\right| \cdot s^{-1}_{\mathrm{thermal},i} \tag{4-32}$$

$$\mathbf{F}_{O,\mathrm{neg}} = \mathrm{diag}\left(\mathbf{s}_{\mathrm{thermal},O}\right)^{-1} \cdot \left|\mathbf{p}_{\mathrm{L},O} + \mathbf{PTDF}_{O,\mathrm{sn-rn}} \cdot \mathbf{x}_{iO,\mathrm{neg}}\right| \quad (4\text{-}33)$$

The resulting branch loading on the branches of set O are checked for plausibility, whereby branches with values above a given border – sensible around $1\ \mathrm{pu}$ – are not considered further as possible critical contingencies. The (n-1)-secure branch loading of branch i equals the minimum of the positive and negative branch loadings. The critical contingency cc_i is the branch of O corresponding to this minimum.

$$F_{i,\mathrm{n1}} = \min\left(\begin{bmatrix}\boldsymbol{F}_{i,pos}\\ \boldsymbol{F}_{i,neg}\end{bmatrix}\right) \quad (4\text{-}34)$$

The computational burden of both discussed methods increases with the number of possible contingencies – in this case the branches in the set O. Therefore, it is recommendable to pre-evaluate the LODFs and only consider branches with at minimum absolute value of the LODF in the set O.

4.2.2 Selection of Load Flow Scaling Nodes for Critical (n-1) Contingency Determination

The (n-1)-secure loading of a branch depends on the location of the branch in the network – defining the LODFs from other branches on the investigated branch – and the load flow. The definition of sending and receiving nodes for the approach to calculate the (n-1)-secure starting from a given base case load flow has therefore a direct influence on the result. To ensure that the results match with reality, the node selection should be ideally based on generation shift keys (GSK) or if they are not available at least on a minimum number $n_{\min}$ of node pairs.

The selection algorithm slightly differs between the use of GSKs and node pairs. If GSKs are available, the zonal PTDFs for each GSK are calculated and possible combinations of these zonal PTDFs are evaluated. The GSKs corresponding to the combination with the highest power flow on the branch under investigation i define the sending and receiving nodes used in chapter 4.2.1.

$$PTDF_{i,\mathrm{Z}k} = \mathbf{PTDF}_i \cdot \mathbf{GSK}_k \quad (4\text{-}35)$$

$$\max\left(PTDF_{i,Zk} - PTDF_{i,Zl}\right), k \neq l, \forall k, l \in M \quad (4\text{-}36)$$

$\mathbf{PTDF}_i$	…	PTDFs for branch i from all nodes of the network $(1\times(N\text{-}1))$
$\mathrm{PTDF}_{i,Zk}$	…	Zonal PTDF for branch i from zone k (1×1)
$\mathbf{GSK}_k$	…	GSK from zone k $((N\text{-}1)\times1)$
M	…	zones with defined GSKs

If no GSKs are available or none of the GSK combinations meets the condition $\max(PTDF_{i,Zk} - PTDF_{i,Zl}) \geq \varepsilon_{\mathrm{GSK}}$, the selection of suitable nodes is based on the possible combinations of single nodes. The load flow sensitivities of the node combinations are written in a sensitivity matrix $\mathbf{S}$. The sensitivities are normalized to the thermal rating of the branch. The rows of $\mathbf{S}$ correspond to the sending nodes, the columns to the receiving nodes. Since reversing the sending and receiving node

only results in a change of the sign, it is sufficient to calculate and evaluate the upper triangular matrix of $\mathbf{S}$. The single elements and the full matrix are calculated as

$$s_{i,rc} = \mathrm{s}_{\mathrm{thermal},i}^{-1} \cdot \left(PTDF_{i,r} - PTDF_{i,c}\right), c \geq r, \forall r, c \in m \tag{4-37}$$

$$\mathbf{S}_i = \mathbf{I} \cdot s_{\mathrm{thermal},i} \cdot \left(\mathrm{diag}\left(\mathbf{PTDF}_{i,m}\right) \cdot \mathbf{U}_m - \mathbf{U}_m \cdot \mathrm{diag}\left(\mathbf{PTDF}_{i,m}\right)\right) \tag{4-38}$$

$\mathbf{PTDF}_{i,m}$	…	PTDFs for branch i from all nodes of the network $(1 \times \#\ \mathrm{of}\ m)$
$\mathbf{S}_i$	…	sensitivity matrix for branch i $(\#\ \mathrm{of}\ m \times \#\ \mathrm{of}\ m)$
$\mathbf{U}_m$	…	upper triangular matrix of ones $(\#\ \mathrm{of}\ m \times \#\ \mathrm{of}\ m)$
m	…	nodes considered for the selection

The algorithm selects all node pairs with a sensitivity value between an upper and lower limit. If the number of selected node pairs is lower than a minimum number $n_{\min}$ additional node pairs closest to a given value – e.g. 0.5 – are added. A recommendation for the application of the selection algorithm is to consider only nodes with generation for a first evaluation and all nodes for a second evaluation, if the minimum number of node pairs is not reached. The sending and receiving nodes of each node pair are sorted in a way that their sensitivity on the branch i is positive for all node pairs. With the resulting node pairs two vectors of power injections $\mathbf{p}_{\mathrm{sn}}$ and $\mathbf{p}_{\mathrm{rn}}$ are created. The only nonzero elements of these vectors correspond to the selected sending and receiving nodes.

The power injections corresponding to the individual node pairs can either be all set to $1\ \mathrm{pu}$ or weighted with the inverse of the corresponding sensitivity. The second variant leads to a higher loading of the surrounding network and ensures, that the power transfer of each node pair has the same effect on the investigated branch.

Pre-evaluating the PTDF of the investigated branch and neglecting nodes with corresponding PTDF under a certain threshold as sending nodes can reduce the computational effort. However, it is important to mention, that the neglected nodes are still available as receiving nodes to the selection algorithm since a complete removal would make the selection sensitive to the slack node. Therefore, it is no longer possible to only evaluate the upper triangle matrix of $\mathbf{S}$.

The general flow chart of the selection algorithm combining the three selection stages based on GSK, node pairs with sensitivities between an upper and lower boundary as well as a selection of a minimal number of nodes is shown in Fig. 4-2.

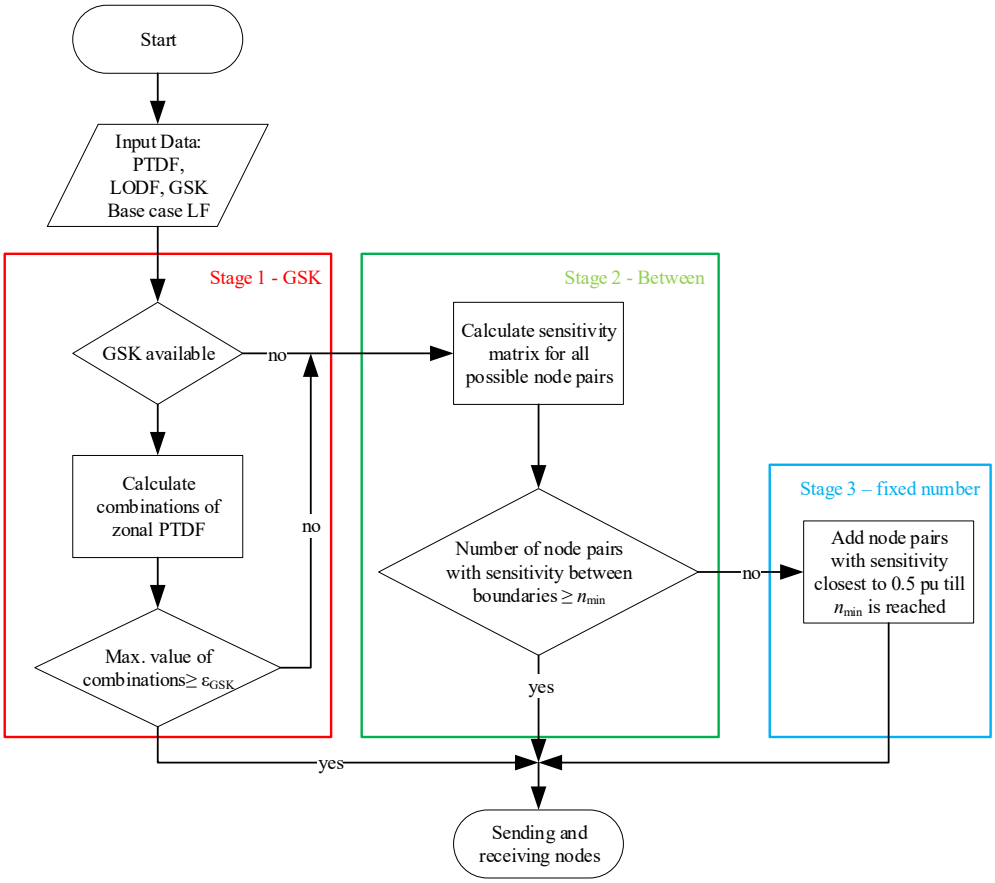

Fig. 4-2 Flow chart of the selection algorithm defining the sending and receiving nodes for the estimation of (n-1)-secure flows and critical contingencies

4.2.3 Comparative Evaluation of the Critical (n-1) Contingency Determination

The effects of the parameters used for the selection of sending and receiving nodes are discussed on the (n-1)-secure flow estimation of selected branches in the ENTSO-E network. The thereby used hourly base case load flows result from a market solution with implemented FBMC in the CWE plus the bidding zones of Czech Republic, Poland, North-Italy and Switzerland for a fictive year 2025. The considered branches correspond to critical network elements of the flow-based market. These elements are determined according to ACER decision [69]. To foreclose a positive bias for GSK based node selection, the parametrized selection algorithm is further applied on branches selected as discussed in chapter 3.1. The considered branches are limited to the Central European area to ensure comparability.

The performance is measured by the stability of the resulting critical contingencies cc for the considered branches over all 8760 hourly base case load flows. The critical contingencies are estimated as described in chapter 4.2.1. With the hourly set of estimated critical contingencies CC, the stability ζ of the result is calculated as the frequency of the mode of the set CC. Lower values of ζ indicated more dependency on the base case load flow. The result stability for a branch i is calculated as

$$\zeta_i = \frac{\sum_{h=1}^{8760}\left(cc_{i,h} == mode(CC_i)\right)}{8760} \tag{4-39}$$

CC_i … set of hourly critical contingencies of branch i

$cc_{i,h}$ … critical contingency of branch i for hour h

The median value and distribution of the result stability for the considered branches is used for the selection of the algorithm parameters and for a comparison between the different parts of the algorithm. The described definition of the result stability is chosen to ensure that determined critical contingencies are not affected by load flow changes based on redispatch activation and changed setpoints of PFCs.

The selection algorithm follows a cascaded process with the deepest stage determining a minimum number of node pairs based on the proximity of their load flow effects on the considered branch to a given value – Stage 3 in Fig. 4-2. For the following evaluation the comparison value is set to 0.5 pu and the minimum number is varied. Further, a minimum PTDF value excluding nodes with only small effects on the considered branch as sending nodes is implemented and varied. The median of the result stabilities – Table 4-1 – based on nodes selected only considering the inner loop of the algorithm indicate little influence on the chosen minimal number of nodes and no effect at all for the pre-selection of sending nodes based on minimal PTDF values on the investigated branch.

Table 4-1 Median result stability of selected node pairs closest to $0.5\ pu$ for a variation of minimal number of nodes and minimal PTDF value

		min. PTDF value			
		0.1	0.2	0.3	0.4
min. number of nodes	10	0.82	0.82	0.82	0.82
	20	0.84	0.84	0.84	0.84
	30	0.84	0.84	0.84	0.84
	40	0.83	0.83	0.83	0.83
	50	0.83	0.83	0.83	0.83

The second stage of the algorithm selects node pairs with an effect on the power flow on the considered branch between a lower and an upper boundary. The values of the lower and upper boundary are varied. The minimum number of nodes selected for the underlaying loop is according to the results above set to 30. The sensitivities on the upper and lower limits are small with a maximal change in the median result stability of bellow 0.02 pu – see Table 4-2. However, it can be seen, that too high lower and upper boundaries slightly worsen the result stability.

Table 4-2 Median result stability of selected node pairs between a variation of upper and lower boundaries

		upper boundary			
		0.6	0.7	0.8	0.9
lower boundary	0.2	0.88	0.88	0.88	0.88
	0.3	0.88	0.88	0.88	0.87
	0.4	0.86	0.86	0.86	0.86

The first stage of the algorithm using GSK is evaluated for a variation of a minimum effect on the considered branch and for seasonal variation in the GSK. The underlaying loops are parametrized with a minimum number of nodes of 30, a lower boundary of 0.2 pu and an upper boundary of 0.6 pu. These

parameter values correspond to the results of the evaluations above. The median result stabilities – Table 4-3 – shows little sensitivity to the varied parameters. The maximal difference for a single parameter is around 0.02 pu.

Table 4-3 Median result stability of selected nodes based on GSK for a variation in the minimal effect on the considered branches and different GSK sets

		GSK Set			
		1	2	3	4
min. effect GSK	0	0.92	0.92	0.93	0.93
	0.05	0.92	0.92	0.93	0.93
	0.1	0.92	0.92	0.92	0.94
	0.15	0.93	0.93	0.92	0.93
	0.2	0.93	0.93	0.92	0.93
	0.25	0.93	0.93	0.91	0.93

The order of the single selection stages is justified by comparing the median values, the 25%- and 75% quantile of the result stability – Fig. 4-3. The selection of the parametrisation of the single selection stages is based on the results above. The minimal PTDF value is set to 0.1 pu, the minimal number of selected nodes to 30, the lower boundary to 0.2 pu, the upper boundary to 0.6 pu, the minimal effect of the GSK to 0.1 pu and the GSK set 4 is used.

As can be seen, any additional stage of the algorithm increases the stability of the selected critical contingency. The estimated critical contingencies are therefore more robust to a variation of the base case load flow, which is of importance for the determination of (n-1)-PTDFs necessary as input for the flow-based market coupling methods and redispatch optimization. The histogram for the result stability of all considered branches is shown in Fig. 4-4. As seen there, the result stability of the individual considered branches are shifted further to the right with each additional stage of node selection. This indicates, that the determined critical contingencies depend less on the base case load flow.

The result stability of the determination based on linear load flow scaling as described in chapter 4.2.1 is added to the figures as comparison.

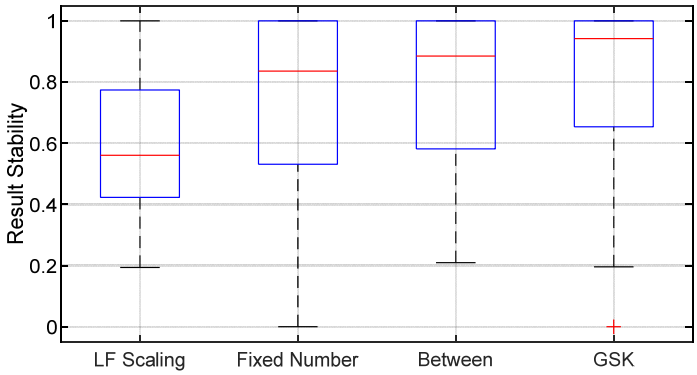

Fig. 4-3 Box plot of result stability distribution with median value, the 25%- and 75% quantile for the evaluation of CNE defined for the flow-based market of the Central European grid area

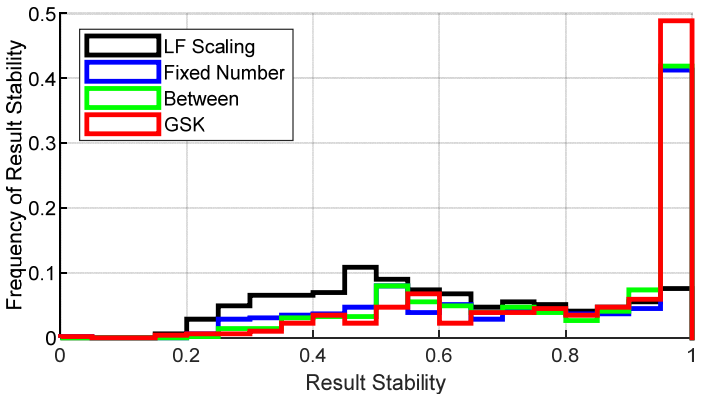

Fig. 4-4 Histogram of result stability of each individual branch for the evaluation of CNE defined for the flow-based market of the Central European grid area

The results for the determination of the critical contingencies for branches influenced by the operational points of HVDC links and PSTs for the parametrisation of the algorithm as given above are summarized in figures Fig. 4-5 and Fig. 4-6.

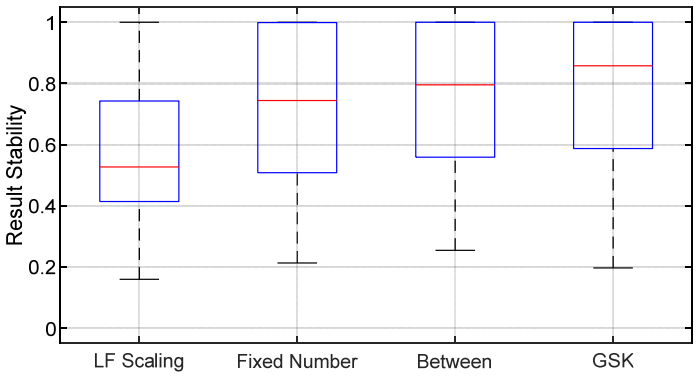

Fig. 4-5 Box plot of result stability distribution with median value, the 25%- and 75% quantile for the evaluation of branches influenced by embedded HVDC links and PSTs

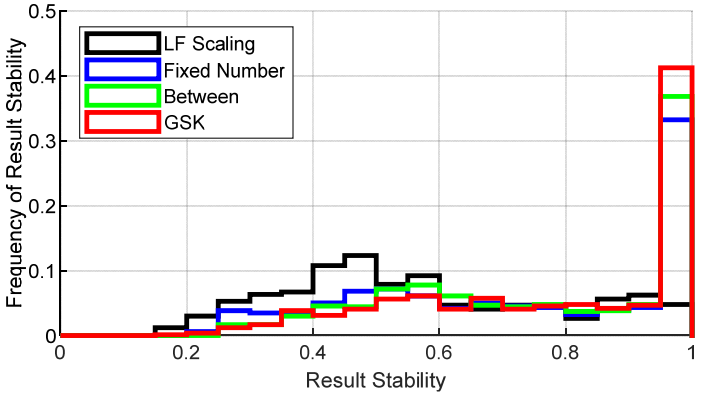

Fig. 4-6 Histogram of result stability of each individual branch for the evaluation of branches influenced by embedded HVDC links and PSTs

The generally lower median of the result stability is caused by the fact, that the influenced branches are also located in highly meshed grid areas whereas due to their definition CNE tend to be in less meshed areas – see Fig. 4-7. The location of branches in highly meshed grid areas causes a higher dependency on the actual base case load flow. The reason therefore is, that more branches with similar LODFs on

the investigated branch exist and they are similarly affected by the additional power flow caused by the determination algorithms. However, the results on these branches confirm the sensibility of the staged algorithm and a positive bias to the GSK based node selection can be foreclosed.

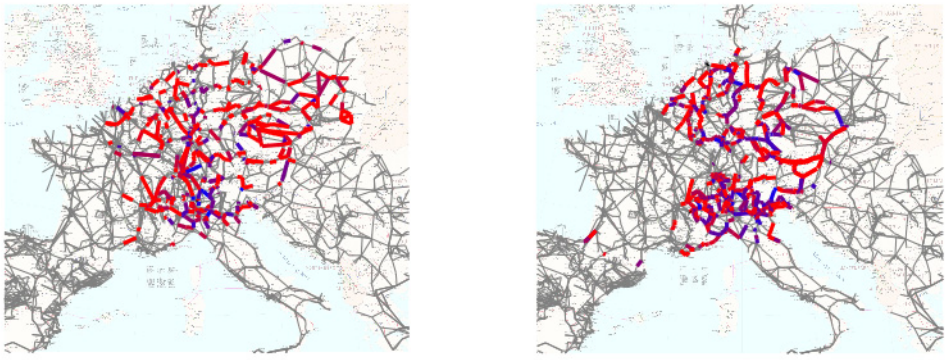

Fig. 4-7 Location of considered branches. Colouring of branches correspond to the result stability. The redder the colour the higher the result stability

4.3 Case Study on Coordinated Control in a FBMC model of Central Europe

The case study aims to highlight the effects of the coordination of redispatch actions and the control setpoints of embedded HVDC links and PST on the redispatch costs. The underlaying scenario is a fictive year 2025 with implemented FBMC in the central Europe grid area including the CWE bidding zones plus the bidding zones of Czech Republic, Poland, North-Italy and Switzerland.

4.3.1 Model Description

The network model represents the 220-kV- and 380-kV-grid of the ENTSO-E region and Great Britain on nodal basis. Subordinate grid levels are in general substituted as residual generation and load, whereby parts of the 110-kV-grid essential for international power flows are modelled in detail. The grid model is based on the static grid model from ENTSO-E and is continuously updated and expanded with public available data, e.g. the ENTSO-E Ten-Year-Network-Development-Plans (TYNDP) and national network development plans. The branch flows are calculated using the linearized DC load flow, what is an adequate tool for techno-economic studies and flow-based market implementation. A more detailed description of the model is given in the Appendix A.

The network is reduced to the ENTSO-E region, whereby power transfers with Great Britain and other grid areas connected asynchronously via HVDC links – e.g. Sardinia, Sweden etc. – are considered as

power injections at the corresponding HVDC terminals. The branches of the remaining network are highlighted as coloured in Fig. 4-8.

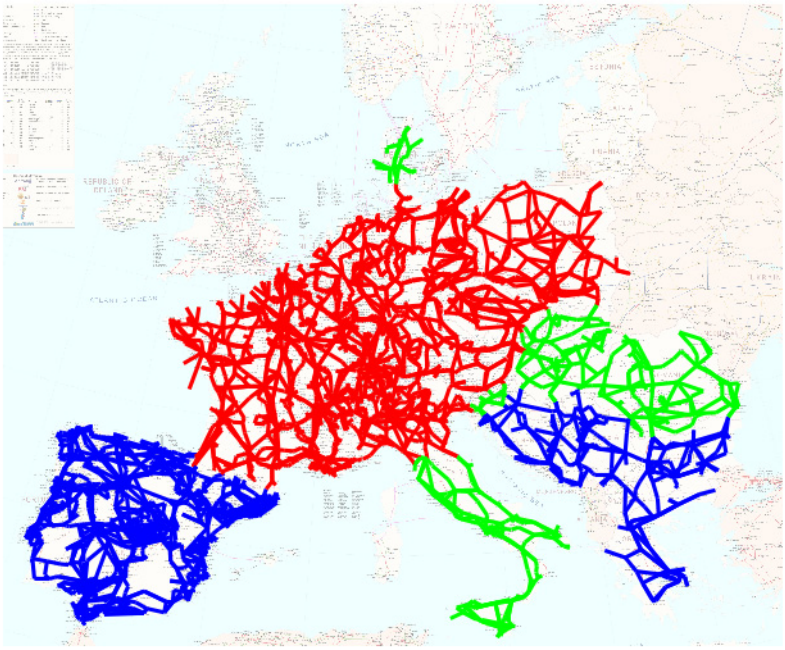

Fig. 4-8 Modelled Grid area. Red FBMC, green and red generation modelled in detail on power plant base and redispatch, blue reference generation scaled with market results

The focus of the studied scenarios is set on the effects of the coordination of PFCs in an assumed FBMC of the CWE plus the bidding zones of Czech Republic, Poland, North-Italy and Switzerland. The branches of bidding zones included in the FBMC are plotted in red in Fig. 4-8. The other bidding zones of the ENTSO-E region and the connected energy markets of Great Brittan, Ireland and Scandinavia are included in the market model in accordance with their expected net transfer capacities of the year 2025.

The generation's level of detail is on single power plant dispatch base including redispatch capability for the red and green marked areas. The blue grid areas' generation is included in the electric grid model by scaling the residual generation of the market result with the static generation data of the basic ENTSO-E model. The loads are implemented by scaling the resulting residual load of the single bidding zones with the corresponding static load data of the basic ENTSO-E model.

The assumed redispatch capacities correspond to the power plant dispatch of the market simulation. This ensures, that positive redispatch – increasing the generation – does not exceed the actual power plants maximum generation and negative redispatch – decreasing the generation – is only available for the amount of generation supplied in the base case. The grid regions, who are modelled with residual generation are not considered for the redispatch optimization. The costs of a redispatch action is based on variable costs – e.g. fuel of thermal power plants – and opportunity costs, if the primary energy source is limited – e.g. for hydro storage power plants. Any change of the control setpoints of the included embedded HVDC links and PSTs are assumed as costless.

A breakdown of the elements included in the used model and grid areas is given in Table 4-4.

Table 4-4 Elements in included in the separated grid areas

		Grid Areas		
		FBMC area	Area w. redispatch	Complete grid
Network Elements	Lines	4839	5598	7686
	Transformers	906	1002	1565
	Power plants	2676	3189	3189
	Redispatch power plants	1028	1223	1223
	PST	43	46	46
	Embedded HVDC	7	9	11

Details of the market simulation are not further discussed in this work, since the market simulation is not part of it and was not performed by the author. Fig. 4-9 shows the work flow and demarcation between the author's work and external data and models.

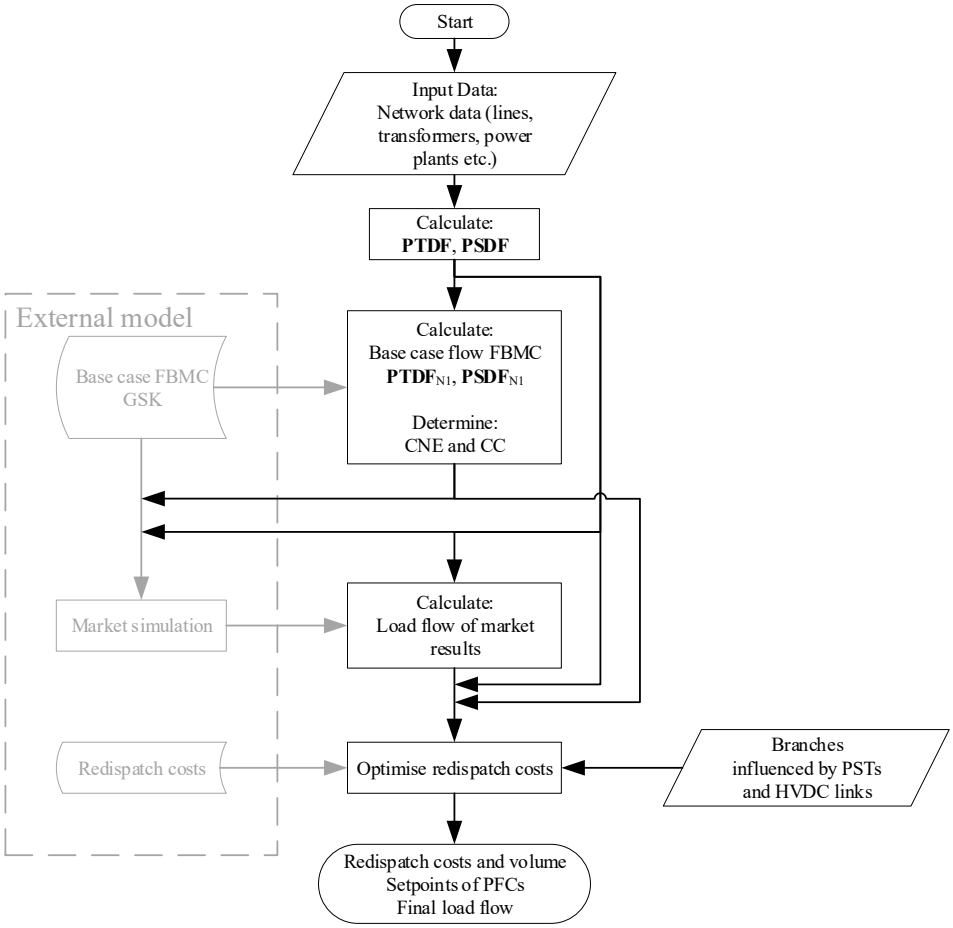

Fig. 4-9 Work flow of the simulations. Black are the author's own contribution, grey are the work steps contributed external

4.3.2 Studied Scenarios

To highlight the effects of a combined optimization of price driven redispatch, and control setpoint changes of embedded HVDC links and PSTs the following seven scenarios are compared. The costs of redispatch actions and the base case load flow are the same for all scenarios. The objective of the optimization is to minimise the overall redispatch costs on an hourly base in the fictive year 2025.

1. Reference Scenario
   The model corresponds to the expected grid situation in 2025 including the realistic AC grid expansion projects finished till 2025. In this scenario PSTs are treated as normal transformers without power flow controlling function and the embedded HVDC links are out of operation. The redispatch is optimised as discussed in chapter 4.1.

2. Uncoordinated PST and redispatch optimization
   The model basic data and branches considered for the redispatch optimization are unchanged to the reference scenario. The PST setpoints are determined before the redispatch optimization. The PST setpoints are determined as the minimal phase shifter angle necessary for (n-1)-security of the branches influenced by the PST. The influenced branches are derived as discussed in chapter 3.1, whereby branches are selected with a change in loading of more than $0.3\ \mathrm{pu}$ caused by one single PST. The thereby selected branches are further reduced to branches of the evaluated bidding zones. The resulting power flow after PST optimization is used as input for the redispatch optimization. The embedded HVDC links are still out of operation.

3. Uncoordinated HVDC link and redispatch optimization
   The model basic data and branches considered for the redispatch optimization are unchanged to the reference scenario. The HVDC link setpoints are derived by minimising the loading of the branches affected by the considered HVDC links under (n-1)-secure AC network conditions. An additional condition added to this optimization problem is a simplified (n-1)-security of the parallel HVDC links in Germany and across the Mediterranean Sea. The condition states, that in case of an HVDC link outage the power transfer of this link can be shifted to the parallel HVDC links without the consideration of possible AC grid overloading[5]. The branch selection for the optimization of the HVDC link is executed as discussed in chapter 3.1, whereby the branches with a change in loading of more than $0.1\ \mathrm{pu}$ caused by one single HVDC link are considered. The thereby selected branches are further reduced to branches of the evaluated bidding zones. The PST are treated as normal transformers without power flow controlling function. The resulting power flow after HVDC link optimization is used as input for the redispatch optimization.

[5] Due to the (n-1)-secure operation of the AC grid in itself, it can be assumed, that the shift of the transferred power to the parallel HVDC links causes no major overloads.

4. Uncoordinated HVDC link, PST and redispatch optimization
   The model basic data and branches considered for the redispatch optimization are unchanged to the reference scenario. The HVDC link setpoints are derived as in scenario 3. The PST setpoints are determined as in scenario 2, but with the power flow after HVDC link optimization as input. The resulting power flow after PST optimization is used as input for the redispatch optimization.

5. Coordinated PST and redispatch optimization
   The model basic data and branches considered for the redispatch optimization are unchanged to the reference scenario. The optimization of the PST setpoints and redispatch activation is executed in parallel as discussed in chapter 4.1. Since the embedded HVDC links are out of operation, the results of this scenario highlight the effect of coordinated PST optimization on the necessary redispatch volume.

6. Coordinated HVDC link and redispatch optimization
   The model basic data and branches considered for the redispatch optimization are unchanged to the reference scenario. The optimization of the HVDC setpoints and redispatch activation is executed in parallel as discussed in chapter 4.1. The simplified (n-1)-security condition for the parallel HVDC links is implemented additionally. In this scenario the effect of the considered embedded HVDC links on the necessary redispatch are highlighted. The PSTs are treated as normal transformers without power flow controlling function.

7. Coordinated HVDC link, PST and redispatch optimization
   The model basic data and branches considered for the redispatch optimization are unchanged to the reference scenario. The optimization is executed as discussed in chapter 4.1 and includes the PST and HVDC link setpoints as well as the redispatch. As in all other scenarios including HVDC links, the simplified (n-1)-security condition for the parallel HVDC links in Germany and across the Mediterranean Sea is implemented.

4.3.3 Results

The high number of branches considered in the optimization cause run times up to several minutes. These run times in combination with the in total seven scenarios make it infeasible to evaluate all branches on an hourly base for a complete year in a decent time frame. This problem is overcome by evaluating all branches only for randomly selected pilot hours and evaluating a reduced set of branches for the complete year. The branches of the reduced set correspond to the critical network elements (CNE) defined for the flow-based market simulation according to the regulatory stated by ACER. The terms CNE and ALL are used in the following figures and tables to label the results according to the used set of branches and hours.

The evaluated pilot hours are randomly selected from the hours of the four seasons corresponding to the load periods defined in the flow-based market simulation. For each of the following seasons $10\ \%$ of the number of hours corresponding to the season are evaluated as pilot hours. Further information on the selection of the pilot hours is given in the Appendix C.

- Off-peak Winter – Season 1
  1st of October – 31st of March, workday 22:00 to 10:00 and weekends
- Off-peak Summer – Season 2
  1st of April – 30th of September, workday 22:00 to 10:00 and weekends
- Peak Winter – Season 3
  1st of October – 31st of March, workday 10:00 to 22:00
- Peak Summer – Season 4
  1st of April – 30th of September, workday 10:00 to 22:00

Fig. 4-10 gives an overview on the geographical distribution of the mentioned reduced sets of branches. The upper left graph shows the CNE branches used for the optimization of the redispatch over the complete year. The upper right graph shows the branches used in the uncoordinated PST optimization and the lower left graph the branches of the uncoordinated optimization of the embedded HVDC links.

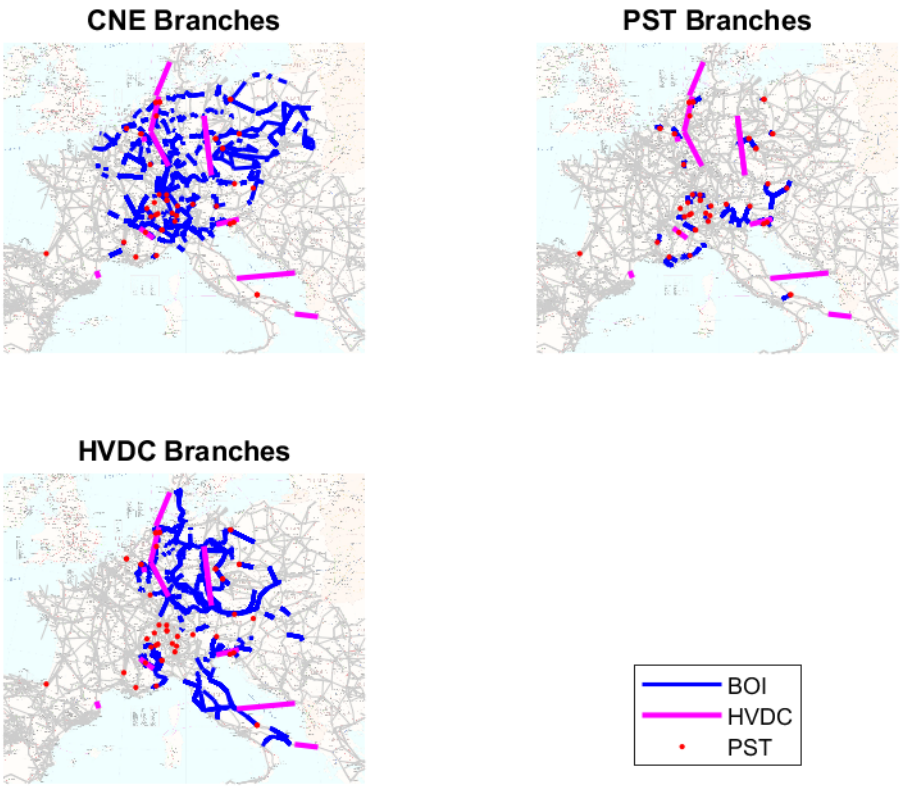

Fig. 4-10 Geographical distribution of considered branches of interest (BOI). Upper left graph for the CNE, upper right graph for PST and lower left graph for embedded HVDC links

In Fig. 4-11 the overloaded branches before and after redispatch optimization are shown. The branches plotted blue correspond to the branches, who are initially overloaded for at least one evaluated hour and

are not overloaded after the redispatch optimization. The red branches correspond to the branches, who are still overloaded after the redispatch optimization for at least one of the evaluated hours. These branches are not solved during the optimization, because no redispatch power plant with suitable free capacity is available. This is caused by an inadequacy of the model's power plant data.

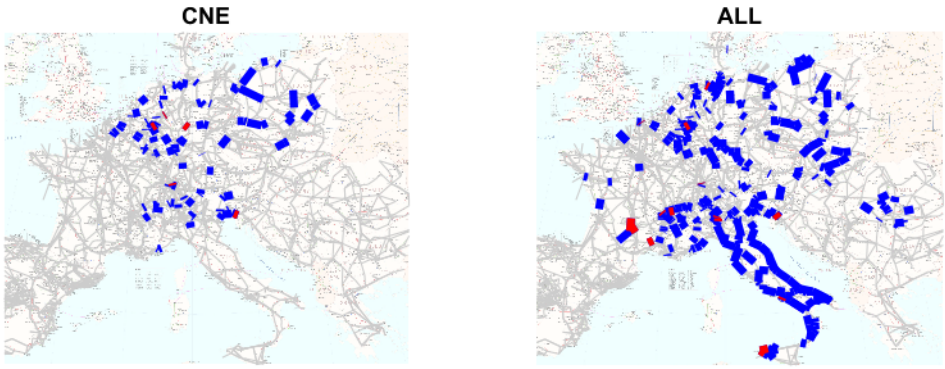

Fig. 4-11 Any initial overloaded branches – blue – and branches overloaded after redispatch optimization over all considered hours. Left graphic for CNE branches, right graphic for all branches in the zones with redispatch

The remaining overload on these branches is included in the overall redispatch costs and redispatch volume with a virtual redispatch activation. This allows a sensible comparison between the different scenarios and number of considered branches. The amount of this virtual redispatch activation calculates from the sum of the remaining overload on branches OL and a utilization factor k_{OL}. k_{OL} gives the efficiency of the virtual redispatch on the branches OL. E.g. a value of 0.5 means, that the virtual redispatch has to be twice the amount of the remaining overload to solve it. To avoid an overestimation of the virtual redispatch, remaining overloads occuring in series to each other are considered only ones.

$$V_{\mathrm{RD,vir}} = \frac{1}{k_{\mathrm{OL}}} \cdot \sum \mathbf{x}^*_{\mathrm{OL}} \tag{4-40}$$

$$V_{\mathrm{sum}} = \sum \mathbf{x}^*_{\mathrm{pos}} + V_{\mathrm{RD,vir}} \tag{4-41}$$

$$C_{\mathrm{sum}} = C_{\mathrm{RD}} + \mathrm{mean}\left(\mathbf{c}_{\mathrm{pos}}\right) \cdot V_{\mathrm{RD,vir}} \tag{4-42}$$

$$k_{\mathrm{OL}} = (0,1] \tag{4-43}$$

$\mathbf{c}_{\mathrm{pos}}$	…	costs of positive redispatch for active power plants
$\mathbf{x}^*_{\mathrm{OL}}$	…	remaining overload in optima for branches OL
$\mathbf{x}^*_{\mathrm{pos}}$	…	positive redispatch activation in optima
$V_{\mathrm{RD,vir}}$	…	Virtual redispatch volume
V_{sum}	…	overall redispatch volume
C_{sum}	…	overall redispatch costs
C_{RD}	…	costs of redispatch activation
k_{OL}	…	utilization factor for virtual redispatch

The results of Scenario 1 are discussed first, since they are used in the following as references to highlight the effects of the different coordination and integration level of the considered PFCs in the other five scenarios. The following results are based on a utilization factor of 0.5.

The seasonal distribution of the hourly redispatch costs and the scaling factors of Scenario 1 grouped to the seasons are depicted as boxplots in Fig. 4-12. The scaling factors are calculated as the ratio of the redispatch costs of the optimization with all branches and the redispatch costs of the optimization with the CNE branches for each pilot hour separately. The median and mean values of the costs and cost scaling factors are given in Table 4-5. The two left columns in the table and the left graph visualising the results for the optimization on the CNE branches for the full year show the expected behaviour with higher redispatch costs in the winter season and during peak hours in the distribution and mean values.

The results for the pilot hours considering all branches in the grid area with available redispatch are given in the two middle columns and the central graph. The redispatch costs for the two winter seasons are as expected higher than the redispatch costs in the summer season.

Table 4-5 Mean and median values for the hourly RD-Costs and Cost Scaling factors of Scenario 1

	Hourly RD-Costs in k€ CNE		Hourly RD-Costs in k€ ALL		Cost Scaling Factor	
	Mean	Median	Mean	Median	Mean	Median
Season 1	218.13	203.97	451.15	400.80	2.11	1.93
Season 2	200.31	186.02	326.61	287.55	1.66	1.56
Season 3	226.69	206.90	513.40	458.18	2.36	2.10
Season 4	216.37	195.31	371.41	323.44	1.78	1.69

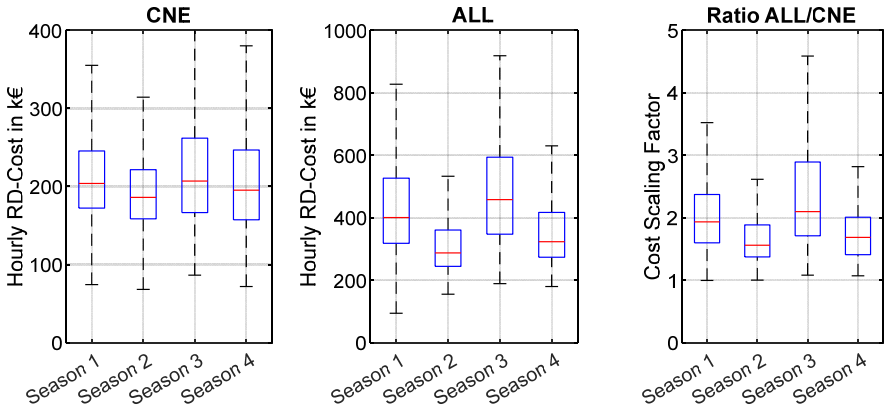

Fig. 4-12 Distribution of RD-Costs and Cost Scaling factors based on the pilot hours for Scenario 1. Left graph shows the results for the CNE branches, middle graph for all branches and the right graph the scaling factors.

In Table 4-6 the hourly redispatch volume and volume scaling factors are given for scenario 1. The corresponding distributions are depicted by the box plots in Fig. 4-13. As expected, the necessary redispatch volume in the winter seasons is higher than for the summer seasons.

Table 4-6 Mean and median values for the hourly RD-Volume and Volume Scaling factors of Scenario 1

	Hourly RD-Volume in GWh CNE		Hourly RD-Volume in GWh ALL		Volume Scaling Factor	
	Mean	Median	Mean	Median	Mean	Median
Season 1	11.73	11.60	16.80	15.87	1.42	1.36
Season 2	11.10	10.95	13.41	12.85	1.21	1.20
Season 3	11.61	11.38	17.89	16.30	1.52	1.39
Season 4	11.45	11.10	14.36	13.46	1.26	1.26

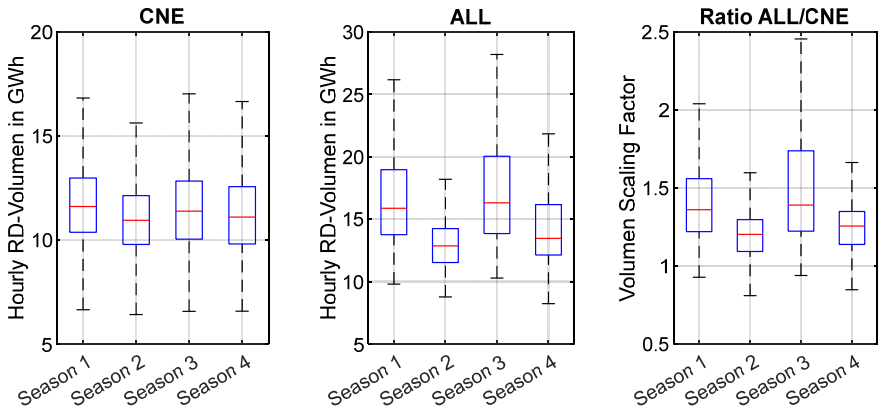

Fig. 4-13 Distribution of RD-Volume and Volume Scaling factors based on the pilot hours for Scenario 1. Left graph shows the results for the CNE branches, middle graph for all branches and the right graph the scaling factors.

Taking a closer look on the cost and volume scaling factors highlights the nonlinearity of the redispatch costs to the redispatch volume. As can be seen, an increase in the volume between 20 % to 50 % cause an increase of the costs around 50 % to 130 %. The much higher increase in the costs is caused by activation of more expensive and less effective redispatch power plants as soon as better located redispatch power plants reach their limitation.

The distribution of the scaling factors over the four seasons show the same general behaviour as the corresponding absolute values, therefore increasing the difference in the results between the single seasons.

The results of the scenarios 2 to 7 are normalized to scenario 1. This means, that the results of scenarios 2 to 7 are divided by the corresponding result of scenario 1 for each hour. Values above 1 pu indicate an increase and values below 1 pu a reduction. The thereby normalized redispatch costs are depicted in Fig. 4-14. The boxplots in the figure are grouped according to the seasons and the single scenarios are marked by the box colours.

The increase of redispatch costs for scenario 2 and 4 – uncoordinated optimization of only PST and uncoordinated HVDC link and PST optimization – is noticeable both in the results for the CNE branches and pilot hours. Since no general increase occurs for scenario 3 – uncoordinated optimization of HVDC links – it can be concluded, that the increasing redispatch costs are caused by the PSTs. This intuitively not expected increase is explained by the considered PSTs reducing power flows on their corresponding BOI and thereby increasing power flows on the other branches in the network. The relief of the BOI

leads to more overloaded and higher overloaded branches in the surrounding network causing additional redispatch forcing the optimizer to use more expensive and less effective redispatch power plants. This effect is further pronounced in the results of the CNE branches, since not all PST's BOI are CNE branches, which cause a higher loading on branches considered in the redispatch optimization without the advantage of less loaded branches. Therefore, a result comparison between the CNE branches' results and the pilot hours' results for scenario 2 and 4 shows, that throughout all seasons the pilot hours' results have smaller values.

The comparison between scenario 5 and 6 shows, that the inclusion of PSTs in a coordinated redispatch optimization leads to a higher cost reduction than the inclusion of HVDC links. This is explained on one side by the distribution of PSTs over a larger network area and on the other side on their location, since PSTs are in general equipped to branches who caused massive power flow restrictions and redispatch costs in the past.

The lowest redispatch costs are obtained as expected in scenario 7 with a complete coordination between PSTs, HVDC links and redispatch activation. It is noticeable, that for the optimization on CNE branches negative redispatch costs appear. This is caused by enabling a substitution of thermal power generation with cheaper sources due to additional transmission capacity.

A comparison of the results between the results on CNE branches and the results for the pilot hours shows, that the cost increasing and decreasing effects are lessened. The reasoning behind this behaviour is, that the share of complete redispatch costs caused by the branches affectable by the PFCs becomes smaller with more considered branches. Further, all PFCs affected branches are also included in the redispatch optimization, thereby avoiding unwanted relief or overloading of branches not in the scope of the optimizer.

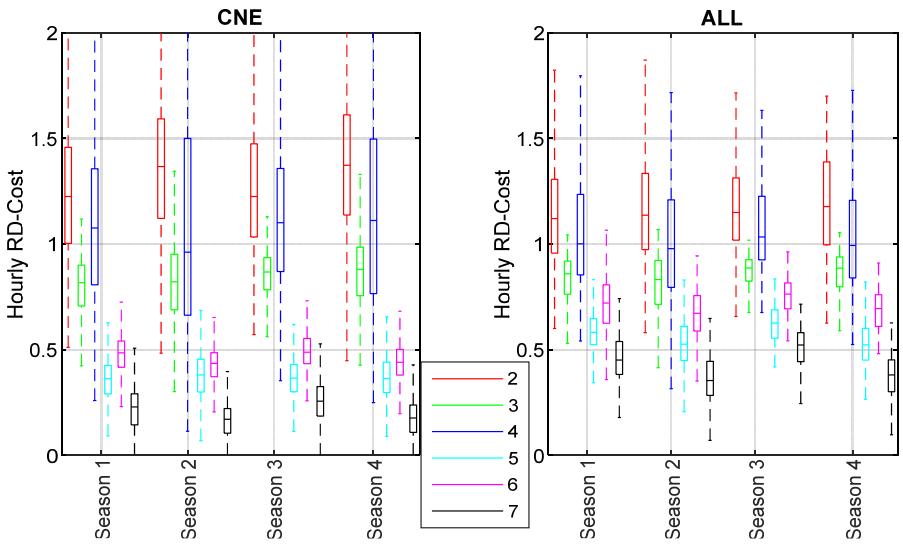

Fig. 4-14 Hourly redispatch costs of the scenarios 2 to 7 normalized to scenario 1. The left graph refers to the results for the CNE branches and the right graph to the results of all branches. The results are grouped by season and the scenarios are indicated by the box colours.

The redispatch volume normalized to scenario 1 is given in Fig. 4-15. The volume increases for scenario 2 and 4 and decreases for the other scenarios, which is in accordance with the change of the redispatch

costs discussed above. However, the volume change is smaller due to the nonlinear relationship between redispatch volume and costs.

Comparing the redispatch volume and costs of scenario 5 and 7 to each other, it is observable, that in scenario 7 less costs are achieved with the use of similar redispatch volume. This shows that the coordination of PSTs and HVDC links enables the use of cheaper redispatch power plants due to effective and efficient redistribution of the power flow.

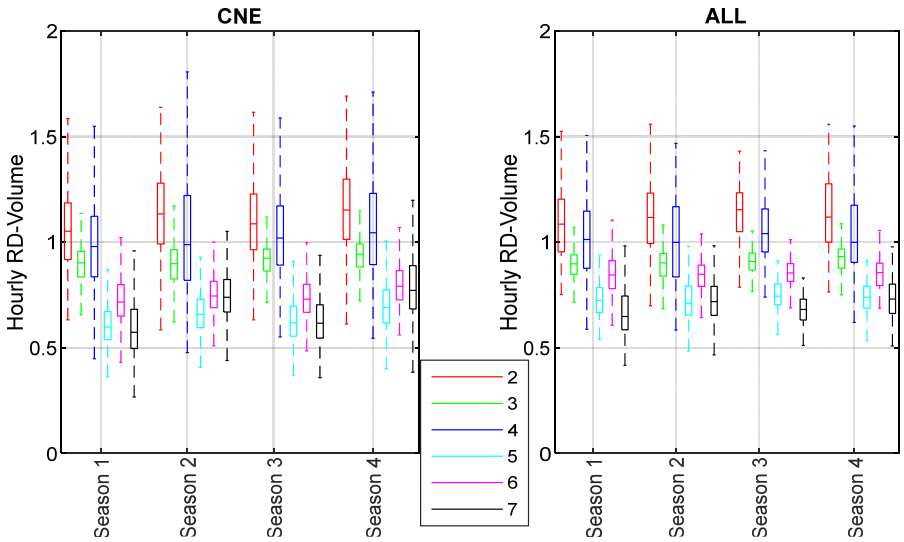

Fig. 4-15 Hourly redispatch volume of the scenarios 2 to 7 normalized to scenario 1. The left graph refers to the results for the CNE branches and the right graph to the results for all branches. The results are grouped by season and the scenarios are indicated by the box colours.

Table 4-7 summarizes the normalized optimization results of the scenarios 2 to 7 by the mean and median values of the hourly results.

Table 4-7 Mean and Median values of the normalized hourly redispatch costs and volumes

	Hourly RD-Costs referred to Scenario 1				Hourly RD-Volume referred to Scenario 1			
	CNE		ALL		CNE		ALL	
	Mean	Median	Mean	Median	Mean	Median	Mean	Median
Scenario 2	1.31	1.30	1.17	1.14	1.11	1.11	1.12	1.12
Scenario 3	0.84	0.84	0.85	0.87	0.91	0.91	0.90	0.91
Scenario 4	1.12	1.09	1.05	1.00	1.03	1.00	1.03	1.01
Scenario 5	0.37	0.36	0.56	0.55	0.65	0.64	0.74	0.73
Scenario 6	0.45	0.46	0.70	0.71	0.76	0.74	0.85	0.85
Scenario 7	0.19	0.20	0.42	0.42	0.70	0.68	0.71	0.70

The virtual redispatch based on the remaining overload and utilization factor described in equations (4-40) to (4-43) influences the results. The figures Fig. 4-16 and Fig. 4-17 show the sensitivity of the redispatch costs and volume to the utilization factor. The sensitivity is calculated by the mean values of the costs and volume normalized to the results based on a utilization factor of 0.5 pu. The utilization factor is varied from 0.25 pu to 1 pu. The resulting changes in the results are well below 0.1 pu for the

CNE branches and the pilot hours. The utilization factor has no significant influence on the quality of the result comparison due to the small values and same direction of its sensitivity in both set of branches.

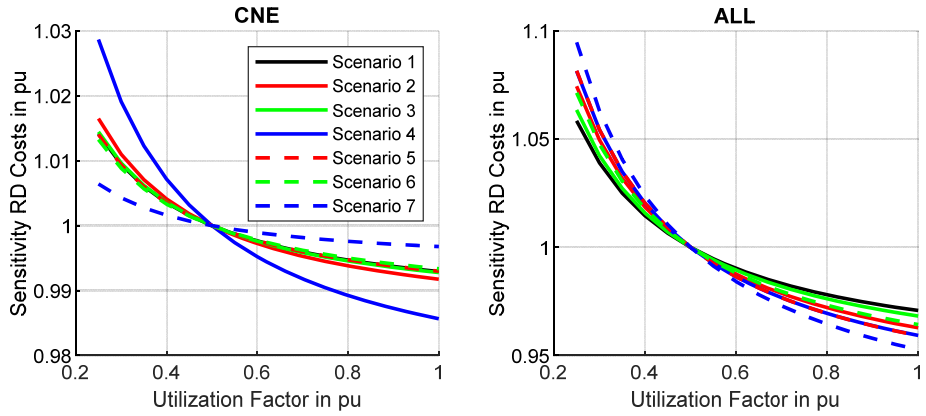

Fig. 4-16 Redispatch cost sensitivity to utilization factor. The left graph refers to the results for the CNE branches and the right graph to the results for all branches.

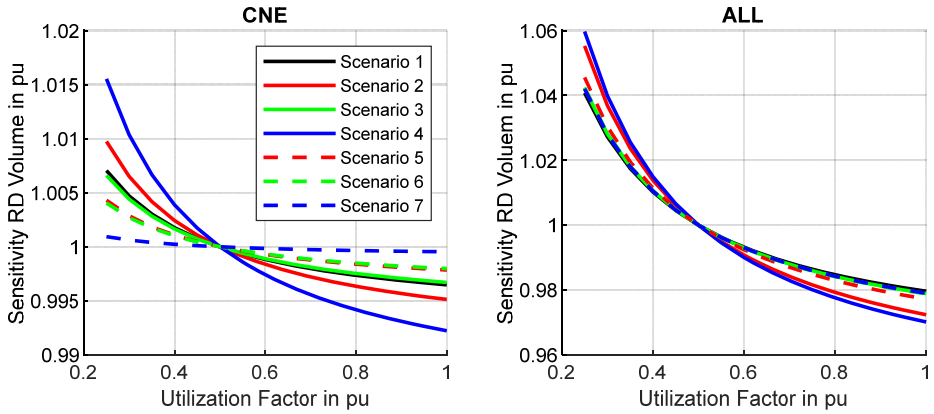

Fig. 4-17 Redispatch volume sensitivity to utilization factor. The left graph refers to the results for the CNE branches and the right graph to the results for all branches.

The influence of the utilization factor on the resulting redispatch cost is overestimated, if the average cost per MWh redispatch activated is smaller than the costs for the virtual redispatch costs. This is especially the case, if only little redispatch is necessary and cheap redispatch power plants or PFC control actions can solve the (n-1)-constraints as happens in scenario 5 and 7.

The ratio between the costs of the virtual redispatch costs and the average costs of the activated redispatch costs is shown in the box plots of Fig. 4-18. The costs overestimation caused by the virtual redispatch increases with higher ratios. The higher ratios in the left graph corresponding to the optimization of the CNE branches result from the generally lower redispatch volume compared to the pilot hours.

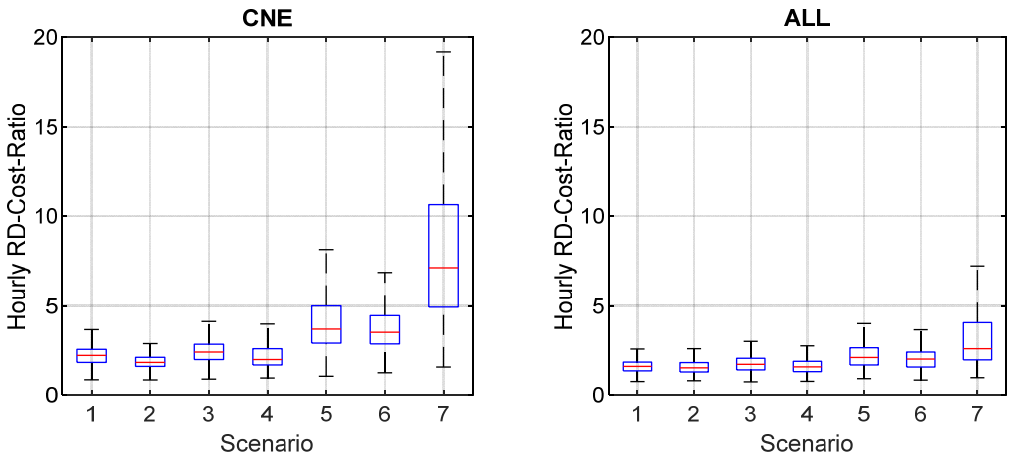

Fig. 4-18 Ratio between MWh-cost of virtual redispatch and average MWh-cost of activated redispatch power plants. The left graph refers to the results for the CNE branches and the right graph to the results for all branches.

4.4 Conclusion on Control Setpoint Coordination and Optimization

In this chapter the effects of coordinating the operation points of PFCs to achieve (n-1)-secure operation of the system with a cost efficient redispatch are evaluated. Therefore, it is assumed, that the redispatch measures are coordinated between the network operators of the considered network area. The redispatch is activated based on the optimization of its costs, whereby depending on the scenario PFCs are either completely excluded for the base case scenario 1, controlled without coordination to the redispatch activation for scenarios 2 to 4 or included into the optimization of the redispatch for the scenarios 5 to 7.

The resulting redispatch costs and volumes allow the following conclusions:

- Uncoordinated control of PSTs (scenario 2) leads to an increase of the redispatch costs. This is explained by the combination of a local focus relieving the PST equipped branches at the costs of causing and/or increasing overloads in the rest of the network and the nonlinearity of redispatch costs. Further, PSTs are mainly located on tie lines and bottle necks between network zones. In general, more options to relieve these branches with redispatch exist than for branches in more meshed network areas. Therefore, the PSTs reliving these branches force the redispatch optimizer to use less efficient redispatch power plants. The cost and volume increasing effect occurs also in scenario 4.
- Uncoordinated control of HVDC links (scenario 3) decreases the necessary redispatch volume and costs in the majority of load situations. The decrease is reasonable since the HVDC links offer additional power transfer capacity. The same effects and also occurs in scenario 4.
- Comparing the effects of coordinated control of PSTs and HVDC links separately (scenarios 5 and 6) shows, that PSTs are more effective in the reduction of necessary redispatch volume and costs. This is caused by their location on historical identified network bottle necks and the

high local power flow sensitivity. The coordination with the redispatch activation prevents unfavourable PST setpoints causing additional overloads.

- The combined coordination PSTs and HVDC links leads expectantly to the highest decrease in redispatch costs. However, the activated redispatch volume is only reduced comparably to scenario 5. This highlights that the optimizer sets the operation points of the PSTs and HVDC links to allow the use of cheapest redispatch power plants and not the most efficient ones.

The result comparison between the seasonal results for the optimization considering only CNE branches and the optimization of the pilot hours considering all branches of the evaluated network area demonstrate, that a qualitative assessment of the scenarios based on critical network elements alone is valid. However, it must be kept in mind, that cost and volume decreasing and increasing effects of PFCs are overestimated, if not all branches are considered for the optimization.

5 Emergency Outage Detection

In contrast to the works discussed in chapter 1.6.2, the goal of the proposed algorithm is to provide an accurate detection of tripped branches based on minimal information which can be used for decentralized emergency control decisions – e. g. to automatically activate a superordinate controller of HVDC links as used in [42] and [76]. Therefore, the computational complexity of the algorithm should be not too demanding to enable decent runtimes for a near to real time detection. Additionally, the algorithm's performance must be independent from the pre-contingency load flow. These postulations encourage the use of linearized cold start models, such as the classical DC load flow [77], for the problem formulation and WAMS measured changes of the node voltage angles caused by the tripped branches.

This chapter is organized as follows. The used basic versions of the optimization methods later adopted for the outage detection are described in the first subchapter. The Nordic-32-Bus system used for the evaluations of the algorithms' performance and the corresponding area of detection and PMU monitored nodes – selected according to chapter 3 – is shown in the second subchapter. After these introduction parts, a simple analytical algorithm to detect the loss of a single branch is discussed in brief. This algorithm is further used as comparison to the optimizer-based algorithms. The main focus of this chapter is set to the optimizer-based algorithms capable to detect an unknown number of tripped branches. Therefore, the three compared optimizers – based on an adapted Newton's method, particle swarm optimization and a hybrid optimizer – are described in detail. Their detection performance is compared using in a first step the node voltage angles obtained by a linearized static simulation of the Nordic-32-Bus system. In a second step a data stream of the node voltage angles from a non-linear dynamic simulation of the Nordic-32-Bus system is used as input for the detection algorithms. The main findings and the developed algorithm is accepted for publication and will appear in [78].

5.1 Optimization Methods

The optimization methods used for the outage detection are selected based on the necessary implementation effort. No predefined optimization toolbox is used to ensure a direct control on the optimizer's parameters. Furthermore, this selection includes an analytic and a stochastic optimizer. This led to the selection of Newton's method on the one hand and particle swarm optimization (PSO) on the other hand. Both are well known and a straightforward implementation is possible in any calculation software.

5.1.1 Newton's method

Newton's Algorithm is an iterative algorithm based on approximation of the objective function as a quadratic model. A quadratic function is the simplest function with a finite minimum. The quadratic approximation in the neighbourhood of an optimality point holds for most functions.

The method evaluates the objective function value $f(\mathbf{x}^{(i)})$, the gradient $\nabla f(\mathbf{x}^{(i)})$ and the Hessian $\mathbf{H}(\mathbf{x}^{(i)})$ of the current value of the trial variable $\mathbf{x}^{(i)}$ at each iteration step i. The value of the trial variable for the next iteration step is calculated by adding the Newton direction $\boldsymbol{\delta}^{(i)}$ – or parts of it – to $\mathbf{x}^{(i)}$.

$$\mathbf{x}^{(i+1)} = \mathbf{x}^{(i)} + \boldsymbol{\delta}^{(i)} \tag{5-1}$$

The Newton direction is derived by the Taylor series of $f(\mathbf{x}^{(i)} + \boldsymbol{\delta}^{(i)})$ completed to the second order, (5-2), and minimizing the change in the approximated objective function value Δf of step i and $i+1$ in respect to $\boldsymbol{\delta}^{(i)}$.

$$f\left(\mathbf{x}^{(i+1)}\right) \approx f\left(\mathbf{x}^{(i)}\right) + \nabla f\left(\mathbf{x}^{(i)}\right)^{T} \cdot \boldsymbol{\delta}^{(i)} + \frac{1}{2}\boldsymbol{\delta}^{(i)^{T}} \cdot \mathbf{H}\left(\mathbf{x}^{(i)}\right) \cdot \boldsymbol{\delta}^{(i)} = f\left(\mathbf{x}^{(i)}\right) + \Delta f\left(\boldsymbol{\delta}^{(i)}\right) \tag{5-2}$$

The first order minimization condition – the gradient is a zero vector – leads to

$$\nabla f\left(\mathbf{x}^{(i)}\right) + \mathbf{H}\left(\mathbf{x}^{(i)}\right) \cdot \boldsymbol{\delta}^{(i)} = \mathbf{0} \tag{5-3}$$

$$\boldsymbol{\delta}^{(i)} = -\mathbf{H}\left(\mathbf{x}^{(i)}\right)^{-1} \cdot \nabla f\left(\mathbf{x}^{(i)}\right) \tag{5-4}$$

If the second order minimization condition – the Hessian has to be positive definite – is violated, the method of Levenberg-Marquardt [79], [80] is used to assure a downhill direction of $\boldsymbol{\delta}^{(i)}$.

The optimal point $\mathbf{x}^{*}$ is reached, if all elements of $\nabla f(\mathbf{x}^{*})$ are smaller than a given border ε and $\mathbf{H}(\mathbf{x}^{*})$ is positive definite.

A detailed review and recent bibliography on Newton's method is given in [81].

5.1.2 Particle Swarm Optimization

The particle swarm optimization (PSO) was introduced as a optimization concept for nonlinear functions in [82] by Kennedy and Eberhart. The particles are initialized with a random position in the search space and with random velocities. The variant of PSO, which is used in this work, updates the velocity vector $\mathbf{v}$ and position vector $\mathbf{x}$ of each particle j in the n-dimensional search space at the iteration step i as follows

$$\mathbf{v}_j^{(i+1)} = w \cdot \mathbf{v}_j^{(i)} + c_1 \cdot r_1 \cdot \left(\mathbf{p}_j - \mathbf{x}_j^{(i)}\right) + c_2 \cdot r_2 \cdot \left(\mathbf{p}_g - \mathbf{x}_j^{(i)}\right) \tag{5-5}$$

$$\mathbf{x}_j^{(i+1)} = \mathbf{x}_j^{(i)} + \mathbf{v}_j^{(i+1)} \tag{5-6}$$

The term $w \cdot \mathbf{v}_j^{(i)}$ describes the inertia proportion of the updated particle's j velocity at iteration i, whereby the value of the inertia constant w is decreasing with each iteration to encourage convergence. The term

$c_1 \cdot r_1 \cdot (\mathbf{p}_j - \mathbf{x}_j^{(i)})$ is referred to as the cognitive component pulling the particle to its personal best location $\mathbf{p}_j$. The term $c_2 \cdot r_2 \cdot (\mathbf{p}_g - \mathbf{x}_j^{(i)})$ is referred to as the social component pulling the particle to the global best location. The resulting total change in velocity is depending on the distance to the personal best location, the global best location, the factors $c_1, c_2 = [0,2]$ and the equally contributed random numbers $r_1, r_2 = [0,1]$. These update formulas implement the standard PSO with inertia weight and constrictions as described in [83]. Violations of search space limitations are treated by setting the value to the closest limitation. This version of PSO is chosen, since it is widely known. Further its simple straight forward implementation allows a good evaluation of the usability of PSO for the given optimization problem. However, implementing more advanced PSO versions, e. g. as described in [84], [85], might improve the results.

The global and personal best location are updated at each iteration step. The iteration is stopped, if either a predefined number of iterations is reached, the global best has not changed significantly over a given number of iterations or a criterion for the function value of the global best is fulfilled.

A closer analysis of algorithms and models available for PSOs is given for instance in Van den Bergh's PhD-thesis [86].

5.2 Branch and PMU Node Selection in the Nordic-32-Bus Test System

The model used for the evaluation of the algorithms' performance is a modified version of the Nordic-32-Bus system with an additional VSC-HVDC link between the buses 4032 and 4045, Fig. 5-1. The network parameter values and position of the embedded HVDC link are taken from [42], [87], [88]. The rated power of the HVDC converter, corresponding to the nominal transmission capacity used in the selection procedure, is assumed as $1000\ \mathrm{MW}$. A description of the test system is given in appendix D.

The selection procedures to define the corresponding areas of control and detection for the embedded HVDC link are applied as given in chapter 3. The sensitivity threshold is set $0.1\ \mathrm{pu}$ and only single branch outages are considered. This leads to the following sets Γ and E – displayed by the corresponding branch indices

$$\Gamma = \{30, 31, 32, 33, 34, 35, 37, 38, 39, 42, 43\} \tag{5-7}$$

$$E = \{20, 21, 22, 24, 26, 27, 28, 29, 30, 31, 32, 33, 34, 35, 36, 37, 38, 39, 42, 43, 46, 48, 57, 58, 59, 60\} \tag{5-8}$$

The selection of the PMU monitored buses is performed for the set E describing the area of detection. The four transformers with the branch numbers $\{57, 58, 59, 60\}$ are excluded from to the set to allow a reduction of possible PMU monitored nodes to the 400-kV system. Excluding the reference node 4032 and node 4031 – it behaves exactly as the reference node for the selected branch set –lead to 17 remaining candidate nodes. The evolution of selected nodes with increasing number of monitored nodes

is shown in Fig. 5-2 for both in chapter 3.3 described selection methods. As can be seen in the figure, the selected nodes are not identical between 9 and 14 monitored nodes. The influence of the selected nodes on the detection accuracy of different emergency detection algorithms is briefly addressed in the Appendix E.

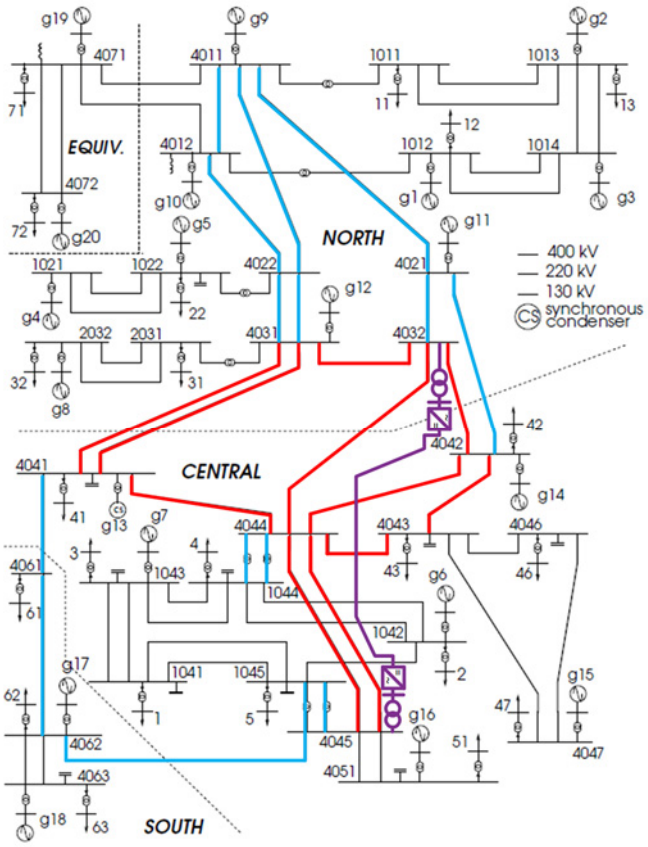

Fig. 5-1 Nordic test system – single line diagram [87] *with HVDC link (violet), the influenced elements (red) and the lines to detect (blue)*

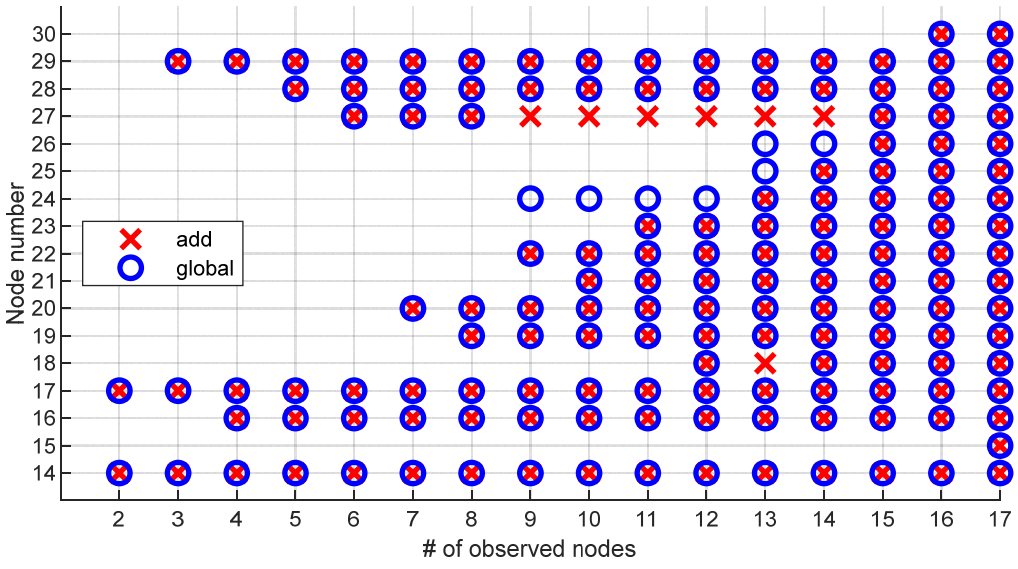

Fig. 5-2 Selected nodes for the adding and global algorithm

5.3 Single Branch Outage Detection

The detection of a tripped branch based on the change of node voltage angles is already addressed in [19]–[21]. The method used in these publications requires several calculation steps to determine the angle change due to fictive changes in power injection based on the pre-contingency branch flow of the tripped branch. The detection of the branch is executed by finding the minimum Euclidean distance between vectors depicting angle measurements and calculated angle changes.

The algorithm described in the following distinguishes only in the way how the expected angle change is calculated and in the metric used to compare the measurements with the calculations. It is further designed to have little calculation effort and it is scalable for any given region of interest to be efficiently implemented in a controller. This analytical algorithm is only used as comparison value for the optimization-based algorithms.

The detection algorithm needs a measurement vector **MAC** containing the actual values of the angle changes due to the branch outage. The measured angle changes are referred to the reference node defined for the calculation of the elements of **BOAC**. The calculation of the BOAC matrix is described in chapter 3.3. The tripped branch o is then identified by the maximum scalar product of the unit vectors of the columns of **BOAC** and the measurement unit vector. The use of unit vectors leads to a well-defined solution space between 0 and 1.

$$\max_{o=[1,B]} \left(\left| \frac{\mathbf{MAC}^{\mathrm{T}} \cdot \mathbf{BOAC}_{\mathrm{i}}}{\sqrt{\mathbf{BOAC}_{o}^{\mathrm{T}} \cdot \mathbf{BOAC}_{o}} \cdot \sqrt{\mathbf{MAC}^{\mathrm{T}} \cdot \mathbf{MAC}}} \right| \right) \tag{5-9}$$

$\mathbf{BOAC}_i$ … vector of node voltage angle changes from outage o $((N\text{-}1)\times 1)$

$\mathbf{MAC}$ … vector of measured voltage angle changes $((N\text{-}1)\times 1)$

The described detection algorithm is demonstrated on generic PMU data achieved by dynamic simulation of the Nordic-32 test system, Fig. 5-1. The results and comparisons to algorithms also suitable for multi branch outages are stated in chapters 5.5 and 5.6.

5.4 Optimization based Multi Branch Outage Detection

5.4.1 Definition of the objective function for the optimization

The problem of multiple branch outage detection based on node voltage angle changes is in principle possible by expanding the algorithm described in the previous chapter or similar methods. However, for the calculation of the necessary data the number of branches on outage and all possible combinations have to be known beforehand. This leads to the necessity to calculate a set of

$$\#\text{combinations} = \frac{L!}{k!\,(L-k)!} \tag{5-10}$$

outage combinations for a network with L branches and an assumed number of k branches on outage at the same instance. Beside the fast-growing amount of pre-calculated data, approaching the detection of multi branch outages with this kind of algorithms leads to different input information for different k. So far, only the detection of double line outages was examined in such a way, [20].

The objective function is defined as the mean square error between the PMU measured voltage angle changes and the estimated voltage angle changes. The estimated voltage angle changes are a function of the trial variable of the optimization based on the linearized DC load flow network model. For the following, an arbitrary network with N nodes and L branches is assumed. Due to the linearization, the node voltage angles $\boldsymbol{\vartheta}$ are calculated solely as a function of the active node power injections $\mathbf{p}_\mathrm{N}$ and the node susceptance matrix $\mathbf{B}$

$$\boldsymbol{\vartheta} = \mathbf{B}^{-1} \cdot \mathbf{p}_\mathrm{N} \tag{5-11}$$

$$\boldsymbol{\vartheta} \in \mathbb{R}^{(N-1)\times 1}, \mathbf{p}_\mathrm{N} \in \mathbb{R}^{(N-1)\times 1}, \mathbf{B} \in \mathbb{R}^{(N-1)\times(N-1)} \tag{5-12}$$

Any change in the active node power injections leads to a change in the node voltage angles. Furthermore, any branch outage not isolating a part of the network can be represented by a power injection at the starting node and an equally high negative power injection at the branch's ending node [89]. The fictional power injections' value is defined by the condition, that the resulting branch load of the tripped branch has to be 0. The change of the node voltage angles $\Delta\boldsymbol{\vartheta}$ is therefore calculated with the fictional power injection vector $\Delta\mathbf{p}_\mathrm{N}$ and the unchanged node susceptance matrix. The resulting change of the node voltage angles corresponds to the effects of a branch outage, if $\Delta\mathbf{p}_\mathrm{N}$ is composed of the fictional power injections modelling a branch outage.

$$\Delta\boldsymbol{\vartheta} = \mathbf{B}^{-1} \cdot \Delta\mathbf{p}_\mathrm{N} = \mathbf{B}^{-1} \cdot \mathbf{NBI} \cdot \Delta\mathbf{p}_\mathrm{NL} \tag{5-13}$$

$$\Delta\boldsymbol{\vartheta} \in \mathbb{R}^{(N-1)\times 1}, \Delta\mathbf{p}_\mathrm{NL} \in \mathbb{R}^{\mathrm{L}\times 1}, \mathbf{NBI} \in \{-1,0,1\}^{(\mathrm{N}-1)\times \mathrm{L}} \tag{5-14}$$

The usage of the node-to-branch incidence matrix $\mathbf{NBI}$ and a vector $\Delta\mathbf{p}_\mathrm{NL}$ containing one value of a fictional power injection for each branch in the network allows a direct linking of multi branch outages to the node voltage angle change. The elements of $\Delta\mathbf{p}_\mathrm{NL}$ are 0 except for those corresponding to the tripped branches. $\Delta\mathbf{p}_\mathrm{NL}$ can easily be calculated if the tripped branches and the change of the node voltage angles are known.

However, since the tripped branches and their number are unknown, a suitable solution for $\Delta\mathbf{p}_{\mathrm{NL}}$ is found by minimizing the mean square error function between the measured and calculated node voltage angle change. The scalar objective function in respect to the trial variable $\Delta\mathbf{p}_{\mathrm{NL}}$ is stated as

$$f(\Delta\mathbf{p}_{\mathrm{NL}}) = \|(\Delta\boldsymbol{\vartheta}_{\mathrm{meas}} - \mathbf{K}_{\mathrm{D}} \cdot \Delta\mathbf{p}_{\mathrm{NL}})\|^2 \quad (5\text{-}15)$$

$$\mathbf{K}_{\mathrm{D}} = \mathbf{B}^{-1} \cdot \mathbf{NBI} \quad (5\text{-}16)$$

$$\mathbf{K}_{\mathrm{D}} \in \mathbb{R}^{(\mathrm{N}-1)\times \mathrm{L}} \quad (5\text{-}17)$$

$\mathbf{K}_{\mathrm{D}}$ is a matrix describing the relation between node voltage angle change $\Delta\boldsymbol{\vartheta}$ and the trial variable $\Delta\mathbf{p}_{\mathrm{NL}}$. The slack node, defining the reference angle, is excluded. In general, not all branches of the network are of interest and not all nodes are equipped with a PMU. The number of branches of interest are denoted in the following as L_{OI} and the number of PMU monitored nodes as N_{PMU}. This leads to the necessity to define incidence matrices that relate PMU monitored nodes and branches of interest to the nodes and branches of the complete network. The PMU incidence matrix $\mathbf{A}_{\mathrm{PMU}}$ relates the nodes and the branch of interest incidence matrix $\mathbf{A}_{\mathrm{BOI}}$ the branches. The objective function changes to

$$f(\Delta\mathbf{p}_{\mathrm{NL}}) = \|\Delta\boldsymbol{\vartheta}_{\mathrm{meas}} - \mathbf{A}_{\mathrm{PMU}} \cdot \mathbf{K}_{\mathrm{D}} \cdot \mathbf{A}_{\mathrm{BOI}} \cdot \Delta\mathbf{p}_{\mathrm{NL}}\|^2 \quad (5\text{-}18)$$

$$\mathbf{A}_{\mathrm{PMU}} \in \{0,1\}^{N_{\mathrm{PMU}}\times(N-1)} \quad (5\text{-}19)$$

$$\mathbf{A}_{\mathrm{BOI}} \in \{0,1\}^{L\times L_{\mathrm{OI}}} \quad (5\text{-}20)$$

From equation (5-13), it is concluded that a minimum of the objective function must exist for a trial variable vector $\Delta\mathbf{p}_{\mathrm{NL}}$ only containing nonzero values at the elements corresponding to the branches actually tripped. The value of the objective function at this optimality point is 0. This is the case if the DC load flow solutions matches the measured data exactly, which is generally not the case. However, due to the relatively small expectable angle error of the DC load flow, it can be assumed that the optimization still finds a $\Delta\mathbf{p}_{\mathrm{NL}}$ vector with dominant values at the elements corresponding to the actually tripped branches.

The representation of double lines in the objective function prevents a distinguishable detection for parallel branches. Without a suitable pre-evaluation of the network topology, the results of the optimizer are not unambiguous, since the outage of one or more of the parallel branches will lead to an optimal trial variable $\Delta\mathbf{p}_{\mathrm{NL}}$. Only the values of the nonzero elements can give further information about the actual outage – higher values can be expected for multi branch outages. However, these values also depend on the pre-fault state of the system, thus making it necessary to include the load flow situation. The distinction between parallel branches does not fall within the focus of this work. Therefore, the correct detection of one of the indistinguishable parallel branches is treated as correct detection, if one or more of these parallel branches are actually tripped.

The authors are aware of the fact that if all nodes of the are monitored, the branches tripped can be derived without an optimizer by solving (5-13) for $\mathbf{NBI}\cdot\Delta\mathbf{p}_{\mathrm{NL}}$ and applying reduction methods. However, as soon as one node is not monitored, this procedure is no longer applicable.

5.4.2 Newton's Method

Using the deterministic Newton's method on the objective function provides a fast solution. The necessary gradient $\nabla f(\Delta\mathbf{p}_{\mathrm{NL}})$ and Hessian $\mathbf{H}(\Delta\mathbf{p}_{\mathrm{NL}})$ of the objective function are calculated as

$$\nabla f(\Delta\mathbf{p}_{\mathrm{NL}}) = -2 \cdot \mathbf{K}_{\mathrm{D}}^{\mathrm{T}} \cdot (\boldsymbol{\vartheta}_{\mathrm{meas}} - \mathbf{K}_{\mathrm{D}} \cdot \Delta\mathbf{p}_{\mathrm{NL}}) \tag{5-21}$$

$$\mathbf{H}(\Delta\mathbf{p}_{\mathrm{NL}}) = \nabla\left(\nabla f(\Delta\mathbf{p}_{\mathrm{NL}})\right)^{\mathrm{T}} = 2 \cdot \mathbf{K}_{\mathrm{D}}^{\mathrm{T}} \cdot \mathbf{K}_{\mathrm{D}}^{\mathrm{T}} \tag{5-22}$$

and an optimal point for $\Delta\mathbf{p}_{\mathrm{NL}}$ can be found. However, due to the definition of the objective function – modelling branch outages as power injections – and the composition of $\mathbf{K}_{\mathrm{D}}$ a multitude of local optima exist as soon as the topology of the network contains a loop sub structure. This leads in general to an optimum with a large number of nonzero elements in $\Delta\mathbf{p}_{\mathrm{NL}}$ not related to the actual outage. This result is reflecting the closest optimum from the starting point – chosen to be the zero vector – and is corresponding to power injections in those nodes to recreate the observed node voltage angle change.

To demonstrate this behaviour, the node voltage angle changes for a double outage of branch 20 and 30 of the Nordic32 test system are calculated using linearized load flow equations. The calculated angle changes are used as fictive measurement data in the objective function. Applying Newton's method with the zero vector as initialisation results in $\Delta\mathbf{p}_{\mathrm{NL}}$ depicted with the blue bars in Fig. 5-3. All elements of the trial variable vector are nonzero, which makes a correct detection of the branches on outage based on the position of the nonzero elements in $\Delta\mathbf{p}_{\mathrm{NL}}$ impossible. Nevertheless, there also exists an optimum for a $\Delta\mathbf{p}_{\mathrm{NL}}$ only consisting of nonzero values in the elements corresponding to branch 20 and 30 containing the necessary information for a correct detection of the branches on outage.

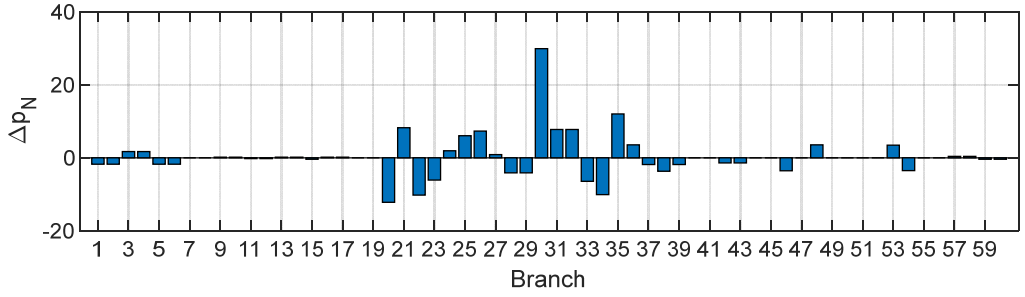

Fig. 5-3 Solution for $\Delta\mathbf{p}_{\mathrm{NL}}$ using Newton's method for the outage of branch 20 and 30 of the Nordic32 test system

Consequently, the problem using Newton's method for multi branch outages is to reach an optimization result of $\Delta\mathbf{p}_{\mathrm{NL}}$ containing the minimum set of nonzero elements. Only in this case the branches on outage will equal the position of nonzero elements of $\Delta\mathbf{p}_{\mathrm{NL}}$.

One approach to overcome this problem is to assume, that elements with absolute values smaller than a threshold ξ are not corresponding to branches on outage. These branches are removed from the objective function. The value ξ is implemented as variable. In the process of removing branches, ξ is increased from an initial value until a given percentage of considered branches are removed. Newton's method is applied on the restated objective function for the reduced set of branches – given by equations (5-18) to (5-20). The elements corresponding to the branches actually on outage are more dominant in

the resulting $\Delta\mathbf{p}_{\mathrm{NL}}$ for the reduced objective function. The new solution is checked again for elements smaller than ξ and a new iteration with a further reduced set of branches is started. The iteration steps are repeated until only a predefined number of branches remains. The flow chart of this iterative process is given in Fig. 5-4.

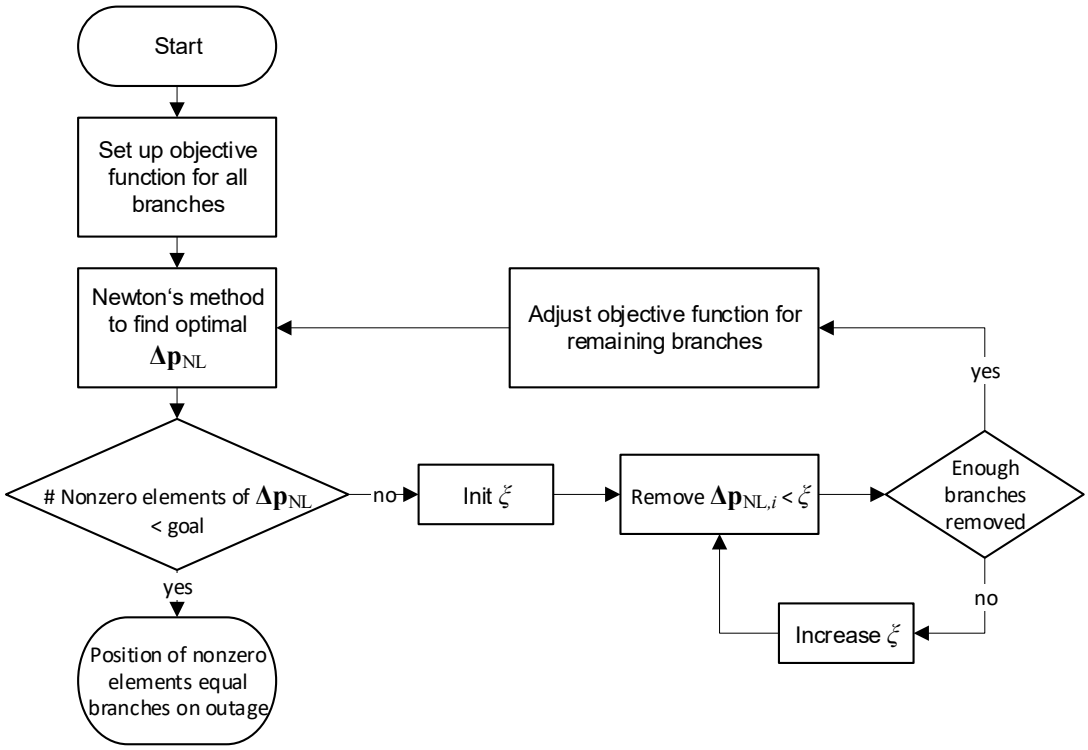

Fig. 5-4 Flow chart of the iterative expansion of Newton's method to detect branches on outage

In an application example, this iterative expansion of Newton's algorithm on the outage of branch 20 and 30 of the Nordic32 test system converges after 6 iterations to a $\Delta\mathbf{p}_{\mathrm{NL}}$ only containing nonzero elements at position 20 and 30. The absolute values of the resulting $\Delta\mathbf{p}_{\mathrm{NL}}$ for each iteration step are shown in Fig. 5-5. The initial value for ξ is set to $1\ \%$ of the maximum absolute value of all elements and increased till a minimum of $25\ \%$ of the branches are removed at each iteration step.

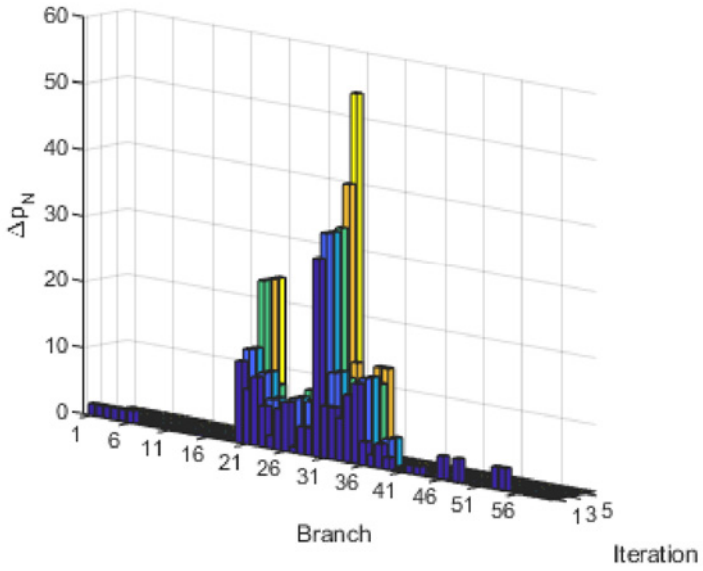

Fig. 5-5 Absolute values of the elements in $\Delta \boldsymbol{p}_{NL}$ using an iterative expansion of Newton's method for the outage of branch 20 and 30 of the Nordic32 test system

An observation from Fig. 5-5 is, that the fictional power injection corresponding to the tripped branches are increasing in each iteration step. This is caused by the reduction of input branches for the optimizer, forcing the fictional power injections of the remaining branches to converge to injections only corresponding to the tripped branches. The element belonging to branch 20 already settles to its final value at iteration step 4. The explanation for this behaviour is, that no parallel structure to branch 20 can be formed with the branches remaining after the reduction of iteration step 3.

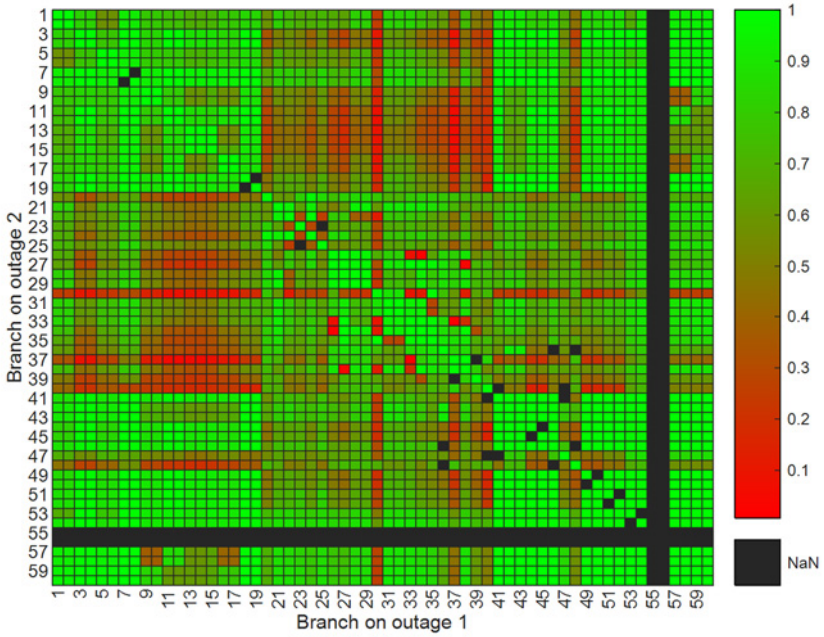

Fig. 5-6 Heat map of the detection ratio for Newton's method of all possible double branch outage combinations averaged over 1000 random pre-contingency load flows

The general performance of the algorithm is tested with simulated data for all possible combinations of double branch outages in the Nordic32 test system. The used node voltage angle changes are

calculated for 1000 randomly created load flow situations in the network. An explanation of the creation of the load and generation is given in chapter 5.5.

The correct detection ratio for any double and single branch outage is visualized in Fig. 5-6, whereby a minimum of $25\ \%$ of the branches are removed at each iteration. The combinations marked black refer to outages leading to islanding. The detection of these outages is not in the scope of the used algorithm. The mean value of the correct detection ratio for all other outages is 0.71. The average run time of the algorithm on one core of a i7-4790 3.60 GHz CPU is $25.6\ \mathrm{ms}$.

5.4.3 Particle Swarm Optimization

The PSO is applied on the objective function (5-18), which leads for a network with L branches to a L-dimensional search space. The expected optimal solution for $\Delta\mathbf{p}_{\mathrm{NL}}$ contains the minimum set of nonzero elements referring to the branches on outage and is given by the global best position after convergence of the PSO.

The main challenges for the optimization with PSO are the high search space dimension equal to the number of branches of interest L_{OI} and the existence of multiple optimal solutions not linked to the actual outage event for a meshed network topology. The cause and effect of the multiple optimal solution are discussed in subsequently. A straight forward implementation of PSO is more likely to converge in one of the optima not linked to the outage. Further, the high number of dimensions increase the calculation time.

In all considerations the vector of trial variables contained information about the branches on outage – given by the position referred to the branch number of the nonzero elements – and the amount of fictional power injections causing the same resulting load flow on the remaining lines – given by the value of the nonzero elements. The use of PSO enables a separation of the branch on outage and the amount of the fictional power injections. Each particle's position is linked to the new trial variables $\mathbf{x}_{\mathrm{B}}$ and $\mathbf{x}_{\mathrm{P}}$. The dimension of each trial variable is reduced to the maximum expected number of branches simultaneously on outage, which the algorithm should be able detect. The dimension of the search space is consequently two times the expected number of detectable simultaneous branch outages.

$\mathbf{x}_{\mathrm{B}}$ is linked to the candidate branches on outage. Therefore, the values of $\mathbf{x}_{\mathrm{B}}$ have to be between 0 and the number of branches in the network L. The objective function (5-18) is reduced according to (5-20), whereby the reduced set of branches is given by the element values of $\mathbf{x}_{\mathrm{B}}$ ceiled to the next integer. The objective function has to be adjusted according to the particle's position $\mathbf{x}_{\mathrm{B}}$ separately for each particle at each iteration step. However, since the reduction is merely a matrix multiplication it is not computational expensive. The resulting two variable objective function is given as

$$f(\mathbf{x}_{\mathrm{B}}, \mathbf{x}_{\mathrm{P}}) = \|(\Delta\boldsymbol{\vartheta}_{\mathrm{meas}} - \mathbf{A}_{\mathrm{PMU}} \cdot \mathbf{K}_{\mathrm{D}} \cdot \mathbf{A}_{\mathrm{BOI}}(\mathbf{x}_{\mathrm{B}}) \cdot \mathbf{x}_{\mathrm{P}})\|^2 \qquad (5\text{-}23)$$

$$\mathbf{K}_{x_B} = \mathbf{A}_{\mathrm{PMU}} \cdot \mathbf{K}_{\mathrm{D}} \cdot \mathbf{A}_{\mathrm{BOI}}(\mathbf{x}_{\mathrm{B}}) \qquad (5\text{-}24)$$

$\mathbf{A}_{\mathrm{PMU}}$ … PMU incidence matrix

$\mathbf{A}_{\mathrm{BOI}}(\mathbf{x}_{\mathrm{B}})$	…	notation for columns corresponding to $\mathbf{x}_{\mathrm{B}}$ of the branch of interest matrix $\mathbf{A}_{\mathrm{BOI}}$
$\mathbf{K}_{\mathrm{D}}$	…	complete correlation matrix between node power injection and node voltage angle change
$\mathbf{K}_{x_B}$	…	correlation matrix between trial variable $\mathbf{x}_{\mathrm{P}}$ and measured node voltage angles

The resulting matrix linking $\mathbf{x}_{\mathrm{P}}$ to $\Delta\vartheta_{\mathrm{meas}}$ is defined as $\mathbf{K}_{x_B}$ for simplified notation.

The velocities $\mathbf{v}_{\mathrm{B}}$ and $\mathbf{v}_{\mathrm{P}}$ and positions $\mathbf{x}_{\mathrm{B}}$ and $\mathbf{x}_{\mathrm{P}}$ of the particles are updated as given in (5-5) and (5-6) at the end of each iteration step. The iteration is stopped, if the global best combination of $\mathbf{x}_{\mathrm{B}}$ and $\mathbf{x}_{\mathrm{P}}$ leads to an objective function value satisfying $a < \varepsilon$ condition or the maximum number of iterations is reached. The implementing of an additional outer iteration loop, which reinitializes the particles positions $\mathbf{x}_{\mathrm{B}}$ and $\mathbf{x}_{\mathrm{P}}$ and velocities $\mathbf{v}_{\mathrm{B}}$ and $\mathbf{v}_{\mathrm{P}}$, if the maximum number of iterations is reached in the inner iteration loop, leads to an improvement of the detection ratio of the algorithm. The flowchart of the PSO variant used is shown in Fig. 5-7.

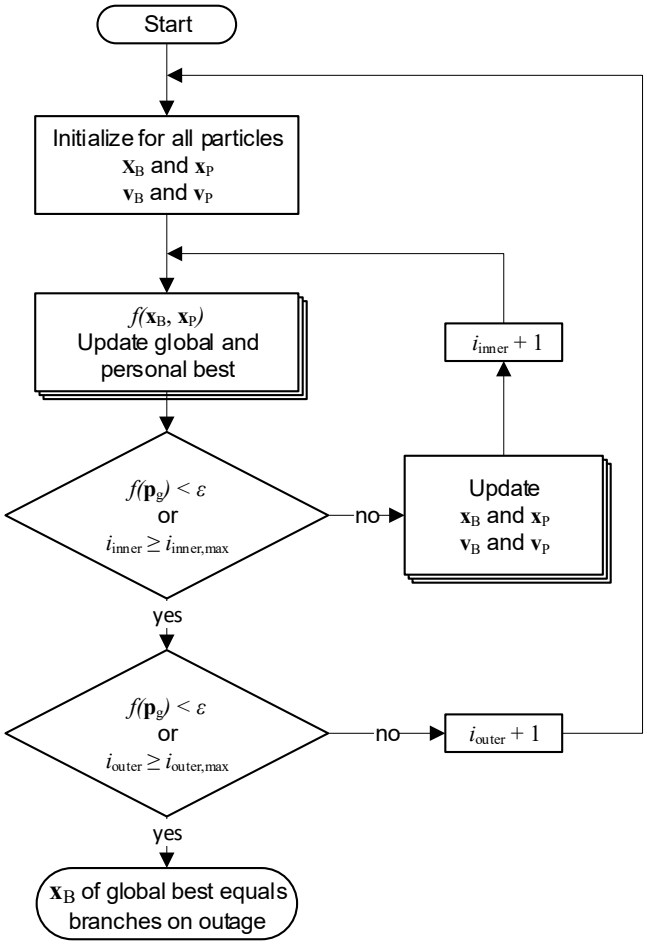

Fig. 5-7 Flow chart of the PSO to detect branches on outage

The general performance of the algorithm is tested on the artificial node voltage angle changes in the Nordic32 test system. The parametrisation of the PSO is given in Table 5-1. The correct detection ratio for any double and single branch outage is visualized in Fig. 5-8. The combinations marked black refer

to outages leading to islanding. The mean value of the correct detection ratio for all other outages – excluding islanding cases – is 0.936. The average run time of the algorithm on one core of a i7-4790 3.60 GHz CPU is 354.3 ms. The average necessary iteration steps leading to an acceptable result is 150.62 for the inner loop and 17.52 for the outer loop. A closer discussion on the performance of the algorithm is given in in chapter 5.5.

Table 5-1 PSO parameters used for evaluating the general performance of the algorithm

w	c_1	c_2	PSO dimension	$i_{\text{inner,max}}$	$i_{\text{outer,max}}$	# particles	*borders* $\mathbf{x}_p$
1 … 0.3	1.05	1.05	4	500	100	40	[-100 100]

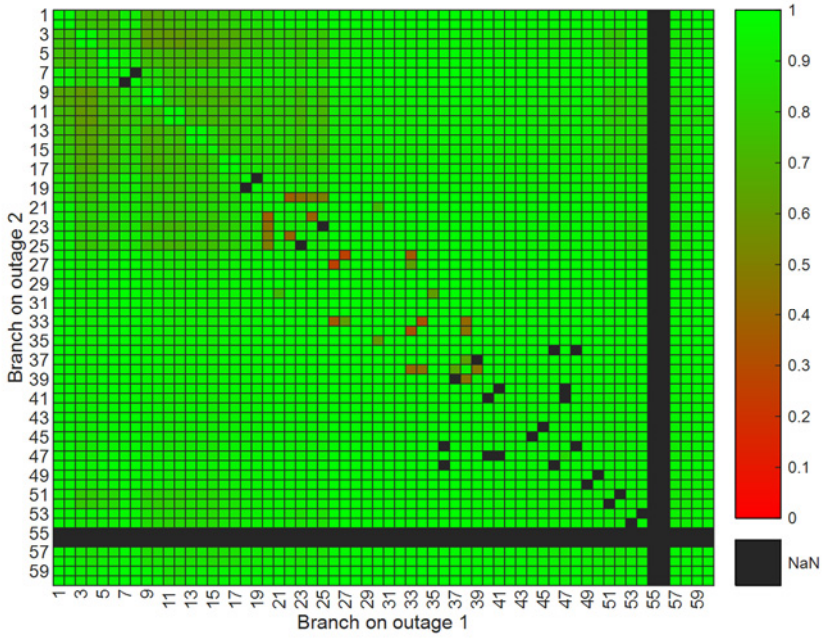

Fig. 5-8 Heat map of the detection ratio for PSO of all possible double branch outage combinations averaged over 1000 random pre-contingency load flows

5.4.4 Hybrid Optimizer

Hybrid optimizers consist of a stochastic part and a deterministic part. The results of the application of Newton's algorithm and PSO indicate a possible improvement on the detection ratio and run time using a hybrid optimizer on the detection problem. In the following the abbreviation HPN (**H**ybrid **P**article Swarm – **N**ewton Optimizer) is used for the hybrid optimizer discussed in this work. The general design approach for the optimizer is based on the separation of $\Delta\mathbf{p}_{\mathrm{NL}}$ into two trial variables as already discussed for the PSO. The first – $\mathbf{x}_{\mathrm{B}}$ – is a vector whose elements describe a subset of branches of interest. Only the branches in $\mathbf{x}_{\mathrm{B}}$ are considered as candidates for an outage. The number of branches in $\mathbf{x}_{\mathrm{B}}$ determines the search space dimension. The second – $\mathbf{x}_{\mathrm{P}}$ – is also a vector and its elements correspond to the amount of fictional power injections on the terminals of the candidate branches in $\mathbf{x}_{\mathrm{B}}$. The resulting two variable objective function is given as

$$f(\mathbf{x}_{\mathrm{B}}, \mathbf{x}_{\mathrm{P}}) = \left\| \Delta\boldsymbol{\vartheta}_{\mathrm{meas}} - \mathbf{A}_{\mathrm{PMU}} \cdot \mathbf{K}_{\mathrm{D}} \cdot \mathbf{A}_{\mathrm{BOI}}(\mathbf{x}_{\mathrm{B}}) \cdot \mathbf{x}_{\mathrm{P}} \right\|^2 \tag{5-25}$$

$$\mathbf{K}_{x_B} = \mathbf{A}_{\mathrm{PMU}} \cdot \mathbf{K}_{\mathrm{D}} \cdot \mathbf{A}_{\mathrm{BOI}}(\mathbf{x}_{\mathrm{B}}) \tag{5-26}$$

The resulting matrix linking $\mathbf{x}_{\mathrm{P}}$ to $\Delta\boldsymbol{\vartheta}_{\mathrm{meas}}$ is further defined as $\mathbf{K}_{x_B}$ for simplified notation. Analysing the objective function separately for each trial variable, it is obvious that a change in $\mathbf{x}_{\mathrm{B}}$ results in a discontinuous change in $\mathbf{K}_{x_B}$ and, consequently, altering the objective function's form. However, the objective function is continuous to changes in $\mathbf{x}_{\mathrm{P}}$ for any given $\mathbf{x}_{\mathrm{B}}$.

Based on this general behaviour towards the trial variables, a two level optimizer HPN is proposed, combining particle swarm optimization PSO [82] and Newton's method [81]. The outer level applies PSO on $\mathbf{x}_{\mathrm{B}}$ defining a continuous objective function f_{N} (5-27). f_{N} is the input for the inner level Newton's algorithm minimizing the function value in respect to $\mathbf{x}_{\mathrm{P}}$. The minimal function value of f_{N} is handed back to the PSO as the function value of f_{PSO} (5-28) for the current value of $\mathbf{x}_{\mathrm{B}}$.

$$f_{\mathrm{N}}(\mathbf{x}_{\mathrm{P}}) = \left\| \Delta\boldsymbol{\vartheta}_{\mathrm{meas}} - \mathbf{K}_{x_B} \cdot \mathbf{x}_{\mathrm{P}} \right\|^2 \tag{5-27}$$

$$f_{\mathrm{PSO}}(\mathbf{x}_{\mathrm{B}}) = \min\left(f_N(\boldsymbol{x}_B)|_{x_B} \right) \tag{5-28}$$

The value of $\mathbf{x}_{\mathrm{B}}$ is the position of the PSO particle at the current iteration step. At each iteration step i, the position and velocity $\mathbf{v}_{\mathrm{B}}$ of the particle are updated as given in equations (5-5) and (5-6). Since $\mathbf{x}_{\mathrm{B}}$ represents the selected candidate branches, the values in each of its dimensions must be discrete integers between 1 and the number of branches in the network L. However, it is obvious that the stated update formulas of PSO lead to continuous values of $\mathbf{x}_{\mathrm{B}}$ and it must be discretized with the prerequisite of equally large intervals.

The personal and global best position store the values of the particle's $\mathbf{x}_{\mathrm{B}}$ leading to the smallest function value of f_{PSO}. The function value of f_{PSO} decreases if branches topologically close to the actually tripped branches are included in the branches of $\mathbf{x}_{\mathrm{B}}$. The function value of f_{PSO} only becomes 0 or satisfies a $< \varepsilon$ condition if the tripped branches are part of the branches of $\mathbf{x}_{\mathrm{B}}$. Therefore, a higher dimension of $\mathbf{x}_{\mathrm{B}}$ – in other words more candidate branches per particle – has the effect of a faster convergence at the cost

of detection accuracy. The decrease in the detection accuracy is caused by the possibility of multiple minima as soon as the branches in $\mathbf{x}_\mathrm{B}$ form a meshed structure.

The gradient ∇f_N and Hessian $\mathbf{H}$ – needed to calculate the Newton step $\boldsymbol{\delta}$ (5-29) – are given by the equations (5-30) and (5-31).

$$\boldsymbol{\delta}(\mathbf{x}_\mathrm{P}) = -\mathbf{H}^{-1} \cdot \nabla f_\mathrm{N}(\mathbf{x}_\mathrm{P}) \tag{5-29}$$

$$\nabla f_\mathrm{N}(\mathbf{x}_\mathrm{P}) = -2 \cdot \mathbf{K}_{x_B}^\mathrm{T} \cdot \left(\boldsymbol{\vartheta}_\mathrm{meas} - \mathbf{K}_{x_B} \cdot \mathbf{x}_\mathrm{P}\right) \tag{5-30}$$

$$\mathbf{H} = 2 \cdot \mathbf{K}_{x_B}^\mathrm{T} \cdot \mathbf{K}_{x_B} \tag{5-31}$$

Due to the optimizer's two-level approach, the equations (5-29) to (5-31) must be evaluated at each PSO iteration step and for each particle separately. However, since the reduction of the matrix $\mathbf{K}_\mathrm{D}$ to $\mathbf{K}_{x_B}$ as well as the calculation of ∇f_N and $\mathbf{H}$ are simple matrix multiplications, it is not computationally expensive. The inverse of $\mathbf{H}$ is constant for the iterations of Newton's method and therefore, must be calculated only once per PSO iteration step and particle.

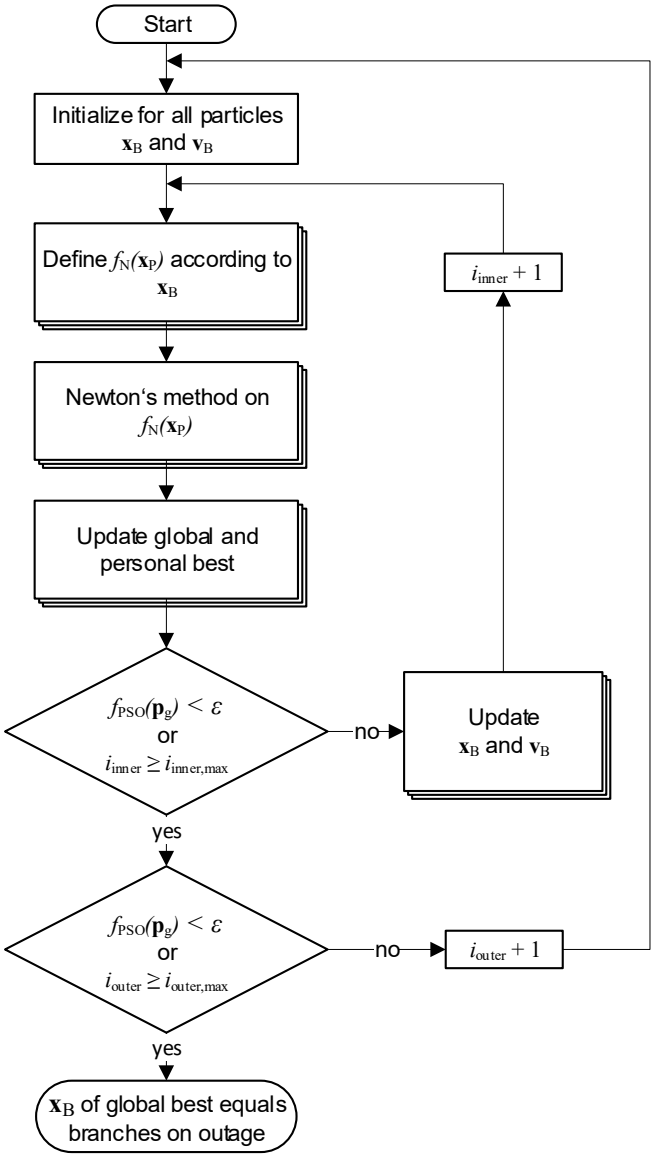

Fig. 5-9 Flow chart of the HPN based on a superordinate PSO and Newton's method

The PSO's iteration is stopped, if $f_{PSO}(\mathbf{x}_B)$ satisfies a $< \varepsilon$ condition or the maximum number of iterations is reached. If a $< \varepsilon$ condition is satisfied, it is assumed that all tripped branches are within the corresponding $\mathbf{x}_B$. If the algorithm is aborted due to maximum iterations, an implemented outer loop reinitializes the particles of the PSO part. The HPN's flowchart is shown in Fig. 5-9.

The general performance of the HPN algorithm is tested on the artificial node voltage angle changes in the Nordic32 test system. The parametrisation of the PSO part is given in Table 5-2. The mean detection ratio for any double and single branch outage is visualized in Fig. 5-10. The combinations marked black refer to outages leading to islanding. The overall mean value of the detection ratio for all other outages is 0.944. The average run time of the algorithm on one core of a i7-4790 3.60 GHz CPU is 74.5 ms. The average necessary iteration steps leading to an acceptable result is 6.49 for the inner loop and 1.008 for the outer loop. A closer discussion on the performance of the algorithm is given in in chapters 5.5 and 5.6.

Table 5-2 Parameters used for evaluating the general performance of the algorithm

w	c1	c2	PSO dimension	$i_{inner,max}$	$i_{outer,max}$	# particles
1 … 0.3	1.05	1.05	4	500	100	40

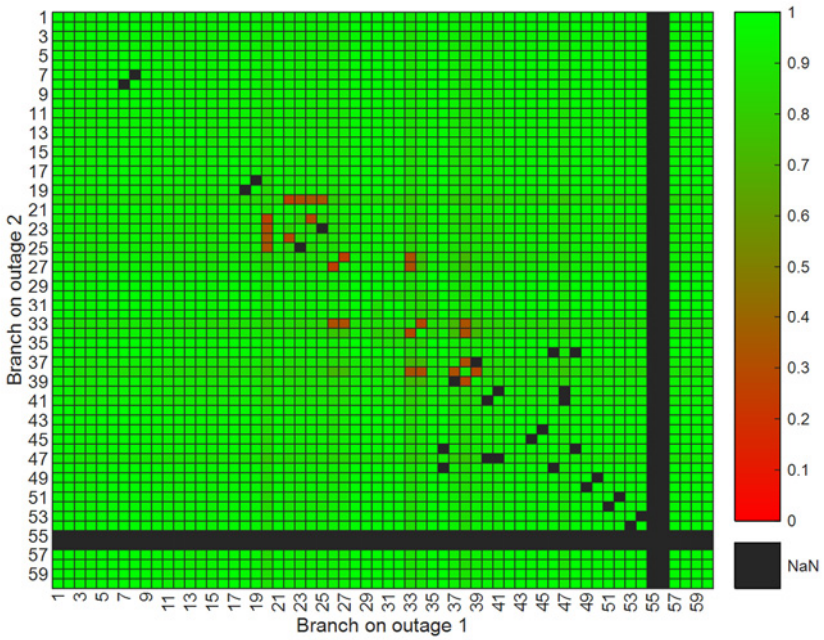

Fig. 5-10 Heat map of the detection ratio for HPN of all possible double branch outage combinations averaged over 1000 random pre-contingency load flows

5.5 Comparative Evaluation on Linearized DC Load Flow Simulations

Simulations with the linearized DC load flow model are used to evaluate the general robustness of the detection algorithm against a variation of the search space dimension, missing information and changed load flow situations. The DC load flow is used for this purpose, since the detection algorithm is based on it. Therefore, the ideal solution is known beforehand and errors due to the linearization do not exist. The linearized DC load flow model of the Nordic-32 Bus system contains only the 32 transmission system nodes, whereby node 4032 is set as the slack node. The loads and generation are shifted from the medium voltage nodes to the corresponding transmission system nodes.

The node voltage angle changes are calculated for each branch outage combination as follows. The index b refers to the network before any branch tripping and index c to the network with the tripped branches removed. $\mathbf{B}^{\mathrm{c}}$ and $\mathbf{B}^{\mathrm{b}}$ are the corresponding system susceptance matrixes. The calculated node voltage angle changes are used as measurement input for the detection algorithms.

$$\Delta\boldsymbol{\vartheta} = \left(\mathbf{B}^{\mathrm{c}^{-1}} - \mathbf{B}^{\mathrm{b}^{-1}}\right) \cdot \left(\mathbf{p}_{\mathrm{gen}} - \mathbf{p}_{\mathrm{load}}\right) \qquad (5\text{-}32)$$

The generation and load data are varied over 1000 load cases to ensure a load flow independent performance test. The distribution is achieved by assigning a uniformly distributed number between 0 and 1 to the corresponding nodes and subsequently scaling to the total network load. The detection performance is then statistically evaluated for all possible single and double branch outages. Significant cases – original load data, worst, mean and best detection ratio – are used for testing the principal applicability of the algorithms on triple branch outages.

This evaluation is important for a better understanding of the algorithms' principal behaviour and dependencies without additional error sources such as linearization error, controller actions and oscillations.

The main performance parameters for the detection algorithms are the detection ratio, the detection runtime and the vulnerability to missing node information. The evaluations are conducted for the detection results of the 1000 load cases, which are created as described above. The detection algorithms are implemented as a MATLAB® script and run on one core of an i7-4790 3.60 GHz CPU.

The correct detection ratio (DR) and mean detection run time (MT) are evaluated for two options:

- The index $_{\mathrm{OC}}$ refers to the simulation results of a specific branch outage combination which is evaluated for all 1000 load cases with equation (5-33).
- The index $_{\mathrm{LC}}$ refers to the simulation results of a specific load case which is evaluated for all possible branch outage combinations with equation (5-34).

$$DR_{\mathrm{OC}} = \frac{\#correct_{\mathrm{OC}}}{\#load\ cases}, MT_{\mathrm{OC}} = \frac{\sum RT_{\mathrm{OC}}}{\#load\ cases} \qquad (5\text{-}33)$$

$$DR_{\mathrm{LC}} = \frac{\#correct_{\mathrm{LC}}}{\#outage\ combinations}, MT_{\mathrm{LC}} = \frac{\sum RT_{\mathrm{LC}}}{\#outage\ combinations} \quad (5\text{-}34)$$

RT	…	detection run time of a single contingency event
$\#correct$	…	number of correct detections per outage combination (OC) or per load case (LC)
$\#load\ cases$	…	number of simulated load cases
$\#outage\ combinations$	…	number of feasible double branch outage combinations

A comparison of the three algorithms based on their overall detection ratio already shows clearly, that PSO ($0.936\ \mathrm{pu}$) and HPN ($0.944\ \mathrm{pu}$) perform way better than the modified Newton's method ($0.71\ \mathrm{pu}$). The modified Newton's method is therefore disregarded as not applicable and not discussed further.

5.5.1 Detection Ratio and Detection Run Time

The following visualizations of the evaluations for the detection results based on node voltage angle information of all 32 nodes uses the kernel density estimation (KDE) based on normal distribution. The KDE parameters are derived using the MATLAB® function 'fitdist' [90]. The per unit reference for the resulting frequency of DR_{OC} and MT_{OC} is 3336, which is the number of single and double branch outage combinations not leading to islanding of network parts and 1000 for DR_{LC} and MT_{LC}. The frequency is interpreted as the relative appearance of the value on the abscissa. E. g. a frequency of $0.001\ \mathrm{pu}$ at a DR_{OC} of $0.9\ \mathrm{pu}$ means that $0.001\ \mathrm{pu}$ of all possible branch outage combinations have a DR_{OC} of $0.9\ \mathrm{pu}$.

5.5.1.1 General Performance Comparation

The following comparison of the detection algorithms with the PSO and the HPN are based on the parameters given in Table 5-1 and Table 5-2. The left graph of Fig. 5-11 showing the frequency of DR_{OC} allows an evaluation of the result stability for a single outage combination. A higher mode with sharper slope and at the same time higher frequency values for DR_{OC} below $0.86\ \mathrm{pu}$ are observed for the PSO based detection algorithm. This indicates, that the correct detection ratio based on the PSO implementation tend to depend more on the outage combination than the correct detection ratio based on the HPN implementation. The right graph depicting the frequency of DR_{LC} enables a conclusion on the influence of the base case load flow. A prominent mode is seen for the HPN based detection algorithm, which indicates a robustness against different load flow situations. The smaller peeks starting to occur at about $0.9\ \mathrm{pu}$ detection ratio are discussed below in the paragraphs focused on the effects of the search space dimension on the detection ratio of the HPN based algorithm. The rather flat frequency curve for the PSO based detection indicates a higher dependency on the base case load flow.

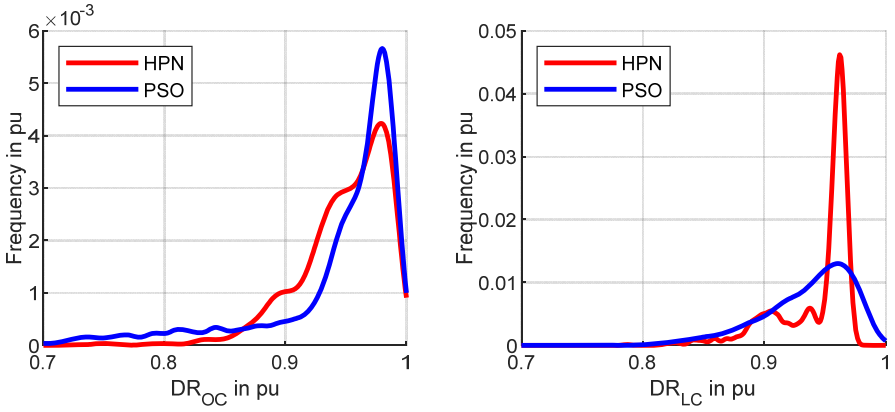

Fig. 5-11 Frequency of correct detection ratio estimated using KDE for PSO and HPN with a search space dimension of 4

The frequencies of the mean detection run time MT, depicted in Fig. 5-12, show a stronger influence of the network topology on the detector performance. The mean detection run time on the abscissa is referred to its mean value –and $354.3\ \mathrm{ms}$ for PSO based algorithm and $74.3\ \mathrm{ms}$ for the HPN based algorithm – to allow a comparison between the algorithms in one graph.

Focusing on the left graph first, a right skewed behaviour is observed for MT_{OC} of both PSO and HPN based algorithms, caused by a small number of outage combinations with higher detection run time. MT_{LC} – depicted on the right graph – shows a nearly symmetrical shape, which indicates only a minor influence of the load flow situation on the detection run time. The smaller and less dominant modes as well flatter profile in both graphs for the PSO based algorithm indicates a greater scattering of the results and therefore a higher dependency on the outage combination and load flow situation.

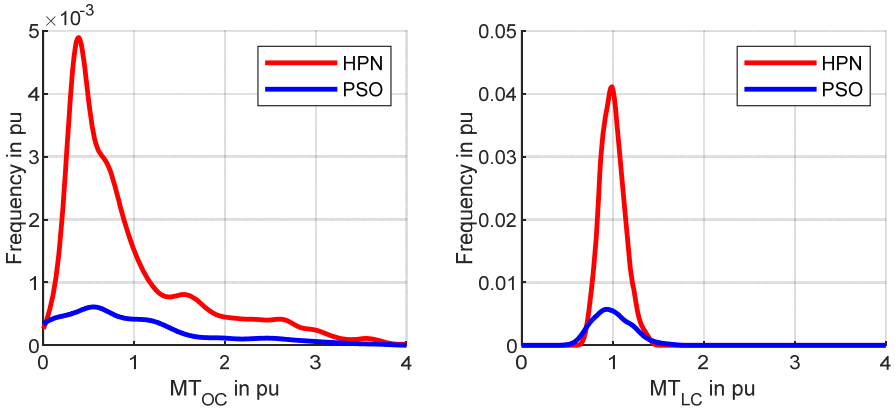

Fig. 5-12 Frequency of the detection run time estimated using KDE. The detection run time is referred to its mean value to allow a comparison between HPN and PSO.

The main parameters of the comparison are summarized in Table 5-3. Comparing the mean correct detection ratio with the correct detection ratio corresponding to the mode, it can be seen, that both algorithms lead to a left skewed result distribution. The mean detection run time is right skewed for the outage-based interpretation MT_{OC}, whereby the HPN based algorithm shows a higher skewness. Summarizing the skewness, it shows that the expectable correct detection ratio is higher than the mean value of the correct detection ratio of the simulation results and has a shorter detection run time.

Table 5-3 Correct Detection ratio and detection run time for PSO and HPN based algorithm

		PSO		HPN	
		OC	LC	OC	LC
DR in pu	Worst	0.266	0.762	0.257	0.787
	Mean	0.936		0.944	
	Best	0.999	0.991	1.0	0.975
	Mode	0.980	0.961	0.979	0.962
MT in ms	Minimum	5.4	163.9	7.7	52.1
	Mean	354.3		74.5	
	Maximum	1253.6	603.9	398.6	105.0
	Mode	196.1	330.7	29.0	74.0

Comparing the results of the PSO and HPN based algorithms shows a slightly higher detection ratio for the HPN based algorithm. Additionally, the HPN based algorithm has a much smaller run time and is therefore superior.

5.5.1.2 Sensitivity to search space dimension

Besides the measurable performance parameters, the algorithms' application limitations and sensitivity to the setting of selected parameter defining the search space have to be considered. One of these parameters is the dimension of the search space for a given number of detectable simultaneous branch outages denoted as k. The PSO search space dimension has to be $2k$, compared to HPN's necessary search space dimension k. In other words, HPN can detect twice the number of simultaneous branch outages with the same dimension of the search space. An increase in k leads to drastically worse detection ratios and longer detection time for the PSO. The HPN reacts to a small increase of k with a slightly worse detection ratio and a decreased detection time. The detection time decrease is explained by the higher chance to include the actual branches on outage in the particle's position with a higher number of dimensions in the PSO part of the HPN. However, if k increases further, the problems with multiple solutions of the deterministic part of the HPN, discussed for Newton's method in 5.4.2, become apparent and lead to a significant worse performance.

A further parameter is the border limitation of the search space. If these limits are chosen insufficient for the optimization problem, the global optimum can either be outside the border – for too small limits – or the necessary iterations and calculation time is insufficient high – for too large limits. For the problem of branch outage detection, the limits for the search space dimensions linked to the candidate branches – $\mathbf{x}_{\mathrm{B}}$ for PSO and the PSO part for the HPN – are uncritical, since they are predefined by the number of branches in network. Therefore, only the chosen limitations of $\mathbf{x}_{\mathrm{P}}$ of the PSO have an influence on the performance. The sensitivities of the algorithms to the search space dimension are summarized in Table 5-4.

Table 5-4 Sensitivity to search space dimension

	max. branches	dimension	Mean detection ratio in pu	Mean detection time in ms
PSO	2	4	0.936	354
	4	8	0.2	959
HPN	2	2	0.967	899
	4	4	0.944	75

In the following a closer look on the evaluation of the results of the 2- and 4-dimensional search spaces of the HPN based algorithm is taken. The frequency of DR_{OC} in Fig. 5-13 shows significant saddles at detection ratios around $0.9\,\mathrm{pu}$ and $0.95\,\mathrm{pu}$ as well as a relative exposed mode at $0.98\,\mathrm{pu}$ for a 4-dimensional search space. The two saddles are caused by topological issues and mainly correspond to three-branch loops, whereby the worst detection ratio occurs for branches participating in more than one three-branch loop. The branch with the smallest impedance in any of the loops is more often wrongly detected, since higher node power injections are necessary to obtain the measured change in node voltage angle. The higher number of wrong detections for these branches results from the tendency of the Newton part optimizing algorithm to find a solution closest to the initial point. The results for the reduced search space dimension to 2 supports this conclusion on the topological effect. Consequently, three-branch loops no longer lead to wrong detection results, since they simply no longer exist in the optimizers search space. That leads to a probability density function with a more pronounced mode. The remaining small saddles are caused by 400-kV-branches in parallel to network parts of lower voltage.

Focusing on the frequency of DR_{LC} in Fig. 5-13 enables conclusions to be drawn on the influence of the load flow situation on the detection ratio. The dominant mode occurring in the data for 2- and 4-dimensional search space indicates a robustness of the detection algorithm against different load flow situations. The smaller peaks starting to occur at about $0.9\,\mathrm{pu}$ detection ratio might be caused by the stochastic PSO part of the HPN.

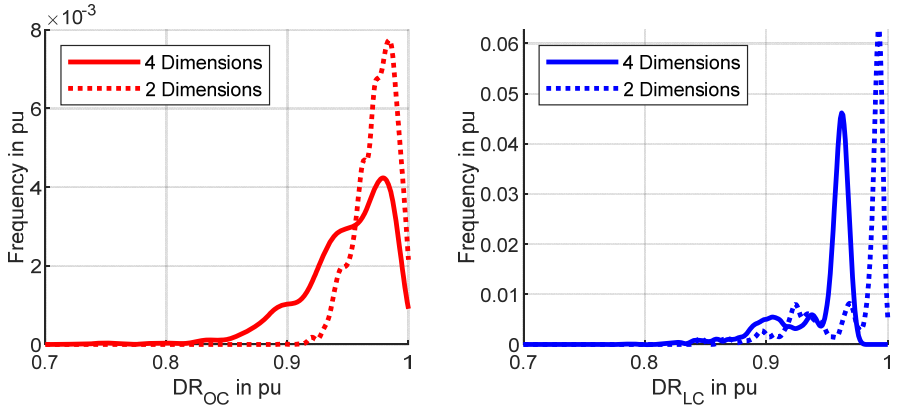

Fig. 5-13 Frequency of correct detection ratio estimated using KDE for HPN based algorithm with 2- and 4-dimensional search spaces

The frequencies of the mean detection run time MT, depicted in Fig. 5-14, similarly show a stronger influence of the network topology on the detector performance. The mean detection run time on the

abscissa is referred to its mean value – 74.3 ms for the 4-dimensional search space and 899 ms for the 2-dimensional search space– to allow a comparison between the search space dimensions in one graph.

Focusing on the results of the 4-dimensional search space first, the mode of MT_{OC} occurs for a detection run time of 29 ms – or 0.39 pu – and has right side skewed behaviour which is caused by a small number of outage combinations with higher detection run times. MT_{LC} has its mode at a detection run time of 74 ms – or 0.99 pu. Its sharp and nearly symmetrical shape indicates only a minor influence of the load flow situation on the detection run time. The evaluations for the 2-dimensional search space have a much flatter frequency profile for both MT_{OC} and MT_{LC} which indicates a greater scattering of the results. However, the principle shape of the frequency profile is comparable between 2- and 4-dimensional search spaces. These observations match with the conclusions drawn from evaluations of the correct detection ratio.

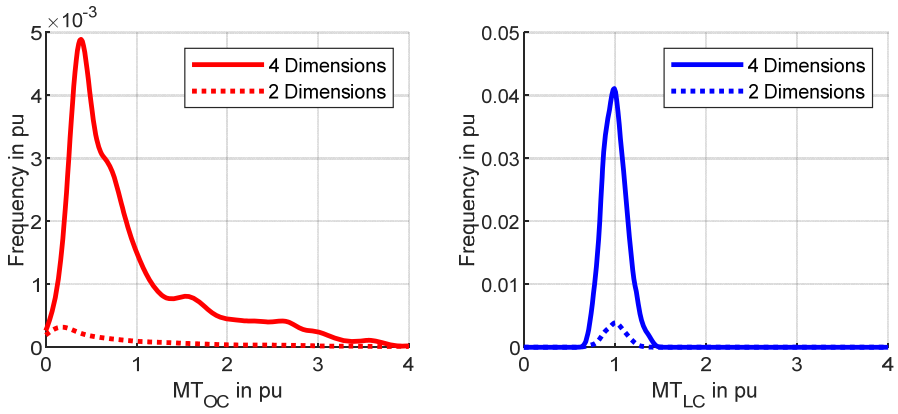

Fig. 5-14 Frequency of the detection run time estimated using KDE. The detection run time is referred to its mean value to allow a comparison between 2- and 4-dimensional search spaces.

The main parameters of the result evaluation are summarized in Table 5-5. Comparing the mean correct detection ratio with the correct detection ratio corresponding to the mode, it becomes obvious that the resulting frequencies are left skewed independently of the search space dimension. The mean detection run time is right skewed for the outage-based interpretation MT_{OC}, whereby the 2-dimensional application has a higher skewness. Summarizing the skewness, it shows that the expectable correct detection ratio is higher than the mean value of the correct detection ratio of the simulation results and has a shorter detection run time.

Comparing the results for 2- and 4-dimensional search spaces shows generally a slightly higher detection ratio for the 2-dimensional search space. The slight increase in the detection ratio comes at the cost of a significant increase in the detection run time. Both effects are explained as follows. An increase in the search space dimensions allows the algorithm to check more branch combinations at each iteration, thus reducing detection run time. However, the increase in the dimension also leads to an increased probability of loops in the selected candidate branches, including the actual tripped branches causing wrong detections.

Table 5-5 Correct detection ratio and detection run time for HPN based algorithm with 2- and 4-dimensional search spaces

		4-dimensional search space		2-dimensional search space	
		OC	LC	OC	LC
DR in pu	Worst	0.257	0.787	0.193	0.845
	Mean	0.944		0.969	
	Best	1.0	0.975	1.0	0.998
	Mode	0.979	0.962	0.984	0.993
MT in ms	Minimum	7.7	52.1	7.0	622.0
	Mean	74.5		899.1	
	Maximum	398.6	105.0	6771.9	1186.9
	Mode	29.0	74.0	155.0	905.0

5.5.1.3 Evaluation of three-branch outages

Based on the results of the double branch outage detection, the original load case as well as the load cases corresponding to the worst, closest to the mean and best load DR_{LC}, are selected to test the PSO and HPN based algorithms on the detection of three branch outages. The parametrisation of the PSO has do be expanded to 6 dimensions, whereby HPN's parameters are unchanged to the comparison of two-branch outages discussed in chapter 5.5.1. Only the original load case and load cases resulting in the worst, mean and best detection ratio for a double branch outage are evaluated. This reduction in evaluated cases is necessary to limit the run time of the simulation to a reasonable time span. In Table 5-6 the mean detection ratio and detection time are stated.

Table 5-6 Correct detection ratio and detection run time for the outage of three branches

		PSO		HPN	
		2 branches out	3 branches out	2 branches out	3 branches out
DR_{LC} in pu	Worst	0.762	0.363	0.787	0.959
	Mean	0.936	0.554	0.944	0.983
	Best	0.991	0.699	0.975	0.981
	Original	0.945	0.582	0.944	0.938
MT_{LC} in ms	Worst	603.9	1822	52.1	923
	Mean	277.6	1525	68.6	900
	Best	163.9	1282	105.0	912
	Original	316.0	1467	59.2	1022

The results for the outage of three branches reflect the basic sensitivities of PSO and HPN in terms of dimension. The PSO results worsen significantly for the detection ratio and detection time with the necessary expansion to a 6-dimensional search space. The distribution of the detection ratio has the same pattern as for the double branch outage, what indicates a rather direct influence of the pre-contingency load flow on the performance.

In comparison, the detection ratio using HPN actually increases. The reason therefore is, that the number of maximal detectable branches and actually tripped branches differ less. Therefore, the possibility of combinations that lead to an optimal minimum of the objective function not linked to the branches tripped decreases and the detection ratio increases. The distribution of the detection ratio is not linked to the results of the double branch outages. This indicates again that the actual pre-contingency load flow has smaller influence on the algorithm's performance than the topology.

5.5.2 Vulnerability on Reduction of Monitored Nodes

A reduction in the number of monitored nodes decreases the input information of the algorithms. In the following the PSO and HPN detection performance is evaluated based on node sets with increasing number of monitored nodes. The monitored nodes in dependency of the number of monitored nodes are given in chapter 5.2 Fig. 5-2. The data set of node voltage angle changes is based on DC load flow calculations and are the same 1000 random load flow cases as already used in the previous chapters.

The results depicted in Fig. 5-15 show a matching behaviour of PSO and HPN with a two-dimensional search space. These variants are able to detect a maximum number of 2 tripped branches. Further, an increase in the search space dimension leads to a higher decreasing effects in the detection ratio based with reduced monitored nodes due to the increased possibility of a meshed structure of the candidate branches used for the optimization. The evaluation for increased search space dimension is only conducted for HPN, since the results of PSO with higher dimensional search spaces are already proved to be unusable in chapter 5.5.1

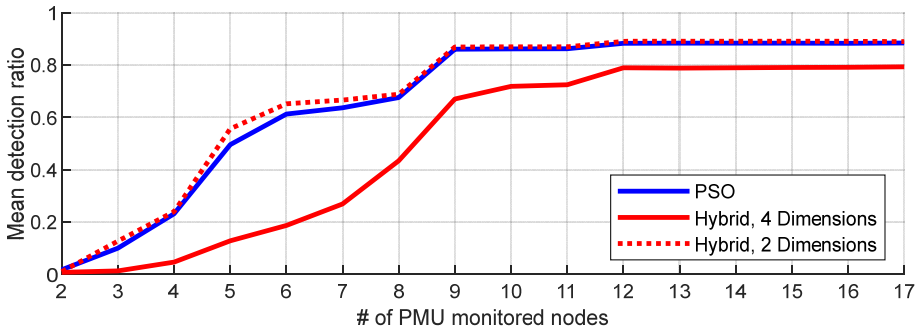

Fig. 5-15 HPN's detection ratio for a double branch outage with reduced set of monitored nodes

The difference in the detection ratio compared to the base cases with all nodes monitored is shown in Fig. 5-16. Due to the higher detection ratio in the base case for the two-dimensional search space, the difference in the results for search space dimensions of 2 and 4 are reduced.

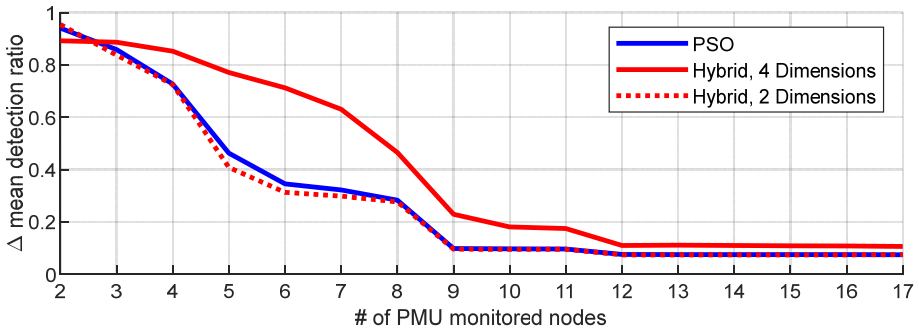

Fig. 5-16 Difference of the achieved detection ratio for reduced set of nodes to the base case with all nodes monitored for 2- and 4-dimensional search space

5.5.3 Summary on the Comparative Evaluation on Linearized DC-Load Flow Simulation

From the compared optimizers, the proposed HPN algorithm is best suited to solve the detection problem. It has a reasonable small runtime and the best mean detection ratio. Further, it has the advantage, that the limitation of the search space is known beforehand. It is also more robust to the pre-contingency load flow and the search space dimension compared to the PSO based detection algorithm.

Focusing on the vulnerability to a reduction of monitored nodes, it can be seen, that the main factor of the vulnerability is the actual dimension of the search space and thereby the maximal detectable tripped branches. The detection ratios of PSO and HPN are affected similarly.

Another reason to prefer the HPN over the PSO based algorithm is the mean value of necessary reinitializations. The mean number of the outer iterations is 17.52 for the PSO based algorithm and 1.008 for the HPN based algorithm.

5.6 Evaluation on Dynamic RMS Simulations

The algorithms' real-world applicability is evaluated by dynamic simulations of the Nordic-32 test system [88] taking oscillations and control actions into account. The angle changes are derived from a dynamic simulation performed with *DigSilent PowerFactory* [91]. Fig. 5-17 shows the test process from the dynamic simulation to the actual detector implemented as MATLAB® script.

The PMU data is the detector's measurement input data stream. The detector applies simple data pre-processing, such as a low pass filter and referencing the measured voltage angles to the reference bus. The detection algorithm is started manually after the outage occurs and is executed repeatedly for $10\ \mathrm{s}$. The start can be automated, e. g. by applying edge detection algorithms as suggested in [19]. However, this falls outside the focus of this work. The change in the node voltage angle is calculated with respect to fixed reference values which are measured $10\ \mathrm{s}$ before the contingency event. Oscillations triggered

by the branch tripping and linearization errors of the objective function can cause different detection results for the individual detection runs. Therefore, the output of the detection process is the branch or branch combination which has the highest overall appearance in the results of the detection runs within the runtime window of $10\ \mathrm{s}$. Detection runs without convergence of the optimizer are included as empty results for the calculation of the appearance. To increase the reliability of the detection, a branch is only marked as tripped if a minimum detection threshold ξ, e.g., $0.4\ \mathrm{pu}$ appearance of all detection runs including empty results – is exceeded. The effects and interpretation of this threshold value are discussed in the following.

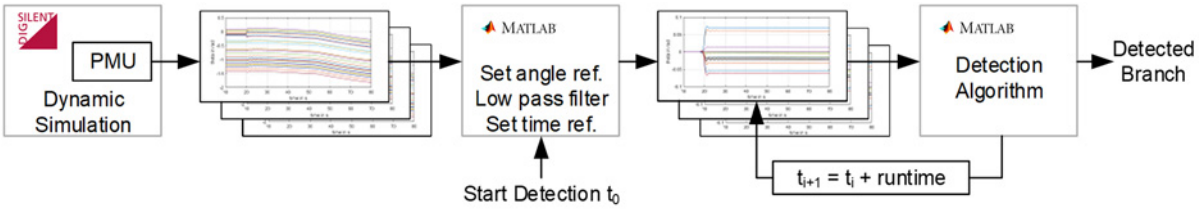

Fig. 5-17 Test process of the detection algorithms with dynamic simulation data

The function diagram of the implemented PMU model is shown in Fig. F-1. The available input is the frequency in pu as well as the sine and cosine of the angle difference $\Delta\vartheta$ between the slack node and the PMU monitored node. The value of $\Delta\vartheta$ in radiant and its sign are calculated from the sine and cosine information. The frequency deviation from the nominal value is multiplied with 2π and integrated to calculate the frequency depending angle drift of the reference node to the fictive global angle reference. The unrestrained node voltage angle of the measured node is derived from the sum of $\Delta\vartheta$ and angle difference of the reference node to the global angle reference. The result is processed further in the portion marked in red to limit the angle to a range between -π and π.

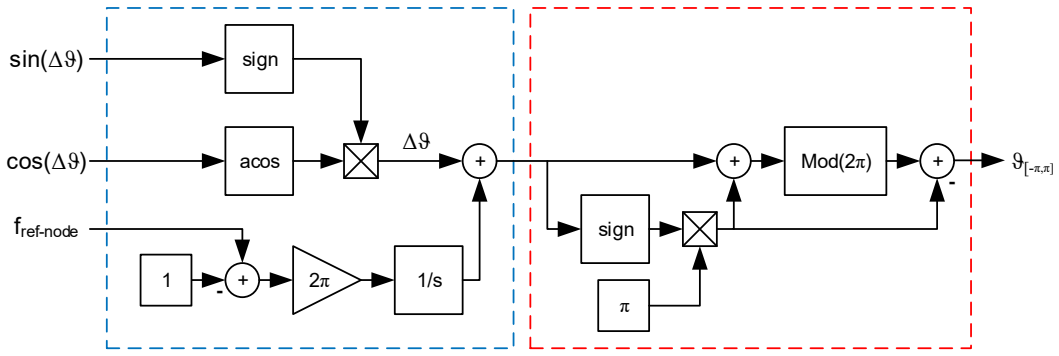

Fig. 5-18 PMU measured node voltage angle model

Example graphs of the output of the PMU and intermediated steps of the data processing are shown in Appendix F.

Based on the evaluation results of the linearized data, the focus of the following is set on the HPN based algorithm. Results for the PSO based detection algorithm are briefly stated in the appendix E.

Due to the small number of necessary outer iterations observed in the evaluation of the linearized data, the HPN algorithm is stripped of its outer loop. Instead of reinitialization of its PSO part, the output is

marked as not valid, if the maximum number of iterations is reached. The flow chart of the adjusted HPN algorithm is depicted in Fig. 5-19.

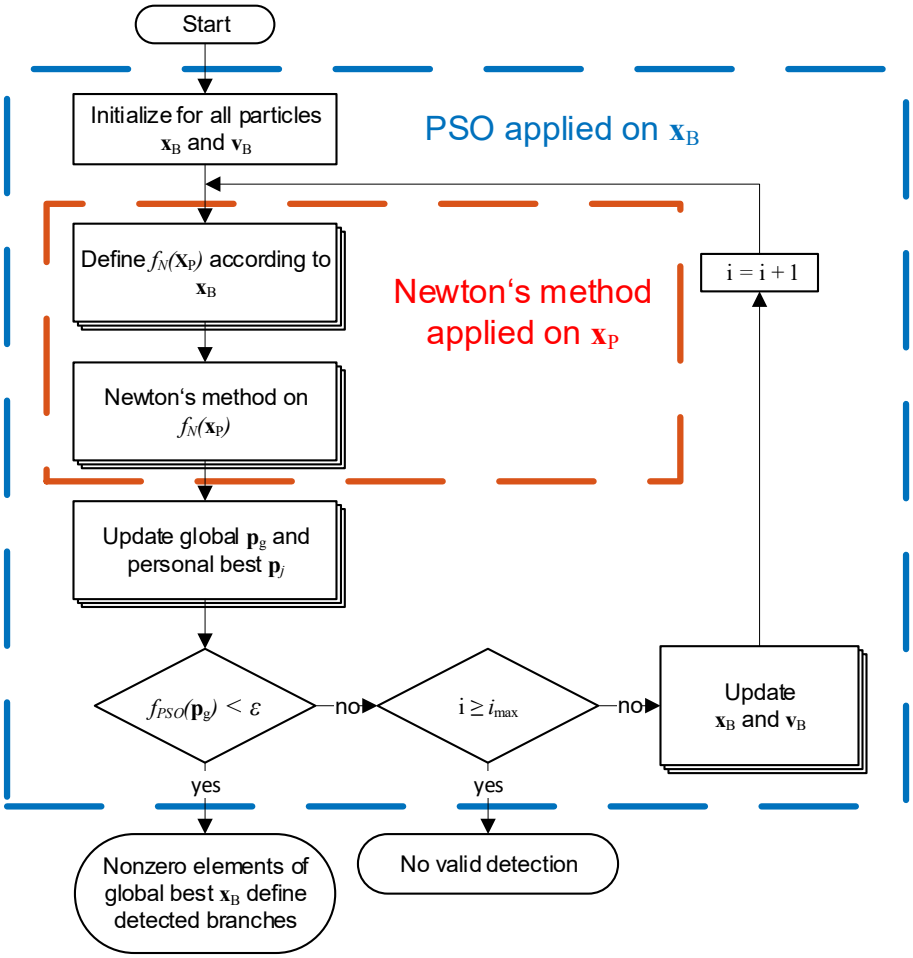

Fig. 5-19 Flow chart of the final HPN based algorithm

The following evaluation is separated into considerations for single branch outages focusing on the detection performance for reduced monitored nodes and considerations for double branch outages. Furthermore, for the single branch outages, a comparison of the detector's detection ratio with the results for an analytical method based on [19], [20] is added. The analytical method does not use a validation check based on a maximum distance criterion.

The optimizer's DC load flow model network representation leads to an immanent linearization error. The optimizer reacts to this by adding small unnecessary power injections at terminal nodes of branches not tripped, consequently causing more non-zero elements to define the detected branches. This effect is avoided by implementing a minimum value for the power injections to be considered. Since their actual values depend on the pre-contingency load flow, the minimum value is referenced to the maximum power injection of the optimizer output. In the following, a cut off ratio of 0.2 pu is used as the referenced minimum power injection value. Due to this, the detection algorithm only considers power injections higher than 0.2 times the maximum power injection for the output selection of the tripped branches.

Additionally, the linearization errors affect the selection of a sensible ε value for the stopping condition. For the following evaluations, ε values of 0.005 rad and 0.02 rad are implemented. However, an optimal

selection of the value ε also depends on the chosen search space dimension and the network topology. Therefore, the search space dimensions with values of 3 and 4 are evaluated.

Table 5-7 summarizes the different parameter sets of the HPN evaluated in the following.

Table 5-7 Optimizer parametrization used for the evaluation of dynamic data

w	c_1	c_2	search space dimension	ε	cut off ratio	max iterations	#particles
1 … 0.3	1.05	1.05	3	0.005	0.2	1000	30
1 … 0.3	1.05	1.05	3	0.02	0.2	1000	30
1 … 0.3	1.05	1.05	4	0.005	0.2	1000	40
1 … 0.3	1.05	1.05	4	0.02	0.2	1000	40

The set of branches and PMU monitored nodes used for the evaluations are provided in chapter 5.2.

5.6.1 Single Branch Outage

The generation and load parameters remain unchanged for the simulation of the single branch outages from the original data from [88]. The monitored nodes in dependency of the number of monitored nodes are given in chapter 5.2 Fig. 5-2. The branch number 21 – the line connecting nodes 4011 and 4021 – is additionally excluded from E, since its outage leads to a voltage instability followed by a loss of synchronization of the generators in the central and south parts of the grid.

Fig. 5-20 shows the correct detection ratio over the number PMU monitored nodes and for different HPN parametrization. The detection threshold ξ in the output appearance for a valid detection result is set to 0.4 pu. The graphs indicate a higher robustness against missing node information with lower search space dimensions, which is reasonable in view of reduced probability of loop structures in the selected candidate branches. The chosen value for ε has only a minor influence on the detection ratio.

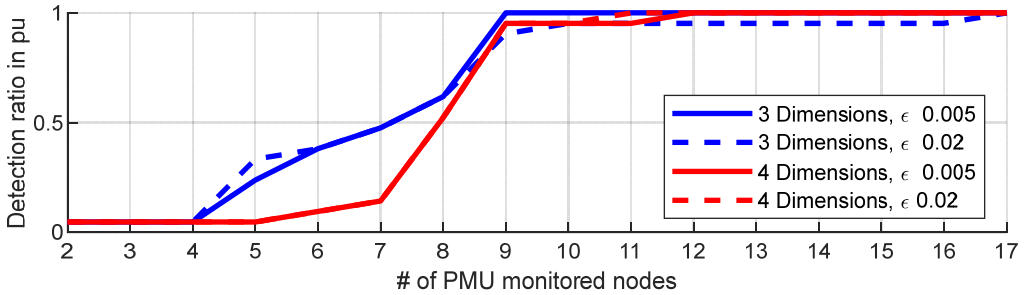

Fig. 5-20 Detection ratio for reduced number PMU monitored nodes for different parametrization and $\xi = 0.4$ pu

The influence of the threshold ξ on the correct detection is depicted in Fig. 5-21, whereby the HPN output data for a search space dimension of 3 and an ε of 0.005 rad is selected for representation. The detection results of an analytical detection algorithm similar to [19], [20] are included for comparison in the figure. However, the detection performance of the analytical algorithm might be overrated, since no validation check as described in [19] and no threshold ξ on the appearance ratio as for the HPN are included. Due to the missing thresholds, the equivalent in the HPN data for a comparison is the green graph for a

$\xi = 0$ pu. Only correct or wrong results exist for a detection threshold of $\xi = 0$ pu. These results are linked to the element with the highest absolute appearance in the detector output stream without any threshold and reflect the maximal reachable ratios. A comparison of these two graphs shows that the HPN performance is equal or slightly better in means of average detection ratio for 5 or more PMU monitored nodes.

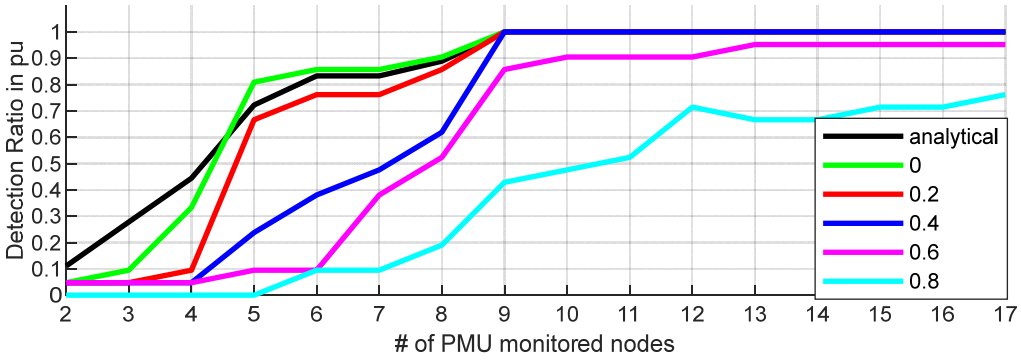

Fig. 5-21 Detection ratio for reduced number of PMU monitored nodes for different ξ values and an HPN parametrization with search dimension 4 and ε of 0.005 rad

However, for $\xi = 0$ pu a single detected element would be interpreted as the solution if it is the only non-empty detection output. With increasing detection threshold values, the detection results become more and more reliable. The decreasing detection ratio with higher detection threshold values is caused by increasing numbers of no-result outputs of the detector. Wrong detections definitely decrease similarly to increasing detection thresholds.

The detection run time of the HPN algorithm naturally depends on the available node information, the search space dimension and the chosen ε, whereby these factors are listed according to their severances. Due to the wide range in the detection run time starting from around 350 ms for 2 monitored nodes and going below 5 ms for 17 monitored nodes, a graphical presentation is set aside. However, the detection run time is well below 50 ms for the numbers of monitored nodes enabling reasonably good detection ratios. This short run times allow enough optimization runs in the 10 s detection window to have a solid decision base.

5.6.2 Double Branch Outage

The loading of the used Nordic-32-Bus system is scaled down to 70 % of the original load data from [88] to enable a stable post contingency state of the double branch outages. However, some outage combinations still have no stable solution – mainly combinations including branch 21. These instable outage combinations and outage combinations leading to the islanding of network parts are not included in the results. This leaves a set of 226 simulated branch outages defining the node voltage angle data for the evaluation of the detection algorithm.

Fig. 5-22 shows the correct detection results on dynamic data for an HPN parametrization with a search space dimension of 4 and an ε of 0.005 rad. All 17 400-kV-nodes are considered as PMU monitored and

the detection threshold ξ is set to 0.5 pu. The green squares indicate a correct detection of the outage combination – the correct combination has an appearance in the output data of the 10 s detection window higher than ξ. The red squares indicate a wrong detection – a wrong output combination has an appearance higher than ξ. The blue squares indicate no detection result – neither a correct nor a wrong combination has an appearance higher than ξ. The black squares reference branch outages either resulting in the islanding of network parts or causing instabilities. The wrong detections are concentrated on combinations including the branches 30, 33 and 48. This is caused for the branches 30 and 33 by their topology-based probability to be the lowest impedance branch of a loop formed by the optimizer's candidate branches and the higher likeliness of wrong detection linked to that. The tripping of branch 48 leads to strong oscillations of the generators $g17$ and $g18$ and therefore causes the wrong detection results.

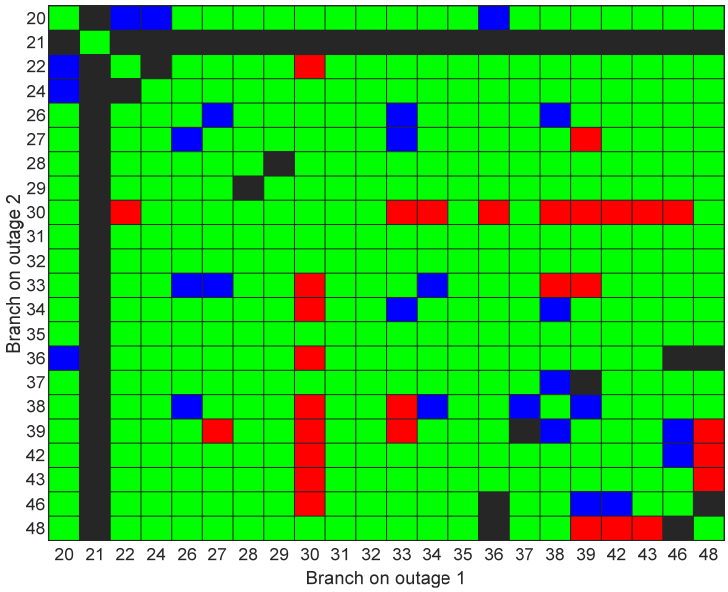

Fig. 5-22 Detection result for a search space dimension of 4, ε *of* 0.005 pu, $\xi = 0.5$ pu *and* 17 *PMU monitored nodes. Green correct detection, red wrong detection, blue no detection, black not evaluated*

The influence of the chosen value of ξ on the overall detection ratio of double branch outages for different values of ε and a search space dimension of 4 are given in Fig. 5-23. The graphs depict the ratios of correct, wrong and no detection for HPN as a function of the detection threshold ξ and 17 PMU monitored nodes. The maximum correct detection ratio is 0.91 pu. The correct detection ratio slowly decreases and forms a knee point at $\xi = 0.6$ pu. The ratio of no results becomes dominant while the correct and wrong detection ratio decreases to 0 with further increasing threshold values, whereby the smaller ε of 0.005 pu enables higher correct detection ratios.

The comparison to the reference detection ratio obtained from the evaluations of the linearized load flow calculations show that the algorithm is performing similarly well on the dynamic data till the knee point at $\xi = 0.6$ pu.

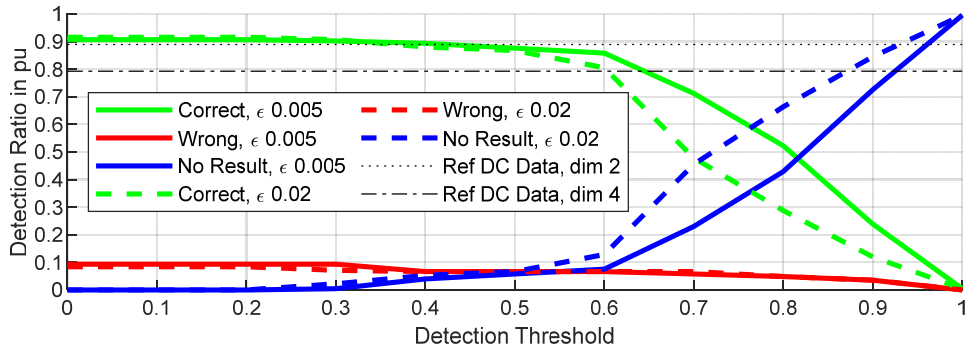

Fig. 5-23 Dependency on threshold for HPN with a search space dimension of 4 *on dynamic simulation data for* 17 *PMU monitored nodes*

In Fig. 5-24 the dependency of the HPN's detection ratio on the number of PMU monitored nodes is depicted for a parametrization with 4-dimensional search space, an ε of 0.005 pu and a threshold of 0.5 pu. The general dependency of the correct detection ratio behaves similarly to correct detection ratio for the single branch outage – Fig. E-1. The comparison with the reference detection ratios obtained from the evaluation of the linearized load flow data (Ref DC Data) shows that with higher numbers of monitored nodes, the influence of the linearization error of the optimizer's underlying model decreases. Furthermore, the graphs highlight that the detector has a constant low ratio in explicitly wrong detections.

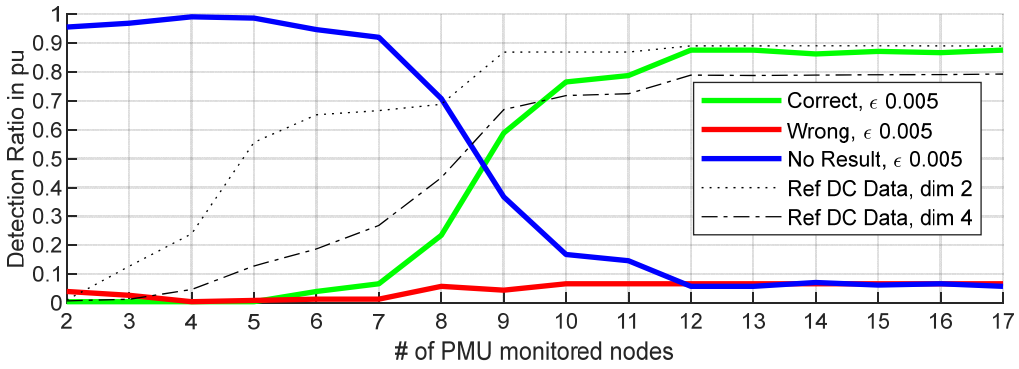

Fig. 5-24 Detection ratio of HPN with a search space dimension of 4*,* ε *of* 0.005 pu*,* $\xi = 0.5$ pu *for dynamic simulation data*

The graphs in Fig. 5-25 show the dependency of the correct detection ratio on the chosen threshold and different parametrizations of the HPN. The value of ε is set to 0.005 pu and the search space dimension is 3 and 4. The black dotted and dash-dotted lines are the detection ratios obtained from the linearized load flow evaluations serve as reference. Comparing the detection ratios of the different search space dimensions and thresholds, it becomes notable that with smaller threshold values – 0 pu and 0.4 pu in the graph – and more than 9 observed nodes, a higher search space dimension yields a better detection ratio. This behaviour contradicts the expectation based on the results from the single branch evaluations. This is plausible by considering that the optimizer is able to compensate the linearization error better in a higher dimensional search space leading to a higher convergence rate and fewer empty results in the detection algorithm. With increasing threshold values, the detection ratio for the smaller search space dimension is better, since the actually detected branches for each individual detection run are more stable. This is caused by the lower probability of forming loops in the candidate branches. The same holds true for the detection ratio for numbers of observed nodes below 8. The probability of candidate

branch loops dominates the decreasing effect for small numbers of observed nodes and higher threshold values. For lower threshold values, the linearization error has a stronger albeit decreasing impact for higher numbers of observed nodes.

The detection runtime for the double branch outages behave similarly to the detection runtime of the single branch outages. This means that enough detection runs are conducted in the $10\,\mathrm{s}$ detection window to have a solid decision base.

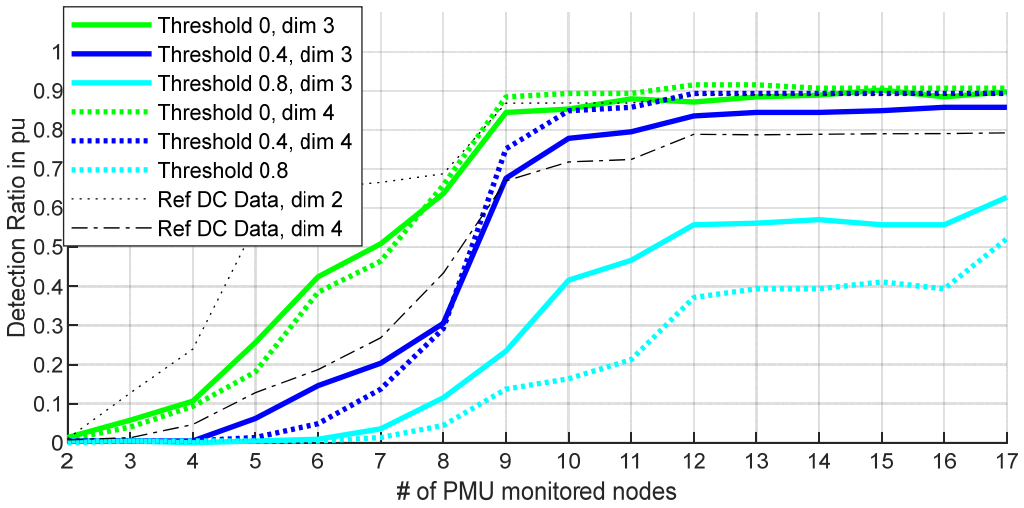

Fig. 5-25 Referenced detection ratio of HPN optimizer for reduced number PMU monitored nodes on dynamic simulation data with different thresholds

5.7 Conclusion on Emergency Detection

In this chapter, three optimization-based approaches for the detection of tripped branches are presented. All of them require only the node voltage angle information provided from PMU measurements as dynamic input and the pre-contingency network topology as static information. The discussed detection algorithms are able to detect multi-branch outages without extensive pre-calculations of possible outage combinations or a predefinition of the expected number of tripped branches.

The comparative evaluation of the three algorithms – based on Newton's method, PSO and a hybrid optimizer combining PSO and Newton's method (HPN) – on linearized load flow data already indicates, that only PSO and HPN are applicable. Focusing on the main performance parameters detection ratio and detection run time, HPN performs better and more robustly than PSO. The reason for this is, that HPN selects the candidate branches using PSO and finds the minimum of the corresponding objective function with Newton's method. Due to this separation of tasks, the major drawbacks of PSO – a rather long detection time and necessary reinitializations – and Newton's algorithm – not applicable on meshed networks without iterative extension – are overcome. The vulnerability of PSO and HPN to reduced monitored nodes are nearly the same for the evaluation of the linearized load cases.

The detection performance of the HPN based algorithm is robust against the loss of node information as long as a certain number of measured nodes are not undershot. Focusing on the basic parametrization, the most critical parameter is the selection of the search space dimension, since it has a negative impact on the detection ratio if chosen to be too small or too large, depending on the network topology and the chosen detection threshold. The choice of the space dimension should consider the maximum sensible number of tripped branches – taking into account general network stability – as well as the linearization error of the underlying model. However, the results show that as long as the linearization assumptions are mostly met, the detection ratios achieved on the data created with the described dynamic nonlinear and stationary linear simulation models are comparable.

The number of explicitly wrong results over the whole range of evaluated threshold values and number of monitored nodes is small for the proposed algorithm. It is therefore a possible tool for future back-up monitoring applications and standalone emergency control actions of decentral resources. The next working steps are to test the detection algorithm on linearized and static AC load flow data of large systems such as the ENTSO-E network and on defining triggers for emergency control actions based on the detection output in dynamic simulations.

6 Emergency Control of Embedded HVDC Links

The outage of network elements can lead to unforeseen critical load flow situations and the need to react accurately to them. The reaction of the responsible network operator can consist of measures in the generation and load distribution, e. g. activation of redispatch power plants or demand side management capacities, and the utilization of the load flow controlling capacities of PFCs. Focusing on the PFCs, their normal operation setpoints are changed in accordance to the contingency causing the critical load flow situation. The emergency control builds on an accurate outage detection, e. g. as discussed in chapter 5, since the contingency defines the necessary PFCs' control reaction.

Embedded VSC-HVDC links offer a high potential for stabilizing a network under strained conditions due to their independent active and reactive power controllability, the additional parallel power transfer path and the in general high rated power of their converters. Thus, these HVDC link will become an essential power flow controlling asset in future grids, especially with facilities already under operation and several more under construction or undergoing their approval process.

The following considerations therefore focus on the control of them under stressed network situations. In contrast to most of the published works discussed in chapter 1.6.3, the decentralized control schemes developed in this chapter shall be able to consider branch loading and long-term voltage stability issues without the necessity of time-consuming optimal power flow calculations or additional extensive data systems and measurement equipment.

This chapter is split into two parts. A review on existing control strategies and a novel advanced control strategy suitable for radial network topologies is discussed in the first subchapter. This includes a static simulation of the existing control strategies as well as a comparison between them and the novel strategy in dynamic RMS simulations of several contingency events. The second subchapter is dedicated to complex network topologies with multiple embedded HVDC links and a control strategy using PMU measurements, a linearized model of the network and a decentralized outage detection based on chapter 5.

6.1 Simple Topology

Previous work on control strategies of embedded VSC-HVDC links [41] focused on deriving active and reactive power setpoints to obtain maximum combined AC-DC power transfer or investigated the improvement by standard control concepts [40]. The comparison of the discussed strategies – maximum active power transfer via the HVDC link, only voltage control on both HVDC terminals and a node voltage angle dependent active and reactive power setpoint – is based on stationary evaluations of a simple network topology, whereby voltage angle dependent control was further successfully applied in a

dynamic simulation of the Nordic-32-Bus system [42]. However, reviewing these strategies taking the loading of the parallel AC lines into account reveals the need of an advanced control strategy to not only avoid voltage collapse but also cascaded line tripping [76]. The following is based on the authors publication [76].

6.1.1 Review on Control Strategies

The following review of emergency control strategies, the introduced advanced emergency control strategy and its implementation in a dynamic simulation are the author's original work and is published in [76]. All values given are in pu, if not stated otherwise. The per unit base values are $S_\mathrm{B} = 100\ \mathrm{MVA}$ and the nominal voltage of the network or network part.

As shown in [41], cos(θ)-control ensures the maximum stationary loading capacity in a simple topology – Fig. 6-1.

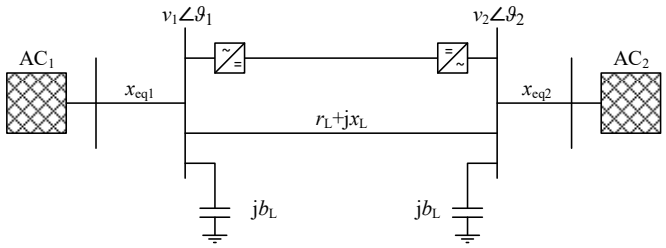

Fig. 6-1 Parallel DC/AC connection of two AC networks for reviewing HVDC link control strategies

The active power of the converter supplying power to the AC grid is therefore set as follows

$$p_\mathrm{DC} = i_\mathrm{conv,max} \cdot v_\mathrm{conv,max} \cdot \sin(\vartheta_\mathrm{remote} - \vartheta_\mathrm{local}) \qquad (6\text{-}1)$$

In the case of power transfer from AC1 to AC2, the right convert is supplying power to the AC grid and consequently the index remote refers to bus 1 and local to bus 2. The remaining capacity of the converter is utilized to control the AC-voltage of the terminal with a maximum reactive power of

$$q_\mathrm{DC} = i_\mathrm{conv,max} \cdot v_\mathrm{conv,max} \cdot \cos(\vartheta_\mathrm{remote} - \vartheta_\mathrm{local}) \qquad (6\text{-}2)$$

In the following the term base is used to describe the scenario without VSC-HVDC link. The term P_{max}-control is used, if the whole capacity of the VSC-HVDC link converters is utilized to transport active power. StatCom-control refers to operation of the VSC-HVDC link in AC voltage control on both terminals without any active power transfer. If the active and reactive power is set according to equations (6-1) and (6-2), the term cos(θ)-control is used.

Besides maximizing the loading capacity and the long-term voltage stability of the embedded system, a certain unloading of the AC lines is a desirable control goal for a stressed system to keep (n-x)-security. Depending on the actual terminal voltage, the most effective unloading is achieved by P_{max}-control at close-to-nominal voltage levels and cos(θ)-control at higher voltage differences between the terminals. The reason for this is the voltage difference causing reactive power transfer on the AC line.

The effects of the three mentioned control strategies on loading capacity and the AC-line currents are demonstrated in the following based on a steady state simulation of the topology depicted in Fig. 6-1. The AC1-network is acting as a slack node, the AC2-network as a simple active power load without any voltage control. The AC system parameters in pu are $x_{eq1} = 0.0014$, $x_{eq2} = 0.0007$, $r_L = 0.0006$, $x_L = 0.0046$, $b_L = 0.0783$, with a base voltage of $V_B = 380\ \mathrm{kV}$. The thermal current limit of the AC line is $33.2\ \mathrm{pu}$. The rated power of the VSC-HVDC link is $6\ \mathrm{pu}$.

The results summarized in Fig. 6-2 and Table 6-1 show clearly the advantage of P_{max}-control in terms of AC unloading and of cos(θ)-control in terms of maximal loading capacity. The stated effectiveness based on the rated power of the VSC-HVDC link is depending on the actual AC network. The efficiency is the ratio of the change in load power before the limitation is reached and the rated converter power.

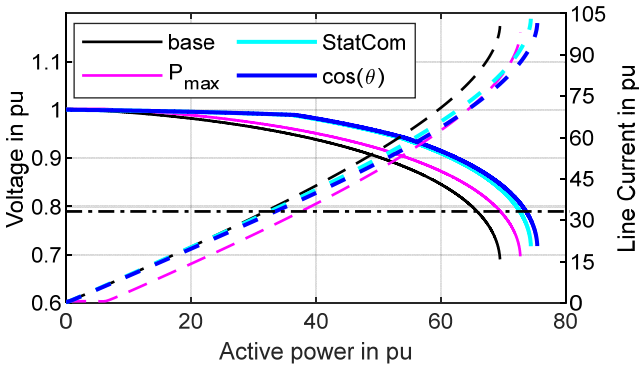

Fig. 6-2 PV curves and line current for different control strategies and base case without HVDC Link. The solid lines are the voltages of the load bus, the dashed lines are the overall currents of the parallel AC lines and the dash-dotted line is the AC current limit.

Table 6-1 Active load power corresponding to voltage stability and line current limits

Control strategy	Active load power, stability limit reached	Active load power, current limit reached	Efficiency increasing the current limit	Efficiency increasing the voltage stability
base case	69.31	31.83	---	---
P_{max}	72.56	37.49	0.94	0.54
StatCom	74.24	32.59	0.13	0.82
cos(θ)	75.27	33.51	0.28	0.99

6.1.2 Introduction of Improved Emergency Control Strategy

The goal of an automated emergency control strategy (ECS) is to increase the loading capacity and to limit the effects of a disturbance on the remaining AC system. With the results of the review available, a practical approach to this goal is to combine the P_{max}- and cos(θ)-controls, whereby a smooth transition between them has to be enabled based on measurable quantities. The obvious choice is the magnitude of the voltage of the converter's point of coupling (POC) v_{POC}. The gradual transition starts if v_{POC} drops under an upper voltage limit $v_{trans,up}$ and is finished if v_{POC} reaches a lower voltage limit $v_{trans,low}$. Consequently, the ECS has a voltage depending control behaviour, which can be split into operation schemes:

1) P_{prior}-scheme ($v_{POC} \geq v_{trans,up}$)
   In this operation scheme the target is to avoid overloading remaining AC lines after a line trip and in the allocation of converter capacity active power has priority. A PI-controller is keeping the node voltage angle difference between the converter terminals at pre-contingency value and is providing the set-point for the active power of the VSC-HVDC link. Remaining converter capacity is used to control the voltage at the terminal.

2) Transition phase ($v_{trans,up} > v_{POC} > v_{trans,low}$)
   With decreasing voltage magnitudes, the AC loading becomes more dependent on the reactive power and the maximum loading capacity becomes an additional issue. As a reaction to that, the active power limit of the controller is gradually reduced to the value stated in equation (6-1). Thus, the voltage controller can utilize more converter capacity.

3) cos(θ)-scheme ($v_{POC} \leq v_{trans,low}$)
   If the voltage at the POC drops below the lower voltage limit for the transition phase, the priority has to be fully set on the maximization of the loading capacity of the system. Therefore, the active and reactive powers are set to the values given by the equations (6-1) and (6-2).

The inclination of the limit curve k_{trans} is introduced to implement this operation behaviour in the control loop of a converter. k_{trans} calculates as follows and is limited to values between 0 and 1. Inherent to the limitation k_{trans} is constant *1* for $v_{POC} \geq v_{trans,up}$ and constant *0* for $v_{POC} \leq v_{trans,low}$.

$$k_{\mathrm{trans}} = \frac{v_{\mathrm{POC}} - v_{\mathrm{trans,low}}}{v_{\mathrm{trans,up}} - v_{\mathrm{trans,low}}}, k_{\mathrm{trans}} \in [0,1] \qquad (6\text{-}3)$$

With the active power limitation given as a function of k_{trans} the three described operation schemes are combined in one control path.

$$p_{\mathrm{DC,lim}} = v_{\mathrm{conv,AC}} \cdot i_{\mathrm{conv,max}} \cdot [k_{\mathrm{trans}} + (1 - k_{\mathrm{trans}}) \cdot \sin(\vartheta_{\mathrm{remote}} - \vartheta_{\mathrm{local}})] \qquad (6\text{-}4)$$

The additional PI controller for the active power setpoint and the equations defining the operation schemes are implemented in the outer control loop of the VSC, see Fig. 6-3. The basic control structure

depicted in [92, p. 222] is used as the basic control design. The additional parts are highlighted with colours.

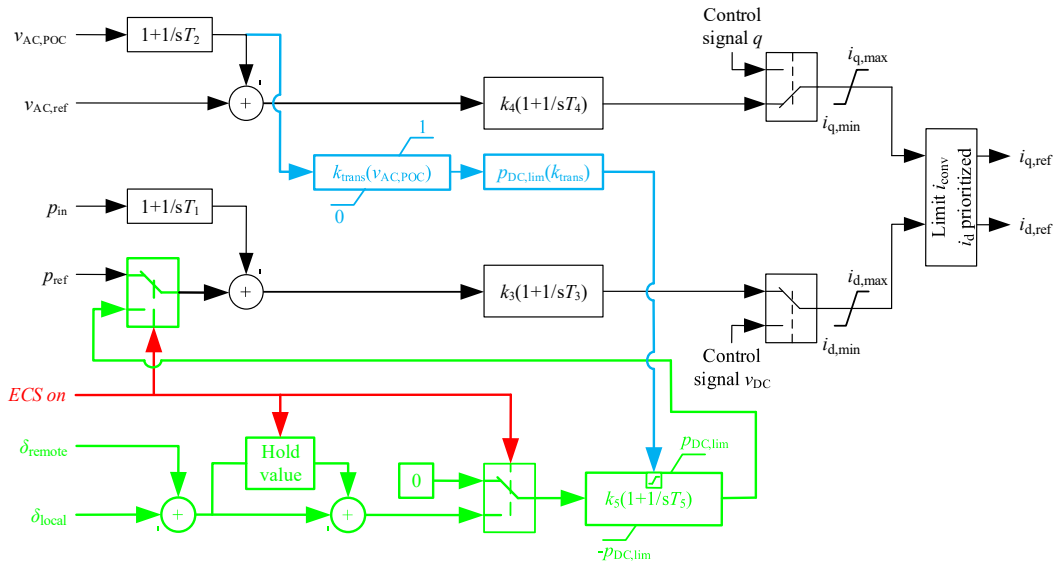

Fig. 6-3 Outer control loop of the VSC converter. Highlighted parts are the changes to the general control loop. The unchanged parallel paths for v_{DC}- and Q-control modes are only implied by their output signals.

The ECS is activated by the signal *ECS on*. The activation freezes the output of the hold block and enables the PI-controller in the voltage angle path and switches its output signal as the active power reference. The state variable of the PI-controller is initialized with p_{ref}, which guarantees a smooth transition between normal operation and the ECS of the converter. This initialization avoids disturbances in the system for unwanted emergency activations. If the q-axis current is in Q-control mode, the activation of the emergency control switches the control mode to voltage control. Further, the converter feeding active power to the AC network is set to active power control, the converter consuming active power from the AC network to DC voltage control.

6.1.3 Application in Demonstration Grid

The principal applicability and dynamic behaviour of the ECS controller is demonstrated in the small demonstration grid shown in Fig. 6-4. The simulations are accomplished in the software DigSilent PowerFactory [91].

The demonstration grid represents a transmission corridor connecting a stiff grid with a remote grid area. The main part of the transmission corridor consists of three 220 kV overhead lines (OHL1 to OHL3) with a length of 150 km parallel to a VSC-HVDC link with converter rating of 600 MVA. The equivalent generator has a rated power of 500 MVA with an inertia constant H of 7 s. For the demonstration of the ECS the equivalent generator does not contribute to the voltage control of the load bus. The system is loaded by two active power loads, modelled with constant impedance characteristic to introduce voltage dependent behaviour. The on-load tap changers of the load transformers enable a simple load recovery for long term voltage stability studies. The main network parameters are given in Table 6-2.

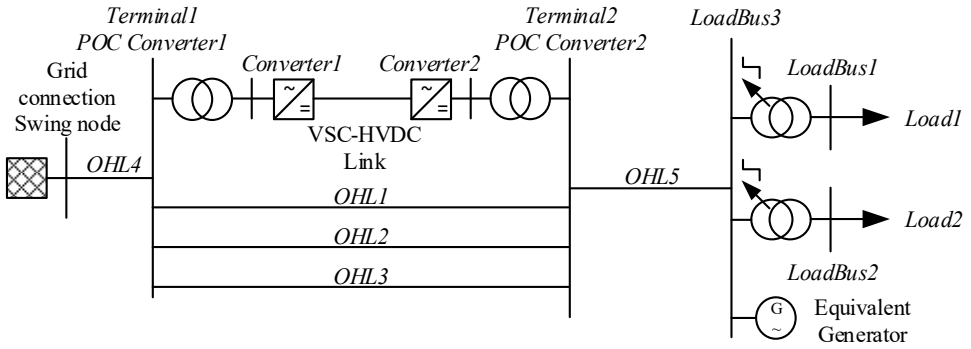

Fig. 6-4 Demonstration grid. For the derivation of the PV-curves the equivalent generator is disconnected and the on-load tap changer is deactivated.

Table 6-2 Main network parameters demonstration grid

	X	R	C	
	Ω	Ω	µF	
OHL1 -3	46.5	9	1.77	
OHL4	2.325	0.45	1.42	
OHL5	3.875	0.75	2.36	
	L	R	C	
	mH	Ω	µF	
DC Cable	38.2	1.5	1.5	
	S	V_p	V_s	u_k
	MVA	kV	kV	%
Converter Transformers	700	220	370	11
Load Transformers	1200	220	110	7.1
	S	V_{AC}	V_{DC}	x_k
	MVA	kV	kV	%
Converter	600	370	300	15

The parameters defining the active control scheme of the ECS – $v_{\text{trans,up}}$ and $v_{\text{trans,low}}$ – are set to 0.95 pu and 0.9 pu for the following simulations.

The first simulation determines the maximum loading capacity at *LoadBus3* by increasing the active power load at this busbar. The load is modelled as a resistive load directly connected to the *LoadBus3*. The equivalent generator, *Load1* and *Load2* are disconnected for this simulation. The resulting PV-curves, AC-line currents and the basic converter behaviour for ECS are shown in Fig. 6-5 to Fig. 6-7. The results confirm qualitatively the steady state simulation of chapter 6.1.1. The ECS reaches the same maximum loadability as the cos(θ)-control, but the loading of the parallel AC-lines is lower. The higher loading of the AC-lines of the ECS compared to the P_{max} control at lower load powers depend on the initial angle difference at activation of the ECS. For the simulation of the PV-curves, the initial load is 400 MW and active power of the VSC-HVDC link before activation of the ECS is 200 MW.

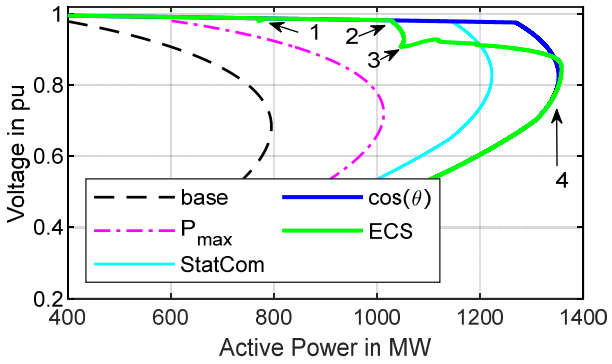

Fig. 6-5 PV curve of the demonstration network at LoadBus3 for the different converter control strategies and without VSC-HVDC link as base case for reference.

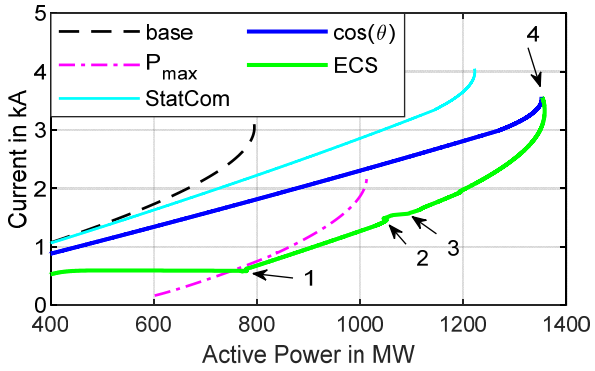

Fig. 6-6 Total current of the three AC-lines for the different converter control strategies and without VSC-HVDC link as base case for reference.

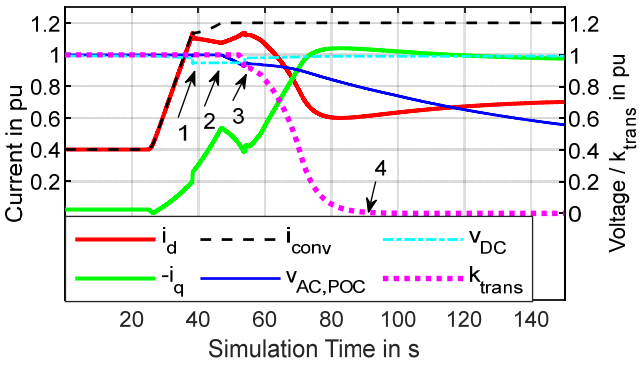

Fig. 6-7 d-axis, q-axis, converter current, ktrans, DC- and AC-voltage of the POC of Converter2 with active ECS during the simulation determining the PV-curve.

In Fig. 6-5 to Fig. 6-7 four moments associated with special critical control actions are marked for the ECS. At ①, *Converter1* – controlling the DC voltage of the VSC-HVDC link – reaches its maximum current of 1.2 pu and v_{DC} drops. *Converter2* reacts by limiting its d-axis current to stabilize v_{DC}. At ②, *Converter2* reaches its current limit too. Since it is still operated in the P_{prior}-scheme, the q-axis current is reduced with rising d-axis current. At ③, the voltage at the terminal of *Converter2* falls below $v_{trans,up}$ and the transition phase begins. With decreasing d-axis current, the DC voltage recovers and the DC voltage control is handled again by *Converter1*. At ④, the transition variable k_{trans} becomes 0 and the ECS behaves identically to cos(θ)-control. Note that the d- and q-axis current are used instead of active and reactive power in Fig. 6-7.

The following simulations of line tripping and generation loss are only performed for the cos(θ)-control and the ECS. For these simulations, the equivalent generator supplies active power without voltage control and the on-load tap changer of the load transformers are activated. The loads *Load1* and *Load2* act as simple impedance loads with unity power factor. The deactivated voltage control of the equivalent generator was chosen to focus on the differences between the compared control strategies of the VSC-HVDC link.

Fig. 6-8 shows the line current in *OHL1* for a line tripping sequence. The equivalent generator operates at 250 MW and the loads are set to 650 MW and 400 MW respectively. The VSC-HVDC is initially loaded with 200 MW, leaving 600 MW for the parallel AC system. Voltage control is done on both HVDC-terminals within the available converter capacity. At $t = 20$ s *OHL2* trips and at $t = 21$ s either the cos(θ)-control or the ECS is activated as a counter measurement to the line tripping. At $t = 35$ s *OHL3* trips as well. The lines are reconnected at $t = 50$ s and $t = 55$ s respectively.

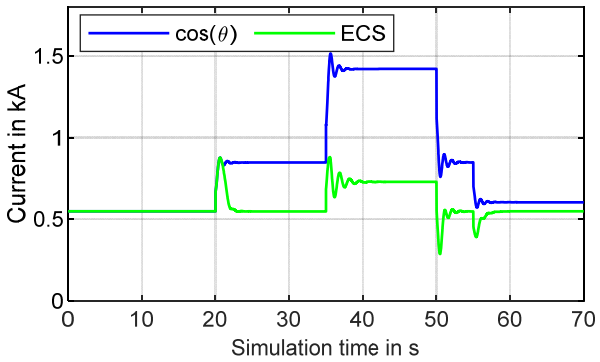

Fig. 6-8 Line current in OHL1 for disconnection and reconnection of the parallel lines OHL2 and OHL3.

The results for cos(θ)-control indicate that the current in the remaining line *OHL1* exceeds the rated current of 1.2 kA after the second line being disconnected. This would force *OHL1* to trip resulting in a network split. A similar sequence of events caused [34].

Using the ECS instead, the current limit of the remaining line *OHL1* is not violated. The ECS tries to control the active and reactive power at *Converter2* in such a way that the remaining AC lines keep their pre-fault loading. However, the rise in the AC line current after the tripping of *OHL3* is caused by the current limitation of *Converter1*. After the end of the disturbance, the AC system reaches its initial state again.

To test the reaction of cos(θ)-control and the ECS in case of loss of generation, the loads *Load1* and *Load2* are set to 650 MW and the equivalent generator feeds 450 MW into the system. The combined load at *LoadBus3* of 1300 MW is close to the maximum loading capacity - 1352 MW for cos(θ)-control and 1358 MW for the ECS respectively. The equivalent generator is disconnected at $t = 20$ s and as reaction either cos(θ)-control or ECS is activated at $t = 21$ s. As shown in Fig. 6-9, both control strategies reach a stable operation point after the load recovers. However, the ECS leads to less loading of the AC lines at a slightly lower terminal voltage.

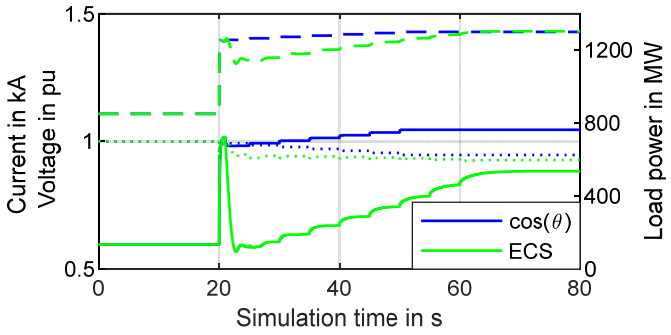

Fig. 6-9 Line current in OHL1 for disconnection and reconnection of the parallel lines OHL2 and OHL3. The continuous lines are the line currents in OHL1, the dashed lines are the load power and the pointed line is the voltage at Terminal2.

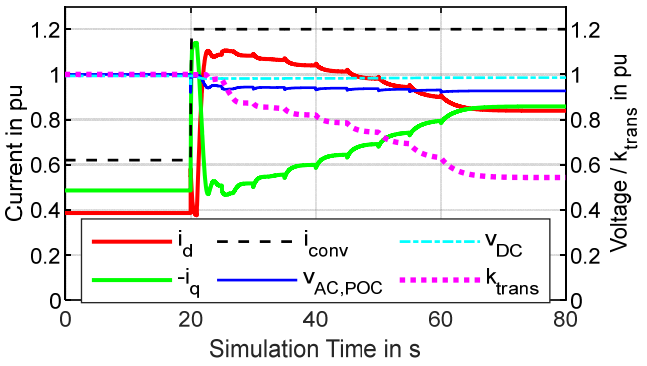

Fig. 6-10 d-axis, q-axis, converter current, ktrans, DC- and AC-voltage of the POC of Converter2 with active ECS for the simulation of loss of generation.

Fig. 6-10 shows the dynamic behaviour of some internal control signals of the ECS. The d-axis current rises with the activation of the ECS at $t = 21$ s, leading to decreasing voltage at the POC due to the reduced capacity used for voltage control. With the recovery of the load by the on-load tap changer, the rising currents in the AC lines lead to a further decrease in the voltage at the POC. According to the equations (6-3) and (6-4), the share of the converter capacity used for voltage control rises and the voltage at the POC and *LoadBus3* stabilizes.

6.1.4 Conclusion on the Emergency Control for Simple Topologies

The conducted simulations demonstrate the advantages and usability of the ECS in improving the voltage stability and support for the parallel AC system. The discussed scenarios show that the ECS improves the system reaction to disturbances. Compared to existing control strategies useable for emergency control, it performs better in terms of unloading the parallel AC-network and at least at the same level in terms of long-term voltage stability. The transferrable power of the test system is increased by the embedded VSC-HVDC link rated with 600 MVA by 557 MW with cos(θ)-control and 563 MW with the ECS respectively. A further advantage of the ECS is, that it does not disturb the system if activated accidentally.

6.2 Complex Topology with Multiple Device Control

The power flows in complex topologies cannot be sensibly reduced to a point to point transfer allowing a HVDC control strategy only based on local voltage measurements and the angle difference between the connection points, which can efficiently relieve overloaded branches and maintaining voltage stability after a contingency event. Further, it might become necessary to coordinate the control actions with other embedded HVDC links and PFCs.

Concepts for this control task range from the derivation of control setpoints by solving optimal power flows exemplary discussed in [1], [50], [51] to rule based methods [93] and the use of adaptive control approaches based multiagent systems [45]. Even if these concepts are not explicitly developed for embedded HVDC links, they can be adapted for them. The necessary calculation time of concepts using optimal power flows are critical since any fast control action after a contingency element should be activated close to real time. Therefore, generally only a given set of contingencies is considered for the optimal power flow, whereby a prioritising based on a risk assessment [74] can improve the concept. Rule based methods need to pre-generate the control rules depending on the topology, which might become time consuming considering multiple contingencies.

From these concepts, only the ones based on optimal power flow using AC-load flow calculations address the branch loading as well as the bus voltages. However, an integration in large networks and consideration of contingencies becomes computational heavy and the optimization might not converge. Other control concepts are solely developed to avoid voltage instabilities exemplarily using critical voltage sensitivities derived via the Jacobian matrix [47], hierarchical voltage control [48] or weighted voltage deviations of limited areas [49].

The following proposed decentral emergency control strategy focusing on network supporting operation of embedded HVDC links has the goal to combine the aspects of branch loading and voltage stability. The term “decentral” accounts in this case for the possibility to implement the control strategy at the converter controllers of the embedded HVDC links without the need of superior coordination from a control centre. However, a sensible network supporting control strategy still needs information about the system state. The proposed control strategy reduces this necessary information to a minimum and builds on the following information and data:

- Topology information (PTDF, LODF, branch impedances, etc.)
- WAMS data (node voltage)

The topology information only needs to be updated, if a scheduled change occurs thereby further reducing the need of fast information transmission. The only remaining time critical data is the synchronised measurements of the node voltages obtained from the WAMS. The node voltage information, separated in magnitude and angle, are further processed to derive the control signals and for the detection of tripped branches as discussed in chapter 5.

The proposed decentral control is placed as an additional control loop on top of the converters active power and voltage controller.

6.2.1 Active Power Control

The branch loading in electric networks is in general dominated by the active power transfer. Therefore, an effective relief of critical overloaded branches can be achieved by varying the active power setpoint of embedded HVDC links. The derivation of the control signals of the active power part require the calculation of the loading of the considered branches and the active power sensitivities of the embedded HVDC link on these branches. It is only necessary to consider the branches, which can be efficiently controlled by the embedded HVDC link. The selection of these branches is carried out as described in chapter 3.1. The branches are given by the set Γ. The loading LD of branch k connecting the nodes i and *j* calculates with neglection of the branch capacities as

$$LD_k = \frac{\left|\left(\frac{\underline{v}_i - \underline{v}_j}{\underline{z}_k}\right)\right|}{i_{k,max}} \cdot sign\left(\Re\left\{\frac{\underline{v}_i - \underline{v}_j}{\underline{z}_k}\right\}\right) \tag{6-5}$$

The active power sensitivity of the embedded HVDC link h on branch k is derived from the PTDF values linked to branch *k* and the nodes of the HVDC terminals m and n.

$$sens_{k,h} = PTDF_{k,m} - PTDF_{k,n} \tag{6-6}$$

To account to the correct sign convention used in the calculation of the PTDFs, the controller of the HVDC converter in node m has to be in active power control mode and the controller of the HVDC converter in node n in DC-voltage control mode. Further, a positive change in active power of corresponds to an additional power injection in node m.

The sensitivities only change with the topology. Therefore, it is sufficient to recalculate them only if the topology is updated or an outage is detected. In cases of topology update, the sensitivities calculate as given above, whereby for the outage of branches O the calculation changes to

$$psens_{k,h} = PTDF_{k,m} - PTDF_{k,n} + \mathbf{LODF}_{k,O} \cdot (\mathbf{PTDF}_{O,m} - \mathbf{PTDF}_{O,n}) \tag{6-7}$$

$psens_{k,h}$	…	sensitivity of branch k to active power change of HVDC link h
$\mathbf{LODF}_{k,O}$	…	multi branch LODF O to k
$\mathbf{PTDF}_{k,m}$	…	PTDF of node m on branch k
$\mathbf{PTDF}_{k,n}$	…	PTDF of node n on branch k
$\mathbf{PTDF}_{O,m}$	…	PTDF of node m on branches O
$\mathbf{PTDF}_{O,n}$	…	PTDF of node n on branches O

The necessary multi branch LODFs are calculated from the single branch LODFs as shown in chapter 2.3.2.

The control signal cs_P for the active power part of the emergency control is composed of branch loading dependent step functions which are weighted with the sign of the sensitivity to the HVDC link for each branch in Γ. The weighted step function and weight for branch k are defined as follows

$$f_k\left(LD_k, psens_{k,h}\right) = w_k(psens_{k,h}) \cdot \begin{cases} 2 & \cdots & LD_k \leq -1.1 \\ 1 & \cdots & -1.1 < LD_k \leq -1 \\ 0.5 & \cdots & -1 < LD_k \leq -0.7 \\ 0 & \cdots & -0.7 < LD_k < 0.7 \\ -0.5 & \cdots & 0.7 \leq LD_k < 1 \\ -1 & \cdots & 1 \leq LD_k < 1.1 \\ -2 & \cdots & 1.1 \leq LD_k \end{cases} \tag{6-8}$$

$$w_k\left(psens_{k,h}\right) = \begin{cases} -1 & \cdots & psens_{k,h} \leq -0.1 \\ 0 & \cdots & -0.1 < psens_{k,h} < 0.1 \\ 1 & \cdots & psens_{k,h} \geq 0.1 \end{cases} \tag{6-9}$$

The control signal calculates from the weighted step functions of the branches in Γ as

$$cs_{\mathrm{P}} = \max(f_\Gamma) + \min(f_\Gamma) \tag{6-10}$$

Composing the control signal from the maximal and minimal value of the weighted step functions of all considered branches avoids the overloading of additional branches. The threshold values can be chosen separately for each branch. The values used in (6-8) allow an overloading of $10\ \%$ of previously not overloaded branches to further relieve overloaded branches. If possible, branches are relieved under 70 %[6] of their nominal current to meet a simplified (n-1)-security condition.

The principal integration of the active power control signal in the converter controller is depicted in Fig. 6-11. The coloured blocks are used to highlight the different functional parts of the control strategy. The blue boxes on the left correspond to the necessary external data delivered from WAMS, periodically/event-based topology update and the output of the outage detection. The green marked part contains the processing of the input data and calculation of the control signal for the converter controller. The red part shows the integration in the actual converter controller. The integrated control signal is added to the active power setpoint, thereby changing the input of the direct current loop of the converter controller. The integrator limits are set to the maximal possible negative and positive setpoint changes and depend on the active power setpoint. The integration time constant T_{p} can be chosen freely. The factor k_{p} is set to the absolute value of the sensitivity of the branch with the highest loading. This selection of k_{p} allows an automated coordination between neighbouring HVDC links, whereby the participation of each HVDC link increases with higher sensitivity to the highest loaded branch. The converter must be operated in active power control.

Fig. 6-12 shows the connection between the branch loading and the control signals in a linearized example. The changes in the loading to the controller action are simply calculated using the corresponding sensitivities. The time constant T_P is set to $5\ \mathrm{s}$, the post-contingency sensitivities of branch a and b are given as $psens_a = -0.25$ and $psens_b = 0.5$.

[6] The 70 % of the example are chosen from empirical values of a TSO. In an actual implementation the value should be adjusted by the responsible TSO based on (n-1)-security analyses.

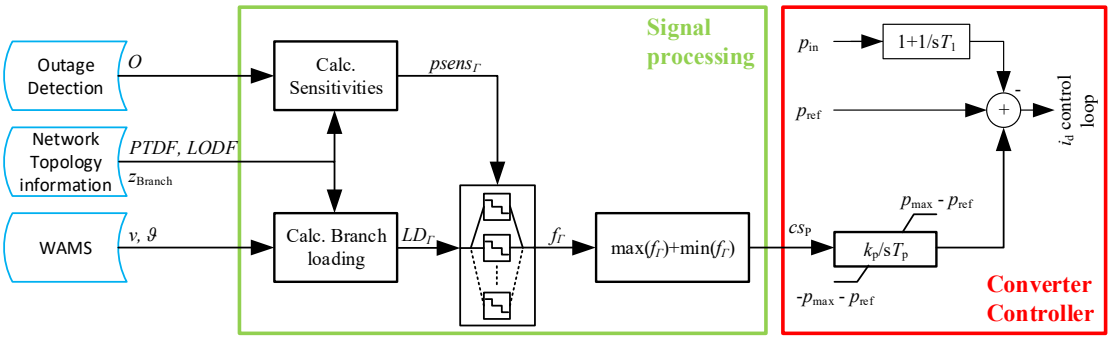

Fig. 6-11 Integration of the active power control signal into the converter controller. Blue external data, green the signal processing to achieve the control signal and red parts of the converter controller

At $t = 10$ s a contingency event causes an increase of the loading of branch a LD_a to 1.4 pu, changing the corresponding step function f_a value to 2 according to equations (6-8) and (6-9). The control signal cs_P equals the function's f_a value leading to an increase of the active power setpoint of HVDC converter. The change in the active power transfer of the HVDC link decreases the loading of branch a (negative sensitivity), but increases the loading of branch b (positive sensitivity). As soon as the loading of branch b exceeds 0.7 pu, the function f_b becomes -0.5 and thus decreases cs_P to 1.5 slowing the change in the active power setpoint and loading of the branches. The loading of branch b reaches around $t = 21$ s a value of 1 pu, which further decreases cs_P. The loading of branch a is still above the allowed overload threshold of 1.1 pu, therefore the active power setpoint change is still relieving branch a, but starts to overload branch b. The control signal cs_P becomes 0 as soon as branch a reaches the overload threshold around $t = 23$ s.

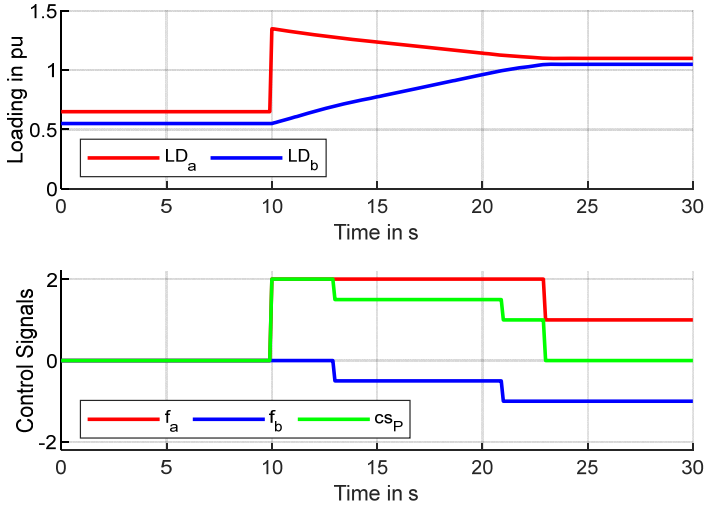

Fig. 6-12 Exemplary branch loading and resulting control signals

The general control behaviour in this simple example already highlights the following important characteristic of the proposed control:

- Fast control reaction, if a critical overload occurs
- Decreasing control speed, if control reaction causes additional branch loading
- Control utilizes an allowed overloading threshold for not overloaded branches to solve critical overloads
- Control does not cause additional critical overloaded branches

6.2.2 Reactive Power Control

Beside the branch loading, the voltage profile is an important operation characteristic of power systems. The main task of the voltage control is to keep the voltage magnitudes of all buses in the network within the limits defined by operational regulations. In high voltage transmission systems, the voltage is strongly coupled to the reactive power injections and only weak to the active power as long as the system is not strained to its limits. An effective controllability of the voltage magnitude by an AVR equipped resource – e. g. a synchronous generator or a converter of a HVDC link or an UPFC – is in general limited to electrical close buses. The affected buses can be determined using sensitivities of the voltage magnitude to the reactive power injection of the voltage-controlled bus.

6.2.2.1 dV/dQ Sensitivity Derivation

The dV/dQ sensitivity can be derived from the Jacobian matrix, which is used in several applications such as modal analysis [94], [95], for the definition of a voltage stability index [96], the assessment of a priced reactive power supply [97], the evaluation of optimal switched capacitor placing [98] or for voltage control algorithms avoiding voltage instabilities [47]. The following is taken from [95] and [99].

The dV/dQ sensitivity is calculated starting from the linkage between node voltage properties and node power injections described by the Jacobi matrix $\mathbf{J}$, equation (6-11). The elements of $\mathbf{J}$ refer to a solved power flow describing a stationary working point.

$$\begin{pmatrix}\Delta\mathbf{p}\\ \Delta\mathbf{q}\end{pmatrix} = \begin{bmatrix}\mathbf{J}_{\mathrm{P}\vartheta} & \mathbf{J}_{\mathrm{PV}}\\ \mathbf{J}_{\mathrm{Q}\vartheta} & \mathbf{J}_{\mathrm{QV}}\end{bmatrix}\begin{pmatrix}\Delta\boldsymbol{\vartheta}\\ \Delta\mathbf{v}\end{pmatrix} \tag{6-11}$$

Assuming controlled power injections in the current working point $\Delta\mathbf{p}$ becomes $\mathbf{0}$ for any change in the voltage magnitude and a reduced Jacobian matrix can be derived. The reduced Jacobian matrix $\mathbf{J}_{\mathrm{R}}$ describes the correlation between reactive power injections and the node voltage magnitudes – equation (6-13) – including the correlating changes of the node voltage angle caused by the changed voltage magnitude – equation (6-12). The dimension of it is for a network with N nodes $(N\text{-}1)\times(N\text{-}1)$, since the slack node is excluded.

$$\Delta\boldsymbol{\vartheta} = -\mathbf{J}_{\mathrm{P}\vartheta}^{-1}\cdot\mathbf{J}_{\mathrm{PV}}\cdot\Delta\mathbf{v} \tag{6-12}$$

$$\Delta\mathbf{q} = \left(\mathbf{J}_{\mathrm{QV}} - \mathbf{J}_{\mathrm{Q\vartheta}} \cdot \mathbf{J}_{\mathrm{P\vartheta}}^{-1} \cdot \mathbf{J}_{\mathrm{PV}}\right) \cdot \Delta\mathbf{v} = \mathbf{J}_{\mathrm{R}} \cdot \Delta\mathbf{v} \quad (6\text{-}13)$$

$$\Delta\mathbf{v} = \mathbf{J}_{\mathrm{R}}^{-1} \cdot \Delta\mathbf{q} \quad (6\text{-}14)$$

The inverse of $\mathbf{J}_{\mathrm{R}}$ gives the dV/dQ sensitivity. However, due to the dependency of $\mathbf{J}_{\mathrm{R}}$ on the node voltage angles and magnitudes and the need of constantly calculating the inverse of several sub matrixes its use for a decentral emergency control is rather impractical.

Another possibility to estimate the dV/dQ sensitivity can be reduced to a modified impedance matrix $\underline{\mathbf{Z}}$'. The basic idea of this concept is to implement all generation and loads as current injections. The node voltage-current correlation including the slack node for the solved load flow is defined by the bus impedance matrix $\underline{\mathbf{Z}}$.

$$\underline{\mathbf{v}} = \underline{\mathbf{Z}} \cdot \underline{\mathbf{i}} \quad (6\text{-}15)$$

Adding an additional current injection at node i leads to changes in the node voltages – equation (6-16). The principle of superposition allows a separation of the node voltage change and additional current injection from the working point at the cost of losing any eventually considered nonlinearities.

$$\underline{\mathbf{v}} + \Delta\underline{\mathbf{v}} = \underline{\mathbf{Z}} \cdot (\underline{\mathbf{i}} + \Delta\underline{\mathbf{i}}) \quad (6\text{-}16)$$

$$\Delta\underline{\mathbf{v}} = \underline{\mathbf{Z}} \cdot \Delta\underline{\mathbf{i}} \quad (6\text{-}17)$$

The bus impedance matrix is calculated by inverting the bus admittance matrix $\underline{\mathbf{Y}}$ and is generally a non-sparse matrix. Therefore, a current injection in a given node i results in a node voltage change in any other node of the network. This contradicts with the behaviour of constant voltage nodes – slack node and PV nodes – requiring a modification of the bus impedance matrix. The constant voltage nodes are assumed as ideal voltage sources with an internal impedance of $0\ \Omega$[7]. Voltage sources are replaced by their internal impedance applying the superposition principle hence leading to infinite main diagonal elements in the modified bus admittance matrix $\underline{\mathbf{Y}}$' corresponding to the constant voltage nodes. The modified impedance matrix $\underline{\mathbf{Z}}$' is the invers of $\underline{\mathbf{Y}}$'. Calculating the voltage changes with $\underline{\mathbf{Z}}$' preserves the properties of voltage-controlled nodes. The node voltage changes in node i and j for an injected current in node i as follows

$$\Delta\underline{v}_i = \underline{z}'_{ii} \cdot \Delta\underline{i}_i \quad (6\text{-}18)$$

$$\Delta\underline{v}_j = \underline{z}'_{ij} \cdot \Delta\underline{i}_i \quad (6\text{-}19)$$

The most effective voltage magnitude change in node i is reached, if $\Delta\underline{v}_i$ is in phase with the node voltage $\underline{v}_i$. Assuming the node voltage angle of $\underline{v}_i$ to be zero and in phase with the real axis, the angle of $\Delta\underline{i}_i$ has to be set to the negative angle of $\underline{z}'_{ii}$ to ensure $\Delta\underline{v}_i$ in phase with $\underline{v}_i$. The relative angle between $\Delta\underline{v}_j$ and $\underline{v}_j$ for the other nodes depend on the working point and the modified coupling impedance $\underline{z}'_{ij}$.

[7] Or with a reasonable small impedance to sufficiently modelling the voltage controlling without the need for infinite values in the adjusted admittance matrix allowing its inversion with applied simplifications.

With the following assumptions, which are valid in high voltage transmission grids, a work point independent estimation of the dV/dQ sensitivity is achieved.

- All elements of $\underline{\underline{\mathbf{Z}}}'$ are assumed to be purely reactive due to the branches small r/x-ratio
- Branch capacities are modelled as voltage depending reactive power injections in the nodes, therefore they are not present in $\underline{\underline{\mathbf{Z}}}'$
- Node voltage angles between neighbouring nodes are small
- Voltage magnitudes are close to $1\ \mathrm{pu}$

With purely reactive elements in $\underline{\underline{\mathbf{Z}}}'$ the current change $\Delta\underline{i}_i$ in node i has to be ± 90° to the voltage in node i. With the node voltage close to $1\ \mathrm{pu}$, the current change can be assumed equal to a change in reactive power in pu. The angle information of the elements of $\underline{\underline{\mathbf{Z}}}'$ and $\Delta\underline{i}_j$ can be included in the sign of the reactive power change. Summarizing these simplifications, the dV/dQ sensitivity can be estimated solely by the absolute values of $\underline{\underline{\mathbf{Z}}}'$.

$$\frac{\partial v_j}{\partial q_i} \sim z_{ij}, \forall i,j \in N \qquad (6\text{-}20)$$

Applying the stated assumptions already before inverting the modified admittance matrix and additionally deleting the column and row corresponding to the slack node, the modified admittance matrix is calculated similar to the susceptance matrix used for the derivation of the DC load flow equations in chapter 2.1.

$$\mathbf{Y}' = \mathbf{NBI} \cdot \mathbf{B}_\mathrm{d} \cdot \mathbf{NBI}^\mathrm{T} + \mathrm{diag}(\mathbf{pv}) = \mathbf{B} + \mathrm{diag}(\mathbf{pv}) \qquad (6\text{-}21)$$

$$\mathbf{Z}' = \mathbf{Y}'^{-1} \qquad (6\text{-}22)$$

$$\mathbf{pv}_\mathrm{i} = \begin{cases} \infty & \cdots \quad i\ is\ PV\ node \\ 0 & \cdots \quad i\ is\ PQ\ node \end{cases}, \forall i \in N/slack \qquad (6\text{-}23)$$

NBI	…	reduced node-to-branch incidence matrix $((N\text{-}1)\times L)$
$\mathbf{B}_\mathrm{d}$	…	diagonal matrix of branch susceptances $(L\times L)$
B	…	reduced system susceptance matrix $((N\text{-}1)\times(N\text{-}1))$
pv	…	vector for adjusting main diagonal elements corresponding to voltage controlled nodes $((N\text{-}1)\times 1)$

The exclusion of the slack node is possible since it is defined as an infinite power bus with unlimited reactive power requiring the corresponding main diagonal element in the adjusted admittance matrix to be infinite. The error in the sensitivity caused by the assumptions composes of the voltage dependency of sources and loads at the affected nodes, the angle differences between the node voltages and the neglection of changing losses.

The sensitivities estimated with $\underline{\underline{\mathbf{Z}}}'$ only depend on the topology and the location of voltage-controlled buses. Any change in topology or loss of voltage-control capability – generator outage or reaching of operation limitations – on any bus requires the recalculation of $\underline{\underline{\mathbf{Z}}}'$, which might become time consuming since it requires the inversion of a $(N\text{-}1)\times(N\text{-}1)$ matrix.

6.2.2.2 Control Signal Composition and Controller Integration

Similar to the active power control path, the reactive power control signal cs_Q is composed step functions. The step functions depend on the voltage magnitude at the nodes and on the ratio between the voltage sensitivity of the corresponding node and the node of the HVDC terminal. The efficiency of control actions decreases with smaller ratios of the voltage sensitivities. Therefore, it is sensible to introduce a minimal value $vsr_{\min}$ and neglect nodes with a smaller voltage sensitivity ratio. The considered nodes are stated in the set Λ. The equation (6-24) gives the step function for node j and a considered HVDC terminal at node i.

$$f_j(v_j, k_{vj}) = \begin{cases} 1 & \cdots & v_j \le v_{\min} - k_{vj} \cdot v_{\mathrm{bw}} \\ 0 & \cdots & v_{\min} - k_{vj} \cdot v_{\mathrm{bw}} < v_j < v_{\max} + k_{vj} \cdot v_{\mathrm{bw}} \\ -1 & \cdots & vj \ge v_{\max} + k_{vj} \cdot v_{\mathrm{bw}} \end{cases} \quad (6\text{-}24)$$

$$k_{vj} = \frac{1 - vsr_{ij}}{1 - vsr_{\min}} \quad (6\text{-}25)$$

$$vsr_{ij} = \frac{z_{ij}}{z_{ii}} \quad (6\text{-}26)$$

k_{vj}	…	utilization factor of voltage bandwidth
$v_{\min}$	…	minimal normal operation voltage
$v_{\max}$	…	maximal normal operation voltage
v_{bw}	…	voltage threshold bandwidth
vsr_{ij}	…	voltage sensitivity ratio between node j and i
$vsr_{\min}$	…	minimal voltage sensitivity ratio

The values of $v_{\min}$ and $v_{\max}$ can be chosen freely according to the operation requirements of the network operator. The voltage sensitivity ratio depending additional part in the conditions of the step function ensure, that the controller only reacts, if more efficient voltage controlling elements are not able to increase the voltage. Fig. 6-13 shows the step functions of the HVDC-terminal on node i and for node a and b with a voltage sensitivity ratios $vsr_a = 0.25$ and $vrs_b = 0.25$. The minimal voltage sensitivity ratio $vsr_{\min}$ is set to 0.1. The vsr of node i is 1 due to its definition and sets the smallest voltage difference triggering a control reaction. The black dashed line indicates the step function for vsr values equal to $vsr_{\min}$.

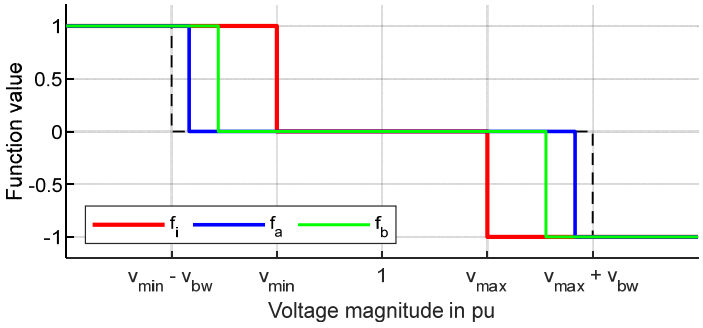

Fig. 6-13 Exemplary step functions for different voltage sensitivity ratios

The control signal calculates from the step functions of the set of nodes Λ as

$$cs_{\mathrm{Q}} = \max(f_{\Lambda}) + \min(f_{\Lambda}) \tag{6-27}$$

The control signal is consequently limited to discrete integer values between -2 and 2, whereby the extreme values -2 and 2 are only reached if all nodes in Λ encounter a too low or too high voltage magnitudes at the same time.

The basic integration of the reactive power control signal into the converter controller's quadrature current control loop is shown in Fig. 6-14. The blue boxes on the left correspond to the necessary external data delivered from WAMS, periodically/event-based topology update and the output of the outage detection. The green marked part contains the processing of the input data and calculation of the control signal for the converter controller. The red part shows the integration in the actual converter controller. The integrated control signal is added to the reactive power setpoint, thereby changing the input of the quadrature current loop of the converter controller. The integration time constant T_{q} can be chosen freely. The integrator limits are set to the maximal possible negative and positive setpoint changes and depend on the reactive power setpoint. The controller must be operated in reactive power control mode, whereby q_{ref} is either given be the reactive power setpoint or set to the actual reactive power output of the converter if the controller is switched from AC-voltage control mode to reactive power control mode.

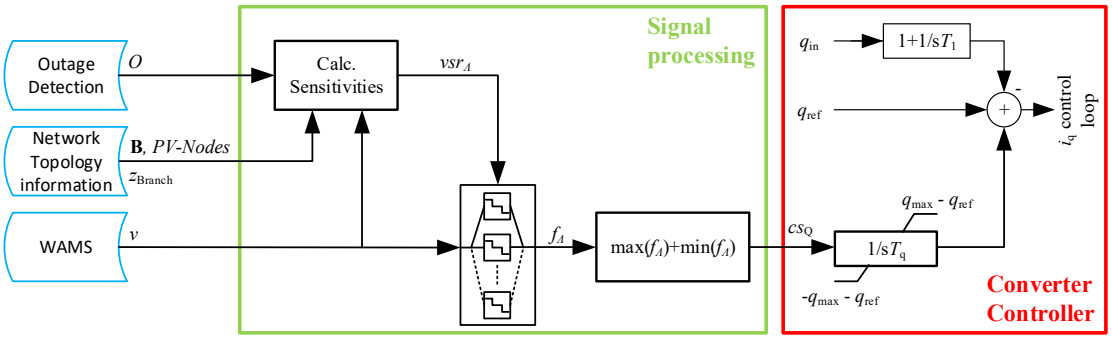

Fig. 6-14 Integration of the reactive power control signal into the converter controller. Blue external data, green the signal processing to achieve the control signal and red parts of the converter controller

6.2.3 Combined Integration in Converter Controller

The combined integration of the proposed active and reactive power control schema in a converter controller utilizing the maximum available converter power capacity require the coordination of the maximal available active and reactive power limits $p_{\max}$ and $q_{\max}$. The physical limiting factor is the maximal converter current $i_{\text{conv,max}}$. Therefore, the following equation must hold for any desired share between active and reactive power limitation.

$$i_{\text{conv,max}} = \frac{\sqrt{p_{\max}^2 + q_{\max}^2}}{v_{\text{conv,AC}}} \tag{6-28}$$

The priority between active and reactive power output of the HVDC converter depends on the network operation status. As long as the voltage magnitudes of all nodes in Λ are inside the allowed voltage bandwidth the emergency control should be allowed to use the converter's complete capacity in the active power control path to relieve branches. The limitation factor $p_{\max}$ of the integrator of the active power control signal cs_{P} is therefore set to $i_{\text{conv,max}} \cdot v_{\text{conv,AC}}$ and the direct axis current i_{d} is prioritised in the input of the subordinated current controller. If the actual active power output is smaller than $p_{\max}$, the free capacity of the converter can be used for voltage or reactive power control. The reactive power output is consequently limited as given in equation (6-29).

$$q_{\max} = \sqrt{i_{\text{conv,max}}^2 \cdot v_{\text{conv,max}}^2 - p_{\text{in}}^2} \tag{6-29}$$

If the voltage of any node in Λ leaves the allowed voltage bandwidth, the priority of the emergency control switches on the reactive power part to either avoid a critical long-time overvoltage or avoid voltage instabilities. The quadrature axis control loop is switched to reactive power control and the quadrature axis current i_{q} is prioritised in the input of the subordinated current controller. To ensure a smooth transition between the control modes, the reference reactive power q_{ref} is set to the reactive power output of the converter at the switching moment. Further, the limitation factor $q_{\max}$ of the integrator of the reactive power control signal cs_{Q} is now set as dominant limitation and the remaining free converter capacity can be used for active power control. The active power is therefore limited to

$$p_{\max} = \sqrt{q_{\max}^2 - q_{\text{in}}^2} \tag{6-30}$$

The value of $q_{\max}$ can be chosen in freely in the a range between 0 and $i_{\text{conv,max}} \cdot v_{\text{conv,AC}}$, whereby literature [41], [42] encourage using a function of the node voltage angles of the HVDC link terminals, equation (6-31), to achieve optimal voltage support in stressed network situation.

$$q_{\max} = i_{\text{conv,max}} \cdot v_{\text{conv,AC}} \cdot \cos(\vartheta_{\text{remote}} - \vartheta_{\text{local}}) \tag{6-31}$$

The subscript $_{\text{local}}$ labels the node voltage angle of the HVDC link terminal connected to the considered converter, the subscript $_{\text{remote}}$ corresponds consequently to the node voltage angle of the other HVDC link terminal. However, it might be possible to find better suited values of $q_{\max}$ depending on the actual operation point of the network as the results of chapter 6.1 suggest.

The additional control path for the emergency control with the signals cs_P and cs_Q are implemented in the outer control loop of the basic control structure of a VSC-controller [92, p. 222] as shown in Fig. 6-15. The selection and calculation of the limitation values p_{max} and q_{max} as well as the selection of the d/q prioritising and switch of the reactive power control mode are summarized in the bloc Limitation Calculation and Logic.

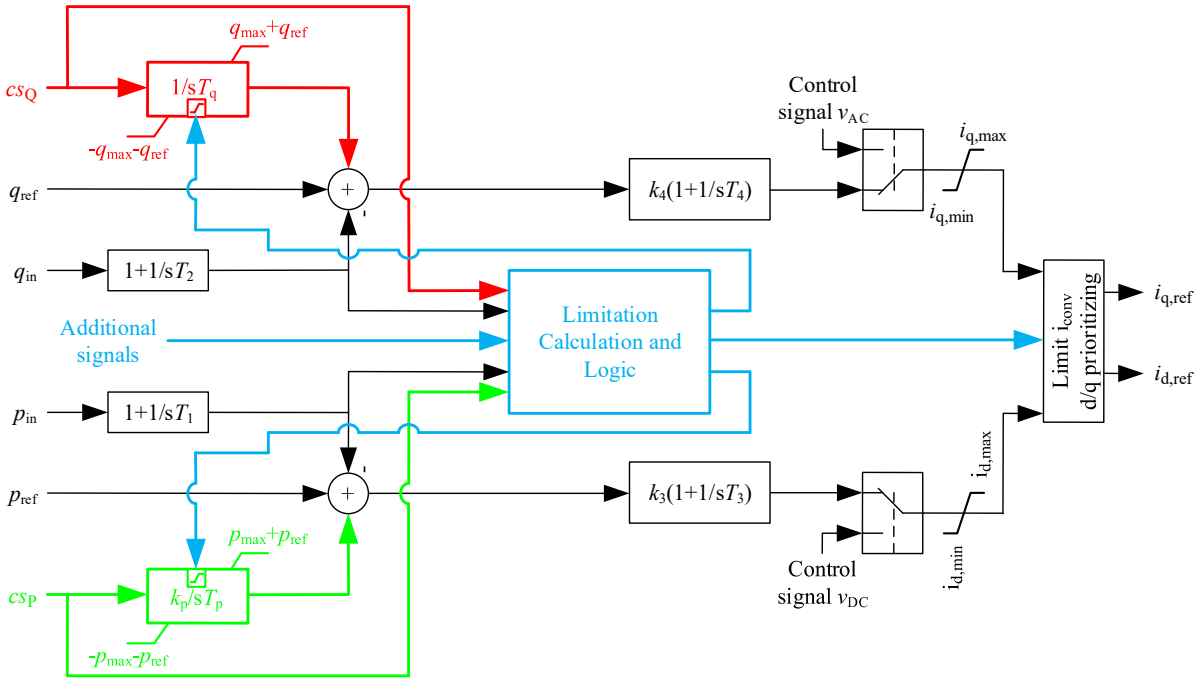

Fig. 6-15 Outer control loop of the VSC converter. Highlighted parts are the changes to the general control loop. The unchanged parallel paths for v_{DC}- and v_{AC}-control modes are only implied by their output signals.

The operation of HVDC links requires balanced active power. The active power of the converter transferring power from the AC grid to the HVDC link has to supply as much active power to the HVDC link as the converter transferring power from the HVDC link to the AC grid plus the losses of the HVDC system. The balanced active power is in general ensured by operating one controller in active power control mode and the other in DC voltage control mode. Due to this coupling of active power setpoints of both controllers, it is only required to activated the implementation of cs_P for the controller in active power control mode.

The reactive power on the other can be controlled independently for each converter. Further, the control signal cs_Q of each controller depends on the voltages in the network area of the HVDC link terminal. Due the in general rather long electrical distances between the terminals, the areas of the controllers do not overlap leading to different cs_Q signals. Therefore, the implementation of cs_Q has to be active in both controllers.

6.2.4 Conclusion on the Emergency Control for Complex Topologies

The proposed ECS for complex topologies focuses on the relief of overloaded branches and avoiding voltage instabilities. Therefore, additional control signals for the active and reactive power control paths using WAMS measurement data and information of the network topology are defined. Due to the implementation of an outage detection and linearized sensitivities, updates of the network information are only necessary for planned topology changes and do not have to be in real time. The linearization errors using linearized sensitivities have no critical effect on the control, since only the control speed directly depends on the actual sensitivity values.

The composition of the active power control signal cs_{P} allows efficient relief of overloaded branches without causing any additional critical overload. The speed of the control reaction of the converter corresponds to the severity of the overload and the sensitivity of the control reaction on the overloaded branch. This ensures fast control reaction for critical overloads and an inherent coordination with other HVDC links affecting the same branch.

The composition of the reactive power control signal cs_{Q} utilizes the necessary reactive power on the converter's point of coupling to stabilize the voltage in the affectable network area. Due to the different bandwidth of voltage deviations triggering a value change of cs_{Q} depending on the voltage sensitivity ratios the control is coordinated and more efficient devices are preferred. Furthermore, the voltage limits on the converter's point of coupling are included in the control signal, if the corresponding $v_{\max}$ and $v_{\min}$ values are set correctly.

7 Summary and Conclusions

Chapter **1 Introduction** consists of the introduction, motivation for the work, a review of the previous literature and the main scientific contributions resulting from this thesis.

In chapter **2 DC Load Flow and its Application** the general equations of the DC load flow, the integration of power flow controlling devices and contingency analyses based on line outage distribution factors are recapitulated. Besides already well-established methods of the DC load flow, the author's novel contributions to the DC load flow are discussed in this chapter. The main contribution of the author in this field are the mathematical proof of the applicability of LODFs in networks with PFCs manipulating the phase angles, e. g. PSTs and UPFCs, and the introduction of calculation rules to compute multi branch LODFs from single branch LODFs thus reducing the computational effort of contingency analysis.

Chapter **3 Grid Areas of Interest** deals with the definition of areas of control, areas of detection and the optimal placement of PMU monitored nodes depending on the area of detection. The areas of control are formed by the branches affected by the PFCs. These branches are important for the optimization of the operation point of the PFCs and for the limitation of corrective emergency control action to network parts efficiently affected by the PFCs.

The areas of detection are formed by the branches, whose tripping have significant influence on the load flow of branches within the areas of control. The thereby identified areas of detection define the considered branches in the emergency detection algorithms.

The selection of the branches forming the areas of control and areas of detection are based on the analysis of the branches' linearized load flow sensitivity to control action of the PFCs and outage sensitivities given by LODFs. The results of simulations on the branch selection allow the conclusion, that the value of the sensitivity selection threshold should only be chosen after an evaluation of its effect on the number of selected branches and number of multiple assigned branches. Considering the typical operation of PSTs and HVDC links, it is reasonable to use higher threshold values for the selection focusing on the branches affected by PSTs than for HVDC link affected branches. However, the actual values always depend on the intended purpose of the selected branches.

The selection of nodes focuses on the location of PMU nodes used for an emergency detection based on node voltage angles. The previously defined areas of detection describe the region of interest for the node selection. Any reduction of the number of PMU monitored nodes lead to a loss of information on the node voltage angle changes. However, if not all nodes can be equipped with PMUs due to economic or other reasons, the selection of the monitored nodes has to ensure to maintain a high level of useful information. The proposed iterative algorithm uses pre-calculated vectors of the voltage angle changes in all network nodes caused by single branch outages and selects the monitored nodes based on the share of redundant information.

In chapter **4 Control Setpoint Coordination and Optimization** the effects of coordination between the setpoints of PFCs and redispatch optimization are evaluated. The focus is set on embedded HVDC links and PSTs and seven scenarios with different degree of PFC availability and coordination in the optimization process. The redispatch costs and volumes obtained from a simulation of the central Europe grid region in the year 2025 are chosen as the comparative measure between the scenarios. The comparison of the scenarios allows the following conclusions:

- Uncoordinated control of PSTs leads to an increase of the redispatch costs. This is explained by the combination of a local focus relieving the PST equipped branches at the costs of causing and/or increasing overloads in the rest of the network and the nonlinearity of redispatch costs. Further, PSTs are mainly located on tie lines and bottle necks between network zones. In general, more options to relieve these branches with redispatch exist than for branches in more meshed network areas. Therefore, the PSTs reliving these branches force the redispatch optimizer to use less efficient redispatch power plants.
- Uncoordinated control of HVDC links decreases the necessary redispatch volume and costs in the majority of load situations. The decrease is reasonable since the HVDC links offer additional power transfer capacity.
- Comparing the effects of coordinated control of PSTs and HVDC links separately shows, that PSTs are more effective in reduction of necessary redispatch volume and costs. This is caused by their location on historical identified network bottle necks and the high local power flow sensitivity. The coordination with the redispatch activation prevents unfavourable shifts causing additional overloads.
- The combined coordinating PSTs and HVDC links leads expectantly to the highest decrease in redispatch costs. However, the activated redispatch volume is only reduced comparably to the coordination of PSTs without HVDC links. This highlight, that the optimizer uses the PSTs and HVDC links to utilize the cheapest redispatch power plants and not the most efficient ones.

Additionally, the result comparison between the implemented seasons for the optimization based only on the CNE branches and the optimization based on all branches demonstrate, that a qualitative assessment of the scenarios on CNE branches alone is valid. However, the cost and volume decreasing and increasing effects of PFCs are overestimated for a reduced set of branches.

The practical implementation of the discussed coordination between PFCs and redispatch planning, would require a European wide price driven redispatch market with optimization-based decision algorithms. Investigations on the effects of the PFCs on the distribution of redispatch cost according to requester and polluter pays principles will bring further insides in the economic benefits of coordinated operation strategies.

Further, a method to determine the critical (n-1)-contingency is developed and applied in a model of the ENTSO-E network to allow a comparative evaluation of different load flow scaling strategies in this chapter.

Chapter **5 Emergency Outage Detection** focuses on the application of optimizers for a robust decentral back up outage detection using only node voltage angle information. The evaluated detection algorithms

use Newton's method, PSO and a hybrid optimizer combining PSO and Newton's method (HPN). The comparison is based on simulations of the Nordic-32-Bus system.

The comparative evaluation of the three algorithms – based on Newton's method, PSO and a hybrid optimizer combining PSO and Newton's method (HPN) – on linearized load flow data already indicates, that only PSO and HPN are applicable. Focusing on the main performance parameters detection ratio and detection run time, HPN performs better and more robustly than PSO. The reason for this is, that HPN selects the candidate branches using PSO and finds the minimum of the corresponding objective function with Newton's method. Due to this separation of tasks, the major drawbacks of PSO – a rather long detection time and necessary reinitializations – and Newton's algorithm – not applicable on meshed networks without iterative extension – are overcome. The vulnerability of PSO and HPN to reduced monitored nodes are nearly the same for the evaluation of the linearized load cases.

The detection performance of the HPN based algorithm is robust against the loss of node information as long as a certain number of measured nodes are not undershot. Focusing on the basic parametrization, the most critical parameter is the selection of the search space dimension, since it has a negative impact on the detection ratio if chosen to be too small or too large, depending on the network topology and the chosen detection threshold. The choice of the space dimension should consider the maximum sensible number of tripped branches – taking into account general network stability – as well as the linearization error of the underlying model. However, the results show that as long as the linearization assumptions are mostly met, the detection ratios achieved on the data created with the described dynamic nonlinear and stationary linear simulation models are comparable.

The number of explicitly wrong results over the whole range of evaluated threshold values and number of monitored nodes is small for the proposed algorithm. It is therefore a possible tool for future back-up monitoring applications and standalone emergency control actions of decentral resources. The next working steps are to test the detection algorithm on linearized and static AC load flow data of large systems such as the ENTSO-E network and on defining triggers for emergency control actions based on the detection output in dynamic simulations.

Open working steps on this topic are the implementation of the algorithm in larger test systems and the combination of the emergency detection with the also discussed emergency control of embedded HVDC links. Improvements of the algorithm's performance might be achieved by implementing a more advanced version of PSO.

In chapter **6 Emergency Control of Embedded HVDC Links** possible automated emergency control strategies (ECS) of embedded HVDC links to avoid branch overloading and voltage instabilities are discussed. Two ECS are proposed. One applicable in simple topologies consisting of an embedded HVDC link in parallel to several AC lines connecting two network areas and a second more general ECS suitable for complex topologies.

The ECS proposed for simple topologies is based on the node voltage angle difference between the HVDC-terminals. If a contingency occurs, the ECS tries to maintain the node voltage angle difference between the HVDC-terminals on its pre-contingency value. Thereby, the effects of the contingency on

the parallel AC system are minimized. The conducted simulations of a radial topology demonstrate the advantages of this ECS in improving the voltage stability and support for the parallel AC system. The discussed scenarios – maximum load ability, loss of generation and branch outage – show that the ECS improves the system reaction to disturbances. Compared to existing control strategies for emergency control, the proposed ECS performs better in terms of unloading the parallel AC-network and at least at the same level in terms of long-term voltage stability. Another, advantage of the ECS is, that it does not disturb the system if activated accidentally.

The proposed ECS for complex topologies focuses on the relief of overloaded branches and avoiding voltage instabilities. Therefore, additional control signals for the active and reactive power control paths using WAMS measurement data and information of the network topology are defined. Due to the implementation of an outage detection and linearized sensitivities, updates of network information are only necessary for planned topology changes and do not have to be in real time. The linearization errors using linearized sensitivities have no critical effect on the control, since only the control speed directly depends on the actual sensitivity values.

The composition of the active power control signal allows efficient relief of overloaded branches without causing any additional critical overload. The speed of the control reaction of the converter corresponds to the severity of the overload and the sensitivity of the control reaction on the overloaded branch. This ensures fast control reaction for critical overloads and an inherent coordination with other HVDC links affecting the same branch.

The composition of the reactive power control signal utilizes the necessary reactive power on the converter’s point of coupling to stabilize the voltage in the affectable network area. Due to the different bandwidth of voltage deviations triggering a value change of the ECS signal depending on the voltage sensitivity ratios the control is coordinated and more efficient devices are preferred. Furthermore, the voltage limits on the converter’s point of coupling are included in the control signal, if the corresponding values are set correctly.

Future work on this topic will have to focus on the derivation of an optimal balance between reactive and active power limitations used for the ECS. Further, the complete system combining the ECS with a WAMS system and online detection algorithms has to be simulated in a suitable network topology.

8 References

[1] G. Glanzmann and G. Andersson, “Coordinated control of FACTS devices based on optimal power flow,” *Proc. 37th Annu. North Am. Power Symp. 2005*, vol. 2005, pp. 141–148, 2005, doi: 10.1109/NAPS.2005.1560515.

[2] G. Hug-Glanzmann and G. Andersson, “N−1 security in optimal power flow control applied to limited areas,” *IET Gener. Transm. Distrib.*, vol. 3, no. 2, pp. 206–215, Feb. 2009, doi: 10.1049/iet-gtd:20080112.

[3] G. Hug-Glanzmann and G. Andersson, “Coordinated control of FACTS devices in power systems for security enhancement,” *2007 iREP Symp. Bulk Power Syst. Dyn. Control - VII, Revital. Oper. Reliab.*, 2007, doi: 10.1109/IREP.2007.4410510.

[4] G. Hug, “Distributed optimization to enable a flexible power grid with corrective power flow control,” *IEEE Power Energy Soc. Gen. Meet.*, 2013, doi: 10.1109/PESMG.2013.6672482.

[5] J. Verboomen, “Optimisation of Transmission Systems by use of Phase Shifting Transformers,” TU Delft, 2008.

[6] R. Bauer, J. Weidner, and S. Salehinajafabadi, “Control strategies of phase-shifting transformers in long-term network development,” *Int. ETG Congr.*, no. Figure 2, pp. 356–362, 2015.

[7] M. Wolfram, A.-K. Marten, and D. Westermann, “A Comparative Study of Evolutionary Algorithms for Phase Shifting Transformer Setting Optimization,” 2016.

[8] J. Verboomen, D. Van Hertem, P. H. Schavemaker, W. L. Kling, and R. Belmans, “Border-flow control by means of phase shifting transformers,” *2007 IEEE Lausanne POWERTECH, Proc.*, pp. 1338–1343, 2007, doi: 10.1109/PCT.2007.4538510.

[9] R. Korab and R. Owczarek, “Impact of phase shifting transformers on cross-border power flows in the Central and Eastern Europe region,” *Bull. Polish Acad. Sci. Tech. Sci.*, vol. 64, no. 1, pp. 127–133, 2016, doi: 10.1515/bpasts-2016-0014.

[10] D. Van Hertem, R. Eriksson, L. Söder, and M. Ghandhari, “Coordination of multiple power flow controlling devices in transmission systems,” *IET Conf. Publ.*, vol. 2010, no. 570 CP, 2010, doi: 10.1049/cp.2010.0961.

[11] D. Van Hertem, J. Rimez, and R. Belmans, “Power flow controlling devices as a smart and independent grid investment for flexible grid operations: Belgian case study,” *IEEE Trans. Smart Grid*, vol. 4, no. 3, pp. 1656–1664, 2013, doi: 10.1109/TSG.2013.2249597.

[12] K. Frey, P. Wiest, K. Rudion, and J. Christian, “Automated operation of parallel VSC HVDC links within an interconnected AC network,” *IEEE Power Energy Soc. Gen. Meet.*, vol. 2016-Novem, pp. 1–5, 2016, doi: 10.1109/PESGM.2016.7741348.

[13] H. Zhang and S. Zhang, “A new strategy of HVDC operation for maximizing renewable energy accommodation,” *IEEE Power Energy Soc. Gen. Meet.*, vol. 2018-Janua, pp. 1–6, 2018, doi: 10.1109/PESGM.2017.8274477.

[14] F. Xu, X. Xie, L. Shi, and L. Yu, “A new operation model of HVDC tie-line for promoting renewable energy accommodation,” *Proc. - IEEE Int. Conf. Energy Internet, ICEI 2019*, pp. 290–297, 2019, doi: 10.1109/ICEI.2019.00058.

[15] J. Zhao, G. Antonio, M. Netto, and S. Member, “Power System Dynamic State Estimation : IEEE Task Force on Power System Dynamic State and Parameter Estimation,” *IEEE Trans. Power Syst.*, vol. 34, no. 4, pp. 3188–3198, 2019, doi: 10.1109/TPWRS.2019.2894769.

[16] J. James and S. Bindu, “Hybrid State Estimation including PMU measurements,” *2015 Int. Conf. Control. Commun. Comput. India, ICCC 2015*, no. November, pp. 309–313, 2016, doi: 10.1109/ICCC.2015.7432911.

[17] E. Farantatos, G. K. Stefopoulos, G. J. Cokkinides, and A. P. Meliopoulos, “PMU-based dynamic state estimation for electric power systems,” *2009 IEEE Power Energy Soc. Gen. Meet. PES ’09*, pp. 1–8, 2009, doi: 10.1109/PES.2009.5275407.

[18] Y. Zhao, J. Chen, A. Goldsmith, and H. V. Poor, “Identification of outages in power systems with uncertain states and optimal sensor locations,” *IEEE J. Sel. Top. Signal Process.*, vol. 8, no. 6, pp. 1140–1153, 2014, doi: 10.1109/JSTSP.2014.2342191.

[19] J. E. Tate and T. J. Overbye, “Line Outage Detection Using Phasor Angle Measurements,” *IEEE Trans. Power Syst.*, vol. 23, no. 4, pp. 1644–1652, Nov. 2008, doi: 10.1109/TPWRS.2008.2004826.

[20] J. E. Tate and T. J. Overbye, “Double line outage detection using phasor angle measurements,” *IEEE Trans. Power Syst.*, vol. 23, no. 4, pp. 1644–1652, 2008, doi: 10.1109/TPWRS.2008.2004826.

[21] H. Sehwail and I. Dobson, “Locating line outages in a specific area of a power system with synchrophasors,” *2012 North Am. Power Symp. NAPS 2012*, no. 2, pp. 1–6, 2012, doi: 10.1109/NAPS.2012.6336315.

[22] M. Alam, B. Mishra, and S. S. Thakur, “A New Approach of Multiple Line Outage Identification Using Phasor Measurement Unit (PMU) with Bad Data,” *Proc. 2018 Int. Conf. Curr. Trends Towar. Converging Technol. ICCTCT 2018*, pp. 1–6, 2018, doi: 10.1109/ICCTCT.2018.8551021.

[23] M. Alam, S. Kundu, S. S. Thakur, and S. Banerjee, “A new algorithm for single line outage estimation,” *Proc. 3rd Int. Conf. 2019 Devices Integr. Circuit, DevIC 2019*, pp. 113–117, 2019, doi: 10.1109/DEVIC.2019.8783954.

[24] K. Sun, S. Likhate, V. Vittal, V. S. Kolluri, and S. Mandal, “An online dynamic security assessment scheme using phasor measurements and decision trees,” *IEEE Trans. Power Syst.*, vol. 22, no. 4, pp. 1935–1943, 2007, doi: 10.1109/TPWRS.2007.908476.

[25] H. Zhu and G. B. Giannakis, “Sparse overcomplete representations for efficient identification of power line outages,” *IEEE Trans. Power Syst.*, vol. 27, no. 4, pp. 2215–2224, 2012, doi: 10.1109/TPWRS.2012.2192142.

[26] T. Banerjee, Y. C. Chen, A. D. Dominguez-Garcia, and V. V. Veeravalli, “Power system line outage detection and identification - A quickest change detection approach,” *ICASSP, IEEE Int. Conf. Acoust. Speech Signal Process. - Proc.*, pp. 3450–3454, 2014, doi: 10.1109/ICASSP.2014.6854241.

[27] Y. C. Chen, T. Banerjee, A. D. Dominguez-Garcia, and V. V. Veeravalli, “Quickest line outage detection and identification,” *IEEE Trans. Power Syst.*, vol. 31, no. 1, pp. 749–758, 2016, doi: 10.1109/TPWRS.2015.2394246.

[28] G. Rovatsos, X. Jiang, A. D. Domínguez-García, and V. V. Veeravalli, “Statistical Power System Line Outage Detection Under Transient Dynamics,” *IEEE Trans. Signal Process.*, vol. 65, no. 11, pp. 2787–2797, 2017, doi: 10.1109/TSP.2017.2673802.

[29] X. Jiang, Y. C. Chen, V. V. Veeravalli, and A. D. Dominguez-Garcia, “Quickest line outage detection and identification: Measurement placement and system partitioning,” *2017 North Am. Power Symp. NAPS 2017*, 2017, doi: 10.1109/NAPS.2017.8107394.

[30] G. Rovatsos, X. Jiang, A. D. Dominguez-Garcia, and V. V. Veeravalli, “Comparison of statistical algorithms for power system line outage detection,” in *2016 IEEE International Conference on Acoustics, Speech and Signal Processing (ICASSP)*, Mar. 2016, pp. 2946–2950, doi: 10.1109/ICASSP.2016.7472217.

[31] R. Emami and A. Abur, “Tracking changes in the external network model,” *North Am. Power Symp. 2010, NAPS 2010*, 2010, doi: 10.1109/NAPS.2010.5618980.

[32] A. Ahmed, M. Awais, M. Naeem, M. Iqbal, and A. Alpalagan, “Efficient multiple lines outage detection in SmartGrid,” *2015 Power Gener. Syst. Renew. Energy Technol. PGSRET 2015*, 2015, doi: 10.1109/PGSRET.2015.7312243.

[33] A. Ahmed *et al.*, “Multiple Power Line Outage Detection in Smart Grids: Probabilistic Bayesian Approach,” *IEEE Access*, vol. 6, pp. 10650–10661, 2018, doi: 10.1109/ACCESS.2017.2710285.

[34] UCTE, “Final report - System disturbance on 4 November 2006,” 2007. [Online]. Available: https://www.entsoe.eu/.../ce/otherreports/Final-Report-20070130.pdf%5Cnhttp://scholar.google.com/scholar?hl=en&btnG=Search&q=intitle:Final+Report+System+Disturbance+on+4+November+2006#1.

[35] UCTE, “Final Report of the Investigation Committee on the 28 September 2003 Blackout in Italy,” 2003.

[36] S. Larsson and A. Danell, “The black-out in southern Sweden and eastern Denmark, September 23, 2003.,” in *2006 IEEE PES Power Systems Conference and Exposition*, 2006, pp. 309–313, doi: 10.1109/PSCE.2006.296324.

[37] G. Andersson *et al.*, “Causes of the 2003 Major Grid Blackouts in North America and Europe, and Recommended Means to Improve System Dynamic Performance,” *IEEE Trans. Power Syst.*, vol. 20, no. 4, pp. 1922–1928, Nov. 2005, doi: 10.1109/TPWRS.2005.857942.

[38] P. Kundur, *Power System Stability and Control*, McGraw-Hil. Toronto, Canada: McGraw-Hili, Inc., 1994.

[39] P. Cholley *et al.*, “System Protection Schemes in Power Networks,” *CIGRE Tech. Broch.*, vol. 187, 2001.

[40] P. Chodura, M. Gibescu, W. L. Kling, and R. A. A. De Graaff, “Investigation of the impact of embedded VSC-HVDC active and reactive power control on power system stability,” *2015 IEEE Eindhoven PowerTech, PowerTech 2015*, 2015, doi: 10.1109/PTC.2015.7232813.

[41] S. Johansson, G. Asplund, E. Jansson, and R. Rudervall, “Power system stability benefits with VSC DC-transmission systems,” in *Cigré Conference Session 2004*, 2004, pp. 1–8, [Online]. Available: http://library.abb.com/GLOBAL/SCOT/SCOT289.nsf/VerityDisplay/504D40276A43FC67C1256EFA002970DE/$File/B4-204.pdf.

[42] M. R. S. Tirtashi, J. Svensson, and O. Samuelsson, “VSC-HVDC application to improve the long-term voltage stability,” *2017 IEEE Manchester PowerTech, Powertech 2017*, 2017, doi: 10.1109/PTC.2017.7980887.

[43] K. Frey, K. Rudion, and J. Christian, “Automated operation approach for embedded HVDC links during (N-1)-conditions in the AC system,” *2016 IEEE Int. Energy Conf. ENERGYCON 2016*, pp. 1–6, 2016, doi: 10.1109/ENERGYCON.2016.7514117.

[44] S. C. Muller, U. Hager, and C. Rehtanz, “Integrated coordination of AC power flow controllers and HVDC transmission by a multi-agent system,” *2013 Work. Model. Simul. Cyber-Physical Energy Syst. MSCPES 2013*, vol. 1511, 2013, doi: 10.1109/MSCPES.2013.6623328.

[45] S. C. Muller, U. Hager, and C. Rehtanz, “A multiagent system for adaptive power flow control in electrical transmission systems,” *IEEE Trans. Ind. Informatics*, vol. 10, no. 4, pp. 2290–2299, 2014, doi: 10.1109/TII.2014.2315499.

[46] L. Robitzky, S. C. Muller, S. Dalhues, U. Hager, and C. Rehtanz, “Agent-based redispatch for real-time overload relief in electrical transmission systems,” in *2015 IEEE Power & Energy Society General Meeting*, Jul. 2015, pp. 1–5, doi: 10.1109/PESGM.2015.7285886.

[47] O. A. Urquidez and L. Xie, “Singular Value Sensitivity Based Optimal Control of Embedded VSC-HVDC for Steady-State Voltage Stability Enhancement,” *IEEE Trans. Power Syst.*, vol. 31, no. 1, pp. 216–225, Jan. 2016, doi: 10.1109/TPWRS.2015.2393253.

[48] I. Erlich, F. Shewarega, and W. Winter, “A method for incorporating VSC-HVDC into the overall grid voltage-reactive power control task,” in *19th Power Systems Computation Conference, PSCC 2016*, Jun. 2016, pp. 1–7, doi: 10.1109/PSCC.2016.7540895.

[49] G. Radman, A. Pama, J. Powell, and D. Gao, “Dynamic voltage stability improvement using coordinated control of dynamic VAR-sources,” *2007 iREP Symp. Bulk Power Syst. Dyn. Control - VII, Revital. Oper. Reliab.*, pp. 5–10, 2007, doi: 10.1109/IREP.2007.4410541.

[50] A. Marinakis, M. Glavic, and T. Van Cutsem, “Minimal reduction of unscheduled flows for security restoration: Application to phase shifter control,” *IEEE Trans. Power Syst.*, vol. 25, no. 1, pp. 506–515, 2010, doi: 10.1109/TPWRS.2009.2030423.

[51] G. Hug-Glanzmann and G. Andersson, “Decentralized optimal power flow control for overlapping areas in power systems,” *IEEE Trans. Power Syst.*, vol. 24, no. 1, pp. 327–336, 2009, doi: 10.1109/TPWRS.2008.2006998.

[52] D. A. Panasetsky and N. I. Voropai, “A distributed control of FACTS devices against line overloading,” *2010 Int. Conf. Power Syst. Technol. Technol. Innov. Mak. Power Grid Smarter, POWERCON2010*, pp. 1–6, 2010, doi: 10.1109/POWERCON.2010.5666633.

[53] K. Van Den Bergh, E. Delarue, and W. D’haeseleer, “DC power flow in unit commitment models,” *TME Work. Pap. Environ.*, no. May, pp. 1–38, 2014.

[54] D. Van Hertem, “The use of power flow controlling devices in the liberalized market,” KU Leuven, 2009.

[55] D. Hertem, J. Verboomen, K. Purchala, R. Belmans, and W. L. L. Kling, “Usefulness of DC power flow for active power flow analysis with flow controlling devices,” *8th Int. Conf. AC DC Power Transm.*, pp. 58–68, 2006, doi: 10.1049/cp:20060013.

[56] D. Oeding and B. R. Oswald, *Elektrische Kraftwerke und Netze*. Berlin, Heidelberg: Springer Berlin Heidelberg, 2016.

[57] G. Balzer, B. Boehle, K. Haneke, H. G. Kaiser, W. Tettenborn, and G. Voß, *Schaltanlagen*, 9., neubea. Mannheim: Cornelsen Verlagsgesellschaft, 1992.

[58] K. Purchala, L. Meeus, D. Van Dommelen, and R. Belmans, “Usefulness of DC Power Flow for Active Power Flow Analysis,” *Power Eng. Soc. Gen. Meet.*, pp. 454–459, 2005, doi: 10.1109/PES.2005.1489581.

[59] J. Machowski, J. W. Bialek, and J. R. Bumby, *Power System Dynamics: Stability and Control*, 2nd ed. Re. Chichester: John Wiley & Sons Ltd, 2008.

[60] M. I. Alomoush, “Derivation of UPFC DC load flow model with examples of its use in restructured power systems,” *IEEE Trans. Power Syst.*, vol. 18, no. 3, pp. 1173–1180, 2003, doi: 10.1109/TPWRS.2002.805002.

[61] S. An, J. Condren, and T. W. Gedra, “An ideal transformer UPFC model, OPF first-order sensitivities, and application to screening for optimal UPFC locations,” *IEEE Trans. Power Syst.*, vol. 22, no. 1, pp. 68–75, 2007, doi: 10.1109/TPWRS.2006.889141.

[62] J. Guo, Y. Fu, Z. Li, and M. Shahidehpour, “Direct calculation of line outage distribution factors,”

IEEE Trans. Power Syst., vol. 24, no. 3, pp. 1633–1634, 2009, doi: 10.1109/TPWRS.2009.2023273.

[63] D. A. Tejada-Arango, P. Sanchez-Martin, and A. Ramos, “Security Constrained Unit Commitment using Line Outage Distribution Factors,” *IEEE Trans. Power Syst.*, vol. 8950, no. c, pp. 1–1, 2017, doi: 10.1109/TPWRS.2017.2686701.

[64] T. Güler, G. Gross, and M. Liu, “Generalized line outage distribution factors,” *IEEE Trans. Power Syst.*, vol. 22, no. 2, pp. 879–881, 2007, doi: 10.1109/TPWRS.2006.888950.

[65] R. Bo, C. Wu, J. Yan, L. Hecker, and Z. Zhou, “LODF-based transmission solution screening method in economic transmission planning,” *IEEE Power Energy Soc. Gen. Meet.*, vol. 2015-Septe, pp. 1–5, 2015, doi: 10.1109/PESGM.2015.7286636.

[66] M. Shahidehpour, H. Yamin, and Z. Li, *Market Operations in Electric Power Systems*. New York, USA: John Wiley & Sons, Inc., 2002.

[67] H. Cetinay, S. Soltan, F. A. Kuipers, G. Zussman, and P. Van Mieghem, “Comparing the Effects of Failures in Power Grids Under the AC and DC Power Flow Models,” *IEEE Trans. Netw. Sci. Eng.*, vol. 5, no. 4, pp. 301–312, Oct. 2018, doi: 10.1109/TNSE.2017.2763746.

[68] S. Polster and H. Renner, “Generalisation of the Line Outage Distribtution Factors on Phase Shifting Transformers,” 2018.

[69] ACER, “Day-ahead capacity calculation methodology of the Core capacity calculation region,” no. July 2015, 2019.

[70] The European Parliament and the Council of the European Union, “Regulation (EU) 2019/943 of the European Parliament and of the Council of 5 June 2019 on the internal market for electricity,” *Off. J. Eur. Union*, vol. 62, no. L158, pp. 54–191, 2019.

[71] J. Boury, “Methods for the determination of flow-based capacity parameters: description, evaluation and improvements,” *Master Thesis - KU Leuven*, no. May 2015, 2015, [Online]. Available: https://www.researchgate.net/profile/Jonas_Boury/publication/313401545_Methods_for_the_determination_of_flow-based_capacity_parameters_description_evaluation_and_improvements/links/58998c03aca2721f0db0ba80/Methods-for-the-determination-of-flow-based-capac.

[72] K. Van den Bergh, J. Boury, and E. Delarue, “The Flow-Based Market Coupling in Central Western Europe: Concepts and definitions,” *Electr. J.*, vol. 29, no. 1, pp. 24–29, 2016, doi: 10.1016/j.tej.2015.12.004.

[73] Amprionapx *et al.*, “Communication to Market Participants: CWE Flow-Based Market Coupling,” 2014. https://www.transnetbw.de/downloads/strommarkt/engpassmanagement/CWE-FB-MC_Additonal-parallel-run-publications_8.12.14.pdf.

[74] K. Köck, “Probability Based Transmission System Risk Assessment,” Graz University of

Technology, 2016.

[75] I. Chychykina and C. K. M. Wolter, “Comparison of different redispatch optimization strategies,” *2017 IEEE Manchester PowerTech, Powertech 2017*, no. 3, 2017, doi: 10.1109/PTC.2017.7981077.

[76] S. Polster, H. Renner, K. Friedl, and O. Samuelsson, “Advanced automated emergency control strategy for embedded VSC-HVDC links,” *e i Elektrotechnik und Informationstechnik*, vol. 137, no. 8, pp. 394–399, Dec. 2020, doi: 10.1007/s00502-020-00831-8.

[77] B. Stott, J. Jardim, and O. Alsaç, “DC power flow revisited,” *IEEE Trans. Power Syst.*, vol. 24, no. 3, pp. 1290–1300, 2009, doi: 10.1109/TPWRS.2009.2021235.

[78] S. Polster, H. Renner, R. Schürhuber, and K. Friedl, “On WAMS based Emergency Outage Detection using Optimization,” *Int. J. Electr. Power Energy Syst.*, 2021, doi: 10.1016/j.ijepes.2021.107006.

[79] K. Levenberg, “A Method for the Solution of Certain Non-Linear Problems in Least Squares,” *Q. Appl. Math.*, vol. 2, no. 2, pp. 164–168, 1944, [Online]. Available: https://www.jstor.org/stable/43633451.

[80] Donald W. Marquardt, “An Algorithm for Least-Squares Estimation of Nonlinear Parameters,” *J. Soc. Ind. Appl. Math.*, vol. 11, no. 2, pp. 431–441, 1963, [Online]. Available: https://www.jstor.org/stable/2098941.

[81] B. T. Polyak, “Newton’s method and its use in optimization,” *Eur. J. Oper. Res.*, vol. 181, no. 3, pp. 1086–1096, 2007, doi: 10.1016/j.ejor.2005.06.076.

[82] J. Kennedy and R. Eberhart, “Particle swarm optimization,” in *Proceedings of ICNN’95 - International Conference on Neural Networks*, 2016, vol. 4, no. 2, pp. 1942–1948, doi: 10.1109/ICNN.1995.488968.

[83] D. Bratton and J. Kennedy, “Defining a standard for particle swarm optimization,” *Proc. 2007 IEEE Swarm Intell. Symp. SIS 2007*, no. Sis, pp. 120–127, 2007, doi: 10.1109/SIS.2007.368035.

[84] M. Zambrano-Bigiarini, M. Clerc, and R. Rojas, “Standard Particle Swarm Optimisation 2011 at CEC-2013: A baseline for future PSO improvements,” *2013 IEEE Congr. Evol. Comput. CEC 2013*, pp. 2337–2344, 2013, doi: 10.1109/CEC.2013.6557848.

[85] M. Ghasemi, E. Akbari, A. Rahimnejad, S. E. Razavi, S. Ghavidel, and L. Li, “Phasor particle swarm optimization: a simple and efficient variant of PSO,” *Soft Comput.*, vol. 23, no. 19, pp. 9701–9718, 2019, doi: 10.1007/s00500-018-3536-8.

[86] F. Van Den Bergh, “An analysis of particle swarm optimizers,” no. November, p. 315, 2001.

[87] T. Report, “IEEE PES Task Force on Test Systems for Voltage Stability Analysis and Security Assessment,” *Ieee*, 2015, [Online]. Available: http://sites.ieee.org/pes-resource-center/files/2015/08/PES_TR19_Test-Systems-for-Voltage-Stability-Analysis-and-Security-

Assessment1.pdf.

[88] L. D. P. Ospina, A. F. Correa, and G. Lammert, “Implementation and validation of the Nordic test system in DIgSILENT PowerFactory,” *2017 IEEE Manchester PowerTech, Powertech 2017*, 2017, doi: 10.1109/PTC.2017.7980933.

[89] A. Wood, B. Wollenberg, and G. Sheble, *Power Generation, Operation, and Control*, 3rd Editio. 2013.

[90] MathWorks, “https://de.mathworks.com/help/stats/fitdist.html.” .

[91] DigSilent, “PowerFactory 2019, SP2 - Academic License,” *PowerFactory 2019, SP2 - Academic License*, 2019. http://www.digsilent.de/.

[92] D. Jovcic and K. Ahmed, *High Voltage Direct Current Transmission*, 1. Auflage. Chichester, United Kingdom: John Wiley & Sons Ltd, 2015.

[93] C. Becker, “Autonome Systeme zur koordinierenden Regelung von FACTS-Geräten,” TU Dortmund, 2000.

[94] B. Gao, G. K. Morison, and P. Kundur, “Voltage Stability Evaluation using Modal Analysis,” *IEEE Power Eng. Rev.*, vol. 12, no. 11, p. 41, 1992, doi: 10.1109/MPER.1992.161430.

[95] P. Kundur and R. I. E. Power, “Power system stability and control,” pp. 1-23+1176 s, 1994, doi: 0-07-035958-X.

[96] P. S. Seshadri and A. D. Patton, “Bus voltage sensitivity: An instrument for pricing voltage control service,” *1999 IEEE Power Eng. Soc. Summer Meet. PES 1999 - Conf. Proc.*, vol. 2, pp. 703–707, 1999, doi: 10.1109/PESS.1999.787403.

[97] H. Moreno, S. Plumel, and P. Bastard, “Assessing the value of reactive power service using OPF of reactive power,” *2005 IEEE Russ. Power Tech, PowerTech*, pp. 1–6, 2005, doi: 10.1109/PTC.2005.4524430.

[98] M. R. Montañés, J. R. Santos, and E. R. Ramos, “Voltage sensitivity based technique for optimal placement of switched capacitors,” *15th Power Syst. Comput. Conf. PSCC 2005*, no. August, pp. 22–26, 2005.

[99] C. W. Talyer, *Power System Voltage Stability*. New York, USA: MacGraw-Hill, 1994.

Appendix

A. Transmission Network Model

The model of the European electricity network used in this thesis. It is useable for DC load flow calculations and expanded with the methods developed in this thesis maps the 220-kV and 380-kV network of the ENTSO-E region and Great Britain in detail. Subordinate voltage levels are generally integrated as equivalent loads or feeds. The exceptions are 110-kV-network parts with integral importance for international electricity flows, which are mapped in detail. The network data is based on the static network model of the ENTSO-E and has been continuously expanded with additional information since 2016. The additional information comes from publicly available sources such as the Ten-Year Network Development Plans (TYNDP) and the network development plans of national transmission system operators. The calculation of the load flows takes place in MATLAB and uses the methods of the linearized load flow (DC load flow), which is an adequate means for techno-economic issues and is also used in the mechanisms of flow-based market.

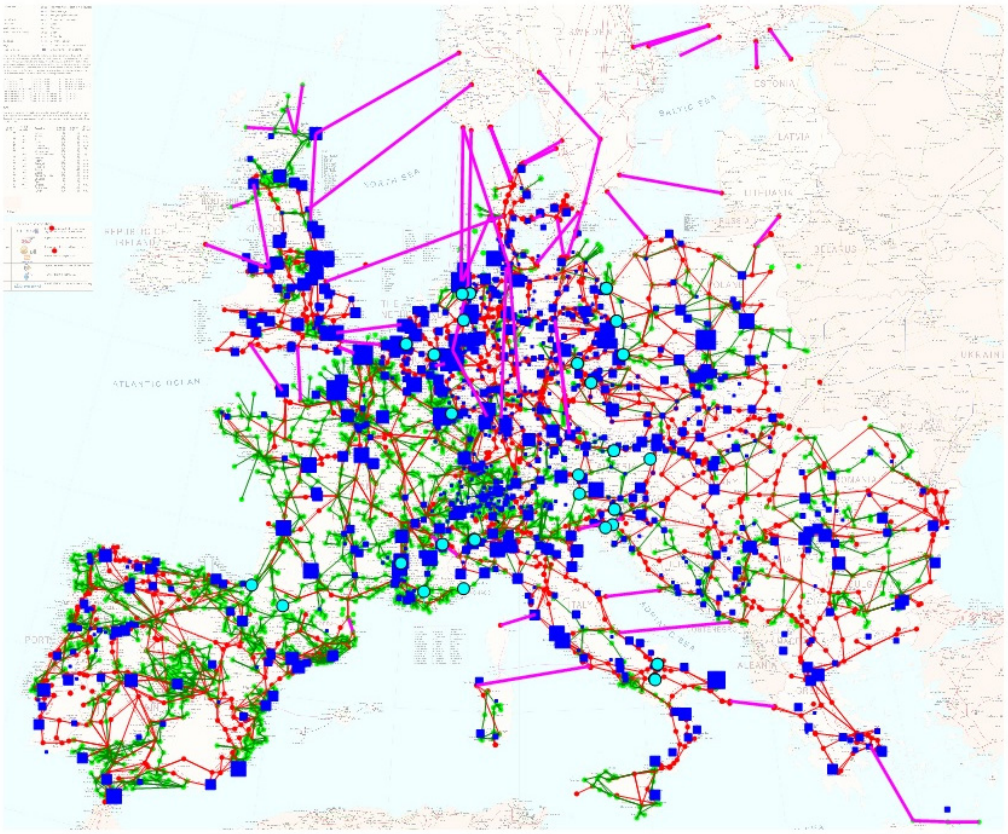

Fig. A-1 Geographic presentation of the modelled transmission network with projects included. 380-kV-branches are coloured red, 220-kV-branches are coloured green and HVDC links are coloured magenta. The red and green circles mark the network nodes. The cyan circles correspond to the location of PST. The power plants are highlighted with the blue squares, whereby their size is scaled with the power plant's nominal powers.

The most important cornerstones and functions of the model are described in the following:

- **Extensive network data** – the continuous expansion with data from network development plans and the adaption of them to the actual development progress and switching status ensures that the network model corresponds to the reality for the time horizon from 2015 to 2030[8]. In detail the network model currently consists of
  - 8237 nodes
  - 9849 power lines, including 368 projects
  - 1775 power transformers
  - 45 phase shifting transformers, including 6 projects
  - 59 HVDC links, including 19 projects
- **Integration of generation and load on node basis**
  - 3382 power plants (nominal power > 50 MW) with interface to include market simulation tools
  - Assignment of residual generation (e. g. solar power in Germany) based on geographic location
  - Load node and load scaling based on ENTSO-E reference load
- **Exchange of individual network areas** – The flexible structure of the model allows an easy exchange of individual network areas to integrate project-specific network data.
- **Loading and contingency analysis** - with the specification of load and generation, the distribution of the load flows and the corresponding utilization of individual transmission elements is calculated via the Power Transfer Factor Matrix (PTDF). Analysis of (n-x) certainties of the load flow are carried out with the help of Line Outage Distribution Factors (LODF).
- **Reproduction of historical load flow situations** – The historical load flow is reproduced based on data subject to publication on trading volumes, physical load flows between countries, national generation according to primary energy source and total load. A fictitious power plant dispatch plan is determined from the generation data and the physical load flows between individual countries. The load flow controlling effects of PSTs are considered for this task.
- **Determination of the flow-based market coupling parameters** – Based on a given reference load flow and the generation shift keys for each bidding zone in the flow-based market area the critical (n-1)-contingency elements, the critical (n-1)-flows and (n-1)-sensitivities are calculated.
- **Redispatch optimization** – Based on the result of an electricity market simulation, a cost-minimized use of redispatch power plants is determined. The optimization uses solvers built into MATLAB.
- **Optimized use of embedded HVDC links and PST** - The operating points of embedded HVDC links and PST are optimized in terms of minimum line utilization, reduction of redispatch requirements or the reduction of undesired loop flows for given generation and load. The optimization uses solvers built into MATLAB.

[8] Known network expansion projects that extend beyond this time horizon are integrated in the model, but have uncertainties due to mostly little detailed information and planning changes.

B. Additional Evaluation on Branch Selection

The assignment of branches to multiple subsets of Γ is shown in Fig. B-1. The bar labels refer to the number of subsets in which multiple selected branches are assigned to. The value of the ordinate corresponds to the number of these branches as proportion of all candidate branches. The left graph refers to branches assigned to several subsets of embedded HVDCs, the middle graph to subsets of PSTs and the right graph to the combination of embedded HVDCs and PSTs. The slower decrease in the proportion in the middle graph compared to the left graph is explained by the electrical close location of several PSTs and their higher number in general.

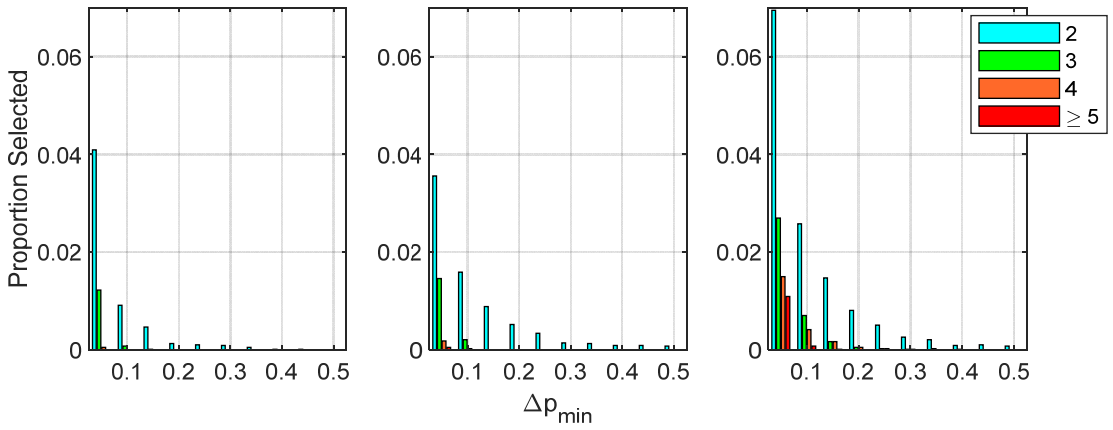

Fig. B-1 influence of Δp_{min} on the number of selected branches affected by more than one PFC, whereby the number of branches is normalized to the number of candidate branches. The left graph only takes embedded HVDCs into account, the middle graph only PSTs. The right graph refers to the combination of embedded HVDCs and PSTs.

C. Distribution of Pilot Hours

The pilot hours are chosen randomly from the hours corresponding to the seasons. To ensure existing solutions for all pilot hours, the optimization is run for $15\ \%$ of the number of hours corresponding to the season. Hours without a suitable optimization result in all scenarios are removed from the set of pilot hours. The thereby remaining pilot hours are further reduced by randomly selecting the necessary number of hours to reach $10\ \%$ of the hours in each season. The final numbers of pilot hours of each season are given in Table C-1. Their distribution is depicted in Fig. C-1.

Table C-1 Pilot hours and season hours

	Season 1	Season 2	Season 3	Season 4
# hours	2808	2820	1560	1572
# pilot hours	281	282	156	158
% of pilot hours	10.01 %	10.00 %	10.00 %	10.05 %

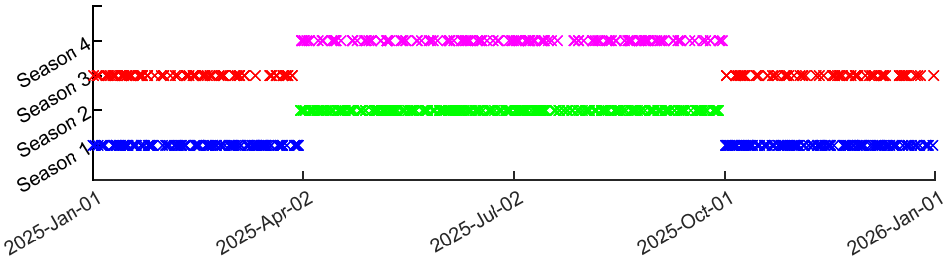

Fig. C-1 Distribution of pilot hours

D. Nordic-32-Bus System

In this work a variant of the Nordic-32-Bus system, Fig. D-1, implemented and validated in DigSILENT is used and expanded. The model is thankfully provided by the authors of [88]. The system mainly consists of 32 nodes representing a transmission grid with the nominal voltages of $400\ \mathrm{kV}$ (nodes 40xx), $220\ \mathrm{kV}$ (nodes 20xx) and $130\ \mathrm{kV}$ (nodes 10xx). The generators and loads are connected to the network with 22 additional medium voltage nodes. The dynamic model includes automatic voltage regulators, over excitation limiters and power system stabilizers as well as a frequency control and saturation effects for the generators. The voltage dependency of loads is modelled by equipping all load transformers with on load tap changers. For a detailed description on the dynamic models see [88].

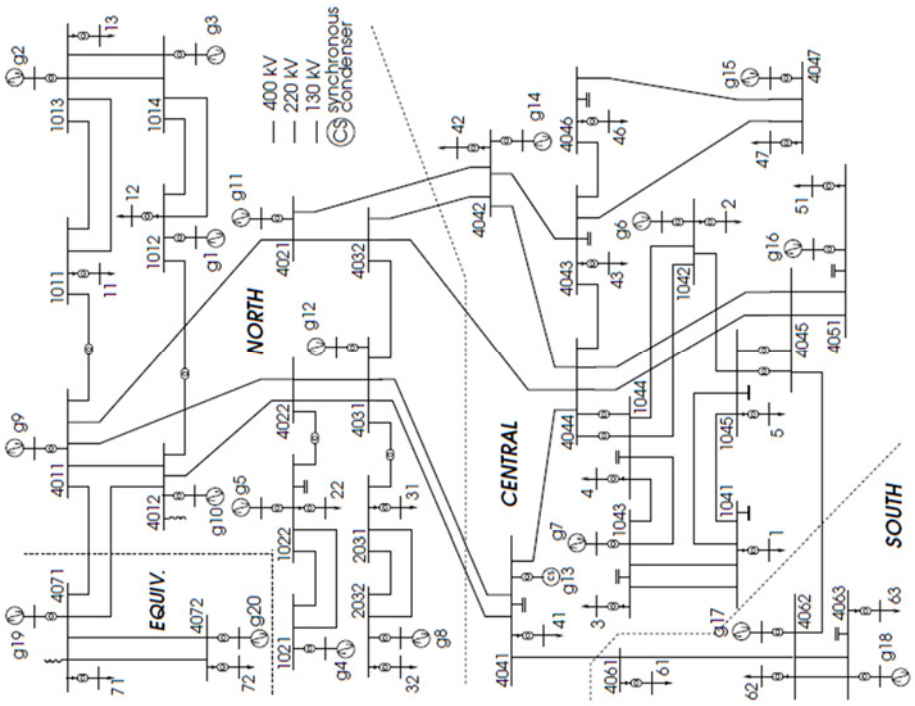

Fig. D-1 Nordic-32-Bus system, [87]

The referenced branch numeration for the transmission lines and transformers is given in Table D-1, the referenced node numeration of the nodes in Table D-2. The numeration is valid for the whole work.

Table D-1 Referenced branch numeration

Nr.	Name	from Node	to Node	Type	Nr.	Name	from Node	to Node	Type
1	1011-1013	1011	1013	Line	**31**	4031-4041	4031	4041	Line
2	1011-1013b	1011	1013	Line	**32**	4031-4041b	4031	4041	Line
3	1012-1014	1012	1014	Line	**33**	4032-4042	4032	4042	Line
4	1012-1014b	1012	1014	Line	**34**	4032-4044	4032	4044	Line
5	1013-1014	1013	1014	Line	**35**	4041-4044	4041	4044	Line
6	1013-1014b	1013	1014	Line	**36**	4041-4061	4041	4061	Line
7	1021-1022	1021	1022	Line	**37**	4042-4043	4042	4043	Line
8	1021-1022b	1021	1022	Line	**38**	4042-4044	4042	4044	Line
9	1041-1043	1041	1043	Line	**39**	4043-4044	4043	4044	Line
10	1041-1043b	1041	1043	Line	**40**	4043-4046	4043	4046	Line
11	1041-1045	1041	1045	Line	**41**	4043-4047	4043	4047	Line
12	1041-1045b	1041	1045	Line	**42**	4044-4045	4044	4045	Line
13	1042-1044	1042	1044	Line	**43**	4044-4045b	4044	4045	Line
14	1042-1044b	1042	1044	Line	**44**	4045-4051	4045	4051	Line
15	1042-1045	1042	1045	Line	**45**	4045-4051b	4045	4051	Line
16	1043-1044	1043	1044	Line	**46**	4045-4062	4045	4062	Line
17	1043-1044b	1043	1044	Line	**47**	4046-4047	4046	4047	Line
18	2031-2032	2031	2032	Line	**48**	4061-4062	4061	4062	Line
19	2031-2032b	2031	2032	Line	**49**	4062-4063	4062	4063	Line
20	4011-4012	4011	4012	Line	**50**	4062-4063b	4062	4063	Line
21	4011-4021	4011	4021	Line	**51**	4071-4072	4071	4072	Line
22	4011-4022	4011	4022	Line	**52**	4071-4072b	4071	4072	Line
23	4011-4071	4011	4071	Line	**53**	1011-4011	1011	4011	Transf.
24	4012-4022	4012	4022	Line	**54**	1012-4012	1012	4012	Transf.
25	4012-4071	4012	4071	Line	**55**	1022-4022	1022	4022	Transf.
26	4021-4032	4021	4032	Line	**56**	2031-4031	2031	4031	Transf.
27	4021-4042	4021	4042	Line	**57**	1044-4044	1044	4044	Transf.
28	4022-4031	4022	4031	Line	**58**	1044-4044b	1044	4044	Transf.
29	4022-4031b	4022	4031	Line	**59**	1045-4045	1045	4045	Transf.
30	4031-4032	4031	4032	Line	**60**	1045-4045b	1045	4045	Transf.

Table D-2 Referenced node numeration

Nr.	Name	Nr.	Name	Nr.	Name	Nr.	Name
1	1011	**9**	1043	**17**	4022	**25**	4046
2	1012	**10**	1044	**18**	4031	**26**	4047
3	1013	**11**	1045	**19**	4032	**27**	4051
4	1014	**12**	2031	**20**	4041	**28**	4061
5	1021	**13**	2032	**21**	4042	**29**	4062
6	1022	**14**	4011	**22**	4043	**30**	4063
7	1041	**15**	4012	**23**	4044	**31**	4071
8	1042	**16**	4021	**24**	4045	**32**	4072

E. Additional Evaluation of Dynamic Data

The following results give a brief overview of the application of the PSO based detection algorithm and comparison to the HPN based and analytical detection algorithm respectively. Further, the effects of a coordinated selection of PMU nodes on the detection is compared to a random selection.

The monitored nodes in dependency of the number of monitored nodes are given in chapter 5.2 Fig. 5-2. The branch number 21 – the line connecting nodes 4011 and 4021 – is additionally excluded from E, since its outage leads to a voltage instability followed by a loss of synchronization of the generators in the central and south parts of the grid. The single outage detection ratio of the set E is compared for the algorithm-based sets of monitored nodes and 1000 sets of random node variations for each number of observed nodes. The detection is executed for the approaches described in the chapters 5.1, 5.4.3 and 5.4.4 – analytical single line outage detection, PSO and HPN. The threshold in the output appearance for a valid detection result is set to $0.6\ \mathrm{pu}$ for both algorithms.

Taking a closer look on the resulting detection ratios over the number of observed nodes – Fig. E-1 – the equivalence of the global and adding algorithms for node selection can be seen clearly. The only exception are the results for the detection based on PSO with 16 and 17 monitored nodes. However, this difference is based on the stochastic behaviour of PSO, since the selected monitored nodes are ident.

The general improvement of the detection ratio by the selection algorithms referenced random node selection is best seen in Fig. E-1 comparing the results of analytical add and analytical random. The better detection ratio of random node selection for small numbers of monitored nodes is based on the tendency of the global and adding algorithm to spread the PMU monitored nodes over the whole network. If too few nodes are monitored, the node voltage angle information is not suitable for a definitely detection of a branch. The detection based on optimization algorithms is even more effected by the lack of information, since more possible branch combinations lead to a suitable solution of the optimizer. This can be improved by reducing the dimension of the search space. The random selection on the other hand has the chance of clustering monitored nodes in a part of the network offering enough information for a definite detection in this network part.

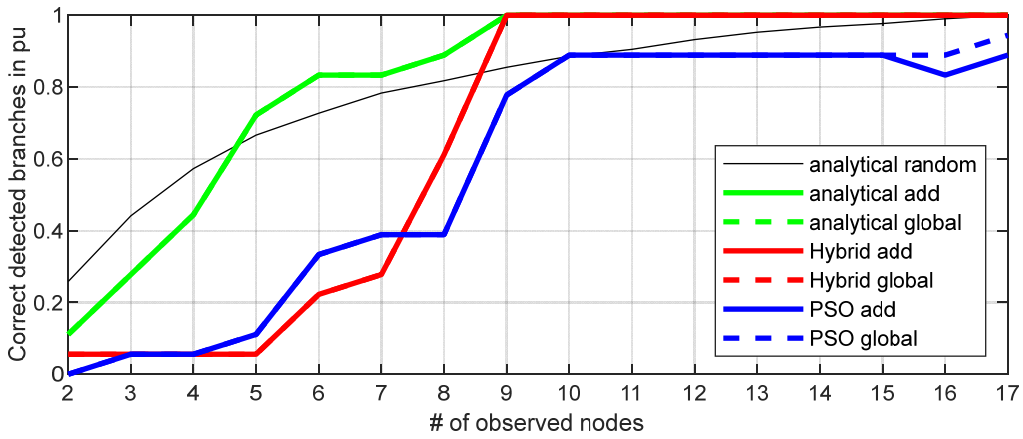

Fig. E-1 Detection ratio for reduced number PMU monitored nodes for different detection algorithms and PMU monitored node selection algorithms

The loading of the used Nordic-32-Bus system is scaled down to $70\ \%$ of the original load data from [88] to enable a stable post contingency state of the double branch outages. However, some outage combinations still have no stable solution – mainly combinations including branch 21. These instable outage combinations and outage combinations leading to the islanding of network parts are not included in the results. This leaves a set of 226 simulated branch outages defining the node voltage angle data for the evaluation of the detection algorithm.

Fig. E-2 shows the correct detection results on dynamic data for the PSO based algorithm for an appearance threshold of $0.5\ \mathrm{pu}$. The green squares indicate a correct detection of the outage combination – the correct combination has an appearance in the output data of the $10\ \mathrm{s}$ detection run higher than the necessary threshold. The red squares indicate a wrong detection – a wrong output combination has an appearance higher than the necessary threshold. The blue squares indicate no detection result – neither a correct nor a wrong combination has an appearance higher than the necessary threshold. The black squares are referenced to branch outages either resulting in islanding of grid parts or causing instabilities.

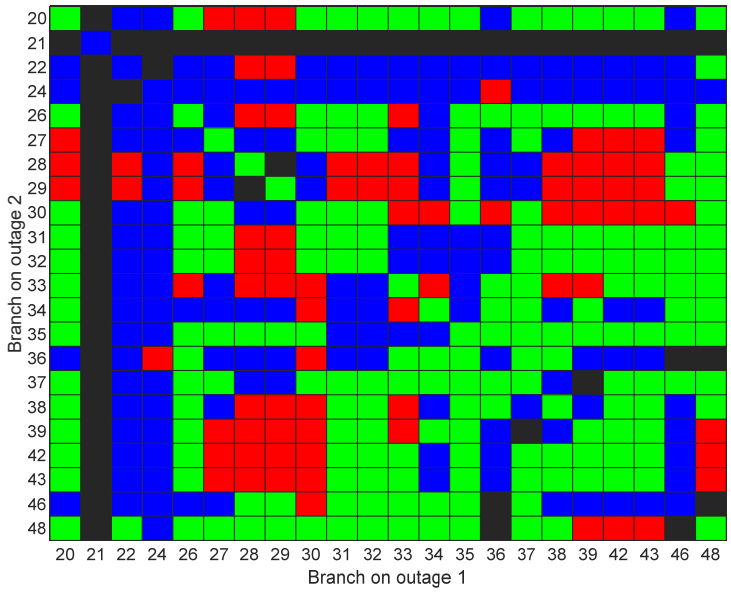

Fig. E-2 Detection result for PSO on dynamic simulation data for an appearance threshold of 0.5 pu*. Green correct detection, red wrong detection, blue no detection, black not evaluated*

The graphs in Fig. E-3 gives the shares of correct, wrong and no detection for the PSO based algorithm over the threshold. Only correct or wrong results exist for a threshold value of 0. These results are linked to the element with the highest absolute appearance in the detector output stream without any threshold and give the reflect the maximal reachable rates. The PSO correct detection ratio reaches 0.69 pu. However, due to the missing threshold one single element would be interpreted as the solution, if it is the only non-empty detection output. With increasing threshold values, the detection results are becoming more and more reliable, but the share of no detection result increases.

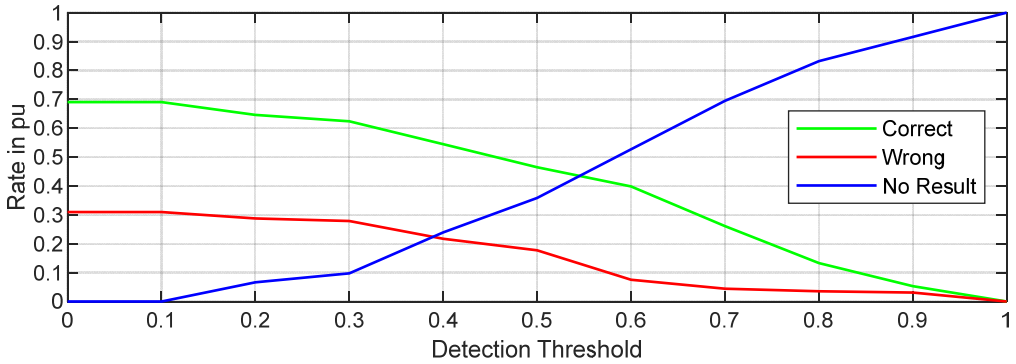

Fig. E-3 Dependency on threshold for PSO on dynamic simulation data for 17 *monitored nodes*

F. PMU Model in DigSILENT and Data processing

The implemented PMU model is composed of standard DigSILENT models [91] and creates quasi continuous data of the node voltage angle. The node voltage angle is calculated from the output of two DigSILENT PLL models “ElmPhi_pll” as shown in Fig. F-1. The first PLL has as output signals the sine and cosine of the angle difference $\Delta\vartheta$ between the measured node and the reference node of the simulation. The angle difference in radiant and its sign is calculated from the sine and cosine information. The second PLL’s[9] output is the frequency of the reference node in pu. The frequency deviation from the nominal value is multiplied with 2π and integrated to calculate the frequency depending angle drift of the reference node to the fictive global angle reference. The unrestrained node voltage angle of the measured node is derived by the sum of $\Delta\vartheta$ and angle difference of the reference node to the global angle reference. The result is further processed in the red marked part to limit the angle to a range between -π and π.

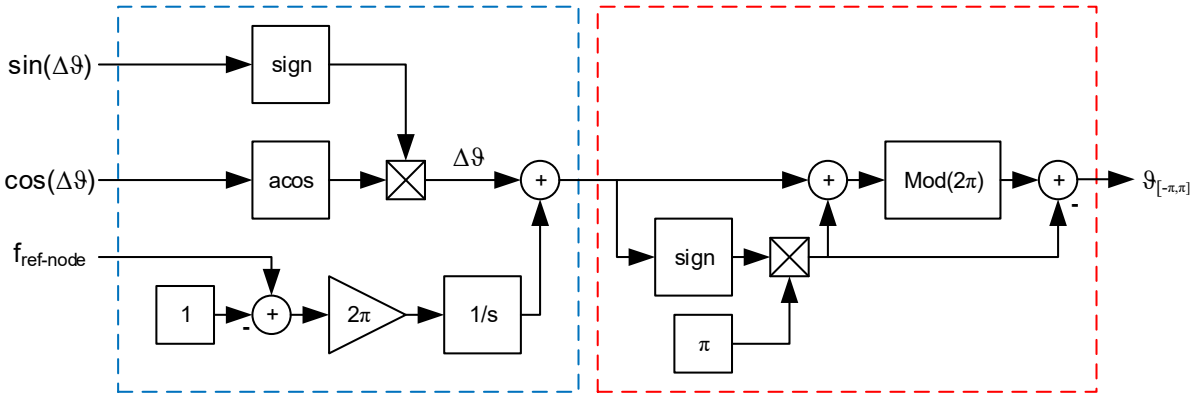

Fig. F-1 PMU measured node voltage angle model

The time course of the node voltage angle of all 32 buses of the Nordic-32 bus system after the outage of branch 24 at $t = 10\ \mathrm{s}$ is shown in Fig. F-2 as example. The resulting time course shows the characteristics of real PMU data concerning the dependency to changing grid frequency and limitation to values between -π and π.

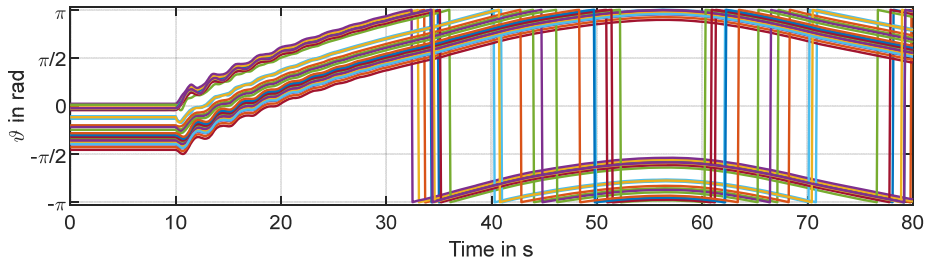

Fig. F-2 PMU measured angles of all transmission nodes in the Nordic-32 Bus system after the outage of branch 24

[9] The PLL model version 2 has to be selected with the parameter blocking voltage set to an unreachable high value to get the frequency of the reference node as output parameter.

The PMU output is referenced to the node voltage angle of the reference node and value steps of 2π are eliminated. The resulting node voltage angle difference between the considered nodes is shown in Fig. F-3. The reference node is node 32.

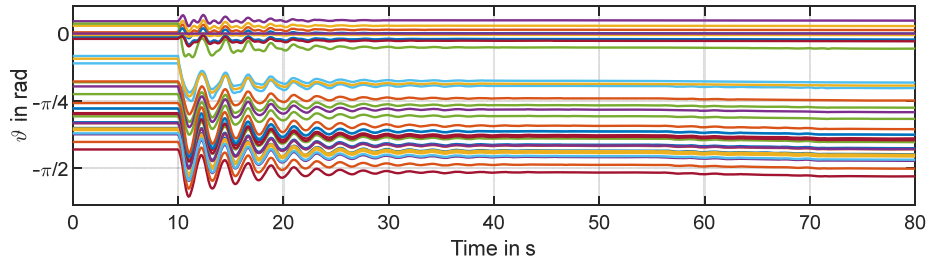

Fig. F-3 Node voltage angles referred to node 32 of all transmission nodes in the Nordic-32 Bus system after the outage of branch 24

Fig. F-4 shows the actual input data stream for the optimizer of the detection algorithm. To achieve this data, the difference of the node voltage angles to their values before the contingency occurs is calculated.

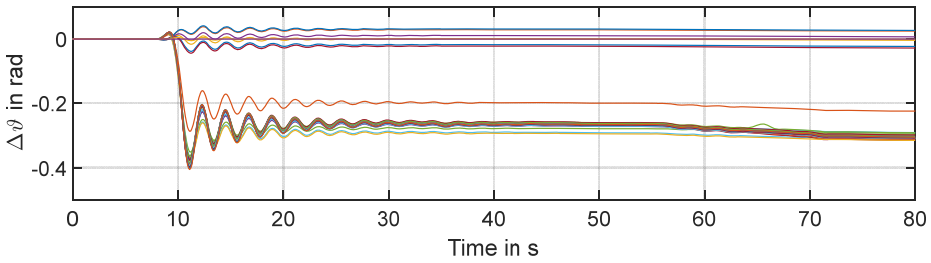

Fig. F-4 Input data stream for the optimizer of the detection algorithm for all transmission nodes in the Nordic-32 Bus system after the outage of branch 24